Sonar Signal Design and Evaluation with Emphasis on Diver Detection

Dissertation

zur Erlangung des akademischen Grades
Doktor der Ingenieurwissenschaften
(Dr.-Ing.)
der Technischen Fakultät
der Christian-Albrechts-Universität zu Kiel

vorgelegt von

Meelis Nõmm

Kiel 2015

Tag der Einreichung: 07.10.2014
Tag der Disputation: 25.02.2015

Berichterstatter: Prof. Dr.-Ing. Peter Adam Höher
Prof. Dr.-Ing. habil. Tobias Weber

Preface

Life moves in mysterious ways...

When I started with my master thesis I was certain that I do not want to do a doctorate. Pretty much my only criteria to my supervisor was that the topic should be standalone and not a prelude for a doctorate.

Things took a different turn, when one of the results from my work showed that something what had been assumed to be quasi optimal, was actually the cause of many peculiarities. I guess some of the praise from my supervisor got through to me and after the master thesis defense, I found myself facing a question: "Would I forgive myself if this will lead to something bigger and I had decided to stop here?"

I decided, I would not. That is how I joined the Information and Coding Theory Lab (ICT), lead by Prof. Dr.-Ing. Peter Adam Höher. I spent some of the best years in ICT. Splendid colleagues, nice environment and probably having one of the best possible chefs for independent research. I learned a lot, most importantly about myself, who I'm, what am I good at, what I do and don't like to do and where are my limits.

I knew beforehand that writing the dissertation would be a pain and it was. But with enough breaks, small steps, plenty of coffee and help from colleagues and friends, I made it. Herewith, I would like to thank all the (kitchen gang) colleagues who made the pleasant environment, especially the ones with whom I had the pleasure to share the room D-020: Christian Schröder, Dapeng Hao, Roman Kreimeyer, Kathrin Wilkens, Gilbert Forkle, Niklas Doose, Abdullah Yaqot, Martin Damrath or work together: Tianbin Wo, Zhenyu Shi, Kathrin Schreiber, Rebecca Adam, Dennis Küter, Duc Nguyen and Tim Claussen. Special thanks goes to Christopher Knievel who had the splendid opportunity to proof read the whole dissertation and probably still recalls me, when he sees sentences constructed with "... , then ... ". Finally, I would like to thank my professor Peter Adam Höher who made it all possible.

Almost forgot. Of course, I also want to thank my family who was in Estonia and who had the patience to wait for my return.

Before I finished in Kiel, people asked me what would I do when I return to Estonia and I would say: "Probably I will look for a job in the telecommunication sector as I don't think sonar detection is such a hot topic in Estonia". Well again, life proved me wrong.

Tallinn, July 2015 Meelis Nõmm

Abstract

Sonar-based underwater surveillance, including the problem of diver detection, is a challenging task. In harbors and coastal areas the environment is often reverberation dominated, due to the numerous backscattering objects and boundaries like ship wrecks, harbor walls, seabed, or the water surface. Reflections from the target and the background are often very similar, except for the fact that the target is typically moving and the background is not. The object movement causes a Doppler effect that can be used to improve the separation of moving objects from the quasi-stationary background. Therefore, the ideal active sonar transmit signal would simultaneously provide very good range and Doppler resolution.

In this work, existing sonar signal designs are thoroughly analyzed and special emphasis is set to understand the sources of their advantages and disadvantages. Among all the investigated waveforms, frequency modulation (FM) signals have the best properties, but they lack Doppler selectivity that is required to detect small moving targets in reverberation limited environments.

This motivates the development of a new design – called cutFM signal. The goal is to create a Doppler selective waveform based on a linear frequency modulated signal. The basic concept is to cut out frequency components from the base signal, in order to obtain a comb like spectrum. The effect of cutting is analyzed in detail and it is shown that the cutting period has to be carefully selected in order to achieve the desired result – a Doppler selective signal.

The cutFM signal is compared theoretically and via simulations with corresponding known alternatives. It is characterized by a very good Doppler processing gain and excellent performance in reverberation limited channels. In addition, compared to the known continuous wave (CW) based signals that have equivalent Doppler processing gains, the cutFM signal provides improved range resolution.

Keywords: Sonar, diver detection, transmit signal design, frequency modulation, Doppler selectivity, ambiguity function, Q-function, moving target, reverberation, detection algorithms, matched filtering.

Kurzfassung

Eine sonarbasierte Unterwasserbeobachtung, einschließlich dem Problem der Taucherdetektion, ist eine schwierige Aufgabe. In Häfen und Küstengebieten ist die Umgebung oft nachhalldominiert aufgrund der vielen reflektierenden Objekte und Grenzflächen wie Schiffswracks, Spundwänden, dem Meeresboden und der Wasseroberfläche. Reflektionen ausgehend vom Zielobjekt und vom Hintergrund sind oft sehr ähnlich mit Ausnahme der Tatsache, dass sich das Zielobjekt häufig bewegt während der Hintergrund quasi-stationär ist. Die Bewegung des Zielobjekts bewirkt eine Dopplerverschiebung, welche zur Trennung zwischen quasi-stationären und beweglichen Objekten genutzt werden kann. Somit zeichnet sich ein ideales aktives Sonarsignal gleichzeitig durch eine sehr gute Entfernungsauflösung als auch durch eine Dopplerauflösung aus.

In dieser Arbeit werden bekannte Sonarsignale ausführlich analysiert, unter besonderer Berücksichtigung der Ursachen hinsichtlich ihrer Vor- und Nachteile. Von allen untersuchten Signalformen erweisen sich frequenzmodulierte (FM) Signale als am besten geeignet, allerdings sind FM-Signale nicht Dopplerselektiv, was notwendig wäre um kleine Zielobjekte in nachhalldominierten Umgebungen detektieren zu können.

Dies motiviert die Herleitung eines neuen Signalentwurfs – cutFM-Signal genannt. Dabei ist das Ziel, eine dopplerselektive Signalform basierend auf einem linear frequenzmodulierten Signal herzuleiten. Die Kernidee besteht darin, Frequenzkomponenten aus dem Basissignal herauszuschneiden, um ein kammförmiges Spektrum zu erhalten. Der Effekt des Herausschneidens wird detailliert analysiert und es wird gezeigt, dass die Auslöschungsperiode sorgfältig gewählt werden muss um das gewünschte Ergebnis zu erzielen – ein dopplerselektives Signal.

Das cutFM-Signal wird analytisch und simulativ mit bekannten alternativen Signalformen verglichen. Es weist einen sehr guten Doppler-Prozessgewinn und eine exzellente Leistungsfähigkeit in nachhallbegrenzten Kanälen auf. Ferner, im Vergleich zu bekannten Continuous Wave (CW) basierten Signalen mit äquivalentem Doppler-Prozessgewinn, weist das cutFM-Signal eine bessere Entfernungsauflösung auf.

Stichwörter: Sonar, Taucherdetektion, Sendesignalentwurf, Frequenzmodulation, Dopplerselektivität, Mehrdeutigkeitsfunktion, Q-Funktion, bewegtes Zielobjekt, Nachhall, Detektionsalgorithmen, Matched Filterung.

Contents

Chapter 1

Introduction

1.1 Background

The term sonar stands for sound navigation and ranging. It is a technique that utilizes sound propagation in a medium to locate obstacles and objects. Animals like whales and bats have been using sound for navigation and communication for a long time. From an engineering aspect, sonar truly rose into focus after the Titanic misfortune in 1912, motivating engineers to design underwater echo sounders to detect icebergs. The next big milestone for sonar was the introduction of submarines during World War I that stimulated development of more sophisticated underwater detection systems. Most of the research in the field of underwater signalling and detection is and has been done considering the target to be a submarine. Nevertheless, underwater detection is no longer a purely military field. Recently diver detection sonar (DDS) systems have become commercially available and have been deployed on various offshore wind farms and big harbors. Similar systems have also been deployed for fish detection and classification. This has given new incentive to develop improved diver detection systems.

Sonar systems can be classified into two groups: passive and active sonar. A passive sonar system only listens to (or receives) the sounds from the environment and is dependent on the object to emit acoustical waves. It is therewith limited in capability and can not be used for standard navigation or ranging of silent objects. Active sonar removes this limitation, by emitting a signal itself and listening to what is reflected back. Active sonar systems can "see" the surroundings and the gained information can be used for target detection and navigation.

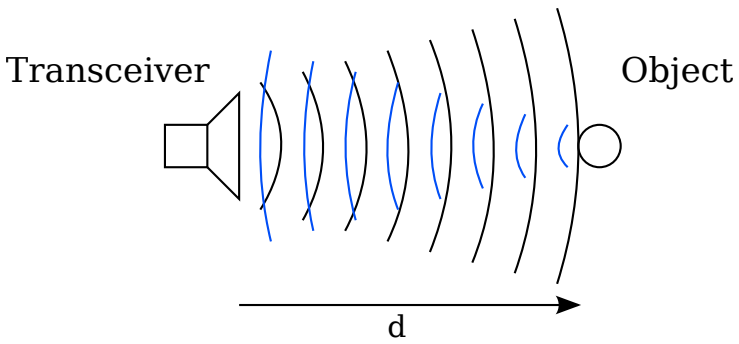

Figure 1.1: Illustration of the working principle of sonar.

So how does an active sonar work? Figure 1.1 illustrates the main working principle of active sonar. The transceiver, a transmitter and receiver in one, emits an acoustic wave. The wave propagates through

the medium with velocity c. Once reaching the object, a part of the acoustic wave is reflected back and the reflected signal is received by the transceiver. By measuring the propagation delay τ of the reflected signal, the system can calculate the distance of the object via

$$d = \frac{\tau c}{2} \, . \tag{1.1}$$

The factor two in the denominator is due to the fact that the acoustic wave has to travel to the object and back. This formula holds for a setup where the transmitter and receiver are collocated – a monostatic system. Given the components are in different locations the system is referenced to as either a bistatic or a multistatic system, in which case more sophisticated ranging algorithms than (1.1) have to be used. Overall, the monostatic setup is the most common choice.

1.2 Motivation and Goal

Early sonars emitted a so called "ping" in a constant interval. The transmit signal was a short single frequency pulse – a continuous wave (CW) signal. Due to these repeated "pings", the process is also called "pinging". The CW signals were easy to generate and robust energy detectors could be used to detect reflections. However, such a short CW pulse has poor performance in low signal-to-noise ratio (SNR) situations, a property attributed to its limited signal energy. The energy can be increased by transmitting a longer signal, but with a CW signal this leads to a decreased range resolution. A second weakness of a short CW signal is that in situations with high background reflections from the environment (seafloor, water surface, harbor walls, or other objects), it becomes very difficult to separate the reflections from a target from the continuous stream of reflections from the environment, known as reverberation. In most cases, there is one property that distinguishes diver/submarine/fish from the background – the diver/submarine/fish is moving, while the dominant background sources are not. The movement of the object alters the frequency of the reflected signal, known as the Doppler effect. This effect can be used to suppress the reverberation and with that improve the detection performance.

This leads us to transmit signal designs. There are three main signal groups: the already mentioned CW signals, frequency modulation (FM) signals and random signals. All three have different advantages and disadvantages:

- CW signals in general have very good Doppler resolution, but weak range resolution.
- FM signals on the other hand have very good range resolution, but are (nearly) Doppler invariant, meaning they can not utilize the object movement to improve detection.
- Random signals aim to combine the benefits of CW and FM, providing good range and Doppler resolution, but are very sensitive to non-linear effects and, as will be shown in Sec. 3.5, can not utilize the Doppler effect to the same extent as the CW signals.

The focus of this work is on diver detection, especially in reverberation limited environments like harbors. In such environment it is often essential to use a Doppler selective transmit signal that can discriminate between moving objects and stationary reverberation. Various Doppler selective signals are known from literature, but all effective ones are based on the CW waveform and therefore all of them inherit the poor range resolution. In this work, the aim is to develop an FM based Doppler selective signal that would improve the range resolution.

The new transmit pulse design is called the cutFM signal. The cutFM signal is based on the linear frequency modulated (LFM) signal. While the LFM waveform is (nearly) Doppler invariant, the cutFM signal is made Doppler selective by periodically cutting out parts of the original LFM waveform. Following

some essential design rules, the cutFM signal offers similar Doppler resolution as the CW signal with significantly improved range resolution.

1.3 Thesis Outline

The thesis is organized as follows.

Chapter 2 provides an overview of fundamental properties of diver detection. Even though the core principles of submarine and diver detection are alike, they differ in details. Topics like center frequency, target speed, target strength, reverberation, etc., are discussed and typical parameter values from literature are provided for reference.

Chapter 3 introduces signal analysis tools like correlation function, ambiguity function and Q-function. These tools are then used to thoroughly analyze existing well-known signals. The capabilities of CW, FM, random signals and their specific modifications are presented. The knowledge about the existing designs builds the foundation to develop a new signal for diver detection. Additionally, the importance of windowing is discussed and a small selection of windowing functions is reviewed.

Chapter 4 is dedicated to the cutFM design. First the basic concept of cutting is introduced that aims to produce a Doppler selective signal. The effects of cutting (or modulation) are analyzed in depth in frequency domain and with the help of the ambiguity function. Based on the analytical results, certain design rules are formulated that assure that the resulting cutFM signal obtains good Doppler selectivity. With Doppler selectivity in mind, an overview of cutFM design parameters is given that can be used as a guide to create a signal with desired properties. These guidelines are then used to design a system for diver detection.

Chapter 5 focuses on detection schemes. First, two channel models for noise and reverberation channels are introduced that are later used for detector comparison via simulations. Square-law, energy, matched filter and principle component inverse (PCI) detectors are studied and briefly analyzed. Finally, the detector schemes are compared via simulations and the two best Doppler selective signals – cutFM and sinusoidal frequency modulated (SFM) signals - are compared in detail.

Chapter 6 summarizes the work.

Chapter 2

Fundamentals

This chapter gives an overview of fundamental properties of diver detection. The focus is on aspects that are more unique to diver detection systems and differ from the common knowledge from submarine detection. For example, due to the significantly smaller size of the diver, the system requires a higher center frequency, that in consequence increases the transmission loss due to higher absorption. The small size of the diver also means that the target strength is low and combined with the increased attenuation, the reflected signal received from the object is weak. The reduced signal strength of the reflection from target is one challenge, the second is the increased interference from the surrounding environment. Diver detection systems are primarily deployed in harbors, a shallow water environment where the interference is mostly dominated by the reflections from the seafloor, surface, and various stationary objects in the surroundings. While the channel conditions for diver detection are much more challenging, the acceptable detection range compared to the submarine case is also smaller. The divers movement speed is considerably lower and the warning has to arrive sufficiently early in order to apply counter measures before the diver reaches the destination.

The following sections introduce the principle challenges in diver detection and aim to familiarize the reader with the specific assumptions about the underwater properties that are going to be used in the later chapters.

2.1 Center Frequency

The center frequency used in diver detection sonar (DDS) systems is mainly in the range of $60-100$ kHz, yet some systems support frequencies up to 300 kHz [KH06]. In comparison, for submarine detection systems the frequencies vary from 300 Hz to 2000 Hz for longer range towed arrays and from 3 kHz to 15 kHz for shorter range hull mounted systems [Wai02]. A few existing DDS examples: The AquaShield from DSIT Solutions uses a 60 kHz center frequency, the Sentinel from Sonardyne and the Westminister Marine Intruder Detection Sonar (WG MIDS) operate at 70 kHz, the DDS900 from Kongsberg Mesotech operates around 90 kHz, and the Cerberus from Atlas Elektronik operates at 100 kHz (sources: [Zha07] and the corresponding datasheets from the companies websites). In this work, without loss of generality, the center frequency is selected to be at 70 kHz and is unchanged throughout the whole analysis in the following chapters.

The increased frequency improves the resolution of the system, but at the same time also increases the transmission loss due to absorption.

2.2 Transmission Loss

The transmission loss in water consists of two additive components, the spreading loss and the attenuation loss (or often also referred to as the absorption loss),

$$TL = A \log_{10} r + \frac{r}{1000} \cdot \alpha \ , \tag{2.1}$$

where A is the spreading coefficient, r the propagation range in meters, and α the attenuation coefficient in dB/km, therefore also the conversion $r/1000$. The spreading loss is frequency independent and purely caused by the diffusion of the acoustic wave. In an unbounded isotropic medium, under the spherical spreading law [Wai02], the spreading loss TL_s is

$$TLs = 20 \log_{10} r \ , \tag{2.2}$$

where $A = 20$. In case of a bounded isotropic environment, where the source is between two parallel planes, under the cylindrical spreading law, the spreading coefficient is reduced to $A = 10$. These two spreading cases correspond to two extremes and they provide the upper and lower limits for the spreading coefficient A. For realistic shallow water environments the value of A is somewhere between these two limits.

In [HCT97], the authors determined the transmission loss during a sea-trial off the coast of Nova Scotia, Canada. The water depth was approximately 100 meters and their estimate for the spreading loss was

$$TL_s = 18.4 \log_{10} r \ . \tag{2.3}$$

The measured estimate for the spreading loss is significantly higher than that predicted for a bounded environment by the cylindrical spreading law. One reason for this is that the seabed and ocean surface are not perfect reflectors as assumed under the cylindrical spreading law. Therefore, without location specific measurements or knowledge about the environment, the factor $A = 18.4 \pm 0.7$ given in [HCT97], can be assumed to be a better approximation for the spreading loss in shallow waters, than applying the cylindrical spreading law with $A = 10$.

The second component of the transmission loss, namely the attenuation loss, is frequency dependent and includes the effects of absorption, leakage out of ducts, scattering and diffraction [Ett96]. The attenuation coefficient α in (2.1) increases with frequency. There are a number of different formulas and tables for the attenuation loss. According to Etter [Ett96] and Hodges [Hod11], the most common formula for α is the one from Thorp [Tho67],

$$\alpha = 1.094 \left[\frac{0.1 f^2}{1 + f^2} + \frac{40 f^2}{4100 + f^2} \right] \ . \tag{2.4}$$

The attenuation α is given in dB/km and the frequency f in kHz. E.g. for $f = 70$ kHz, $\alpha = 23.9$ dB/km. Inserting $A = 18.4$ and $\alpha = 23.9$ into (2.1), the approximate transmission loss in shallow water for $f = 70$ kHz over the propagation range is shown in Fig. 2.1. According to the figure, the two-way path loss for a target at 1000 m ($r = 2000$ m) would be 108 dB.

The formula for the attenuation coefficient in (2.4) gives a rough estimate. A more comprehensive formula for the absorption is given by François–Garrison [FG82], where additionally the water temperature, salinity, pH, and depth are taken into account.

The terms attenuation and absorption are often used interchangeably. In most cases, like in [FG82], the formula for the α coefficient is derived in coincidence with measurements where the absorption is the dominant term (e.g. deep sound channels in oceans). Therefore, often the scattering (or part of it) is instead included in the spreading loss. The spreading loss with $A = 18.4 \pm 0.7$, given in [HCT97], was

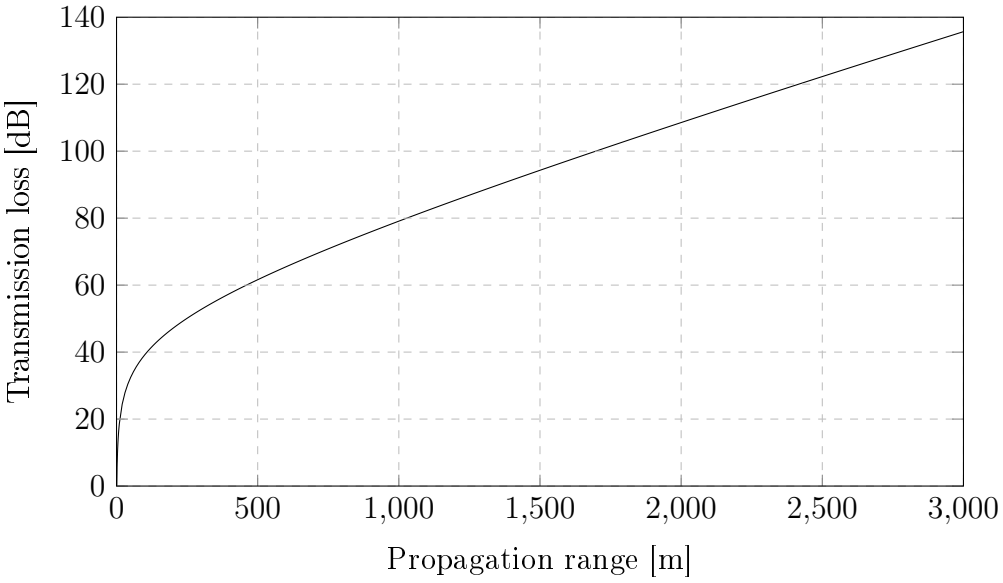

Figure 2.1: Transmission loss.

calculated from the total transmission loss minus the absorption loss (calculated using [FG82]). Therewith, the interaction with the boundaries was inherently included into the spreading loss. Additionally, considering that the authors reported steady strong southeast wind ($12 - 15$ m/s) during the measurements and that the seabed was rough (mainly cobble), then the $A = 18.4$ value can be considered to be a pessimistic estimate and for more favorable channel conditions, the A value can be expected to be lower.

2.3 Speed of Sound

Concerning target detection, the speed of sound is relevant for two aspects. In case of a moving target, the resulting Doppler effect (cf. Sec. 2.5) can be used to improve the detection probability and the Doppler frequency shift depends on the speed of sound. The Doppler analysis is a core part of this work and will be used extensively in the following chapters. The speed of sound is also used for detailed modeling of the channel, using methods like ray tracing. Ray tracing can be used to predict the sound propagation in the water, based on the information like the bathymetry, boundary reflection coefficients, sea state (wave height), attenuation, and the sound speed profile (SSP) (extensive overview of modeling is given by Etter in [Ett96]). Sound propagation modeling is not included in this work, but in general (if possible) such wave propagation prediction methods should be used before installing a DDS, to identify shadow zones – regions from where the system receives no or too weak returns.

The speed of sound in water is around 1500 m/s, but it varies with the water temperature, pressure, and salinity [Hod11]. Therefore, instead of a single value often the SSP over the water depth is given. A simple approximation for the sound speed, used in [FG82], is given by

$$c = 1412 + 3.21\mathcal{T} + 1.19S + 0.0167D \ , \tag{2.5}$$

where $\mathcal{T}$ is the temperature in ℃ , S is the salinity in ppt (parts per thousand), and D is the depth in meters. Various empirical formulas exist for calculating the speed of sound. The above given formula is a rough approximation, for better (more detailed) approximations cf. [Ler69, MA64, Del74, CM77].

It is evident from (2.5), that the temperature has a significant influence on the sound speed. Especially in shallow water environments, where the temperature can be strongly time variant, depending of the

location and the season of the year. The water temperature changes due to the heating from the sunlight and significant fluctuations of the water temperature are caused by currents, tidal flows, and the wind direction. In [CCHM09] a DDS test at Shearwater, Nova Scotia, Canada, in 2008 is described. Over the course of the test, the measured water column temperature profile changes greatly over the days, from near constant +15 ℃ over the whole 20 m depth to just +10 ℃ in the upper 5 m, decreasing to around +4 ℃ for depths beyond 10 m. This also shows the difficulty of modeling a shallow water environment.

In [LZ13] the authors show the SSP variability based on another measurement campaign. The sound speed varies in the range of $1465 - 1510$ m/s and for the same depth over multiple measurements the difference is as high as 30 m/s. Hence, clearly the speed of sound is not constant and if it is assumed to be a constant at 1500 m/s, then a possible error of around 40 m/s or 2.7% should be considered. For modeling, a good estimate for the SSP is crucial, but for the calculation of the Doppler effect, as will be shown later, the influence of the inaccuracy is marginal.

2.4 Target Speed

As mentioned earlier, in order to improve submarine or diver detection, a system can utilize the fact that the object is moving and the reflections from surroundings are (near) stationary. As much as one can find from forums in the Internet, a scuba diver with gear can travel longer distances without much effort with 0.5 knot (0.26 m/s). Divers with good physical condition and training can increase the speed to 1.0 knot (0.514 m/s) or even up to 2.0 knot for shorter distances. In addition, movement aids for divers should be considered. A number of various underwater scooters exists. Common underwater scooters like the Sea-Doo GTI or RS1 move with speeds up to $1.1 - 1.7$ m/s. The so called "worlds fastest" SEABOBF7 is said to be able to achieve speeds up to 8.7 mph (3.9 m/s). Therefore, a DDS should cover movement speeds from $0.0 - 4$ m/s. Concerning, the Doppler analysis in the later chapters, velocity of most interest is selected to be in the range of $0.3 - 3$ m/s.

2.5 Doppler Effect

A signal reflected from a moving object is altered by the Doppler effect. Essentially, when an object is moving towards the source, the sound waves are compressed by a factor related to the object velocity, due to the reduced traveling distance till reflection. The Doppler scaling factor is given by [KW65, Lin88, Col96]

$$\eta = \frac{1 + v/c}{1 - v/c} = \frac{c + v}{c - v} = 1 + \frac{2v}{c - v} \ , \tag{2.6}$$

as $v << c$, then

$$\eta = 1 + \frac{2v}{c - v} \approx 1 + \frac{2v}{c} \ . \tag{2.7}$$

The signal reflected from an object moving with velocity v towards the receiver is compressed by a factor η. The compression (or stretching) leads to a frequency shift, called the Doppler frequency shift or often also just the Doppler shift [Hod11, Wai02], given by

$$f_D = \frac{2v_t \cos(\phi) f}{c} = \frac{2vf}{c} \ , \tag{2.8}$$

where v_t is the target velocity and $v = v_t \cos(\phi)$ is the radial velocity towards the receiver. Throughout this work, the velocity always refers to the radial velocity. Hence, the frequency of the signal after the Doppler effect is

$$f^D = f + f_D = f\left(1 + \frac{2v}{c}\right) = f\eta \ . \tag{2.9}$$

E.g. for $f = 70$ kHz, $v = 0.5$ m/s, $c = 1500$ m/s, the $f_D = 46.7$ Hz. The Doppler frequency shift can be used to discriminate reflections caused by moving targets from reflections caused by stationary background, using their spectral difference.

From (2.9), it seems as the signal would experience "a" frequency shift, but as f_D in (2.8) is a function of the signal frequency, f, then for wideband signals the frequency shift is variable. This affect will be discussed in more detail in Chapter 3.

Earlier it was brought out that the speed of sound is not a constant, but has an uncertainty of about 2.7%. However, for the Doppler analysis this ambiguity is not significant and for this reason, it is uncritical to assume a constant speed of sound for the Doppler frequency shift calculations.

2.6 Target Strength

Along with the transmission loss, the target strength (TS) of the reflecting object influences the received signal strength. The target strength of an object is related to its cross-section. A diver swimming towards the receiver has a relatively small acoustic cross-section. The main reflective surfaces are the head, torso, and the air tank. In [HKP06] the authors show that the scattering at 100 kHz from a divers body, suit, and air tanks varies between -18 dB to -27 dB, averaging about -23 dB. The dB values are given in reference to an object with 1 m^2 cross-section, i.e. dB re m^2. The scattering strength from the bubbles exhaled by the diver is in the range of -10 dB to -20 dB, averaging -15 dB. These estimates are used and confirmed by Zhang in [Zha07], that focuses on diver target strengths based on the average human lung size and structure. This provides an estimate for the target strength of a diver and gives the baseline for comparison with reverberation.

2.7 Ambient Noise

Ambient noise consist of all the noise sources from the environment. Dominant noise sources in the higher $60 - 100$ kHz range are the wind (air bubbles from breaking waves), rain, marine life, and thermal noise. The noise level is given in comparison to the reference sound intensity having a root mean square pressure of 1 µPa (micropascal), denoted dB re 1 µPa [Wai02]. The average noise level at 70 kHz, according to [Hod11, Wai02], is around 40 dB re 1 µPa. In case of heavy rain or strong winds the level can increase to 60 dB re 1 µPa. In [DMCA07] the authors give an overview of underwater ambient noise and based on [AG71], state that in ports the noise level can be expected to the about $10 - 20$ dB higher than usual. Hence, a conservative estimate for the noise level in harbors would be around 60 dB re 1 µPa.

2.8 Reverberation

Ambient noise is a type of interference that is independent of the sonar system activity. On the other hand, reverberation is interference caused by the active sonar transmitting a signal. Excluding the reflections from the target and other target like objects, the reverberation encloses all reflections from the underwater environment. The reverberation sources include the sea bottom, the surface, and the water volume. The bottom and surface are both two-dimensional scatterers and hence can be considered jointly as boundary reverberation. Volume reverberation is caused by bubbles, marine life, and other inhomogeneities in the water.

Reverberation is a summation of signals that stem from the transmitted signal and are scattered back in the direction of the source from the environment, therefore its spectral characteristics are nearly the same as that of the transmit signal. The nature of the interference makes it difficult for the receiver to

distinguish the target from the reverberation. Additionally, if in noise limited case the signal-to-noise ratio (SNR) can be improved by increasing the transmit power, then reverberation can not be overcome by increasing the transmit power, as the signal strengths of both the target and reverberation are affected equally.

2.8.1 Backscattering Strength

The fundamental quantity that is used to describe the reverberation intensity is the backscattering strength, BS, or also referred to as scattering strength [Ett96, Wai02]. The backscattering strength is given as the ratio (in dB) of the intensity of the sound scattered (back to the sonar) by a unit area or unit volume, I_s, referred to a distance of 1 m, to the intensity of the incident plane wave, I_i,

$$BS_{b,v} = 10 \log_{10} \frac{I_s}{I_i} \ , \tag{2.10}$$

where $BS_{b,v}$ denotes the backscattering strength for boundary (b) or volume (v) reverberation.

2.8.2 Volume Reverberation

The backscattering strength of volume reverberation in shallow waters varies depending on the density of the marine life and air bubbles in the water column. According to Ainslie [Ain10], the suggested BS_v values for shallow waters are -85 dB for sparse, -72 dB for intermediate, and -62 dB for dense marine life. Volume reverberation in shallow waters can be expected to be significantly higher than in oceans, as the water may carry around a high amount of sediment particles or various floating objects. Even so, for shallow waters the boundaries are the dominant source of reverberation.

2.8.3 Surface Reverberation

Surface reverberation depends on the grazing angle, the wind speed, and the signal frequency. In underwater environments, the grazing angle, the angle between the incident plane wave and the surface, illustrated in Fig. 2.2, is used instead of the angle of incidence.

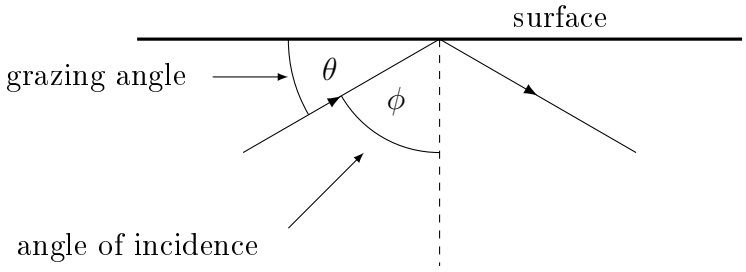

Figure 2.2: Illustration for grazing angle.

Surface backscattering strength, BS_s, is directly related to the roughness of the surface. The main physical mechanics causing the backscatter are the specular (mirror-like) scatter from facets of the surface at high grazing angles and at low grazing angles the backscatter from subsurface air bubbles. The contribution from the bubbles is particularly evident for frequencies higher than 10 kHz [Hod11]. In [SS64], Schulkin and Shaffer give an empirical formula based on the Rayleigh roughness parameter, fitted to a number of surface backscatter data, for the surface backscattering strength

$$BS_s = 9.9 \log_{10}(fh \sin\theta - 45.3) \ , \tag{2.11}$$

where f is the frequency in kHz, and h is the wave height. The wave height can be calculated from the wind speed (in knot),

$$h = 0.0026v^{\frac{5}{2}} \ . \tag{2.12}$$

Figure 2.3 shows the BS_s estimates for various wind speeds, using (2.11). According to [McD93], in shallow waters the surface backscattering strengths for lower grazing angles can be up to 10 dB higher than for oceans. It is assumed that this is caused by the increased level of bubbles in the water, due to the waves breaking at lower wind speeds. Nevertheless, according to multiple sources, e.g. [Hod11, HE97], the sea bottom scattering is the dominant source of reverberation in shallow waters.

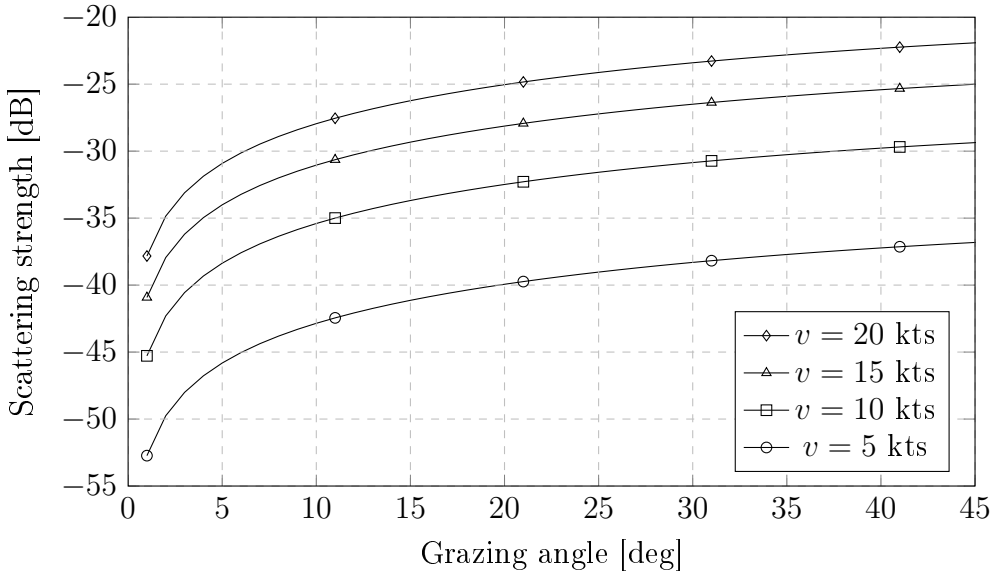

Figure 2.3: Surface backscattering strength estimates for various wind speeds and grazing angles.

2.8.4 Bottom Reverberation

Bottom scattering can be much more complex than surface scattering. Bottom backscattering strongly depends on the seabed type, i.e. sand, gravel or rocks. Additionally, the acoustic waves can interact with different bottom layers and sound can be reflected back from these lower layers. Therewith, a seabed can not be characterized by a single roughness value, as was the case for the surface. Another difference between the two boundaries is that, given a certain wind speed, the surface roughness can be assumed to be constant over the whole detection range. For a seabed, the characteristics of the bottom roughness and composition can vary over the distance, increasing the variance of the measured backscattering strength. In addition to the bottom type, the backscattering is strongly affected by the bathymetry and often the seabed is not flat.

The bottom backscattering strength, BS_b, is often estimated using the Lambert's law

$$BS_b = 10\log_{10}\mu + 10\log_{10}(\sin^2\theta) \ , \tag{2.13}$$

where μ is the bottom backscatter constant. The bottom backscattering strengths are usually given in terms of the $10\log_{10}\mu$, known as the "Lambert's parameter". According to [Ain10], the $\sin\theta$ dependence stems from the increasing scattering area as the grazing angle increases. A few scattering strength curves based on (2.13) are shown in Fig. 2.4. For clarity it should be mentioned that originally in optics, the

Lambert's law is given over the cosine of the angle of incidence, also known as the Lambert's cosine law and therefore occasionally (2.13) has a different form.

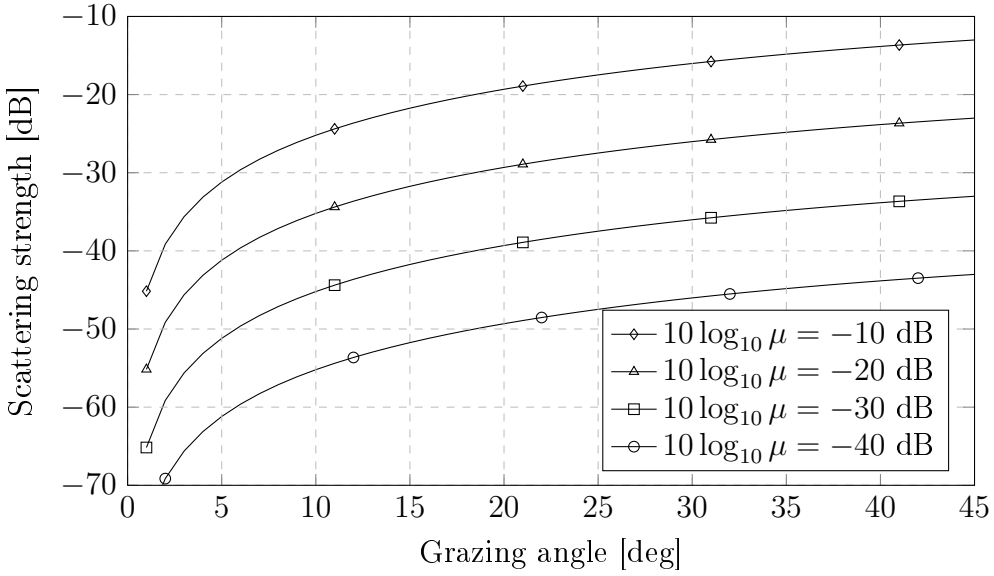

Figure 2.4: Scattering strength as a function of grazing angle and the Lambert's parameter.

Unfortunately, due to the complicated and varying nature of the seabed, there are no concrete values for the BS_b [Ain10]. However, there are estimates for the Lambert's parameters for various bottom types. Based on the values summarized in [Ain10], for rock bottoms the $10\log_{10}\mu$ estimates vary from -2 dB to -11 dB, for gravel from -7 dB to -19 dB and for unconsolidated sediments (i.e. sand, silt, clay) the estimates vary from -16 dB to -30 dB. The uncertainty is big and the estimates found in the literature vary significantly. For example, Hodges in [Hod11] suggests $10\log_{10}\mu = -45$ dB for mud and -25 dB for rock bottom. However, in conjunction with the backscatter strength estimates from e.g. [LA99], it seems that the values suggested by Hodges are lower than other authors report from measurements.

The bottom backscattering strength is also frequency dependent, but only partially. Namely, for smoother sea floor types it is frequency dependent, but independent for rougher (gravel, rock) bottoms. For medium sized sand (grain size in the range of $250 - 500$ µm), it has been shown that the Lambert's parameter increases with frequency according to [GHM04]

$$10\log_{10}\mu_{sand} = -40 + 14.7\log_{10}(f/5)\ , \tag{2.14}$$

where f is the frequency in kHz. According to (2.14), for $f = 70$ kHz, $10\log_{10}\mu_{sand} = -23$ dB. In case the seabed consists of a mixture of sand and gravel, then the Lambert's parameter should be increased accordingly.

2.8.5 Reverberation Target Strength

The reverberation strength depends on the area or volume illuminated by the transmitter and on the part seen by the receiver. The same way as the diver has a target strength based on its physical dimensions, the reverberation target strength, TS_r, is given by

$$TS_r = BS_{b,v} + 10\log_{A,V}\ , \tag{2.15}$$

where A and V are the total reverberating area or volume, respectively [Wai02]. The reverberating volume is illustrated in Fig. 2.5 and is given by

$$V = \int_V B_T B_R dV = \frac{cT}{2} R^2 \int_V B_T B_R d\Theta \ , \tag{2.16}$$

where $d\Theta$ is the solid angle element. Correspondingly, B_T and B_R are the transmitter and receiver beam patterns. The reflections from all the scatterers in the elemental volume dV arrive at the receiver simultaneously. The front end of the pulse scattered back from more distant scatterers arrives at the same time as the back end of the pulse scattered back from the front scatterers. Therefore, the height (or length) of the cylinder is $cT/2$, where T is either the duration of the transmit signal (CW) or the coherence time $T_c = 1/BW$ for wideband signals.

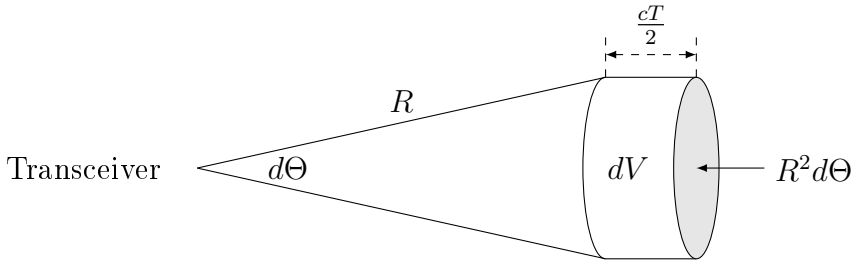

Figure 2.5: Reverberating volume.

According to [Wai02], if R is large compared to the volume cross-section, the volume calculation can be simplified to

$$V = \frac{cT}{2} \frac{R^2 \pi \theta_h \theta_v}{4} \ , \tag{2.17}$$

where θ_h and θ_v are the equivalent two-way horizontal and vertical beamwidths in radians.

Similarly for boundary reverberation, the reverberating area depends on the equivalent two-way horizontal beamwidth

$$A = \frac{cT}{2} R \theta_h \ . \tag{2.18}$$

Therewith, assuming $R = 500$ m, $\theta_h = 3^\circ (0.052$ rad), $T = 0.1$ s, $c = 1500$ m/s, and the $BS_b = -30$ dB, the reverberation target strength is

$$TS_r = -30 + 10 \log_{10} A = -30 + 10 \log_{10} 1963 \approx 3 \ , \tag{2.19}$$

approximately 3 dB. In comparison, the average target strength of the diver is between -25 dB to -15 dB (cf. 2.6).

In conclusion, the diver detection in harbors is no easy task. The reflection from the target is weak, the target is small and the attenuation of the signal at the needed frequencies is high. In addition, the reflection from the small target has to be distinguished from the reverberation returns. In shallow waters the boundaries can not be avoided and depending on the bathymetry and seabed characteristics, the reverberation from a much larger seabed area can have a stronger signal strength than the target. In such unfavorable conditions, the system can improve the detection probability by utilizing the fact that the target is moving towards the transceiver. The Doppler effect provides the possibility to distinguish the target from the reverberation. Yet, not all transmit signals can use this effect equally well. For this reason, in Chapter 3 the characteristics of different transmit signals shall be analyzed based on their range-Doppler properties.

Chapter 3

Transmit Signals

In general, the approaching divers do not emit strong enough signals to enable detection with passive sonar. Therefore, diver detection systems use active sonar, where the detection is based on the reflections of transmitted signals. The transmit signal propagates through the medium, reflects back from various objects and boundaries. These reflections are received and processed in order to find objects of interest. Historically, the first signals were short single tone sinusoids, also known as continuous wave (CW) signals. The CW signal is the simplest signal form and it is easy to generate via an oscillator at a fixed frequency. As more advanced signal generators became available, the sonar systems started to use frequency modulated (FM) and modified CW signals. Along with the growing number of possible signal forms, came the need to compare their properties. Methods like cross-correlation, ambiguity diagrams and the Q-function have become the standard in evaluating the properties of signal designs.

3.1 Analysis Tools

3.1.1 Auto- and Cross-correlation

The correlation function is the basis of the signal evaluation methods. The autocorrelation function (ACF) for a complex continuous signal is defined as

$$R_x(\tau) = \int_{-\infty}^{\infty} x^*(t)x(t+\tau)dt = \int_{-\infty}^{\infty} x^*(t-\tau)x(t)dt \tag{3.1}$$

where x^* denotes the complex conjugate of x, τ is the time shift and the second formula uses a redefinition of the time, $t = t - \tau$. The correlation is a function of τ and not of t and describes the similarity between $x(t)$ and a shifted version of itself. For real-valued signals the autocorrelation function is an even function and for complex-valued signals the autocorrelation function is a Hermitian function

$$R_x(-\tau) = R_x^*(\tau) \ . \tag{3.2}$$

The cross-correlation function for complex continuous signals is defined as [OL02]

$$R_{xh}(\tau) = x(\tau) ** h(\tau) = \int_{-\infty}^{\infty} x^*(t)h(t+\tau)dt = \int_{-\infty}^{\infty} x^*(t-\tau)h(t)dt \ , \tag{3.3}$$

where $**$ denotes the cross-correlation operation. Some authors define the cross-correlation via $x(t)h^*(t-\tau)$ [CCR02], what by (3.3) would correspond to R_{hx}. This is relevant due to the fact that the cross-correlation function is not commutative

$$x(\tau) ** h(\tau) \neq h(\tau) ** x(\tau) \ , \tag{3.4}$$

instead, according to (3.3)

$$R^*_{xh}(\tau) = R_{hx}(-\tau) \ , \tag{3.5}$$

$$\int_{-\infty}^{\infty} x(t)h^*(t+\tau)dt = \int_{-\infty}^{\infty} h^*(t)x(t-\tau)dt \ . \tag{3.6}$$

This can be shown by substituting $t = \alpha - \tau$ and comparing with (3.3)

$$R^*_{xh}(\tau) = \int_{-\infty}^{\infty} x(t)h^*(t+\tau)dt = \int_{-\infty}^{\infty} x(\alpha-\tau)h^*(\alpha)d\alpha = R_{hx}(-\tau) \ . \tag{3.7}$$

For real-valued signals it means, the two cross-correlation functions are mirrored copies of each other around the delay axis. The Wiener–Khinchin theorem states that the power spectrum of a square-integrable signal or a wide-sense stationary process is equal to the Fourier transform of the autocorrelation function [Ric03]

$$S_x(f) = \mathcal{F}\{R_x(\tau)\} = X^*(f)X(f) \ , \tag{3.8}$$

where $\mathcal{F}\{\}$ denotes the Fourier transformation and $X(f)$ the spectrum of the $x(t)$ signal. Similarly, the cross power spectrum of a signal forms a Fourier pair with the cross-correlation function,

$$S_{xh}(f) = \mathcal{F}\{R_{xh}(\tau)\} = X^*(f)H(f) \ . \tag{3.9}$$

This property can be proved via the Fourier transform of the convolution function. The cross-correlation is closely related to the convolution function. The later is defined as

$$x(t) * h(t) = \int_{-\infty}^{\infty} x(\alpha)h(t-\alpha)d\alpha \ , \tag{3.10}$$

where the time for the second signal runs in the negative direction. From (3.3) and (3.10) it becomes clear that if $t = -\alpha$ is inserted into (3.3) then the relation between cross-correlation and convolution function is

$$R_{xh}(\tau) = \int_{-\infty}^{\infty} x^*(t)h(t+\tau)dt = \int_{-\infty}^{\infty} x^*(-\alpha)h(\tau-\alpha)d\alpha \ = x^*(-\tau) * h(\tau) \ . \tag{3.11}$$

Therefore, the following relations hold [Yar10]:

$$R_{xh}(\tau) = x(\tau) ** h(\tau) = x^*(-\tau) * h(\tau) \ , \tag{3.12}$$

$$R_{hx}(\tau) = h(\tau) ** x(\tau) = h^*(-\tau) * x(\tau) \ . \tag{3.13}$$

The Fourier transform of a convolution in time domain is a multiplication in the frequency domain

$$\mathcal{F}\{x(t) * h(t)\} = X(f)H(f) \ . \tag{3.14}$$

Hence, when inserting (3.12) into the formula above and knowing that $\mathcal{F}\{x^*(t)\} = X^*(-f)$, then

$$\mathcal{F}\{R_{xh}\} = \mathcal{F}\{x^*(-\tau) * h(\tau)\} = X^*(f)H(f) \ . \tag{3.15}$$

One of the main reasons why cross-correlation is the basis for active sonar signal analysis lies in the fact that the replica correlator or matched filter detector (cf. Sec. 5.2.4) is optimal for detecting signals in additive white Gaussian noise (AWGN) [Ric03] and is therefore widely applied. The matched filer and the cross-correlation are compared in the following, in order to explain the relation of the two in more detail. The matched filter detector output is defined by the convolution of the input signal with the matched filter signal (for simplicity the equations are given for real-valued signals):

$$y(t) = x(t) * h(t) = \int_{-\infty}^{\infty} x(\alpha)h(t-\alpha)d\alpha \ . \tag{3.16}$$

The impulse response of the matched filter $h(t)$ is given as

$$h(t) = s(T - t) \ , \tag{3.17}$$

where $s(t)$ is the signal to be matched (e.g. the transmit signal) and T is an arbitrary time shift that is used in practice to assure that $h(t)$ is causal, i.e. for $t < 0$, $h(t) = 0$. However, setting the arbitrary time shift to $T = 0$, the matched filter signal becomes

$$h(t) = s(-t) \ . \tag{3.18}$$

With this, (3.16) can be rewritten via (3.12) as

$$y(t) = x(t) * h(t) = x(t) * s(-t) = s(\tau) * * \ x(\tau) = R_{sx}(\tau) \ . \tag{3.19}$$

The matched filter detector correlates the reference signal with the input signal.

As mentioned earlier, the matched filter detector is optimal for detecting signals against white noise, also known as the noise-limited situation. Yet, the underwater environment often introduces also more complex effects, where modified versions of the matched filter receiver outperform the original. Even so, in order to investigate the signals analytically, the matched filter receiver is assumed. If the received signal is an attenuated and delayed version of the transmit signal, then the matched filter output signal will be a scaled and shifted version of the autocorrelation function of the transmit signal. However, if the transmit signal experiences distortions due to target movement, then the output signal will be the cross-correlation function of the distorted and undistorted transmit signal.

3.1.2 Ambiguity Function

The ambiguity function or the ambiguity diagram of a transmit signal visualizes the matched filter (cross-correlation) output, as a function of delay and Doppler shift. The Doppler frequency shift, f_D, of an echo reflected from a target moving with radial velocity, v, towards the receiver is given by

$$f_D = \frac{2vf}{c} \ , \tag{3.20}$$

as defined in Sec. 2.8. For the case of narrowband transmit signals, where the change in the echo pulse length $\Delta T = 1 - 2v/c$ is considerably smaller than the inverse of the signal bandwidth [KW65]

$$\Delta T \ll \frac{1}{BW} \ , \tag{3.21}$$

the pulse compression from object movement is neglected and a constant Doppler shift can be assumed. With these simplifications, the ambiguity function of a narrowband signal $s(t)$ is given by [GBS70, CA98]

$$\chi_s(\tau, f_D) = \int_{-\infty}^{\infty} s^*(t) s(t + \tau) \exp(j2\pi f_D t) dt \ . \tag{3.22}$$

When dealing with wideband signals, the pulse compression can not be neglected and the Doppler frequency shift can no longer be assumed to be constant. The Doppler scaling factor is defined:

$$\eta = \frac{1 + v/c}{1 - v/c} \approx 1 + \frac{2v}{c} \ , \tag{3.23}$$

which corresponds to the compression ratio. Effectively, the wave compression due to target movement can be calculated by resampling the transmit signal by factor η. The ambiguity function for the wideband signals is thus defined as [KW65, Lin88]

$$\chi_s(\tau, \eta) = \int_{-\infty}^{\infty} s(t) s^*(\eta(t - \tau)) dt \ . \tag{3.24}$$

For the ambiguity function, the following properties hold:

1. The amplitude of the ambiguity function at the origin is equal to the energy of the signal

$$|\chi_s(0,0)| = \int_{-\infty}^{\infty} s^2(t)dt = E_s \ . \tag{3.25}$$

2. The maximum value of the ambiguity function is always at $|\chi_s(0,0)|$, and in general either E_s is normalized to 1 or the ambiguity function is, so that

$$|\chi_s(0,0)| = 1 \ . \tag{3.26}$$

3. The ambiguity function is symmetric to the origin

$$|\chi_s(\tau, f_D)| = |\chi_s(-\tau, -f_D)| \ . \tag{3.27}$$

4. The total volume under the normalized magnitude-squared narrowband ambiguity function is unity [Col96]

$$\int_{-\infty}^{\infty}\int_{-\infty}^{\infty} |\chi_s(\tau, f_D)|^2 dt df_D = 1 \ . \tag{3.28}$$

   This total volume property does not hold for wideband signals, but it has been shown in [ST81] to yield a lower limit for the volume under the wideband signals ambiguity function.

The total volume property provides an important understanding that the ambiguity can be shifted in the two dimensional plane, but can not be removed.

In the literature, the ambiguity function is defined in various ways:

1. Via $\chi_s(\tau, \eta)$, as given in (3.24), sometimes also called as uncertainty function [Ric03] or as Doppler autocorrelation function [Ain10].

2. Via $|\chi_s(\tau, \eta)|$. The advantage of taking the magnitude of the correlation function is that the unnecessary details in the form of phase information is removed, improving the visual representation.

3. Via the magnitude squared version $|\chi_s(\tau, \eta)|^2$. In addition to the visual improvement, ambiguity functions property four can be directly applied and it also corresponds to the output power of the correlator [SW59].

The ambiguity function can be used to predict the performance of a transmit signal in reverberation limited environments. Assuming certain simplifications, the performance can be characterized via the Q-function.

3.1.3 Q-function

The Q-function provides a means to estimate the reverberation level of arbitrary signal designs. In [SW59] it is brought out that if the propagation losses for reverberation and the target reflections are identical, then the reverberation level can be calculated by integrating the product of $|\chi_s(\tau, \eta)|^2$ and the reverberation distribution function over the range and Doppler. However, under the extended assumption about the reverberation distribution function, namely that all the scatterers are stationary, uniformly distributed over the range and having a constant target strength [SW59, CA98], the expected reverberation levels can be calculated via the Q-function, given as [BZHE93, CA98]

$$Q_s(\eta) = \int_{-\infty}^{\infty} |\chi_s(\tau, \eta)|^2 d\tau \ . \tag{3.29}$$

The quantity $Q_s(\eta)$ can be interpreted as the volume of a certain Doppler cross-section in the ambiguity function. The assumptions made about the reverberation distribution function are unrealistic, nevertheless the Q-function still provides a measure to compare different signal designs in reverberation dominated environments. Additionally, in [War01], the author describes a sea trial, where the Q-function predictions quite accurately agree with the measured reverberation levels. Therewith, the Q-function might not be accurate enough for all environments, yet provides an usable approximation.

3.2 CW Signals

When starting to analyze different signal designs, it is appropriate to begin with the oldest and the most straightforward pulse form – the continuous wave (CW) signal. This simple signal design has spun a variety of extended designs. Despite differences in the various designs, they belong to the class of CW signals, since they are all based on the same signal. A selection of extended designs is discussed in the following.

3.2.1 CW

The continuous wave (CW) is a windowed single frequency sinusoidal signal,

$$s(t) = w(t)\exp(j2\pi f_c t) \ , \tag{3.30}$$

where f_c is the center frequency and $w(t)$ is a window or envelope function that is used to alter the spectrum of the signal. In case of a pulse of length T and a power normalization to unity, the rectangular window is given as

$$w(t) = \begin{cases} \frac{1}{\sqrt{T}}, & \text{for } 0 \leq t \leq T \\ 0, & \text{otherwise.} \end{cases} \tag{3.31}$$

The ambiguity function for a CW with a rectangular window has a simple closed form solution

$$\chi_s(\tau, f_D) = \frac{T - |\tau|}{T} \frac{\sin(\pi f_D (T - |\tau|))}{\pi f_D (T - |\tau|)} \ . \tag{3.32}$$

In the delay domain, the function behaves as a triangle $(1 - \frac{|\tau|}{T})$ and in the Doppler shift domain it behaves as a $\sin(x)/x$ function (later simply referred to as the sinc function). The ambiguity diagram for a CW with rectangular window, $f_c = 70$ kHz, and duration of 100 ms is shown in Fig. 3.1.

The ambiguity diagram has three dimensions: delay, velocity, and ambiguity (calculated via $|\chi_s(\tau, \eta)|^2$). The delay, τ, is given in seconds, the Doppler scaling factor, η, is converted to velocity via (3.23), assuming $c = 1500$ m/s. The ambiguity is given in logarithmic scale, using a gray-style color coding. The y-axis can be given in various ways, either as velocity, Doppler scaling factor or as Doppler frequency shift, while the x-axis can be referred to representing either delay or range. Therefore, in the following, sometimes the axes will be referred to using one of the alternatives, rather than the labels used in the figures.

The ambiguity function withholds multiple signal parameters of interest, like:

- The range resolution, relevant ambiguity width in the delay axis ($\Delta\tau$),
- The pulse compression ratio, $T/\Delta\tau$,
- The Doppler resolution, relevant ambiguity width in the Doppler axis.

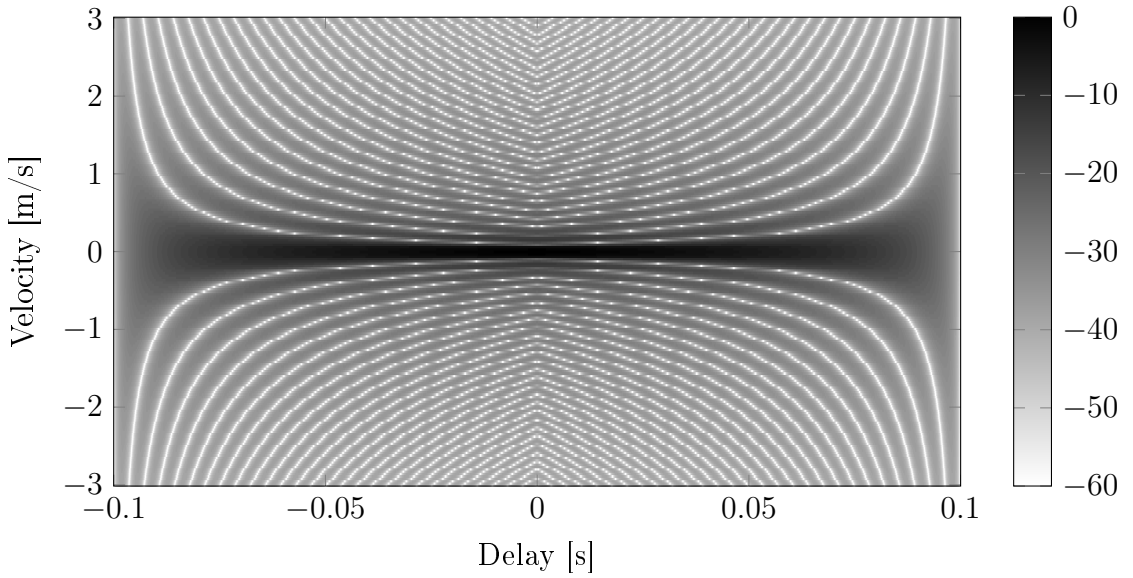

Figure 3.1: Ambiguity diagram of a 70 kHz rectangular windowed CW of duration 100 ms.

The resolution values are not uniquely defined, as they depend on the selection of the threshold value and on the selected ambiguity function definition. A common threshold value in the literature is chosen to be at a level of -3 dB. However, for signals with more complex ambiguity forms, lower threshold values or additional form factors (like periodicity) should be considered. By observing the velocity axis in Fig. 3.1, it is evident that the CW signal is Doppler selective. From literature it is known that the -3dB width in the Doppler axis is given by $0.88/T$ in Hz, for a 100 ms signal that is 8.8 Hz and according to (2.8) this translates to 0.094 m/s. The measured -3 dB width is 0.1 m/s. Knowing this Doppler width relation, then in order to improve the Doppler resolution of the CW signal, the signal duration should be increased. On the other hand, its range resolution is bound to its length. In the literature, the -3 dB width in the range axis is $0.6T$. For the given signal, the theoretical value would be 60 ms and the measured -3 dB width from the ambiguity diagram is 58.4 ms. The poor range resolution of the CW signal can be linked back to the simplicity of its signal form. The same sinusoidal waveform repeats for the whole pulse duration T. Hence, the autocorrelation function for CW is similar to correlating two rectangular signals – a triangle. Therefore, in order to improve the range resolution, the pulse should be made shorter. This leads to the very well known trade-off for CW signals:

- Short signal duration: good range resolution, poor Doppler resolution,
- Long signal duration: poor range resolution, good Doppler resolution.

This relation follows the ambiguity functions constant volume property. By increasing the pulse length, the ambiguity in the Doppler direction is reduced, but it reappears in the range direction. The ambiguity is simply shifted. It should be noted that all the above given theoretical and measured values are valid for the CW signal with a rectangular window. Different window functions alter the signal's resolution values.

In addition to time domain analysis, the frequency domain, in the form of power spectral density (PSD), can be used to better understand the ambiguity function of the pulse. The PSD of the 100 ms CW signal with rectangular window is shown in Fig. 3.2a.

The spectrum of a windowed sinusoidal wave is a double Dirac delta function at $\pm f_c$ Hz, convolved with the spectrum of the window, that in this case has a form of a sinc function. The longer the pulse/window,

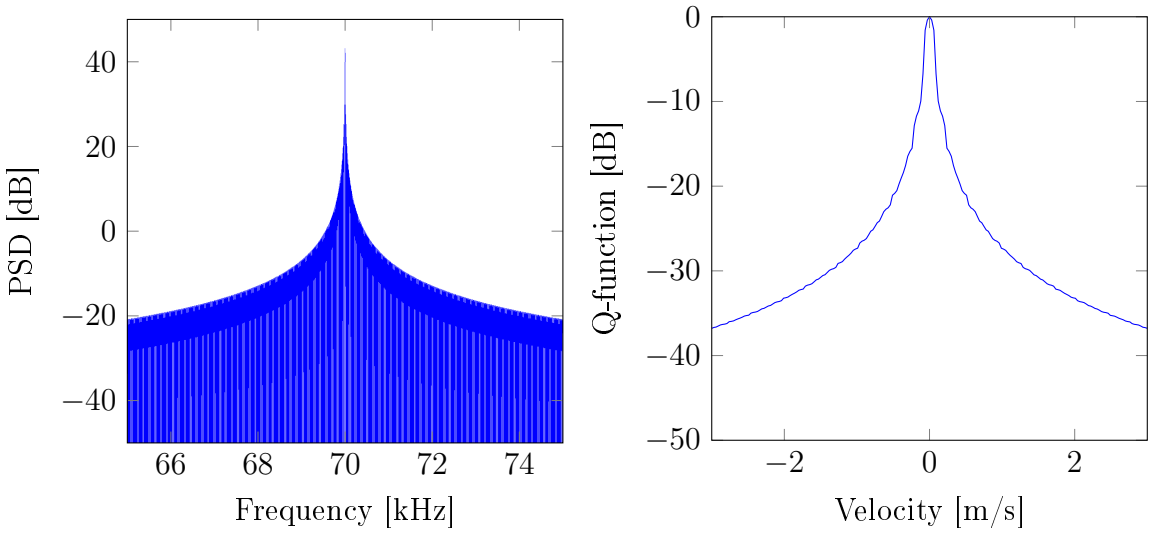

(a) PSD

(b) Q-function

Figure 3.2: Characteristic plots for a 70 kHz rectangular windowed CW of duration 100 ms.

the smaller the bandwidth (BW) of the CW signal, which results in the typical time-frequency relation that is given by

$$BW = \frac{1}{T} \,. \tag{3.33}$$

Hence, if the Doppler frequency shift of the reflected signal from a moving object is larger than the BW, the spectrum of the reflected and transmitted signal will consist of different frequency components and the correlation value between the two will be low. The very same frequency relation can also be seen in the ambiguity diagram, in form of the width of the ambiguity in the Doppler domain.

The Q-function visualizes the signal's reverberation processing characteristics. The Q-function for the rectangular windowed CW signal is shown in Fig. 3.2b. Essentially, the Q-function shows the influence of stationary reverberation at various target velocities. Let us consider the following example:

1. The system is looking for a small stationary target. The reverberation has nearly identical signal characteristics with the reflected signal from the target. As the receiver is tuned to look for a target with 0 m/s, then the reverberation level after the correlator detector is at its maximum.

2. The system is looking for a small target moving with the radial velocity of 1.0 m/s. From the Q-function it can be predicted that the reverberation level is at −27 dB. This reverberation suppression comes from the fact that the receiver is tuned to look for signals with a certain Doppler shift and therefore the stationary reverberation has a frequency mismatch.

In general, one can see from Fig. 3.2b that the CW signal is Doppler selective and given moving targets, the receiver can improve the detection probability by suppressing the reverberation.

So far, only the rectangular window has been considered. However, already with a different window function the ambiguity function can be significantly altered. From literature it is well known that the rectangular window has high spectral sidelobe levels [Sko90]. Different window functions are known to reduce the sidelobe levels at the cost of widening the main lobe. Further details are given in Sec. 3.6. One popular window function is the Hann window, the half period of the sine squared function. The ambiguity diagram of a 70 kHz Hann windowed CW signal of 100 ms duration is given in Fig. 3.3.

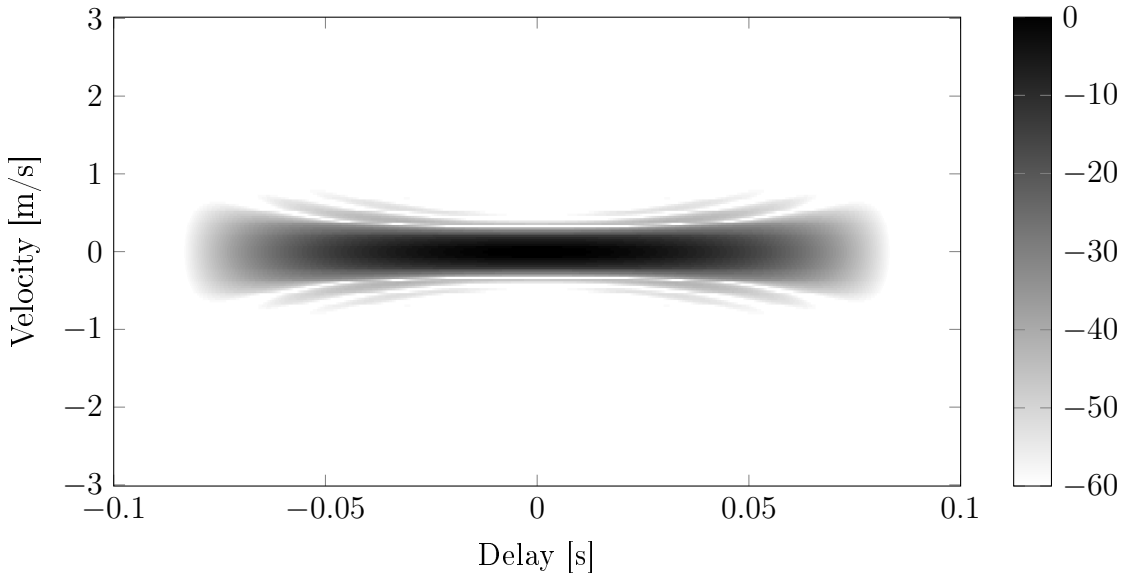

Figure 3.3: Ambiguity diagram of a 70 kHz Hann windowed CW signal of duration 100 ms.

Compared to the ambiguity diagram in Fig. 3.1, the change is clearly notable. The sidelobe levels in the velocity axis are significantly suppressed and the main lobe has become wider. Comparing the -3 dB levels, then in the range axis the width has changed from 58.4 ms to 44.4 ms and in the velocity axis the width has changed from 0.1 m/s to 0.18 m/s. The decrease of the -3 dB width in the range axis is related to the non-constant window function that reduces the signal level at the edges. The PSD of the Hann windowed CW signal, shown in Fig. 3.4a, gives further insight to the changes in the ambiguity function.

The widening of the main lobe is not visible in this plot, but the reduction of the sidelobe levels is obvious. As an example, with the rectangular window at 72 kHz the PSD is at a level of -13 dB, while with the Hann window at the same frequency the level is at -107 dB (for both the peak at 70 kHz is around 40 dB). The Q-function, shown in Fig. 3.4b, displays both the main lobe widening and sidelobe suppression. When before the expected reverberation level for 1.0 m/s was at -27 dB, then now with the Hann window for the same velocity the factor would be -66 dB below the maximum level of -3.5 dB at 0 m/s. In the following, all signal designs are analyzed with the Hann window, in order to better see the characteristics of the signal and not the combination of the signal and the rectangular window.

The biggest strengths of the CW signal are its simple generation and its good Doppler resolution. If the target is moving fast enough, then the reverberation is not an issue. However, if the target is moving slowly, the capabilities of the CW signal in reverberation-limited environments need to be improved. For this reason, various modifications have been introduced to the CW signal, to shift some of the ambiguity from the near zero velocity range to velocities of no interest.

3.2.2 SFM

In case of sinusoidal frequency modulation (SFM), the base CW signal is modulated by another sinusoid according to

$$s(t) = w(t) \exp[j2\pi f_c t + j\beta \sin(2\pi f_m t)] \ , \tag{3.34}$$

where $w(t)$ is the amplitude window of the pulse, f_m is the modulation frequency and β is the modulation index. The frequency of the second sinusoid, f_m, defines the frequency spacings of the spectral peaks,

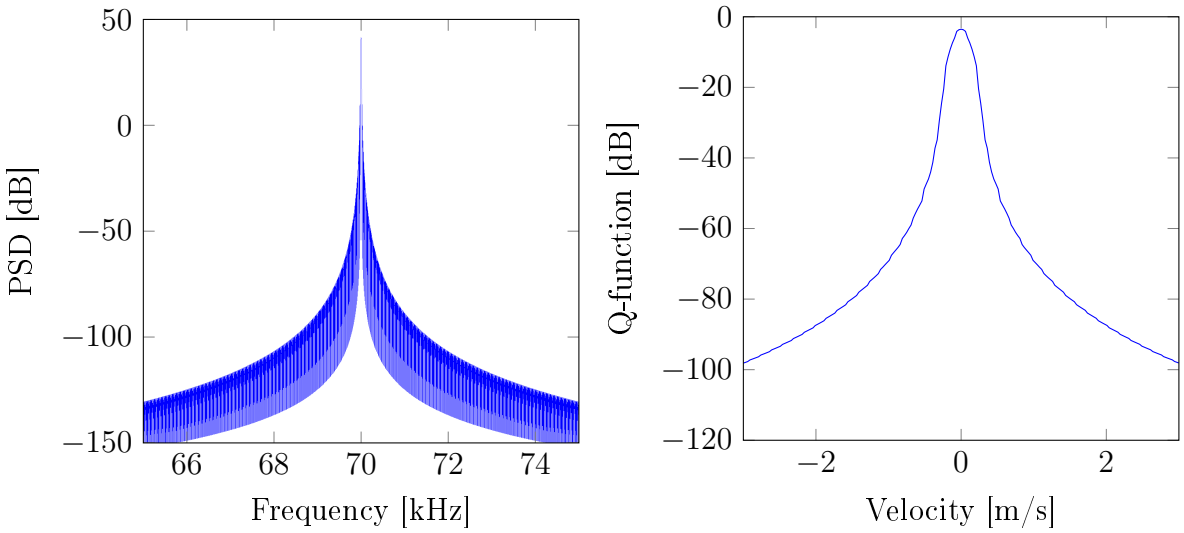

(a) PSD (b) Q-function

Figure 3.4: Characteristic plots for a 70 kHz Hann windowed CW signal of duration 100 ms.

and the modulation index, β, determines the bandwidth of the signal. The effective bandwidth can be approximated by [CA98]

$$BW \approx 2f_m(1+\beta) \ . \tag{3.35}$$

Fig. 3.5 shows the ambiguity diagram of a SFM signal with a Hann window, 100 ms duration, $f_m = 375$ Hz, $\beta = 9$ and $BW = 7500$ Hz.

At first glance it looks very similar to the Hann windowed CW ambiguity diagram given in Fig. 3.3. At closer look, one can see that the modulation of the CW signal introduces a periodic modulation to the correlation function of the SFM signal. Fig. 3.6a shows the ambiguity function for zero Doppler shift or equivalently the magnitude squared autocorrelation function for CW and SFM signals. The curve for the CW signal is the envelope for the SFM signal. In order to better see the details, the central ± 4 ms section is brought out in Fig. 3.6b.

The SFM curve has peaks with a 2.67 ms period, the time difference when the two signals are again in-phase and is directly related to the period of the 375 Hz modulation signal. On large scale the ambiguity functions of CW and SFM signals are the same. Nevertheless, the periodic structure of the SFM correlation function does give finer details about the reflections and in some cases allow to separate nearby targets. The PSD of the SFM signal, shown in Fig. 3.7a, gives further details about the pulse properties. The spectral peaks are symmetric about the center frequency, f_c, and there are 10 higher peaks to both sides, with a spacing of 375 Hz. The magnitudes of the peaks are not uniform, but could be calculated using Bessel functions [CA98]. The benefit of such a comb spectrum is that the energy is not concentrated to a single peak anymore, but spread out. Following the Wiener-Khinchin theorem and the ambiguity volume rule, this reduces the Q-function around the zero Doppler. As a consequence, there are Doppler ambiguities at multiples of ± 4.02 m/s or equivalently at $f_D = 375$ Hz. The Doppler ambiguities are directly related to the modulation frequency f_m and the velocity. The position of the first ambiguity peak can be calculated via (2.8)

$$v_{amb} = \frac{f_m c}{2f_c} \ . \tag{3.36}$$

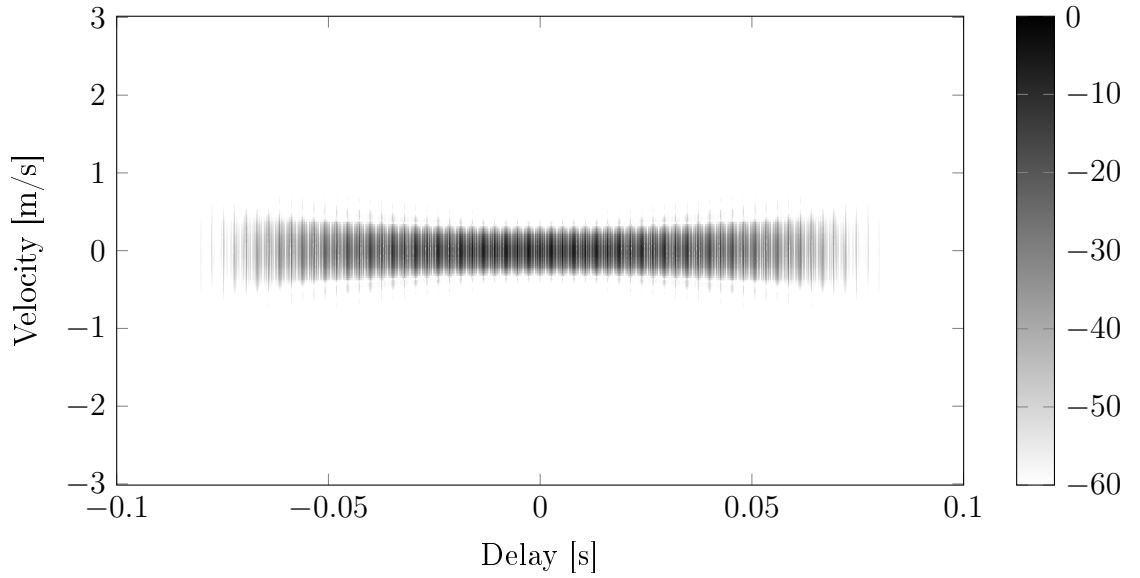

Figure 3.5: Ambiguity diagram of a Hann windowed SFM signal with $T = 100$ ms, $f_m = 375$ Hz, $\beta = 9$, and $BW = 7500$ Hz.

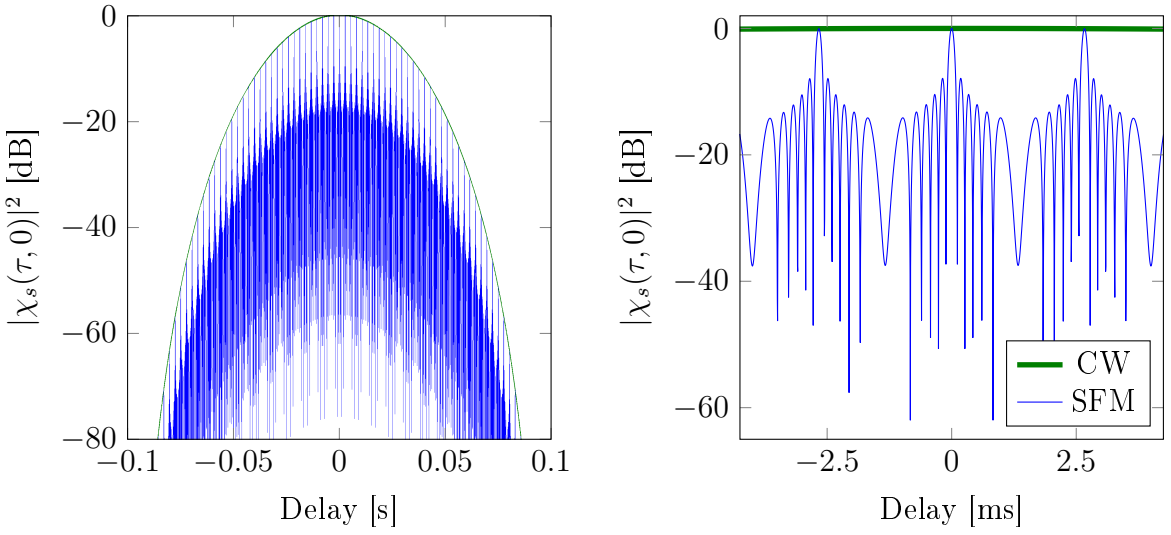

(a) Full ±100 ms

(b) Central ±4 ms

Figure 3.6: Autocorrelation plots for 70 kHz Hann windowed CW and SFM signals with $T = 100$ ms, $f_m = 375$ Hz, $\beta = 9$, and $BW = 7500$ Hz.

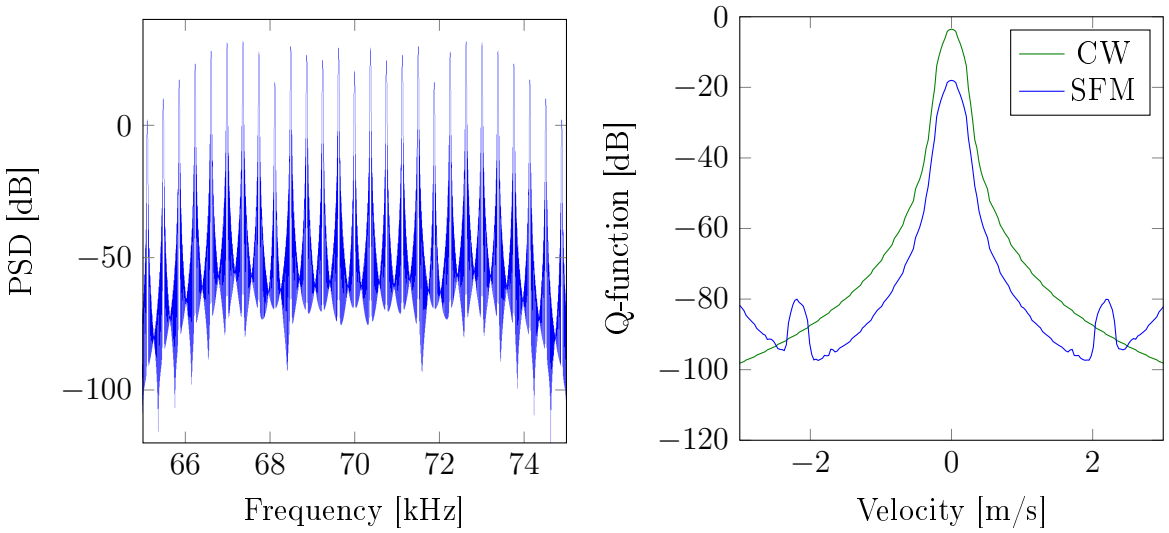

(a) PSD (b) Q-function

Figure 3.7: Characteristic plots for a Hann windowed SFM signal with $T = 100$ ms, $f_m = 375$ Hz, $\beta = 9$, and $BW = 7500$ Hz.

These Doppler ambiguities can be confirmed with a SFM ambiguity diagram using $f_m = 240$ Hz, $\beta = 14$, shown in Fig. 3.8. The parameters f_m and β can be freely chosen, but their effect to the performance is that of an another trade-off. Given a bandwidth, BW, N spectral peaks fit into that frequency range

$$N = \frac{BW}{f_m} + 1 = 2(\beta + 1) + 1 \ , \tag{3.37}$$

where the second equality is determined via (3.35). If the frequency spacing, f_m, is too close, then the Doppler ambiguities will start to overlap. On the other hand, as the spacing increases, the gain versus CW signal decreases. Hence, the parameter should be selected with care.

As mentioned earlier, the design goal of the SFM signal is to reduce the reverberation level near the zero velocity range, by shifting some of the ambiguity to velocities of no interest. The effectiveness of the design can be seen from the Q-function plot, shown in Fig. 3.7b. Two significant properties can be observed. Firstly, the reverberation level for the zero velocity has reduced to -18 dB from -3.5 dB, compared to that of the Hann windowed CW signal. Secondly, one can see that at about ± 2 m/s the Q-function starts to increase. This concurs with the fact that the first Doppler ambiguities will be at ± 4.0 m/s. It is of importance to be noted that the small peaks at ± 2.2 m/s are inaccuracies due to the Doppler shift implementation and can be ignored.

Another way to generate a signal with a comb like spectrum, is to superimpose multiple CW signals, which results in the co-called Cox comb.

3.2.3 Cox Comb

The Cox comb is a superposition of multiple single frequency sinusoids [CL94]

$$s(t) = w(t) \sum_{n=1}^{N} \exp[j2\pi f_n(t + \alpha)] \ . \tag{3.38}$$

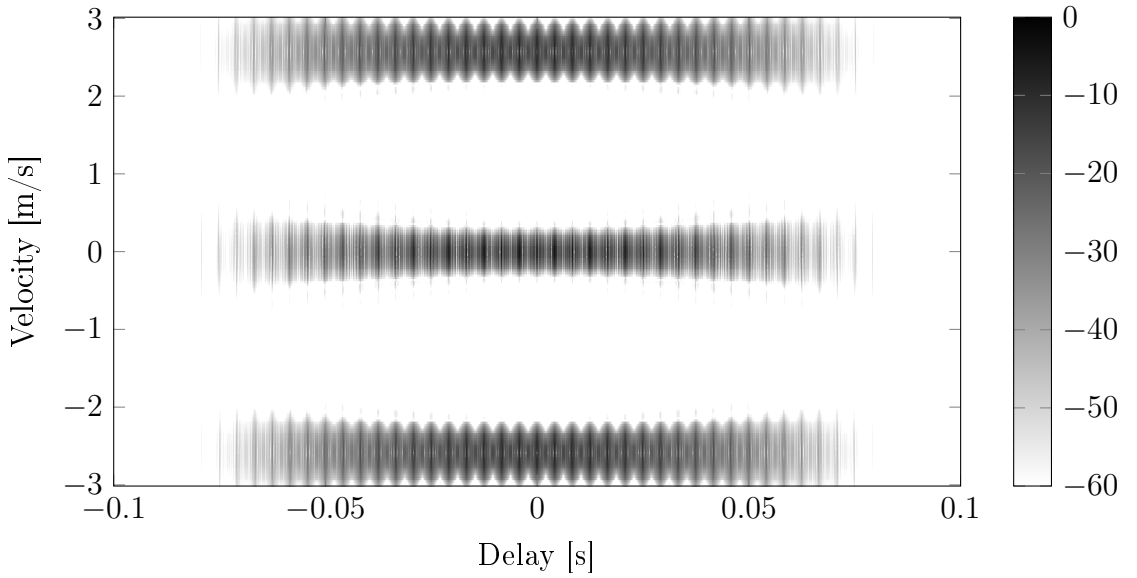

Figure 3.8: Ambiguity diagram of a Hann windowed SFM signal with $T = 100$ ms, $f_m = 240$ Hz, $\beta = 14$, and $BW = 7500$ Hz.

The frequencies are determined by

$$f_n = \begin{cases} f_c - BW/2, & \text{for } n = 1 \\ f_{n-1} + r^{n-2}\Delta f, & \text{for } n \in \{2 \dots N\} \end{cases} \tag{3.39}$$

where the Δf is the spacing between the two lowest frequencies and α is an arbitrary time shift parameter that can be used to reduce the peak-to-average power ratio (PAPR) [CA98]. The value of r is slightly larger than one, leading to an increasing frequency step. The idea behind using non-equal frequency steps follows from two different effects. First, given equal frequency steps the component signals are harmonics shifted in frequency and experience periodic constructive and destructive superposition. Consequently, the signals add coherently after a certain period, leading to a non-uniform amplitude envelope, with greatly increased PAPR. Hence, in order to avoid this coherent superposition, non-equal frequency steps can be used. The signal will still have a non-uniform envelope, but the maximum level will be reduced. Additionally, due to the non-periodic structure of the superimposed signal, the secondary peaks in the autocorrelation function will be reduced, providing an improved range resolution. Secondly, the Doppler shift is frequency dependent and unless the frequency steps are matched to the Doppler shift the width of the Doppler ambiguities will be increased. In order to achieve the best fit, the frequencies should follow the geometric progression, given by $r = 1 + \Delta f / f_1$ [CL94].

The ambiguity diagram of a Hann windowed Cox comb of duration 100 ms with r following the geometric progression, $\Delta f = 375$ Hz, $N = 20$, $f_c = 70$ kHz and $BW = 7500$ Hz is shown in Fig. 3.9. The ambiguity diagram looks nearly identical to that of SFM signal in Fig. 3.5. The main difference between the two is that the range sidelobes for the Cox comb case are smeared and consequently reduced by $6 - 10$ dB, because of the effect of non-equal frequency steps mentioned earlier. The PSD, shown in Fig. 3.10a, demonstrates the comb like spectrum of the signal. Due to the fact that the Cox comb transmit signal is a pure superposition of multiple single tone sinusoids, all the peaks in the spectrum are of equal magnitude. The position of the peaks are predefined by the selection of f_n. In case of r

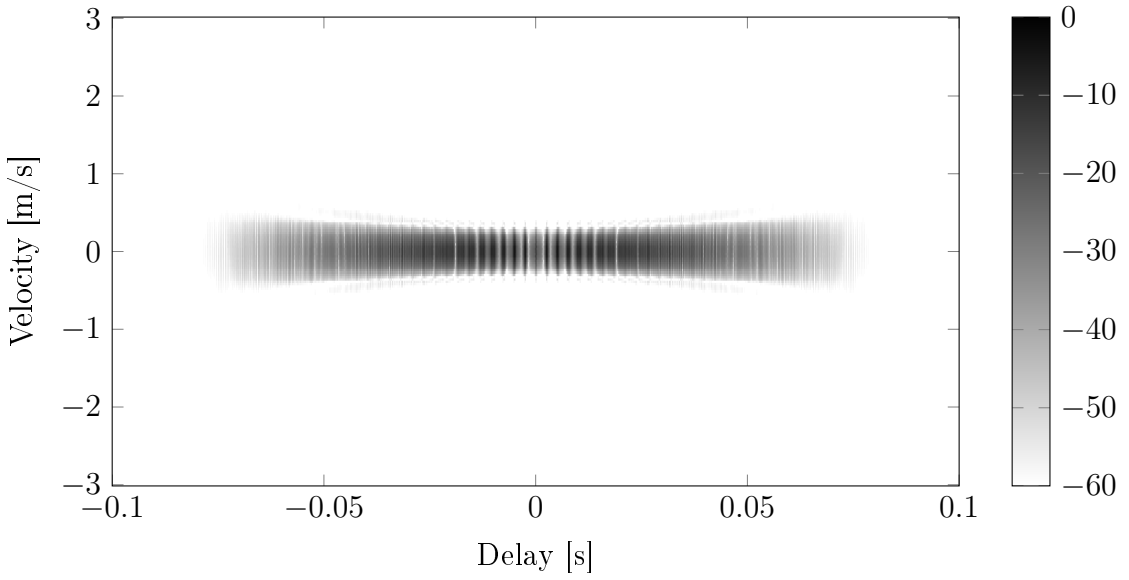

Figure 3.9: Ambiguity diagram of a Hann windowed Cox comb signal with $T = 100$ ms, $\Delta f = 375$ Hz, $N = 20$, and $BW = 7500$ Hz.

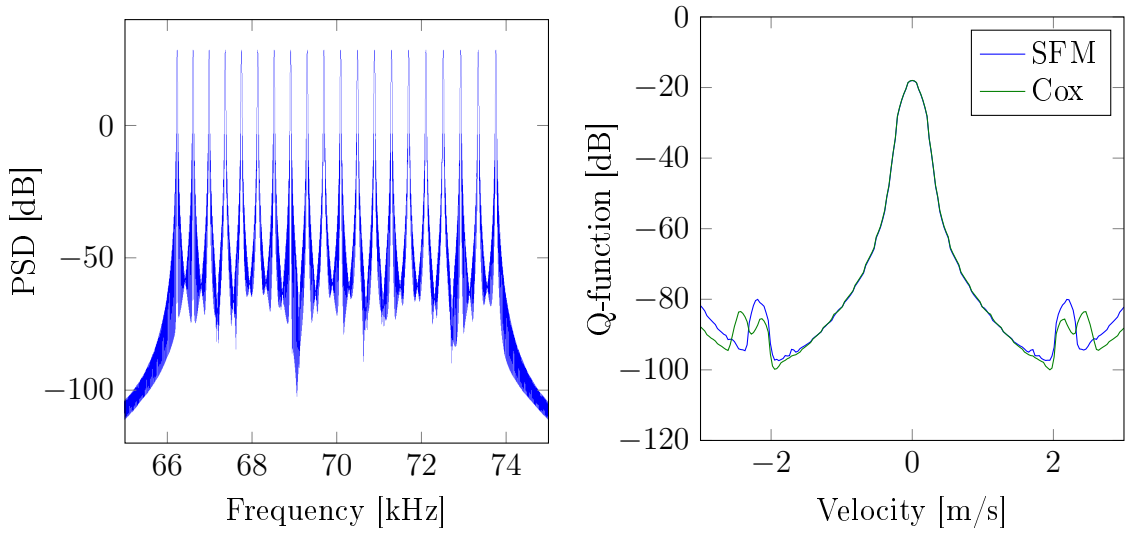

(a) PSD

(b) Q-function

Figure 3.10: Characteristic plots for a Hann windowed Cox comb signal with $T = 100$ ms, $\Delta f = 375$ Hz, $N = 20$, and $BW = 7500$ Hz.

following the geometric progression, the BW can be calculated by

$$BW = \Delta f \sum_{n=0}^{N-2} r^n = \Delta f \left(\frac{1 - r^{N-1}}{1 - r} \right) \ . \tag{3.40}$$

The reverberation processing performance of a Cox comb signal according to the Q-function, shown in Fig. 3.10b, is the same as that of an SFM signal and in the central section the two curves overlap. The Cox comb seems to have several benefits over SFM, like reduced range sidelobes and much better confined PSD with equal power distribution among the spectral peaks. Nonetheless, the Cox comb also has a significant drawback. Due to the superposition of N sinusoids, the PAPR of the signal is high. Depending on the amplifiers, this can lead to severe non-linear effects and to significant performance degradations. In practical systems the PAPR is an important issue and hence, the SFM signal design is preferred over the Cox comb design [CA98].

3.3 Sequence of CW Signals

As mentioned earlier, the duration and bandwidth of the CW signal are directly related by $BW = 1/T$, creating a direct trade-off between range and Doppler resolution. The ACF of the SFM signal had the same envelope as that of the CW signal, but with finer details that in some conditions would result in an improved range resolution. This improvement comes from the increased bandwidth of the SFM signal. In general, a broadband signal provides a certain pulse compression compared to a narrowband signal of the same duration. The range resolution of a narrowband signal is related to its pulse duration T,

$$S_{narrow} = \frac{cT}{2} \ , \tag{3.41}$$

while for a broadband signal the range resolution is related to its coherence time T_c

$$S_{broad} = \frac{cT_c}{2} \ , \tag{3.42}$$

where the coherence time is $T_c = 1/BW$. That leads to the pulse compression ratio (PCR)

$$\text{PCR} = \frac{S_{narrow}}{S_{broad}} = \frac{2cT}{2cT_c} = T \cdot BW \ , \tag{3.43}$$

which describes the ratio between the range resolution of an unmodulated pulse and that of a modulated pulse of the same length. As the compression ratio is given by the product of time and bandwidth, then often in the literature the time-bandwidth (BT) product is brought out as a relevant signal parameter.

The CW signal has a $BT = 1$ and one way to increase the BT product would be to periodically repeat the transmit signal, creating a pulse train.

3.3.1 CW Train

The basic CW train repeats a short CW pulse with a certain period T,

$$s(t) = \sum_{n=1}^{N} s_1(t - nT) \ , \tag{3.44}$$

where N defines the number of repetitions. The base CW pulse has a duration of T_1 and is given by

$$s_1(t) = \begin{cases} \exp(j2\pi f_c t), & \text{for } 0 \leq t \leq T_1 \\ 0, & \text{otherwise} \ . \end{cases} \tag{3.45}$$

In order to understand the principle of a CW train, let us first look at the time-frequency relation of a periodic signal. An arbitrary periodic function $x(t)$, can be represented by convolving the signal $x_T(t)$, that withholds one period of the periodic function, with an impulse train $p(t) = \sum_n \delta(t - nT)$,

$$x(t) = x_T(t) * p(t) = x_T(t) * \sum_{n=-\infty}^{\infty} \delta(t - nT) = \sum_{n=-\infty}^{\infty} x_T(t - nT) \ . \tag{3.46}$$

The spectrum of $x(t)$ is the result of the multiplication of the spectra of $x_T(t)$ and $p(t)$:

$$x(t) = x_T(t) * p(t) \overset{\mathcal{F}}{\Longleftrightarrow} X(f) = X_T(f)P(f) \ . \tag{3.47}$$

Given that the spectrum of $x_T(t)$ is known and utilizing the fact that the spectrum of an impulse train is also an impulse train,

$$P(f) = \sum_{n=-\infty}^{\infty} \exp(-j2\pi nTf) = \frac{1}{T} \sum_{n=-\infty}^{\infty} \delta\left(f - \frac{n}{T}\right) \ , \tag{3.48}$$

the spectrum of a periodic signal is given by

$$X(f) = X_T(f) \left(\frac{1}{T} \sum_{n=-\infty}^{\infty} \delta\left(f - \frac{n}{T}\right) \right) \ . \tag{3.49}$$

In other words, $X(f)$ is a sampled version of $X_T(f)$, with spectral lines at multiples of $f = 1/T$. Given that $x_T(t)$ is a rectangular pulse, the evolution of the spectrum of a periodic train of rectangular signals is shown in Fig. 3.11. Now coming back to the CW train signal, the only thing that changes in the

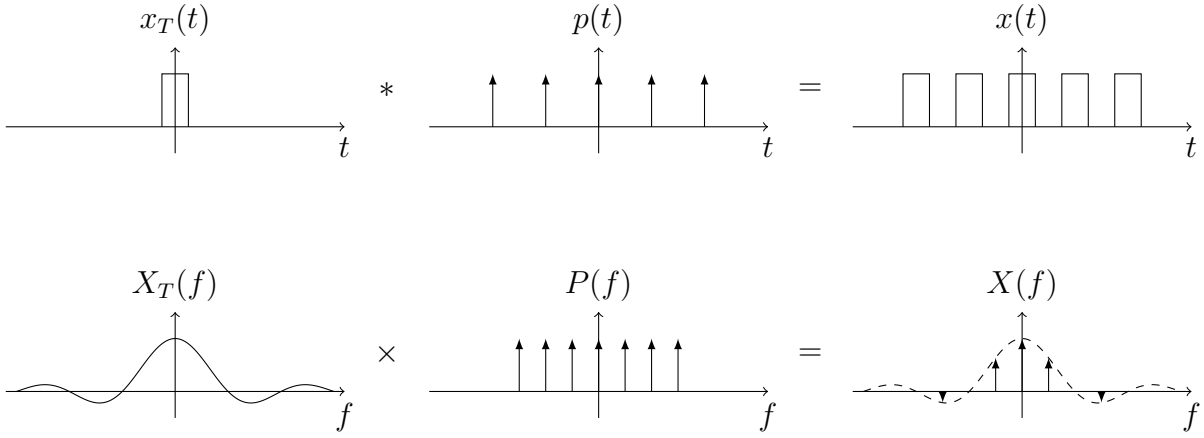

Figure 3.11: Evolution of the spectrum of a periodic signal.

evolution of the spectrum of the signal, $s(t)$, is that the periodic signal $x(t)$ is time-limited or multiplied with a rectangular window of duration NT. This multiplication in time domain leads to a convolution in frequency domain. Therefore, instead of a train of impulses, $S(f)$ will consist of sinc functions with zero crossings at $1/NT$. Knowing the shape of the spectrum of the CW train signal, it becomes evident, why using a train improves the time-bandwidth product of the signal. Compared to the short CW signal of duration T_1, the new signal has a duration NT, while having the same bandwidth as the short CW signal, resulting in a BT product of NT/T_1, instead of $BT = 1$.

In the following, a CW train signal, with center frequency at 70 kHz, repetition period of $T = 20$ ms, 50% duty cycle ($T_1 = T/2$), and $N = 5$, is considered. The ACF of such a CW train of total duration of $T_t = 100$ ms, is shown in Fig. 3.12.

As the envelope of the signal $s(t)$ is a sequence of rectangles, the ACF should be a sequence of triangles with decreasing amplitudes. One could draw a line through the triangle peaks which would correspond to the ACF of a signal CW pulse of duration NT. Effectively, due to the shorter base CW pulse, $s_1(t)$, the range resolution has been increased by a factor of $NT/T_1 = 2N$. Fig. 3.13a shows the spectrum of $s(t)$. As expected, the spectrum consists of sinc functions, spaced in $1/T$ Hz steps and the peaks sample a sinc function with zero-crossings at $1/T_1$ Hz. The Q-function, shown in Fig. 3.13b, simply confirms the existence of Doppler ambiguities and that the width of the peaks is related to the total pulse duration T_t.

In conclusion, given that one compares the CW train signal with a CW pulse of the same duration NT, the frequency resolution is the same, but the range resolution has been improved by a factor of NT/T_1. However, ambiguities both in frequency and time domain have appeared and that sets a constraint on the applicability of the signal design.

The CW train still consists of repetitions of single frequency sinusoidal signals, where different signal sections are identical and have a high correlation value. In order to alter this, one could use a train of CW pulses with different center frequencies – Costas codes.

3.3.2 Costas Codes

The Costas code [Cos84] signal is a sequence of CW pulses with different center frequencies

$$s(t) = \sum_{n=1}^{N} s_n(t - nT) \ , \tag{3.50}$$

where

$$s_n(t) = \begin{cases} \exp(j2\pi f_n t), & \text{for } 0 \leq t \leq T \\ 0, & \text{otherwise} \end{cases} \tag{3.51}$$

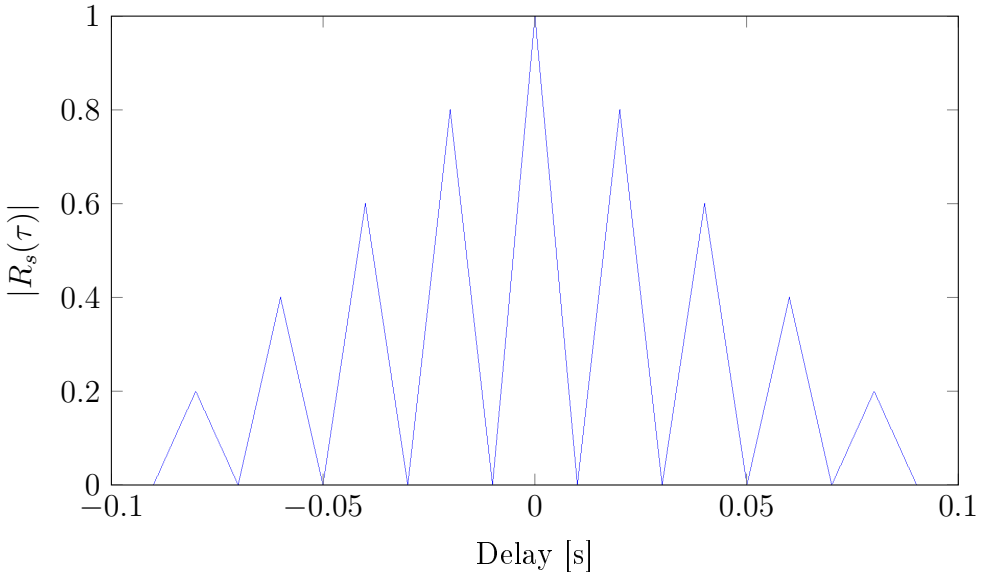

Figure 3.12: Normalized autocorrelation function for a rectangular windowed CW train signal with $T = 20$ ms, 50% duty cycle, and $N = 5$.

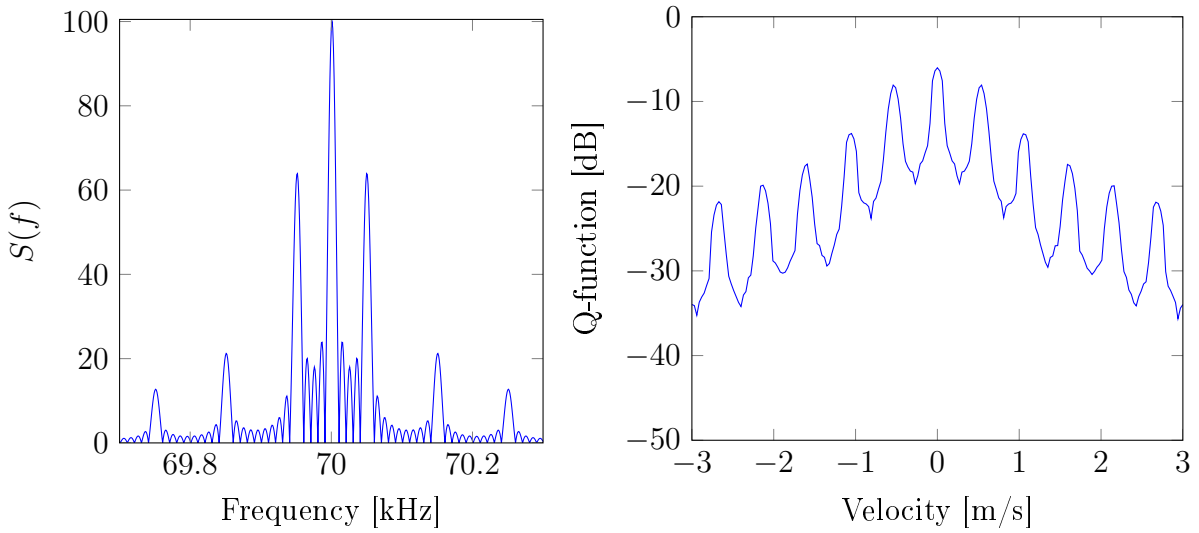

(a) Spectrum

(b) Q-function

Figure 3.13: Characteristic plots for a rectangular windowed CW train signal with $T = 20$ ms, 50% duty cycle and $N = 5$.

and the total pulse duration is $T_t = NT$. The frequency of each of these sub-pulses is given by [BT88]

$$f_n = f_0 + c_n \Delta f \quad n = 0, 1, \ldots, N-1 \ , \tag{3.52}$$

where f_0 is the starting frequency and c_n is a value from a set of ordered integers that have certain properties: the difference between adjacent integers should be unique and the unique difference also applies for integers apart by any value L [Cos84]. One possibility to generate the integers is to use the Welsch theorem that utilizes the primitive root modulo prime n "algorithm". An example Costas array for $N = 10$, also called "Welch-10", is generated via [GT84]

$$c_n = g^n \bmod p \quad n = 1, \ldots, N \ , \tag{3.53}$$

with parameters $p = 11$ and $g = 2$ is:

$$c_n = [2, 4, 8, 5, 10, 9, 7, 3, 6, 1] \ . \tag{3.54}$$

Various Costas array construction methods exist and a good overview of possible orderings is given in Costas original paper [Cos84] and further analysis is presented by Golomb in [GT84]. The Costas signal design aims for a pulse with constant envelope and each frequency component appearing only once. The selection of the frequency sequence, implemented via c_n, assures that the designed signal pulse has low cross-correlation with Doppler shifted versions of itself. In Costas [Cos84] paper the Δf is defined as

$$\Delta f = \frac{1}{T} \ , \tag{3.55}$$

where T is the duration of the sub-pulse. Such a Δf selection fulfills the orthogonality condition, where for zero Doppler the peak of the cross-correlation function of each sub-pulse aligns with the zeros of other sub-pulse cross-correlation functions. In this case high secondary peaks, also known as grating lobes, are avoided. These peaks stem from constructive superposition of various components. However,

this imposes a constraint to the pulse design. The sub-pulse duration, bandwidth, and the number of sub-pulses are related via the frequency step, Δf:

$$\Delta f = \frac{1}{T} \quad \text{and} \quad BW = N \cdot \Delta f \ . \tag{3.56}$$

Assuming that the total signal duration is fixed ($T_t = NT$), then if BW is increased, the number of sub-pulses together with Δf have to be increased, while the sub-pulse duration has to be decreased. In case the orthogonality condition is fulfilled, the BT product will be $((N/T) \cdot NT = N^2)$. In order to increase the BT product, one can increase the BW disregarding the orthogonality constraint. Meaning the frequency step is defined only by BW and the number of sub-pulses:

$$\Delta f = \frac{BW}{N} \ . \tag{3.57}$$

The new BT product is increased by a factor of $BW \cdot T/N$ or by the ratio between the new and previous bandwidth. On the other hand, grating lobes will appear in the autocorrelation function and the number of significant peaks will be determined by the BT increment factor. Fig. 3.14 shows the central section of

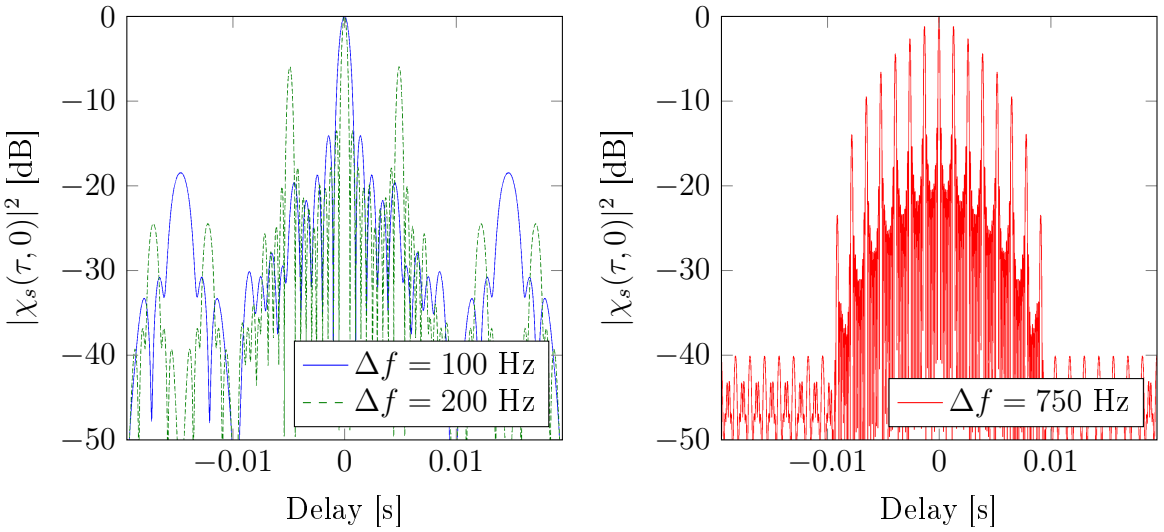

(a) $BW = 1000, 2000$ Hz

(b) $BW = 7500$ Hz

Figure 3.14: Autocorrelation plots for rectangular windowed Costas code signals with $T = 100$ ms, and $N = 10$.

the autocorrelation functions for Costas codes with various Δf values. In Fig. 3.14a the solid blue curve corresponds to the case where Δf fulfills the orthogonality condition given in (3.55). One can see that indeed there is only one higher peak in the ± 10 ms range. The green dashed curve is for $\Delta = 200$ Hz selection that no longer fulfills the orthogonality condition and as mentioned before, in such case grating lobes will appear. Two peaks at ± 5 ms can be clearly identified. Likewise, the BT product increment can be confirmed from the plot. If for $\Delta f = 100$ Hz the -3 dB width is approximately 1 ms, then for $\Delta f = 200$ Hz the width has been reduced to 0.5 ms. Another effect worth pointing out is that the peak sidelobe level decreases with increasing BW. In Fig. 3.14b an identical plot is shown for the $\Delta f = 750$ Hz selection. As expected, there are 7 grating lobes at both sides, but the peak sidelobe level has been reduced from around -20 dB to -40 dB. The sidelobe level reduces, as due to the increased Δf, the spectral peaks corresponding to each sub-pulse no longer overlap in the PSD. The range resolution

of Costas code pulses is very good. Even with multiple grating lobes the autocorrelation function has higher values maximally in the range of ±10 ms and then there is a plateau where the sidelobes have a constant level. However, the Doppler resolution is determined by the duration of the sub-pulse. Even for a Costas code with length $N = 10$, the signal's Doppler resolution compared to that of CW or SFM is reduced by a factor of N. Meaning, the Doppler resolution of the signal is unsuitable for enhancing the reflections from slow moving divers against the stationary reverberation.

The ambiguity diagram of a Hann windowed Costas code signal with code length $N = 10$, $BW = 7500$ Hz, and duration of 100 ms is given in Fig. 3.15. The 10 pulse structure is clearly evident and most of the ambiguity has been shifted from range to Doppler domain. In this case, the rectangular window instead of a Hann window is used, because the Hann window over the complete pulse would differently weight the sub-pulses, resulting in a non-uniform comb spectrum. The PSD and Q-function are given in Fig. 3.16. The PSD has a comb like shape, with peaks at f_n. Comparing the given spectrum to that of SFM or Cox comb, then there are a few differences. First, the width of the spectral peaks are widened by a factor of N, due to the reduced sub-pulse lengths. Secondly, the peak-to-valley difference is only around 20 dB, when for SFM and Cox comb signals the difference is around 90 dB. Instead of applying the Hann window over the whole signal, each of the sub-pulses could be Hann windowed in order to reduce the spectral leakage, greatly lowering the range sidelobe levels and increasing the peak-to-valley separation in the PSD. Ambiguity, PSD and Q-function plots are shown in the appendix. The drawback of Hann windowing the sub-pulses is that the signal envelope will no longer be constant.

For reverberation limited diver detection systems, the suitability of Costas codes signal design can be seen from the Q-function. Due to the widening of the Doppler main lobe, the Q-function is basically flat over the ±3 m/s range. The reverberation processing performance could be somewhat improved by Hann windowing the individual sub-pulses, but even then the signal does not have the required Doppler resolution.

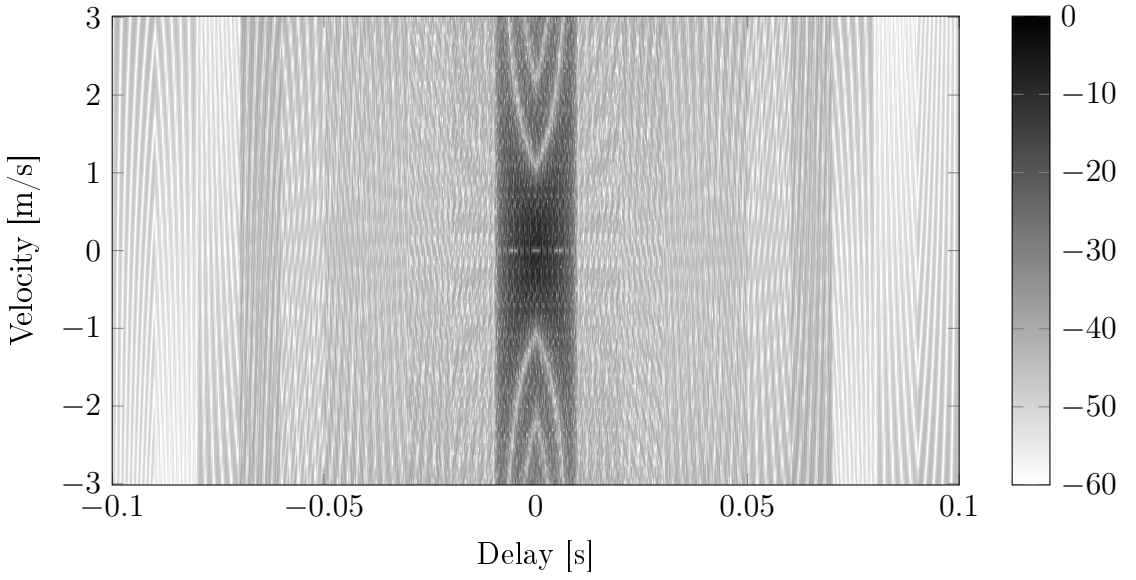

Figure 3.15: Ambiguity diagram of a rectangular windowed Costas code signal with $T = 100$ ms, $BW = 7500$ Hz, and code length $N = 10$.

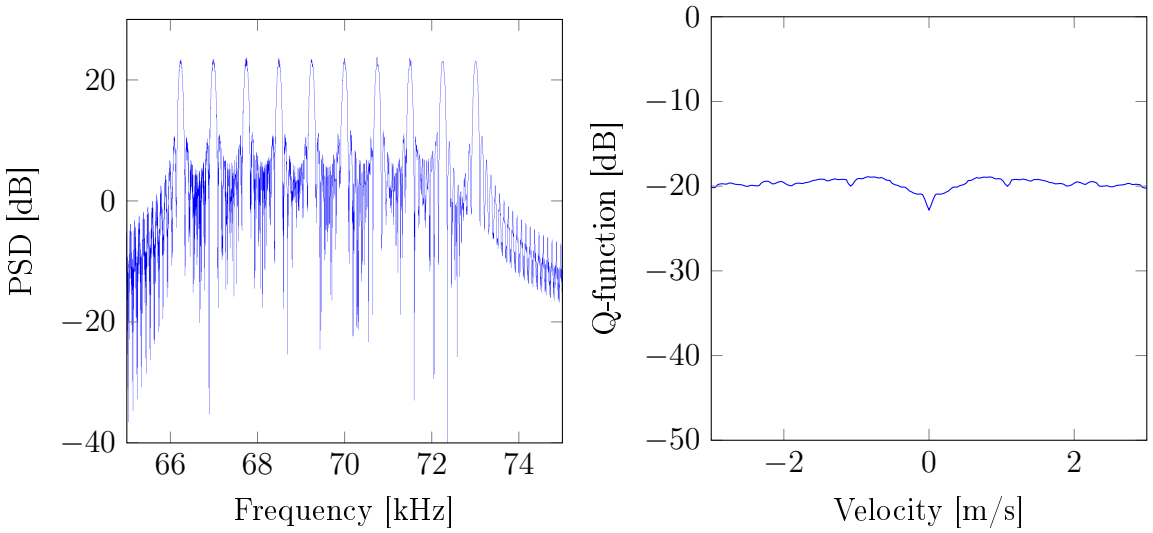

(a) PSD

(b) Q-function

Figure 3.16: Characteristic plots for a rectangular windowed Costas code signal with $T = 100$ ms, $BW = 7500$ Hz, and code length $N = 10$.

3.4 FM Signals

In the previous section on the class of CW signals, all signal designs were based on a constant frequency sinusoid. Various modifications were described that aimed to improve the range resolution of the base signal or its reverberation processing performance near the zero velocity. The SFM and Cox comb signal designs presented a high pulse compression (BT) factor, but effectively the range resolution was dominated by high secondary peaks that appear due to the underlying CW pulse shape. As mentioned earlier, the term BT factor comes from the fact that the range resolution of a modulated pulse is reduced from T to approximately its coherence time, $T_c = 1/BW$, providing a compression factor of $T \cdot BW$, cf. (3.43). In case of frequency modulated signals, their instantaneous frequency is constantly changing and in general, the $1/BW$ coherence time is valid over the whole pulse length, unlike to SFM, where the signal repeats itself after a certain period, determined by the modification frequency. In the following, a selection of FM designs is analyzed and for all signals the frequency is selected to be monotonically increasing (also known as up-sweep).

3.4.1 Linear FM

In case of linear frequency modulation (LFM), the instantaneous frequency $f(t)$ varies linearly with time:

$$f(t) = f_0 + kt \ , \tag{3.58}$$

where f_0 is the starting frequency and

$$k = \frac{BW}{T} \tag{3.59}$$

defines the slope of the frequency function. In time domain, the LFM signal is given by

$$s(t) = w(t) \exp\left(j2\pi\left(f_0 t + \frac{BWt^2}{2T}\right)\right) \ , \tag{3.60}$$

where T is the pulse duration and the instantaneous phase is given by the integration over the instantaneous frequency $f(t)$, multiplied with 2π. As mentioned earlier, the coherence time for frequency modulated signals is $T_c = 1/BW$, meaning that if the signals are shifted in time by more than T_c, then the correlation between the shifted and unshifted signal reduces significantly. This is visualized in Fig. 3.17, by means of the autocorrelation function. Compared to the autocorrelation functions for CW

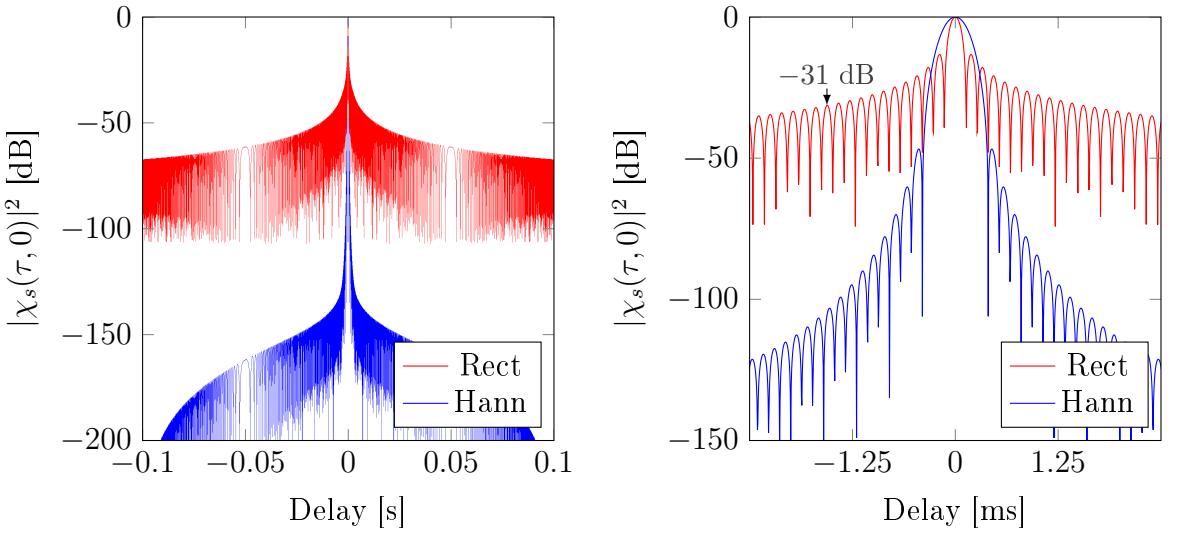

(a) Full ±100 ms

(b) Central ±2.5 ms

Figure 3.17: Autocorrelation plots for an LFM signal with $T = 100$ ms, $BW = 7500$ Hz, and various windowing.

based signals, it is obvious that the width of the main lobe is greatly reduced. The figures also show the significance of windowing. This again shows the duality between the time and frequency domain. Previously, for the CW signals windowing was introduced to shape the spectrum, then for LFM signals an identical effect can be seen in the time domain in the form of sidelobe reduction in the autocorrelation function. Fig. 3.17b shows the suppression of the sidelobes, while broadening the main lobe. The ACFs -3 dB width of rectangular windowed LFM is 0.12 ms and for Hann windowed LFM the width is 0.25 ms. In literature, the ACFs -3 dB width of an LFM signal is given by $0.88/BW$, or 0.117 ms in combination with $BW = 7500$ Hz that complies with the measured value (rectangular window). However, the major difference is in the sidelobe levels. At around 1.5 ms delay, the corresponding values are at -31 dB and at -103 dB. In comparison, a CW signal with the same -3 dB width according to Sec. 3.2.1 would have to have a duration of $T = 1.17 \cdot 10^{-4}/0.6$ ms $= 1.95 \cdot 10^{-4}$ ms ≈ 0.2 ms, reducing the transmitted signal energy by a factor of 500.

FM signals are well known for two properties, their very good range resolution and their Doppler invariance. As explained earlier in the section about the ambiguity diagram, the Doppler effect can be described by resampling of the signal by a factor $\eta \approx 1 + 2v/c$, given in (3.23). Hence, when initially the instantaneous frequency of LFM signal is given by (3.58), then for a Doppler shifted signal, by inserting $t = \eta t$ into (3.60) and taking the time derivative of the phase modulation function divided by 2π [Col96], the instantaneous frequency becomes

$$f^D(t) = f_0\eta + k\eta^2 t \ . \tag{3.61}$$

The Doppler effect does not just shift the frequency by a constant factor η, the first term in (3.61),

but it also alters the rate the frequency changes over time, the second term. As an illustration, the instantaneous frequencies of an LFM and an LFM signal reflected from a target moving with 10 m/s, are shown in Fig. 3.18, where the LFM signal has a center frequency of 1 kHz and a bandwidth of 750 Hz.

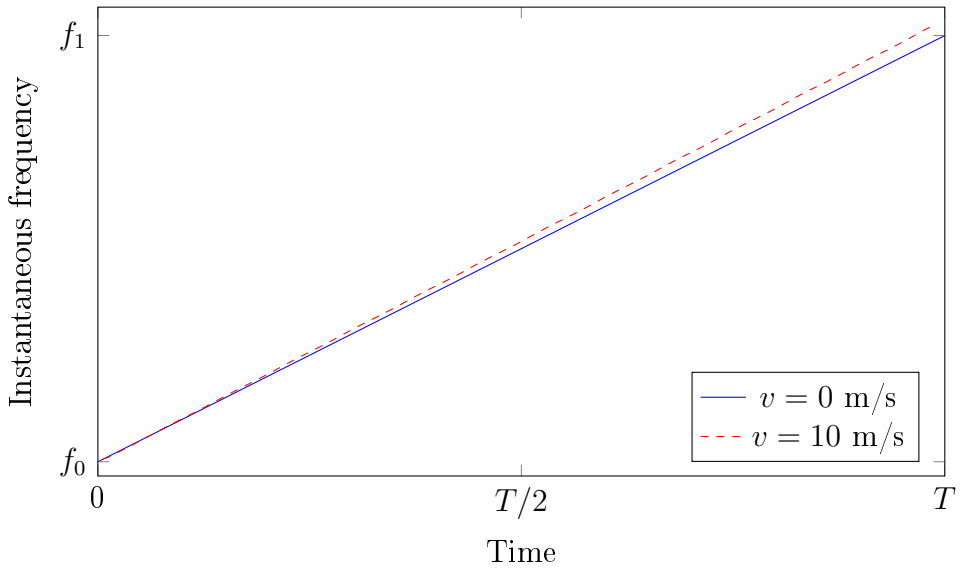

Figure 3.18: Instantaneous frequency of an LFM signal reflected from a target moving with various speeds, center frequency at 1 kHz and $BW = 750$ Hz.

Due to the modification of the rate the frequency changes over time, there is no time shift when the two frequency functions would exactly align. Instead there is a certain timespan when different parts of the function coincide. This leads to a certain mismatch that is clearly visible in the normalized cross-correlation function, shown in Fig. 3.19. Instead of a single peak, as seen for the autocorrelation function plotted in blue, the cross-correlation function in red is shifted by a certain delay to compensate for the Doppler frequency shift. The peak becomes smeared and the maximal value is reduced by a factor of 4. The peak correlation reduction depends on the frequency slope k, pulse duration T, and on the velocity. In this case, the parameters are purposely selected such that the Doppler shift effect would be more visible. In general, this mismatch is considered relatively small and in many applications is ignored. In order to reduce the mismatch, a different frequency function could be used that leads to the hyperbolic FM signal, introduced in the next subsection.

As the LFM signal is nearly Doppler invariant, the ambiguity diagram will be a thin line over the velocities of interest, shown in Fig. 3.20. The line is slightly diagonal, due to the time shift needed to match the frequency shift of the Doppler effect. This property leads to a certain range estimation error, which depends on the velocity of the target. The error can be compensated, if the system is able to estimate the velocity by some algorithm. Essentially, the Doppler mismatch for LFM increases with increasing velocity (widened peak and lower maximal value), but in the ± 3 m/s range, the effect is marginal.

The PSD plots for LFM with rectangular and Hann window are shown in Fig. 3.21. In the left figure, one can see the well known band-limited spectrum with ripples at the edge frequencies and the beginning of the conversion to the spectral floor, caused by the rectangular windowed pulseform in time domain. For the Hann windowed signal, the PSD levels outside of the signal's bandwidth are greatly reduced, providing a much better confined spectrum.

The ambiguity diagram already showed the Doppler invariance of the LFM signal in the velocity range

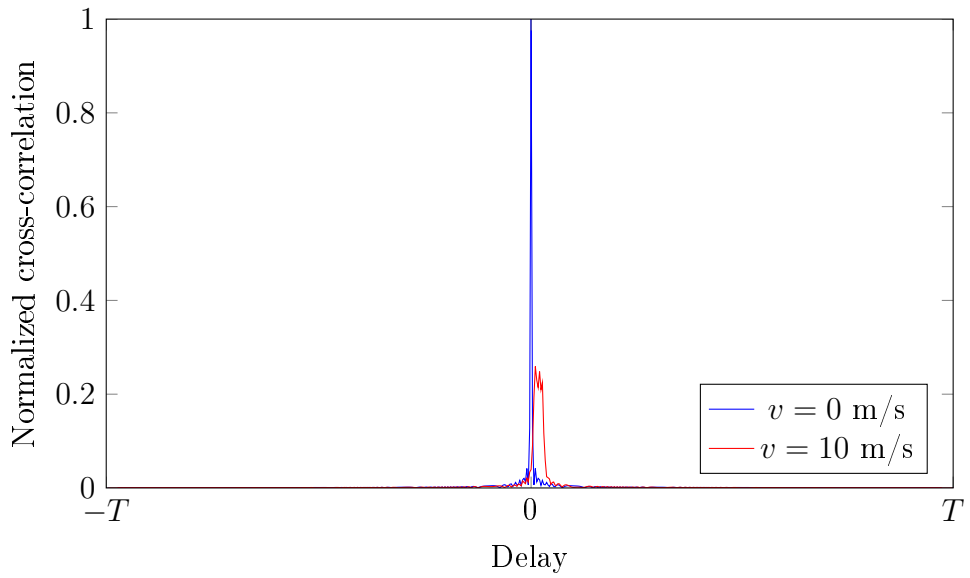

Figure 3.19: Normalized cross-correlation function of an original LFM signal and a signal reflected from a target moving with various speeds, $T = 1$ s, $f_c = 1$ kHz, and $BW = 750$ Hz.

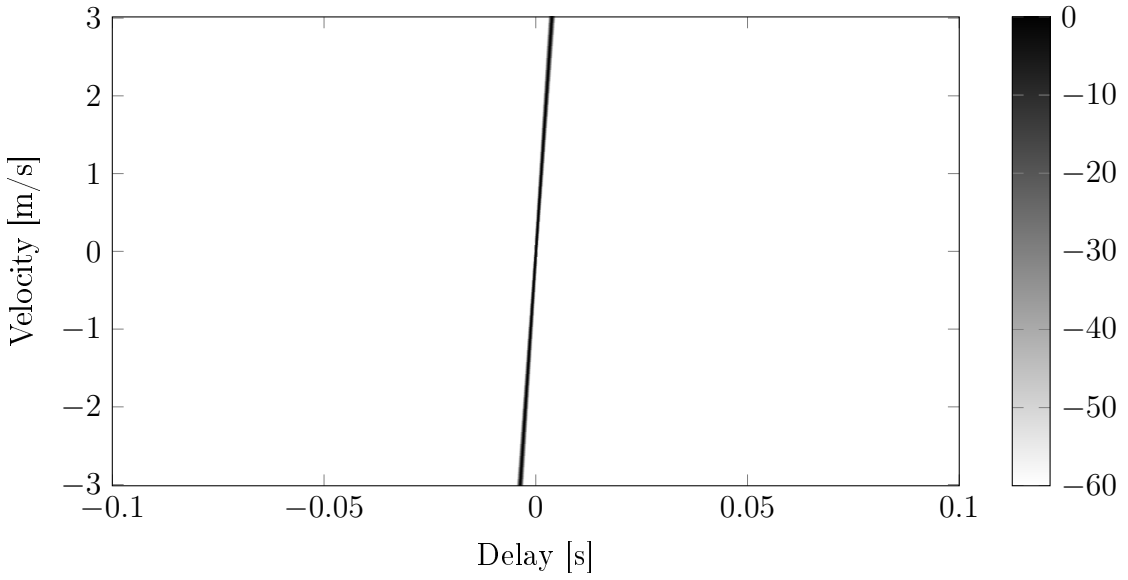

Figure 3.20: Ambiguity diagram of a Hann windowed LFM signal with $T = 100$ ms and $BW = 7500$ Hz.

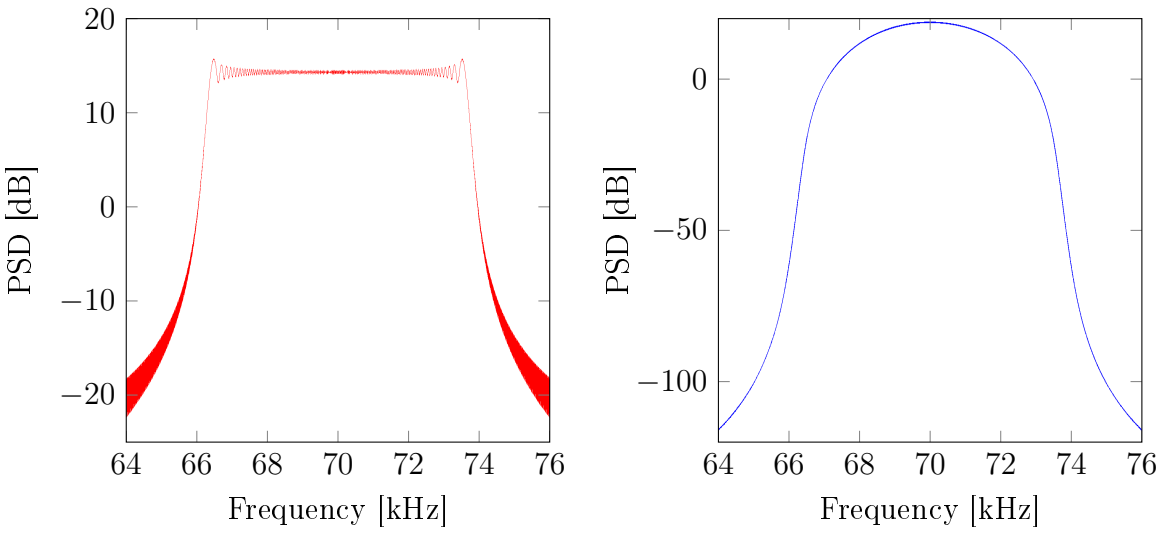

(a) Rectangular window

(b) Hann window

Figure 3.21: Power spectrum for LFM signals with $T = 100$ ms, $BW = 7500$ Hz, and various windowing functions.

of interest. Therefore, the Q-function results for an LFM signal, shown in Fig. 3.22, are as expected – nearly flat over the velocity range. Even when looking at a much wider velocity range of ±30 m/s, the

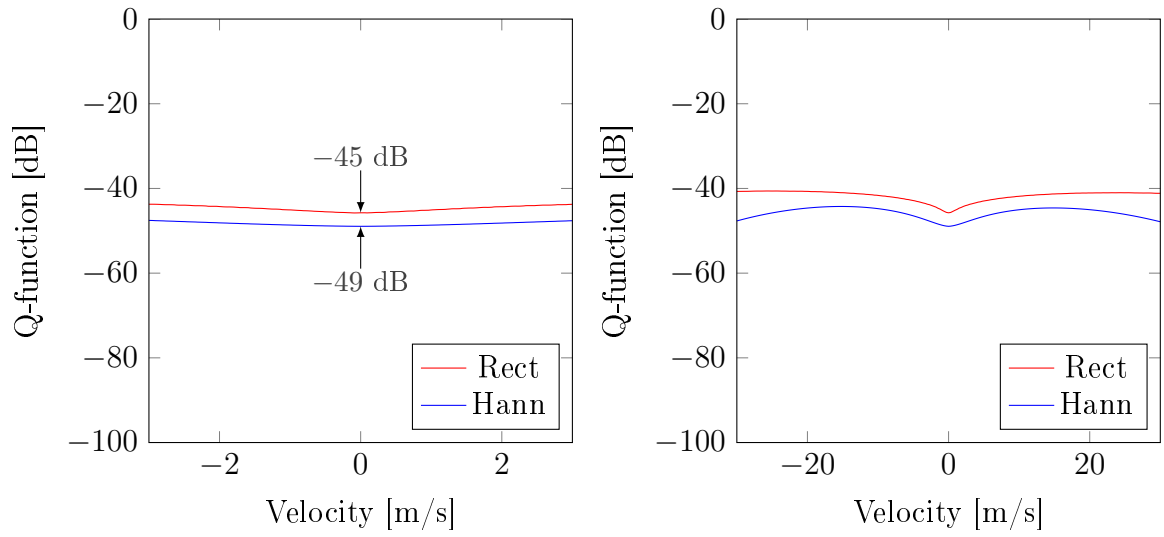

(a) ±3 m/s

(b) ±30 m/s

Figure 3.22: Q-function for LFM signals with $T = 100$ ms, $BW = 7500$ Hz, and various windowing functions.

Q-function curves are nearly flat. The maximal correlation value reduces with increasing velocity, but on the other hand the width of the line in the ambiguity diagram is increased, meaning the integration result stays nearly constant.

3.4.2 Hyperbolic FM

As mentioned earlier, the LFM signal has a certain mismatch when the reflected signal is Doppler shifted. Basically, the Doppler frequency shift, f_D, is frequency dependent and therefore for frequency modulated signals, f_D is non-constant. Previously, it was shown that the instantaneous frequency function of a Doppler shifted signal, $f^D(t)$, can not be matched by the instantaneous frequency function, $f(t)$, of an LFM signal with any time shift, leading to a correlation loss. In order to avoid this loss, the frequency function should fulfill the following condition [Kro69]:

$$f(t) = f^D(t - t_0) \ , \tag{3.62}$$

where $t_0 = f_D/k$ is the time shift needed to match the Doppler frequency shift. When following the derivation in [Kro69], the desired frequency modulation turns out to be a hyperbolic one, given by

$$f(t) = \frac{1}{1/f_0 + kt} = \frac{1}{T_0 + kt} \ , \tag{3.63}$$

where T_0 is the carrier period at $t = 0$. As the instantaneous frequency is the inverse of the instantaneous period $T(t)$ [Kro69], then

$$T(t) = T_0 + kt \ . \tag{3.64}$$

Instead of a linearly increasing frequency, this signal has a linearly increasing period. Therefore, this signal is also called linear period modulation (LPM) [Kro69].

Given that f_0 is selected to be the starting frequency and the time t varies from 0 to T, then k is given by

$$k = -\frac{BW}{f_0 T(f_0 + BW)} \ . \tag{3.65}$$

When integrating (3.63) over time t, the hyperbolic FM (HFM) signal in time domain is given by

$$s(t) = w(t) \exp\left(j\frac{2\pi}{k} \ln(1 + kf_0 t)\right) \ , \tag{3.66}$$

where the phase follows a logarithmic modulation. Hence, some authors also call it logarithmic phase modulation [Tho62, Min02]. The name hyperbolic FM (HFM) or hyperbolic chirp seems to be most widely used and follows the convention that the name is based on the frequency function of the signal.

By inserting $t = \eta t$ into (3.66), the Doppler shifted HFM signal can be written as

$$s(\eta t) = w(\eta t) \exp\left(j\frac{2\pi}{k} \ln(1 + kf_0 \eta t)\right) \ . \tag{3.67}$$

Again taking the time derivative of the phase modulation function divided by 2π, the frequency function becomes

$$f^D(t) = \frac{\eta}{T_0 + k\eta t} = \frac{1}{T_0/\eta + kt} \tag{3.68}$$

and therewith the instantaneous period function is given by

$$T^D(t) = T_0/\eta + kt \ . \tag{3.69}$$

The Doppler shift causes just a constant shift in the period function that can be matched by a certain time shift. The time shift τ can be calculated by solving the following equation

$$T(t) = T^D(t + \tau) \ . \tag{3.70}$$

Extending the above equation with (3.64) and (3.69), the equality becomes

$$T_0 + kt = T_0/\eta + k(t + \tau) \ . \tag{3.71}$$

Solving the equation for τ, gives

$$\tau = \frac{T_0(1 - 1/\eta)}{k} \ , \tag{3.72}$$

that is the time shift, when the two functions align. The instantaneous period and frequency functions of an illustrative HFM signal are given in Fig. 3.23. Consequently, the FM signal becomes truly Doppler

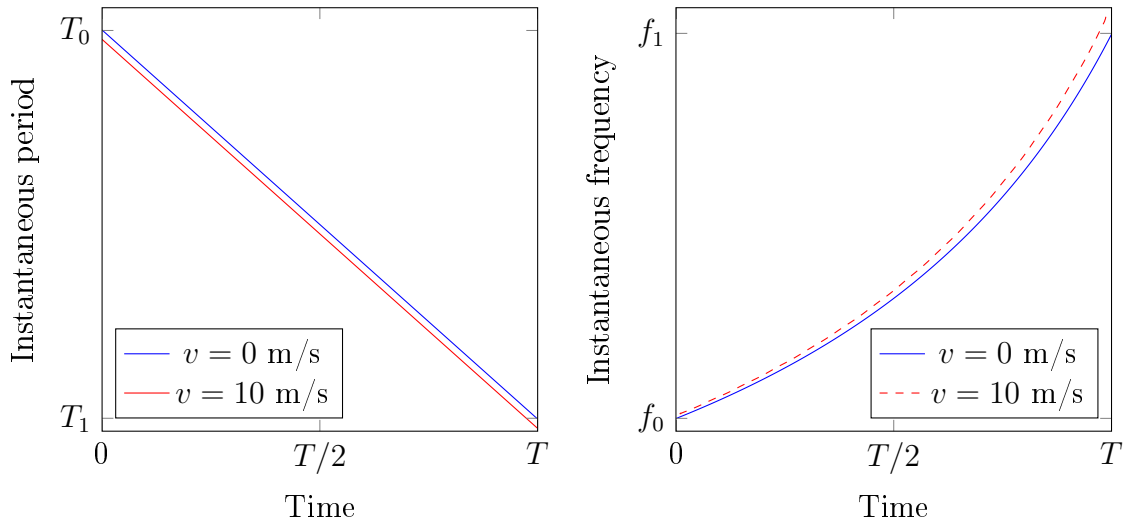

(a) Instantaneous period

(b) Instantaneous frequency

Figure 3.23: Instantaneous period and frequency of a HFM signal reflected from a target moving with various speeds, center frequency at 1 kHz, and $BW = 750$ Hz.

invariant, without a mismatch correlation loss in the matched filter. The normalized cross-correlation function of an LFM signal is shown in Fig. 3.24. The cross-correlation peak for the Doppler shifted reflection is a peak shifted in time. The residual loss in the correlation comes from the edges of the frequency function. This effect could be compensated at the receiver side, by extending the frequency range of the reference signal [Col96]. The ambiguity diagram, PSD and Q-function plots are nearly identical to those of LFM in the ± 3 m/s range and hence, are not repeated.

The HFM signal is the optimal choice, if a wide range of target velocities should be covered and if the channel is not reverberation limited. In such case, Doppler processing is not necessary and the signal provides excellent range resolution and Doppler invariance.

3.4.3 Exponential FM

Exponential FM, also known as exponential chirp signal, is another FM signal design that tries to reduce the Doppler induced mismatch of the LFM signal. The instantaneous frequency, $f(t)$, of the signal varies exponentially with time

$$f(t) = f_0 k^t \ , \tag{3.73}$$

where k is given by

$$k = \left(\frac{f_0 + BW}{f_0}\right)^{\frac{1}{T}} \ . \tag{3.74}$$

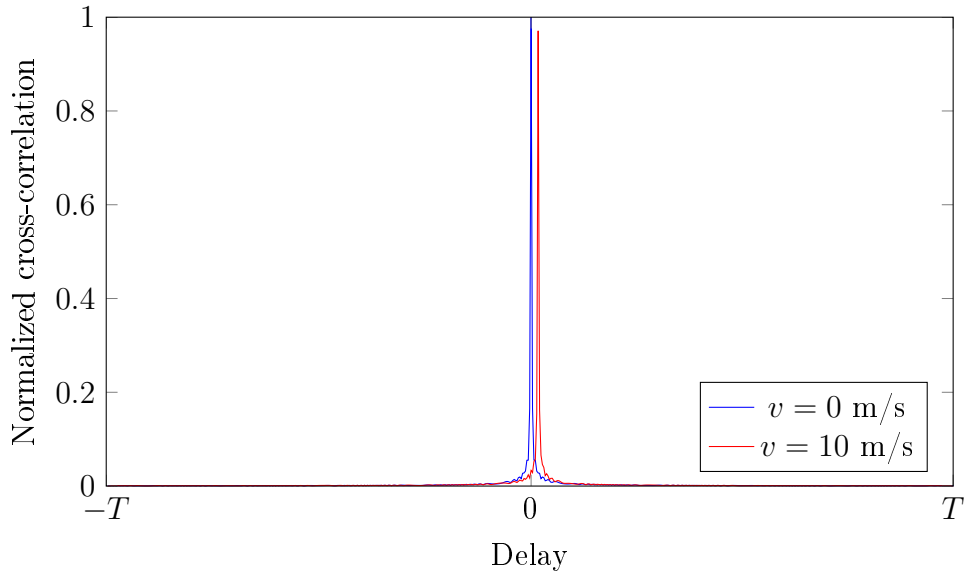

Figure 3.24: Normalized cross-correlation function of an original HFM signal and a signal reflected from a target moving with various speeds.

In time domain, the exponential FM signal is given by

$$s(t) = w(t) \exp\left(j2\pi f_0 \left(\frac{k^t - 1}{\ln(k)}\right)\right) \ . \tag{3.75}$$

The frequency function follows the idea that the Doppler frequency shift, f_D, increases with increasing signal frequency. However, as illustrated in Fig. 3.25 the exponential frequency functions only approaches the optimal hyperbolic frequency function. Indeed, the exponential chirp will have a smaller mismatch caused by Doppler than LFM, but the signal is not Doppler invariant.

Essentially, the exponential FM signal has no benefits over the HFM signal design and therefore, further analysis is not conducted.

3.4.4 Doppler Sensitive FM

If the HFM and the exponential FM signal designs aimed to remove or reduce the mismatch introduced by the Doppler effect, then the Doppler sensitive FM signal design does the opposite, it enhances the mismatch. The idea behind Doppler sensitive FM pulses is to keep the very good range resolution of the FM signal and to add a certain level of Doppler resolution to it. The Doppler sensitive FM pulse was first introduced by Rosenbach and Ziegenbein [RZ96] and later extended by Collins in [Col96, CA98]. In [Col96], the frequency function of the signal is given by

$$f(t) = f_0 + BW - BW\left(1 - \frac{t}{T}\right)^{\alpha} \ , \tag{3.76}$$

where α is a variable greater or equal to one. In the case of $\alpha = 1$, the frequency function becomes linear. For any α value greater than one, the signal becomes Doppler sensitive, where the effect increases with the value of α. Common α values are 2 and 4. In time domain the Doppler sensitive FM signal is given by

$$s(t) = w(t) \exp\left(j2\pi \left[f_0 t + BWt - \frac{BW(T-t)^{\alpha+1}}{(\alpha+1)T^{\alpha}}\right]\right) \ . \tag{3.77}$$

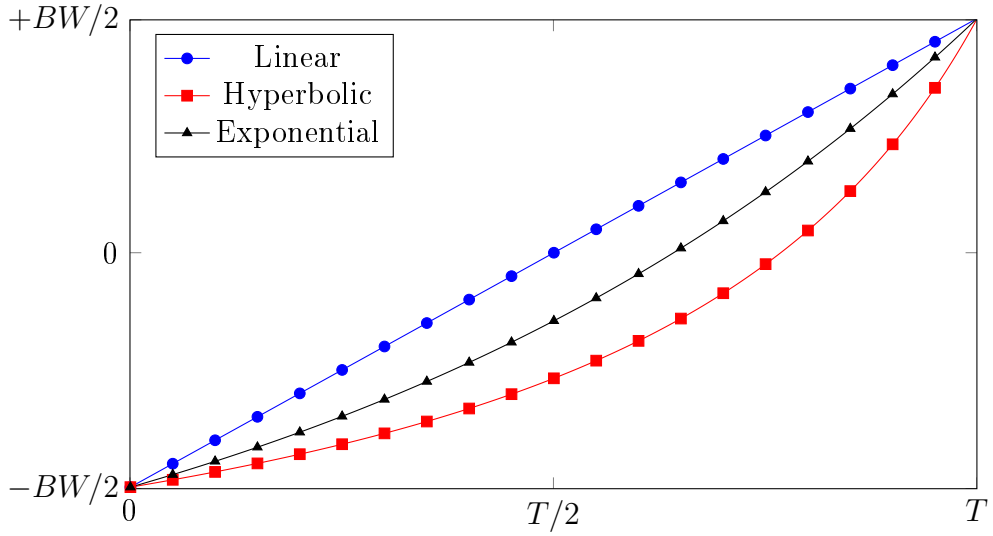

Figure 3.25: Instantaneous frequency of different FM signals.

The comparison of the instantaneous frequency functions of different FM signals is shown in Fig. 3.26. The α value for the Doppler sensitive FM signal in the figure is two. The frequency function of the Doppler

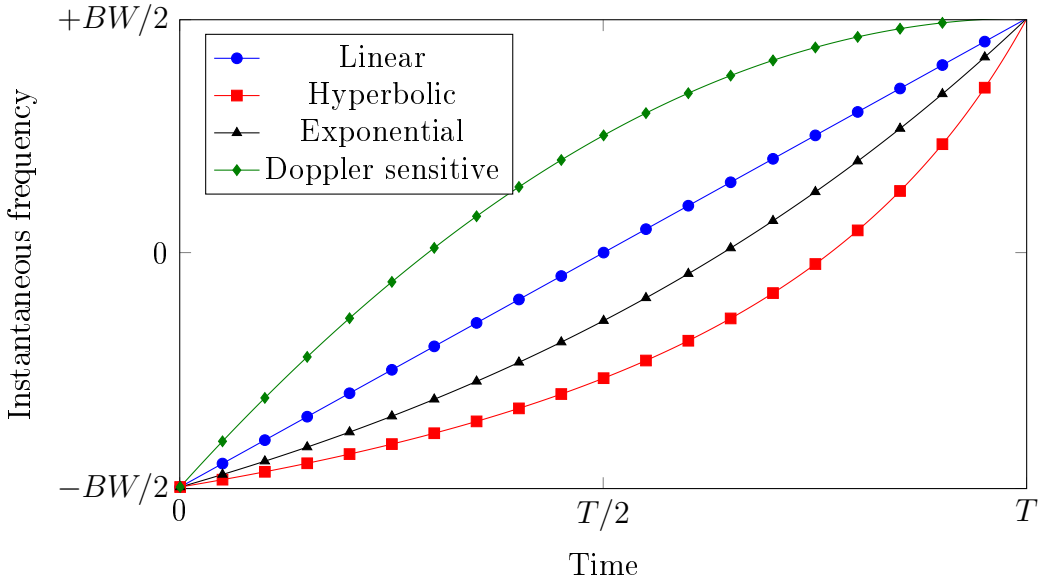

Figure 3.26: Instantaneous frequency of different FM signals.

sensitive FM signal looks like a mirrored version of the hyperbolic FM signal. This disparity leads to the effect that with increasing Doppler, the peak correlation value reduces significantly and the correlation is spread over a wider timespan. The ambiguity diagram in Fig. 3.27 clearly confirms the expectation. One might be tempted to modify the frequency function to be even more extreme, yet eventually as the slope at the beginning of the frequency function increases, the majority of the frequency sweep is done at the very beginning of the pulse. This however, can lead to problems in practical high-power transmitters, where certain time is needed to reach maximal power levels and therewith will alter the pulse-shape and

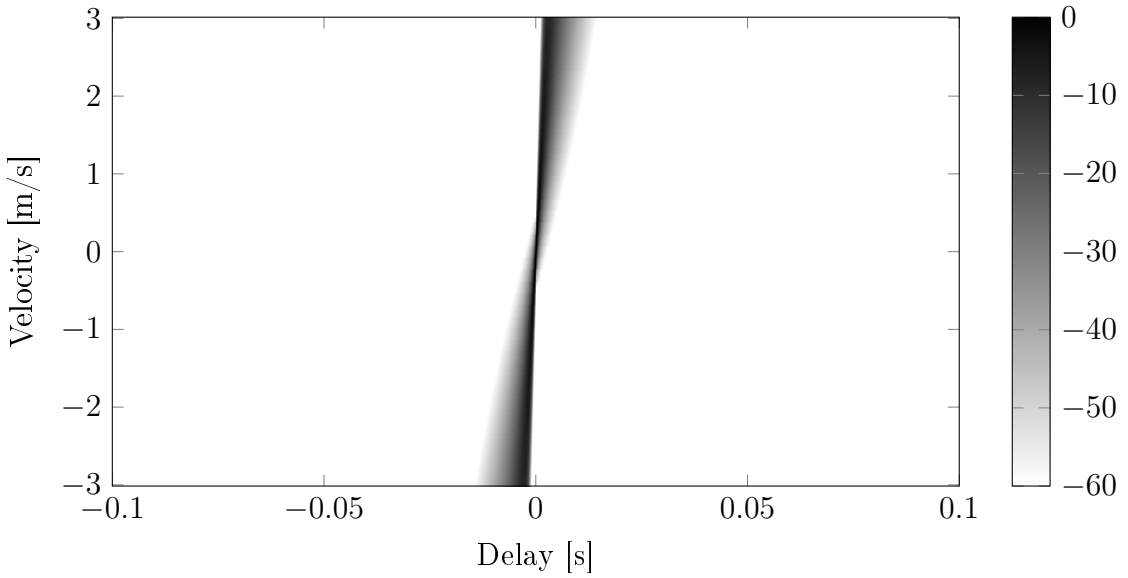

Figure 3.27: Ambiguity diagram of a Hann windowed Doppler sensitive FM signal with $T = 100$ ms, $BW = 7500$ Hz, and $\alpha = 2$.

its effectiveness.

In order to see the direct effect of Doppler on various FM signal designs, Fig. 3.28 shows the maximal cross-correlation value over a wide range of velocities for different signals. Even though the HFM signal is Doppler invariant, as mentioned before, the cross-correlation still has a slight degradation due to the different frequency ranges of the two corresponding signals. At a target velocity of 20 m/s the cross-correlation peak for the Doppler sensitive FM signal is roughly 20 dB lower than that of a stationary target. Nevertheless, comparing these results to signals like CW or SFM, where a similar peak level reduction is achieved at 0.25 m/s, then it becomes clear why one talks about Doppler sensitive signals and not of Doppler selective signals. Especially, when considering velocities relevant to diver detection, ± 3 m/s, then these peak value reductions become even more insignificant. Additionally, the maximal correlation value is just one aspect. The frequency components of the original and Doppler shifted signals are largely still the same, they just might not align at a single time shift, but over a longer time interval. Meaning the correlation is not reduced, but relocated. Therefore, the Q-function for all the introduced FM signals is nearly flat over the velocities and thus, in environments with high reverberation these signals can not utilize Doppler processing, to improve detection of moving targets.

3.5 Random Signals

The last important class of pulses are random signals. The goal of these designs is to generate random sequences that have near ideal autocorrelation properties, in order to achieve very good range resolution. The concept is built on the fact that the correlation will be high only if the patterns of the two signals match. This means that also the Doppler shift will alter the signal enough to destroy the match and lower the correlation. These two properties lead to the well known thumbtack-like ambiguity diagram, where in the center there is a narrow peak in both the time and velocity axis, surrounded by a reduced constant sidelobe level over the whole axis range.

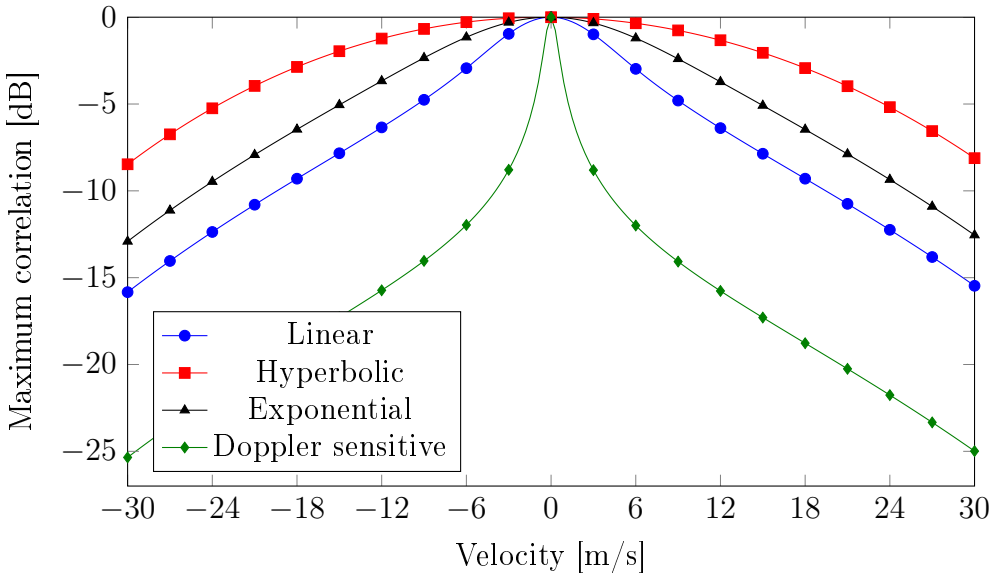

Figure 3.28: Maximal cross-correlation value over the velocities for different Hann windowed FM signals.

3.5.1 Barker Codes

In 1953, Barker introduced a set of binary sequences that possess ideal autocorrelation properties [Bar53]. These codes were used for synchronization purpose in telecommunications. The binary Barker codes consist of ± 1's entries, meaning the corresponding signals have a constant amplitude with a phase alternating between 0 and π. The autocorrelation function of a length N Barker code satisfies

$$|R_x(\tau)| = \begin{cases} N, & \text{for } \tau = 0 \\ \leq 1, & \text{otherwise.} \end{cases} \tag{3.78}$$

In other words, the sequence has maximal correlation of N at zero shift and for all other shifts the value is zero or one. Binary Barker codes for lengths $N = 2, 3, 4, 5, 7, 11$ and 13 are known. Table 3.1 lists all known Barker codes (excluding reversed sequences and inversions) and gives the corresponding peak sidelobe level (PSL) in dB [Pac09]. Due to the design constraint, given in (3.78), the PSL equals $1/N$. Two example autocorrelation functions for $N = 5$ and 13 are shown in Fig. 3.29. The longest Barker code with $N = 13$ has a PSL level of -22.3 dB. Barker codes are often used because of their good autocorrelation property. However, the length of Barker codes is limited to $N = 13$. Therefore, if a CW signal is modulated with a Barker code, then the range resolution of the resulting pulse is limited

Table 3.1: Known Barker Codes

Length	Codes	PSL [dB]
2	$+1-1$, $+1+1$	-6.0
3	$+1+1-1$	-9.5
4	$+1-1+1+1$, $+1-1-1-1$	-12.0
5	$+1+1+1-1+1$	-14.0
7	$+1+1+1-1-1+1-1$	-16.9
11	$+1+1+1-1-1-1+1-1-1+1-1$	-20.8
13	$+1+1+1+1+1-1-1+1+1-1+1-1+1$	-22.3

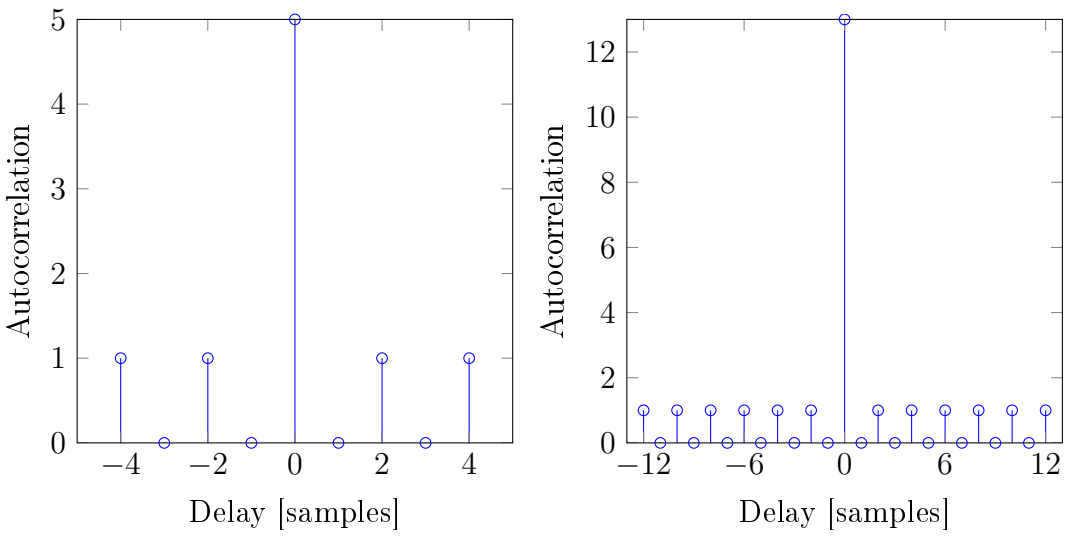

(a) $N = 5$ (b) $N = 13$

Figure 3.29: Autocorrelation plots for Barker codes with various lengths N.

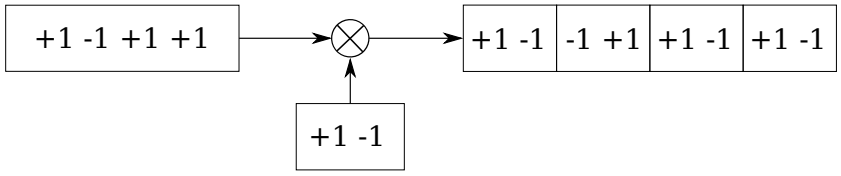

Figure 3.30: Concatenating a length 4 Barker code with a length 2 Barker code.

by the bit length, in this case 1/13th of the pulse duration. In order to improve the range resolution, longer sequences are required. One way to achieve this is to compound multiple Barker codes. This way, for example, every bit/symbol of a length 13 Barker code is "coded" by a length 13 Barker code (code in code), giving a sequence of length $13 \cdot 13 = 169$. The concatenation principle is shown in Fig. 3.30, where a length 4 barker code is concatenated with a length 2 code. The compound codes improve the compression gain, but the peak sidelobe level will stay unchanged. The $13 \circ 13$ compound Barker code provides the longest sequence with a single concatenation, yet more than two codes can be concatenated to generate even longer codes.

In order to compare the Barker code to previous signal designs, a $13 \circ 13 \circ 5$ code concatenation is selected that generates a code of length 845. The Barker code is used to modulate a CW signal. Given that the pulse duration is 100 ms, then the CW with the code of length 845 has a bandwidth of 8450 Hz. Fig. 3.31a shows the autocorrelation function for the $13 \circ 13 \circ 5$ compound Barker code and Fig. 3.31b shows the ACF for the 100 ms modulated CW pulse. The ACF of the bit sequence has a single bit peak at zero delay. Followed by two 14 dB lower peaks at $\tau = 2, 4$ samples (plus the same for negative delays). These two peaks are related to the length 5 Barker code. If one chooses to ignore these two peaks, then the PSL level of the length 845 compound Barker code is at -22.3 dB, that of the length 13 Barker code. However, at the same time the range resolution is just a single bit. When modulating the CW signal with the Barker code, then as can be seen from Fig. 3.31b, the ACF largely preserves the structure that the bit sequence has. Additionally, knowing the periodic structure of the correlation function, the secondary peaks could be removed by later signal processing steps. The -3 dB width of the ACF is just 0.07 ms

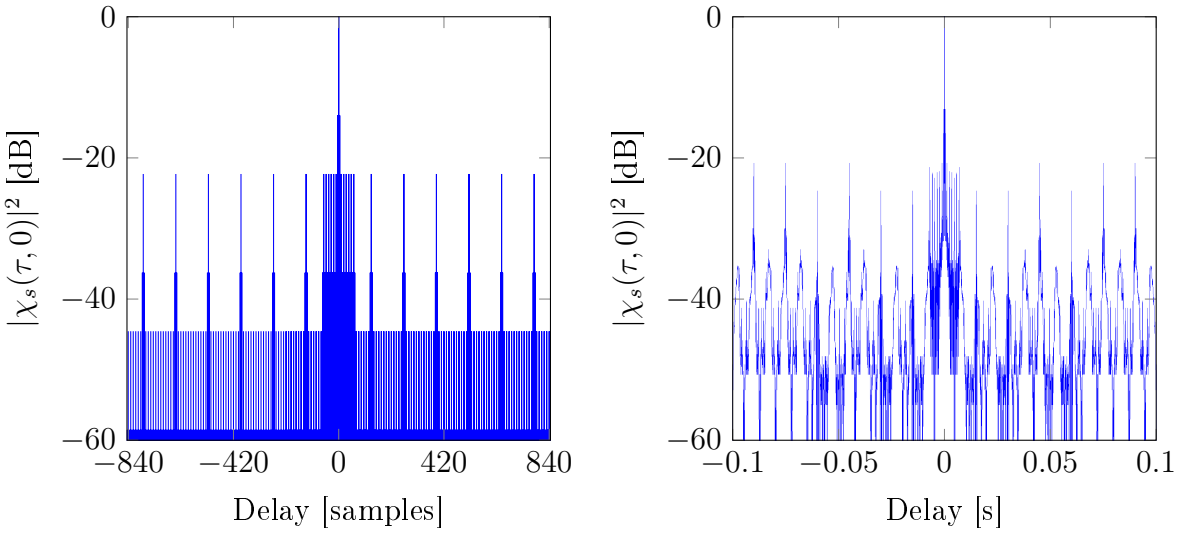

(a) Bit sequence

(b) CW modulated

Figure 3.31: Autocorrelation plots for a length 845 compound Barker code or for a CW signal modulated with the same Barker code.

or $0.6T_b$, where T_b is the duration of one bit in the CW signal. However, the signal has a bandwidth of 8450 Hz and the spectrum of a modulated CW signal is not well confined, meaning the true used bandwidth (due to π phase shifts) is bigger. If the signal would be bandlimited by a bandpass filter, then the -3 dB ACF width would be identical to that of an LFM signal, namely $0.88/BW$. Clearly, the range resolution of such a modulated CW signal is extremely good. However, as always, it comes with a price. The PSD of the signal is shown in Fig. 3.32a. The spectrum has a small peak at 70 kHz, but otherwise it is fairly flat in the range of ± 5 kHz around the center frequency. Certainly, one could use a bandpass filter to limit the spectral levels outside of signal bandwidth without inflicting big distortions to the signal. A more important characteristic is shown in Fig. 3.32b, the influence of the Doppler effect to the Barker coded CW signal. Already at 0.5 m/s the maximum correlation is reduced by the Doppler effect by 10 dB, but it reaches a floor at -15 dB. This Doppler sensitivity together with the ACF describe the characteristic thumbtack-like ambiguity diagram of the random signals.

The ambiguity diagram is shown in Fig. 3.33. The small peak (the stretched black dot) in the center of the diagram is the thumbtack and it is surrounded by a sidelobe level varying between -10 to -40 dB below the maximum. In noise dominated environments with good SNR or in cases where there are just a few reflecting objects, such a thumbtack-like ambiguity peak is very beneficial, as it provides very good range resolution and a possibility to discriminate between targets with different velocities. Yet, if the environment is reverberation dominated, then the high sidelobe levels will mask the desired target.

The above described Barker codes are based on binary sequences. One possibility to create Barker codes with lengths beyond 13, would be to use a base higher than two, for example three, four or six. Codes that use more than two phase values, namely the standard 0 and π, are called polyphase codes. Herewith, polyphase sequences that fulfill the Barker condition are called polyphase Barker codes/sequences [Fra80, BF05] and the combination of binary and polyphase sequences are called generalized Barker sequences [GS65]. Essentially, the higher degree of freedom makes it possible to find longer Barker codes. In [BF05], polyphase Barker sequences up to a length of 63 are published.

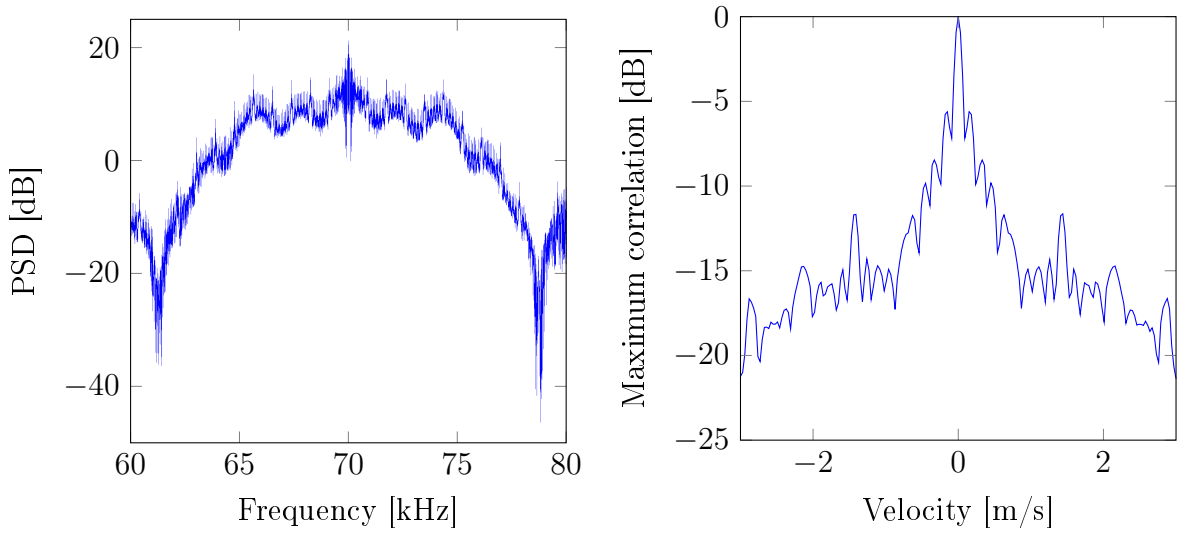

(a) PSD

(b) Doppler effect

Figure 3.32: Power spectrum for a 70 kHz CW modulated with a compound Barker code and the maximum correlation for different velocities.

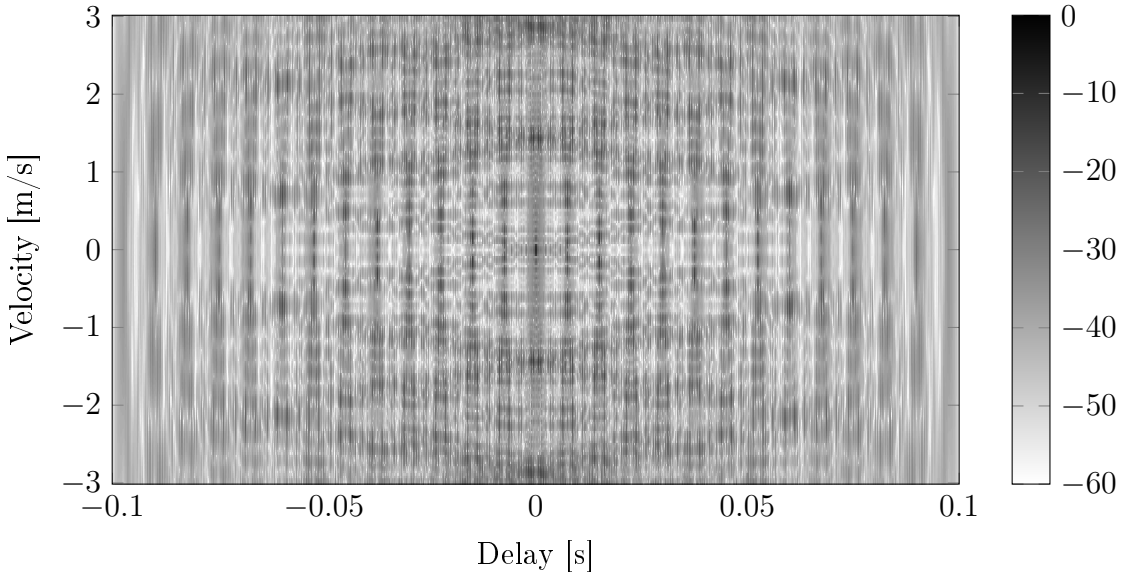

Figure 3.33: Ambiguity diagram of a Barker coded CW signal with $BW = 8450$ Hz and duration of 100 ms.

3.5.2 PRN

Pseudo-random noise (PRN) signals [May83] are a group of signals that consist of random elements and their spectrum is flat over a certain frequency range. These signals resemble white Gaussian noise and their autocorrelation functions have a impulse-like shape. PRN signals may have an arbitrary length and can be generated using different methods:

- Generating a white Gaussian noise sequence of length N, where N equals the pulse duration, T, times the sampling frequency, and bandlimiting the signal by means of filtering.
- Generating a random binary sequence of length N. Mapping the bits to ± 1 values and again bandlimiting the signal.
- Generating a random binary sequence of length $BW \cdot T$, where BW is the desired bandwidth of the signal, and as with the Barker codes, using the sequence to modulate a CW signal of duration T.

Due to the various generation methods, it is also natural that these signals have alternative names, like pseudo-random bit sequence (PRBS) [Col96] or binary phase-shift keying (BPSK) modulated CW signal [JH91].

Fig. 3.34a shows the ACF of a length 750 BPSK modulated CW. Compared to the ACF of a length

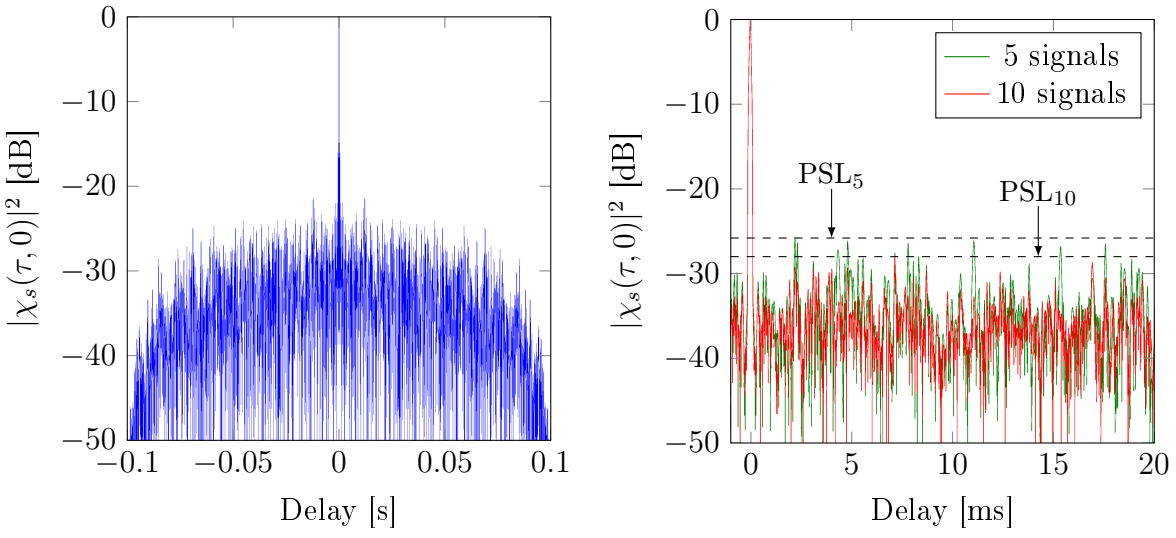

(a) Full ACF of a single pulse

(b) Average ACF

Figure 3.34: Autocorrelation plots for PRN signals, $T = 100$ ms and $BW = 7500$ Hz.

845 compound Barker code shown in Fig. 3.31a, that had a clearly visible structure, the ACF of the PRN signal looks random. The PSL for this PRN sequence of length 750 is at -21.5 dB. Interestingly, the PSL of the given PRN signal is higher than that of a length 13 Barker code. The random nature of PRN signals leads to the fact that each sequence that is generated will have a different structure and PSL. In [Col96] it is brought out that the mean sidelobe levels of PRN signals is at $1/\sqrt{BT}$, where BT is the time-bandwidth product. For example, for a signal with a 7500 Hz bandwidth and signal duration of 100 ms, the mean level is at -28.75 dB. Clearly the peak levels are much higher. Nevertheless, when using randomly generated PRN signals, one can exploit the fact that each time the peak sidelobe levels will appear at different positions (time shifts), by averaging over multiple transmissions. Fig. 3.34b shows

the mean ACF when averaged over multiple random signals. The PSL after averaging over 5 signals is at -25.8 dB and after 10 realizations the PSL is at -28 dB. Therewith, with increasing number of signals the peak sidelobe level converges to the mean level of a single signal at $1/\sqrt{BT}$.

The range resolution of the PRN signals is still very good and the ambiguity diagram in Fig. 3.35 shows a narrow peak in the center and an uniform sidelobe level in both range and Doppler axis. Nevertheless, as also mentioned for Barker codes, in a strongly reverberation limited environment, the superimposed sidelobe levels will mask the narrow peak at zero time shift.

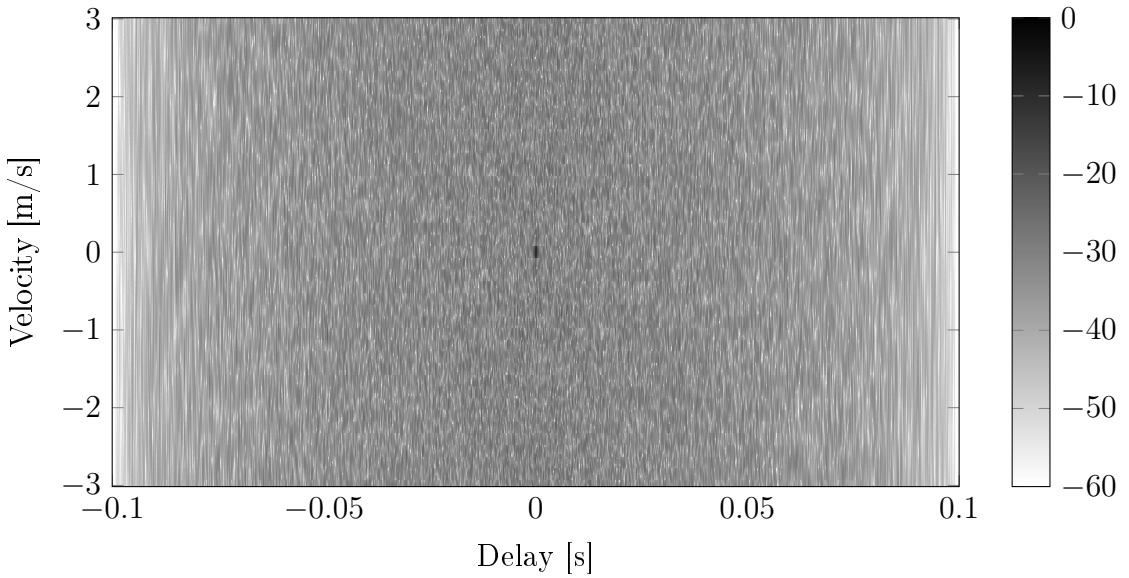

Figure 3.35: Ambiguity diagram of a rectangular windowed BPSK coded CW signal with $BW = 7500$ Hz and duration of 100 ms.

Earlier, it was mentioned that PRN signals have a flat spectrum in their bandwidth range and for confirmation the PSD of length 750 BPSK coded CW signal is shown in Fig. 3.36a. Hann windowing can be used to reduce the spectral sidelobe levels, but in the ACF or in the ambiguity diagram the effect is hardly noticeable. This can be reasoned by the fact that the high sidelobe levels are caused by the randomly correlating signal parts and not by the sharp transitions at the signal edges. The Q-function in Fig. 3.36b confirms the earlier statement that in reverberation limited environments the PRN signals can not be used to discriminate moving targets against the stationary reverberation. Another matter to keep in mind, is that practical transmission systems will have difficulties with the rapid changes in the signal, caused by the random 180° phase shifts. In order to avoid the mismatch between the intended and the transmitted signal, the pulses should be smoothed by bandlimiting the signal.

The PRN signals are quite often preferred if the system should operate below the noise level. As the signal looks like noise and the energy can be distributed over a wide bandwidth, then the signalling activity is harder to detect. Additionally, if for every ping a new random sequence is generated, then jammers can not insert false targets, by repeating the signal they had previously received [Nas04].

When considering a single PRN signal, then its PSL is poor and somewhat unpredictable. One possibility would be to search for PRN sequences that have a desired ACF or another possibility would be to design sequences that are a priori better than the average PRN sequence. One group of signals that have been found to have good ACF properties are called maximum length sequences.

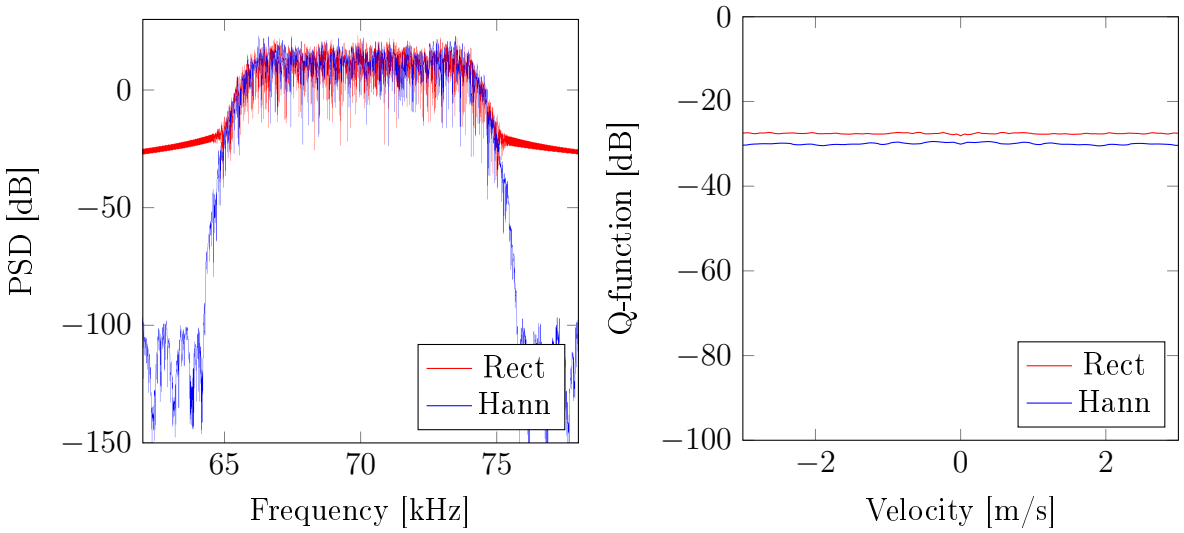

(a) PSD (b) Q-function

Figure 3.36: Characteristic plots for length 750 BPSK coded CW signals, $T = 100$ ms and $BW = 7500$ Hz.

3.5.3 Maximum Length Sequences

Maximum length sequences (MLS) or also known as M-sequences are a special sub-group of pseudo-random sequences. These sequences are generated by linear-feedback shift-registers [Sko90]. Depending on the shift-register length L, the maximal length of the sequence, before it starts to repeat itself, is $N = 2^L - 1$, wherefrom also its name. Fig. 3.37 depicts a shift-register of length 5, where the bits from positions 3 and 5 are fed back. Not all feedback position combinations generate a maximum length sequence. A number of suitable polynomials are listed in [PW72, Dav70, Sko90, Nas04] and Table 3.2 list one possible polynomial for each shift-register length from $L = 1 \ldots 10$.

Interestingly, the listed MLS with $L = 2, 3$ are also Barker codes. Depending on the prime factors of the MLS length N, multiple polynomials exist. However, their PSL values are not equal. For example for $L = 4$, with $\{2, 3\}$ the PSL is at -11.5 dB, while with $\{1, 3\}$ the PSL is at -14 dB. Herewith, if one is looking for the MLS with optimal PSL, then all possible valid polynomials have to be tested, to find the best. Additionally, the number of MLS becomes important, if the system should alternate its transmit sequence for cross-talk or security reasons.

When for PRN signals the mean sidelobe level was at $1/\sqrt{BT}$, then for MLS signals the same level, $1/\sqrt{BT} = 1/\sqrt{N}$, is a good approximation for the peak sidelobe level. Furthermore, the shift-register can be initialized with any non-zero vector, the output sequence will be the same, just starting at a different position. Commonly, the all ones sequence is used as the initialization vector. It is also possible to use

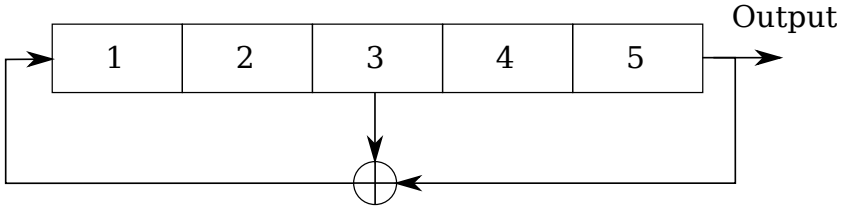

Figure 3.37: Linear-feedback shift-register setup for MLS of maximum length 31.

Table 3.2: Maximum length sequences

L	MLS length	No. of MLS	Feedback positions	PSL [dB]
2	3	1	{1,2}	−9.5
3	7	2	{2,3}	−16.9
4	15	2	{3,4}	−11.5
5	31	6	{3,5}	−15.9
6	63	6	{5,6}	−17.9
7	127	18	{6,7}	−19.2
8	255	16	{1,6,7,8}	−23.5
9	511	48	{5,9}	−26.2
10	1023	60	{7,10}	−28.6

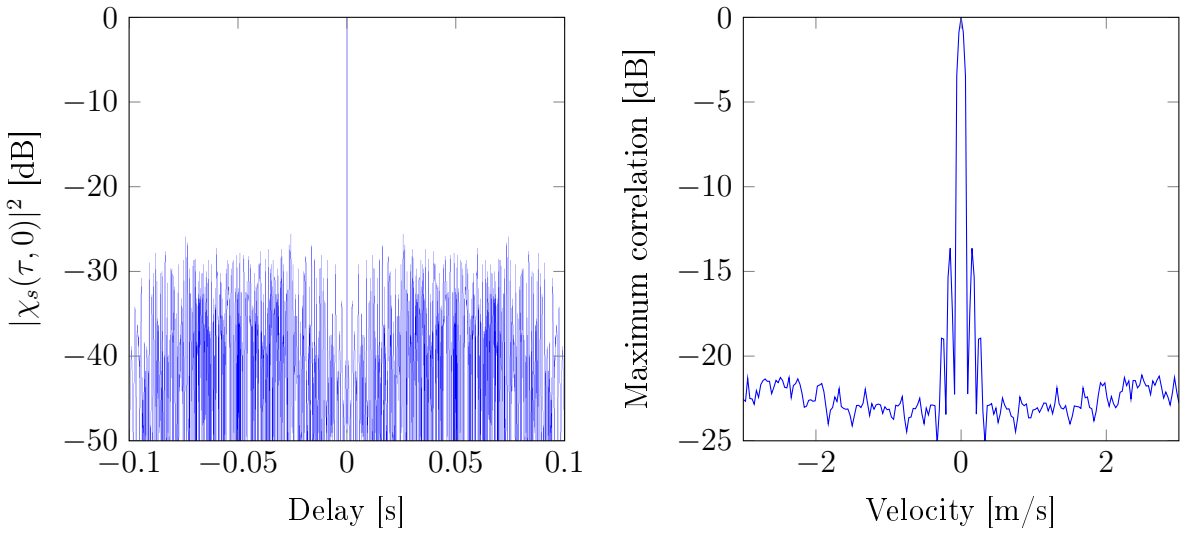

(a) ACF

(b) Doppler effect

Figure 3.38: Range and Doppler resolution plots for a length 511 MLS coded CW signal, $T = 100$ ms and $BW = 5110$ Hz.

a maximum length sequence with a shortened length, for example using only the first n symbols of the length N sequence, but doing this degrades the PSL of the signal. If this is required, one should closer investigate the effect of clipping.

The maximum length sequences, sometimes also called pseudonoise (PN) sequences [CA98], have a pseudo-random structure and therefore also their ACF has the properties of random sequences. The ACF of a 100 ms CW signal coded with a MLS of length 511, $L = 9$ and the feedback positions at 5 and 9 is shown in Fig. 3.38a. The peak sidelobe value is at −26 dB and the ACF −3 dB width is 0.12 ms (or $0.6T_b$), where T_b is the duration of one bit in the CW signal or if the signal is bandpass filtered, then would have a width of $0.88/BW$. The ambiguity diagram is shown in Fig. 3.39. Interestingly, the ACF or the cross-correlation with 0.0 m/s signal has a lower sidelobe level, than if the signal has a non-zero velocity. Consequently, the sidelobe level for the Doppler effect plot in Fig. 3.38b is higher than the PSL for the ACF. The Q-function would still be a flat line over the velocities, but for certain channel conditions, such a thumbtack-like ambiguity function can be very desirable. For this reason the MLS are

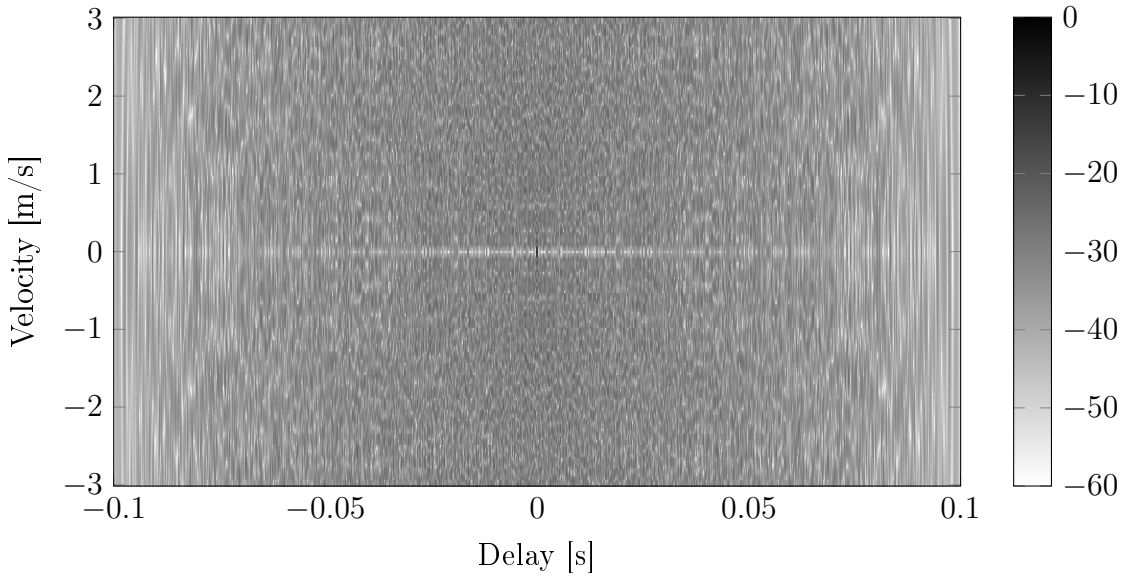

Figure 3.39: Ambiguity diagram of a rectangular windowed MLS coded CW signal with, $L = 9$, $BW = 5100$ Hz and duration of 100 ms.

often used for channel impulse response measurements. In conjunction with the possibility to implement the correlator detector for MLS using the fast Walsh-Hadamard transformation [CL77], the maximum length sequences are an attractive solution for channel impulse measurements with low complexity and good precision.

In conclusion, random signals are designed to have a very good ACF and due to their structure they have a thumbtack-like ambiguity function. However, recalling the constant total volume property of the ambiguity function, cf. Sec. 3.1.2, the thumbtack has a relatively small volume. Hence, the ambiguity has to be distributed around the peak, over a larger area. In a way, the ambiguity diagram of the MLS coded CW signal in Fig. 3.39 visualizes this perfectly. The ACF PSL level is at -26 dB, while the sidelobe level for any non-zero Doppler is higher. These special maximum length sequences shift some of the ambiguity from the ACF somewhere else in the ambiguity diagram. When considering the Doppler selectivity via the Q-function, then the volume of the central peak is too small, compared to the relatively high sidelobe level over a much longer length. Hence, the random signals are not Doppler selective, but Doppler sensitive, what for some tasks is enough. Finally, for direct comparison, Fig. 3.40 shows in one plot the Doppler sensitivity of earlier analyzed random signals.

3.6 Windowing

In Sec. 3.2.1, where the CW signal was introduced, the effect of different windowing functions, namely the rectangular and Hann windowing, was presented. In this section, the aim is to give a brief overview of a few windowing functions and to present their main benefits and drawbacks.

Essentially, if the transmit signal is time-limited, no windowing means rectangular windowing. The Fourier transform of a rectangular shape of width T, is a sinc function, with zeros at multiples of $1/T$. Hence, the PSD of the rectangular pulse will have a peak sidelobe level 13.3 dB lower than the main lobe. Consequently, a rectangular windowed CW pulse of duration T, will have in its Doppler response (ambiguity diagrams cross-section at $\tau = 0$) a secondary peak positioned at $1/(1.5T)$, 13.3 dB lower than

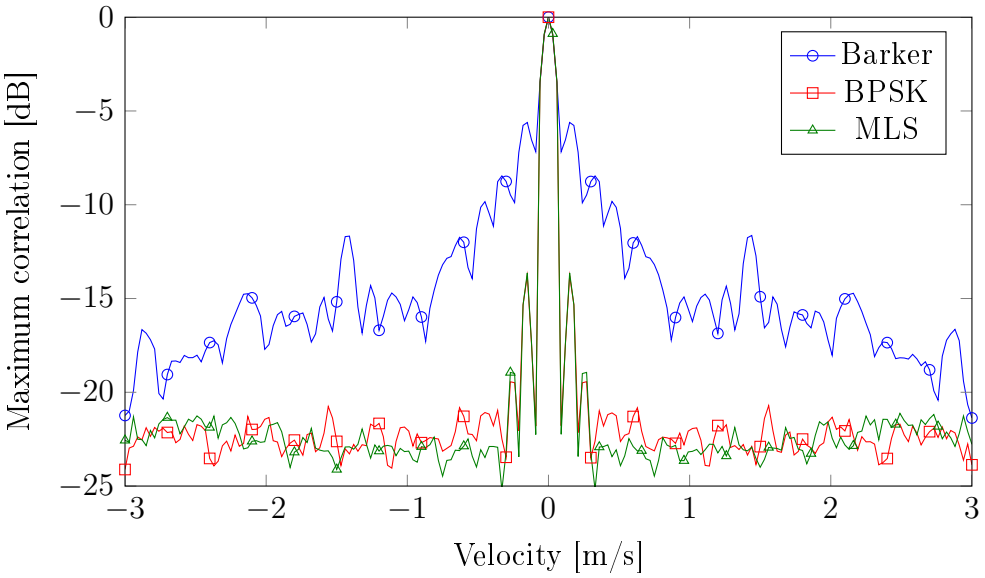

Figure 3.40: Maximal cross-correlation value over the velocities for different random signals.

at the zero Doppler. Such a high sidelobe level is unwanted and should be lowered.

The goal of windowing (in time domain), or also called time weighting, is to shape the Doppler response of the signal by altering the shape of the waveforms envelope [Sko90]. Therefore, in order to improve the Doppler response of the signal a (non-rectangular) windowing/weighting function should be used. Fig. 3.41 shows three possible window functions: Hamming, Hann, and Blackman.

All three belong to the family of generalized cosine windows or earlier also called Harris windows

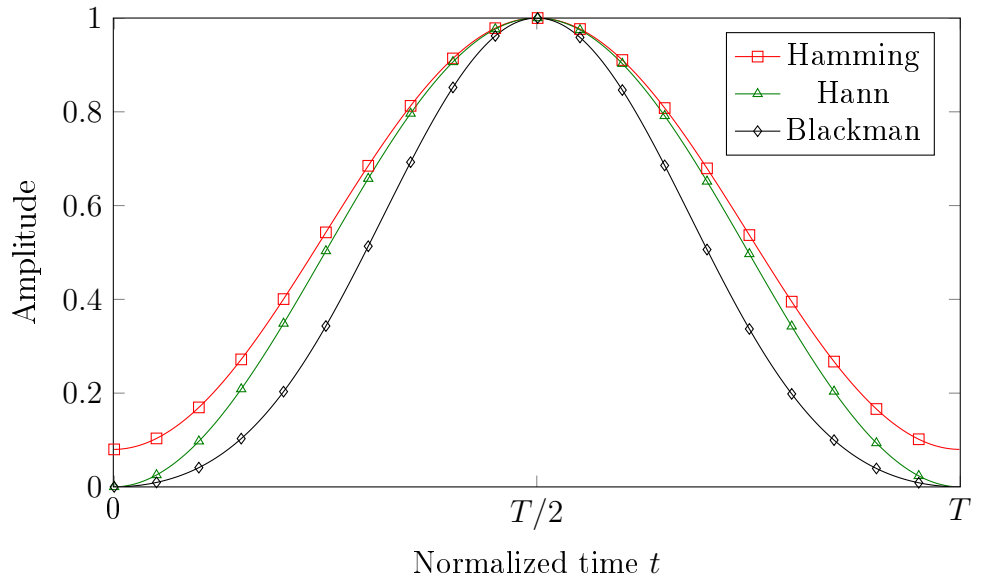

Figure 3.41: Window functions.

[Nut81], given by

$$w(t) = \sum_{k=0}^{K} (-1)^k a_k \cos(2\pi k t/T), \quad \text{for} \quad 0 \leq t \leq T \tag{3.79}$$

where a_k are real-valued constants and T is the window length. Note that, if the time axis would be symmetric about $t = 0$, then the $(-1)^k$ term would be dropped. The Hann window, also known as Hanning window, has only two non-zero coefficients

$$a_0 = 0.5, \quad a_1 = 0.5 \ , \tag{3.80}$$

and the Hann window function is given by

$$w_{Hann}(t) = 0.5(1 - \cos(2\pi k t/T)) \ . \tag{3.81}$$

In fact, the Hann window can also be written as a cosine squared function

$$w_{Hann}(t) = 1 - \cos^2(\pi t/T) \tag{3.82}$$

that follows from the double-angle formula known from trigonometry

$$\cos(2\theta) = 2\cos^2(\theta) - 1 \ . \tag{3.83}$$

The Hamming window is very similar, also with two non-zero coefficients

$$a_0 = 0.54, \quad a_1 = 0.46 \ . \tag{3.84}$$

The main difference between Hann and Hamming window is that the later does not start and end at the zero value (red curve in Fig. 3.41). The (pedestal) height can principally take any value between 0 and 1, but the 0.08 level generated by the above stated coefficients, minimizes the peak sidelobe level. In order to further reduce the peak sidelobe level, more than two coefficients have to be used and so one arrives to the Blackman window with three coefficients

$$a_0 = 0.42, \quad a_1 = 0.5, \quad a_2 = 0.08 \ . \tag{3.85}$$

The normalized PSD for all four window functions are shown in Fig. 3.42 and the overview of different windowing functions is given in Table 3.3.

Figure 3.42 shows the characteristics of the windowing functions. Clearly, the rectangular window has the highest sidelobe levels. Other windows significantly reduce the sidelobe levels at the expense of broadening the main lobe. Along with the -3 dB main lobe width and PSL, Table 3.3 also lists SNR loss and the PSD falloff per octave. Given that the hydrophone has a maximal output level, then windowing reduces the total power of the transmit signal, resulting in a certain SNR loss. Lastly, the falloff factor is clearly visible in the PSD figure, where the PSD for Hann and Blackman windows declines at an increased rate, compared to that of rectangular and Hamming windows.

Table 3.3: Overview of different windowing functions

Windowing function	SNR loss [dB]	Main lobe width	PSL [dB]	Falloff [dB]
Rectangular	0	0.88/T	−13.3	6 dB/octave
Hamming	1.34	1.33/T	−42.7	6 dB/octave
Hann	1.76	1.46/T	−31.5	18 dB/octave
Blackman	2.37	1.66/T	−58.1	18 dB/octave

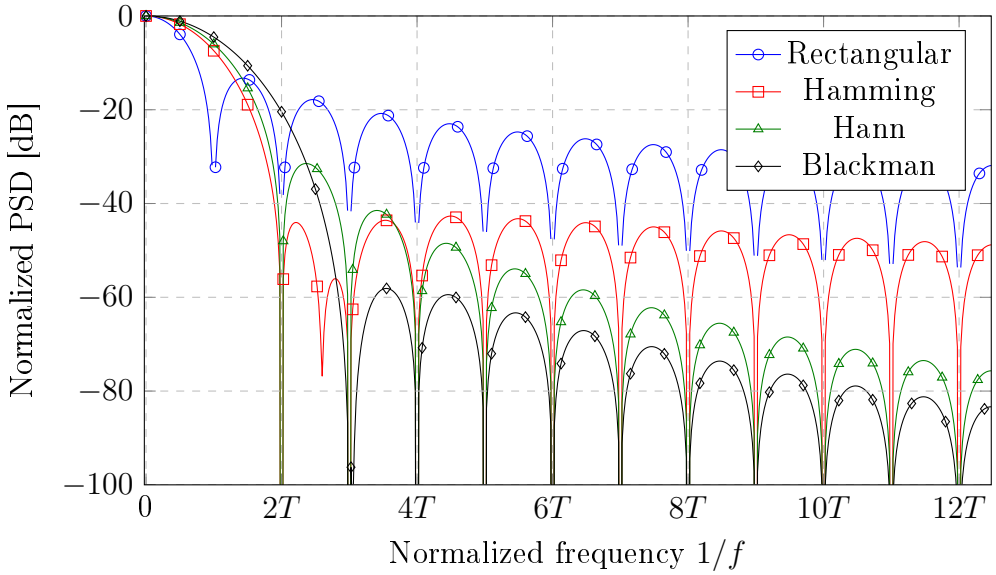

Figure 3.42: PSD of four window functions.

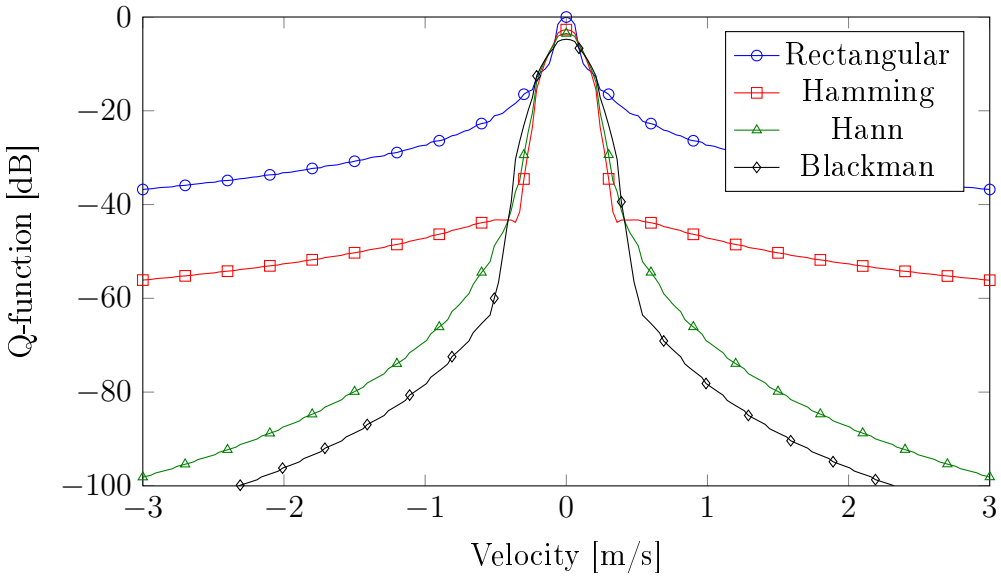

Figure 3.43: Q-function of a 70 kHz CW signal with $T = 100$ ms and various window functions.

Considering the aim of the given work, then either the Hamming or Hann window could be used. However, as can be seen from the Q-function plot for 100 ms CW signal with various windowing functions, shown in Fig. 3.43, then the Hann window is selected because of its superior falloff rate. The drawback from a broader main lobe is acceptable and due to a reverberation limited scenario, the SNR loss is irrelevant. Finding the optimal window function is out of the scope of this work, but a more comprehensive list of window functions can be found in [Sko90] and [Ain10].

3.7 Summary

In this chapter, three main groups of signals, namely CW, FM, and random signals have been analyzed. In the following, a brief summary of characteristic signals is given.

- CW:
  The CW signal is very simple and robust. Its main strength is its Doppler resolution, where for a rectangular windowed signal the -3 dB width is approximately $0.88/T$ Hz. However, the -3 dB range resolution is $0.6T$, meaning one can either have good range or Doppler resolution, but not both at the same time.

- SFM:
  The SFM signal is a modification of the CW signal. Essentially, the additional phase modulation is used to spread the energy of the spectrum in the spectrum. The bandwidth of the signal is an additional design parameter, unlike for CW, where the bandwidth is given by the signal duration T. From one side, the time-bandwidth (BT) product of the signal is significantly increased, but as the envelope of the ACF is identical with the ACF of the CW signal, the -3 dB range resolution does not necessarily improve. Yet, the modification fulfills its purpose, at shifting some ambiguity from the zero Doppler shift and by that improving the performance of the signal in reverberation. The improvement of the Q-function is visualized in Fig. 3.44.

- FM:
  FM signals fully utilize the given bandwidth to improve the range resolution. The -3 dB width is approximately $0.88/BW$. The Doppler behavior varies depending on the frequency function. The HFM signal is Doppler invariant and in literature the Doppler resolution is said to be $0.6BW$. In Fig. 3.28 the Doppler resolution was shown in the form of maximal cross-correlation over the velocities and one could see that the -3 dB width can be significantly reduced, using signal designs like the Doppler sensitive FM. Regardless, the Q-function for FM signals is basically flat over the velocities of interest.

- PRN:
  Pseudo-random noise signals are created with the aim to have an ACF that resembles a Dirac delta function. Often random signals initially have a very wide bandwidth and have to be bandlimited to conform with hardware limitations. Given that a PRN signal is limited to a certain bandwidth, its range resolution is identical to that of FM signals, $0.88/BW$ and at the same time its Doppler resolution is identical to that of a CW signal, $0.88/T$ Hz. Nevertheless, the benefits come with a drawback. Attributed to its random nature, PRN signals have a certain base correlation level, a sidelobe, that never disappears. In reverberation limited environments, this high sidelobe level over a longer duration masks the "perfect" correlation peak of the wanted object.

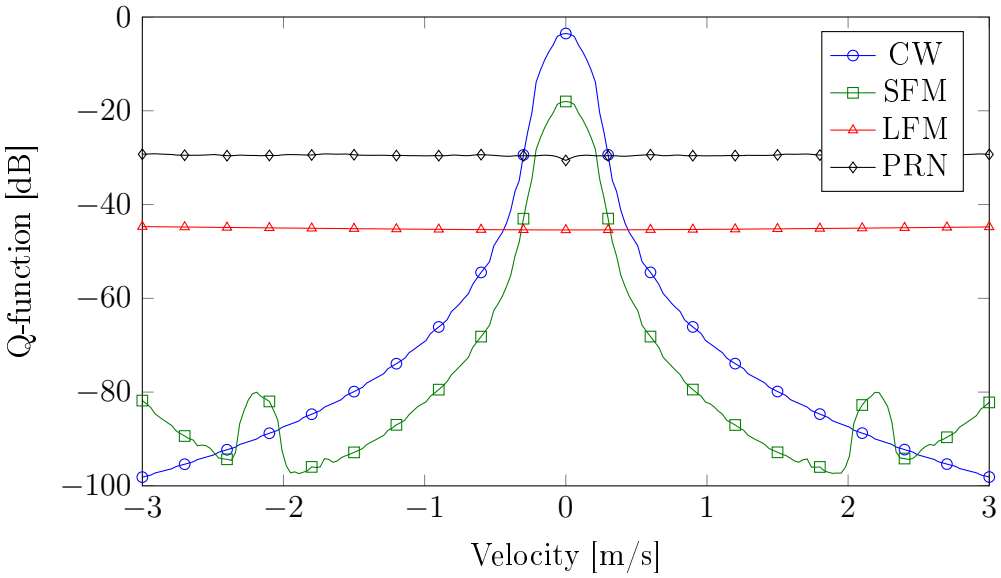

Figure 3.44: Q-function of various signal designs with comparable duration and/or bandwidth.

Chapter 4

CutFM Signal

In the previous chapter, a variety of different known transmit signals were introduced and the class of FM signals presented some of the best properties, most important of them being its excellent range resolution. In addition, as FM signals are (nearly) Doppler invariant, just one reference signal is needed for the correlation detector to cover the target velocities of interest. FM signals, mainly LFM and HFM, have been used in practice for a while and have proven to be relatively robust against hardware imperfections.

In the summary of the last chapter, it was brought out that in noise limited environments, the FM signal together with the optimal matched filter provide maximal SNR and optimal range resolution. In reverberation limited environments, the pulse selection comes down to either CW or FM based signals. Given that the reverberation does not mask the target, the FM signal with its excellent range resolution is the best choice. However, if the reverberation is too strong, a CW signal could be used to enhance the reflection from the moving target against the stationary reverberation. Furthermore, modified versions of the CW signal like the SFM and Cox comb have been developed in order to improve the Q-function. Yet, for all CW based signal designs, the poor range resolution is a major drawback. This gives rise to the idea, to instead use the FM signal as the base and to alter it so that it becomes Doppler selective, while retaining most of its strengths.

4.1 Basic Concept

In Sec. 3.4, it was shown that in general FM signals are Doppler invariant. For some signal designs, like HFM, this assumption is valid for any velocity range and for LFM, the signal can be considered Doppler invariant, for a limited velocity range. For HFM it was shown in Sec. 3.4.2 that the Doppler shift can be matched by a signal time shift, meaning the cross-correlation between the Doppler shifted and the original signal will still have a single high peak, only suffering a slight loss due to the frequency components at the signal edges. One way to illustrate the Doppler shift of an FM signal is shown in Fig. 4.1. The original FM signal starts at frequency f_0 and ends at frequency f_1, where the bandwidth is, $BW = f_1 - f_0$. The Doppler shifted FM signal, in this case assuming a positive angular velocity, starts at frequency f_0^D and ends at frequency f_1^D, where according to (2.8)

$$f_i^D = f_i(1 + v/c) \ . \tag{4.1}$$

Essentially, the frequency components are shifted by a certain factor. Nevertheless, besides the slight "shift", the two signals largely consist of the same frequency components and the components have the same order (not mixed, as for random signals). Therefore, at a certain time shift (or a timespan), the

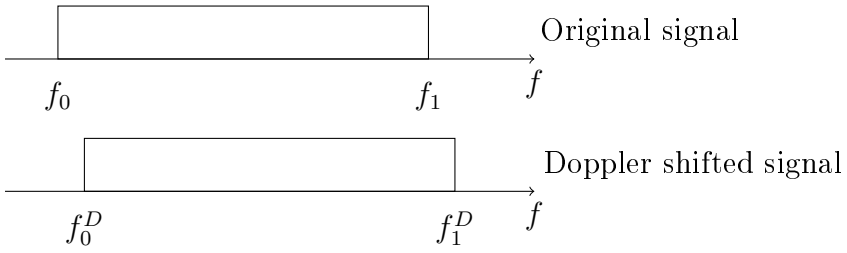

Figure 4.1: Illustration of the Doppler shift on an FM signal.

two signals will have a high correlation. Thinking back, SFM and Cox-comb signals also had a wide bandwidth, but they had a comb spectrum. The gaps in the spectrum made it possible to stay Doppler selective, just as the base CW signal. In order to make FM signals Doppler selective and achieve a similar Q-function as CW or SFM signals, it would also need a comb spectrum, with gaps or "missing frequency components". One possibility to achieve this would be to periodically cut out frequency components from an FM signal. For simplicity and convenience, the LFM signal is selected for the following illustration. The LFM signal has a linearly increasing instantaneous frequency function over time, hence the cutting can be done in the time domain and the effects directly translate into the frequency domain. The concept of periodic cutting is illustrated in Fig. 4.2.

Due to the fact that the new signal is a cut version of the original FM signal, we call it the cutFM signal [NH13, NH15]. In this particular case, after every 2 seconds the next 2 seconds of the signal is cut out (or set to zero), giving a 50% duty cycle or a $1:1$ cut ratio, 1 part kept, 1 part cut out. The cutting repetition period is denoted by T_r. Effectively, certain frequency components in the cutFM signal are removed. Now, for the cutFM signal, the effect of a Doppler shift is illustrated in Fig. 4.3. As the cutFM signal is periodically missing frequency components, then with increasing Doppler shift, the two signals will have less and less common frequency components, till a minimum is reached and after that point the "teeth" start to overlap again. Hence, the signal becomes Doppler selective, but has periodic Doppler ambiguities, just like the SFM or Cox-comb signals.

This concludes the basic idea behind the cutFM signal design. In the following, the effect of cutting is analyzed in detail and from there, the proper design parameters will be derived.

4.2 CutFM Signal Design

The cutFM signal is given by the multiplication of a LFM signal with a "cutter" signal, $s_{cut}(t)$, according to

$$s(t) = s_{LFM}(t) \cdot s_{cut}(t) \ , \tag{4.2}$$

where the LFM signal has been defined in Sec. 3.4.1 as

$$s_{LFM}(t) = w(t) \exp\left(j2\pi\left(f_0 t + \frac{BWt^2}{2T}\right)\right) \ . \tag{4.3}$$

The cutter signal is a periodic signal, where the sub-pulse $s_s(t)$ is repeated with a period T_r and the duration of $s_{cut}(t)$ is T

$$s_{cut}(t) = \sum_{n=1}^{N} s_s(t - nT_r) \ , \tag{4.4}$$

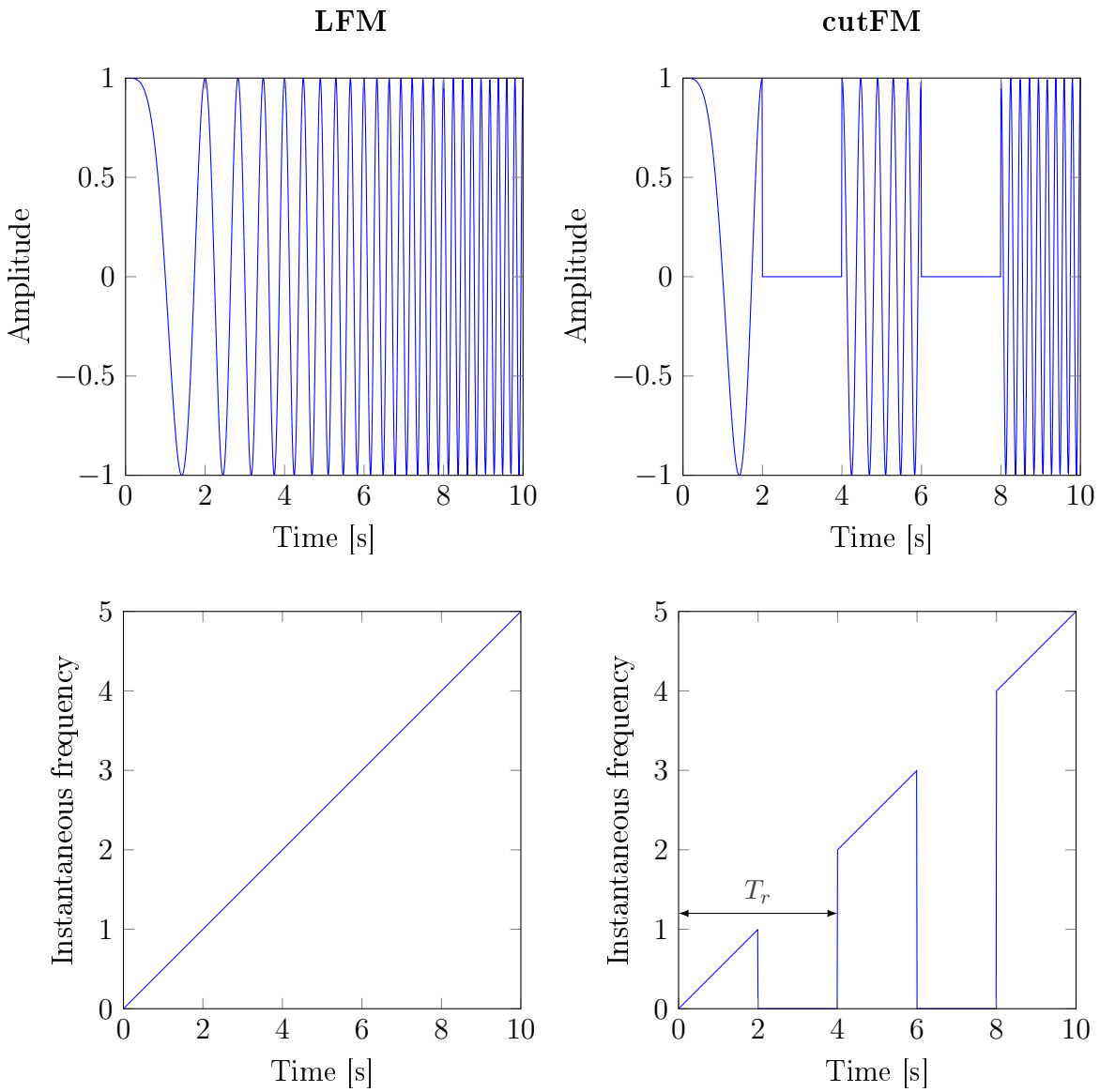

Figure 4.2: The concept of periodic cutting and a comparison of LFM and cutFM signals.

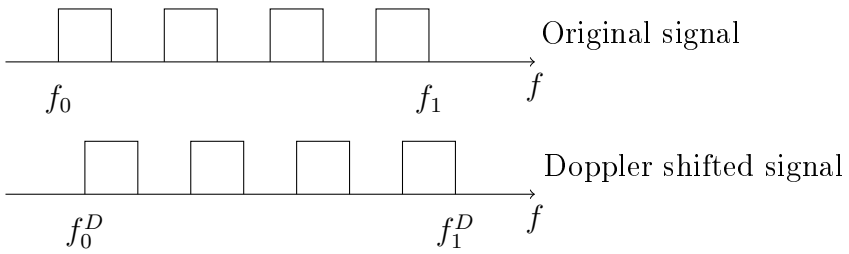

Figure 4.3: Illustration of the Doppler shift on a cutFM signal.

with $N = T/T_r$. The sub-pulse $s_s(t)$ is given by

$$s_s(t) = \begin{cases} w_1(t), & \text{for } 0 \leq t \leq T_w \\ 0, & \text{otherwise} \end{cases} \tag{4.5}$$

where $T_w \leq T_r$ and $w_1(t)$ is a window function of duration T_w (rectangular, Hann, etc.). At this point, the author would like to point out that compared to the section on CW train signals, cf. Sec. 3.3.1, the pulse duration T now refers to the cutFM signal duration and not to the duration of the sub-pulses. A few example cutter signals are shown in Fig. 4.4, where for the first two cutter signals the windowing function is rectangular and for the third it is a Hann window. The signal levels vary between one and zero. The duration of the cutter signal is T, the same as that of the original LFM signal. In addition to the three durations, T, T_r, T_w, the T_w/T_r ratio or the duty cycle, D, is an important design parameter that describes the proportion of the original LFM waveform in the cutFM signal.

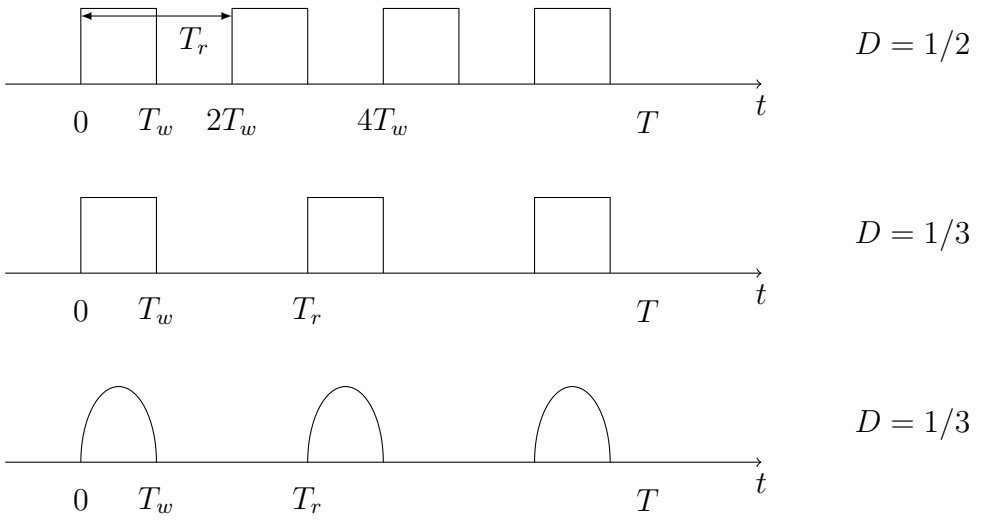

Figure 4.4: Example cutter signals with various windowing functions and duty cycles.

4.3 Frequency Analysis

The cutFM signal is generated by multiplying the LFM signal with the cutter signal in the time domain, therefore the spectrum of the cutFM will be the convolution of the two individual signal spectra. The aim of the cutFM signal design is to create a comb spectrum and hence, it is relevant to analyze the signal in the frequency domain. The spectrum of the LFM signal is already known from Sec. 3.4.1 and the cutter signal is very similar to the CW train analyzed in Sec. 3.3.1. Nevertheless, due to the redefined pulse durations, we would like to repeat some of the analysis in order to emphasize a few of the key factors for cutFM signal design.

The evolution of the spectrum of a periodic signal is shown in Fig. 4.5. Basically, the spectrum of the periodic signal is a "sampled" version of the single pulse spectrum. However, as the cutter signal is not of infinite duration, but time limited, then instead of Diracs the spectrum consist of sinc functions, due to the rectangular windowing of length T. The envelope of the cutter signals spectrum is determined by the window function, $w_1(t)$, used in the sub-pulse and the spectral peaks are separated in frequency by $f = 1/T_r$. Based on the properties of different windowing functions, namely the peak sidelobe level and

the PSD falloff per octave, summarized in Sec. 3.6, from here on, the Hann window of duration T_w is used in the cutter signal.

The normalized PSD of the Hann window, $W_1(f)$, and of the cutter signal with $D = 1/2$ duty cycle are shown in Fig. 4.6. Recalling Sec. 3.6, the red curve for the Hann window is already familiar. It has its first zero at $f = 2/T_w$ and the peak sidelobe level is at -31.3 dB. The blue curve for the cutter signal has spectral peaks at multiples of $1/T_r$. The width of the spectral peaks or of the sinc functions are determined by the signal duration T and the sinc function has its first zero-crossing at $f = 1/T$, in this example $T \approx 30T_r$. Fig. 4.7 shows the normalized PSD of the cutter signal with $D = 1/4$. Note that this plot was created using the same T and T_r, resulting in a reduced T_w and a different scaling of the x-axis. The red curve for the spectrum of the Hann window, $W_1(f)$, is identical to that in the previous figure with $D = 1/2$. Effectively, with decreasing duty cycle the spectrum of the sub-pulse is sampled at an increased rate. From the PSD plots it can be concluded that the spectrum of the cutter signal has peaks at multiples of $1/T_r$ and the envelope is determined by the windowing function used in the sub-pulse.

Earlier, it was mentioned that the spectrum of the cutFM signal is a result of a convolution between the LFM and the cutter signal. However, before going to the result there is one more consequence of the cutting that needs to be addressed. Namely, the cutter in combination with the LFM signal has a two-fold effect on the cutFM spectrum:

1. Recalling the basic concept of cutFM signal design illustrated in Fig. 4.2, the cutter periodically removes frequency components from the LFM signal. The remaining frequency components are separated by
$$f_{diff} = T_r k = \frac{T_r \cdot BW}{T} \ , \tag{4.6}$$
where $k \in \mathcal{R}$ is the frequency slope of the LFM signal.

2. In the spectrum of the cutter signal there are periodic spectral peaks at multiples of
$$f_r = \frac{1}{T_r} \ . \tag{4.7}$$

Now, in order to produce a comb spectrum, the new frequency components, introduced by the modulation (cutting), have to be aligned with the uncut frequency components of the LFM base signal, by fulfilling the following condition:
$$f_r = f_{diff} \Rightarrow \frac{1}{T_r} = \frac{T_r \cdot BW}{T} \ . \tag{4.8}$$

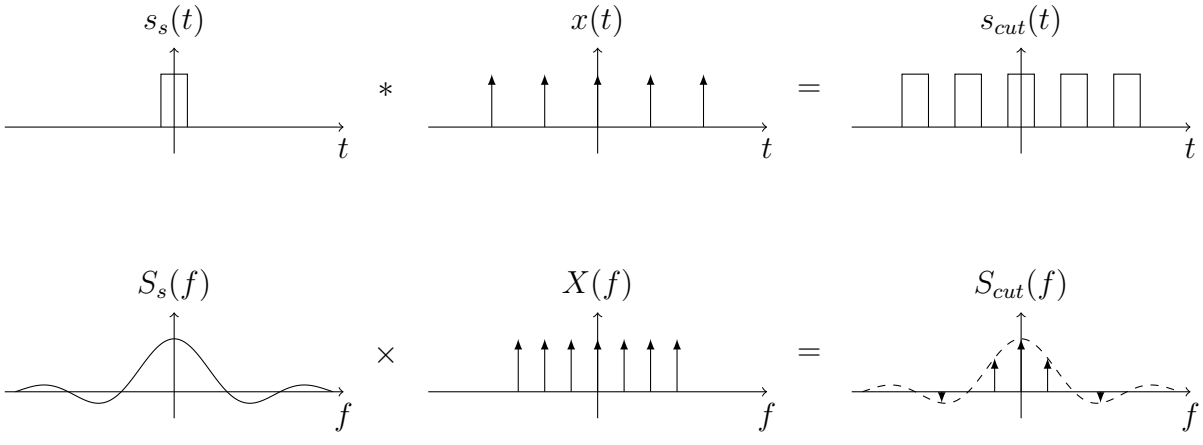

Figure 4.5: Evolution of the spectrum of a periodic signal.

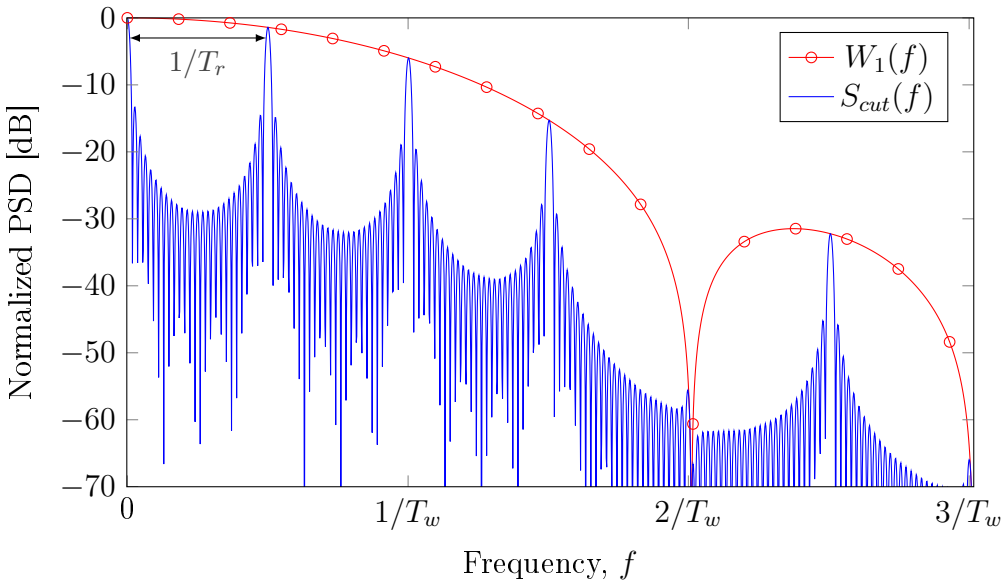

Figure 4.6: Normalized PSD of the Hann window $w_1(t)$ (red curve with circle marks) and the cutter signal with a 1/2 duty cycle.

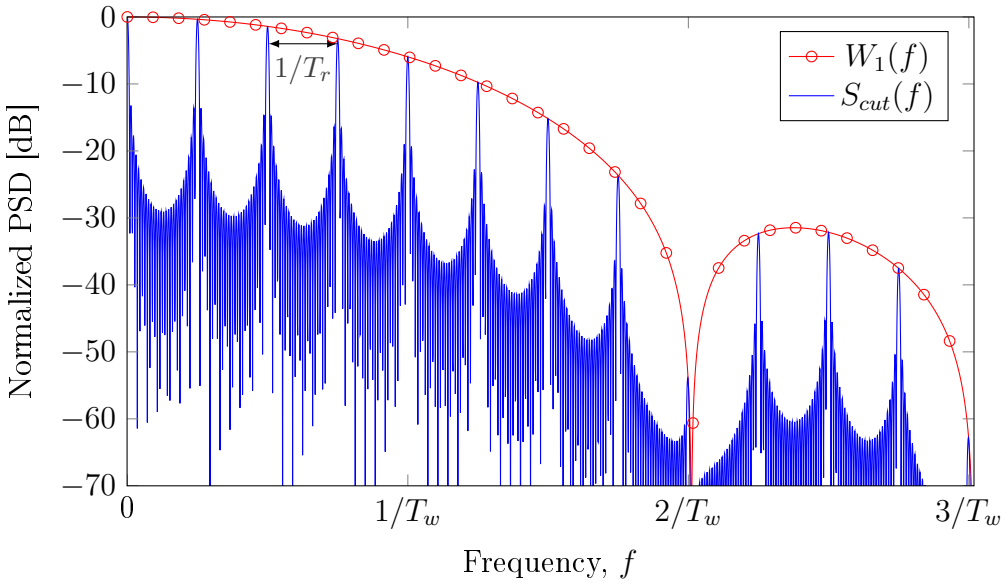

Figure 4.7: Normalized PSD of the Hann window $w_1(t)$ and the cutter signal with a 1/4 duty cycle.

Solving (4.8) for T_r, it follows that the cutting repetition period T_r can not be selected arbitrarily, but should be calculated according to

$$T_r = \sqrt{\frac{T}{BW}} \ . \tag{4.9}$$

The above formula can be extended, by considering the fact that a valid solution for the frequency components alignment would also be achieved for

$$f_r = i \cdot f_{diff} \ , \tag{4.10}$$

where i is an non-zero positive integer. This results in an updated formula for the T_r calculation, given as

$$T_r = \sqrt{\frac{T}{iBW}} \ . \tag{4.11}$$

This is a good point to highlight the importance of an LFM signal being the base signal. In order to fulfill the condition in (4.8), a constant frequency step, f_{diff}, between consecutive uncut signal sections is vital and this is fulfilled for an FM signal with a linear frequency function.

The PSD of a cutFM signal with $T = 100$ ms, $BW = 7.5$ kHz, $D = 1/2$, T_r calculated using (4.9), and $w_1(t)$ being a Hann window, is shown in Fig. 4.8. Both figures present a comb spectrum. The comb teeth

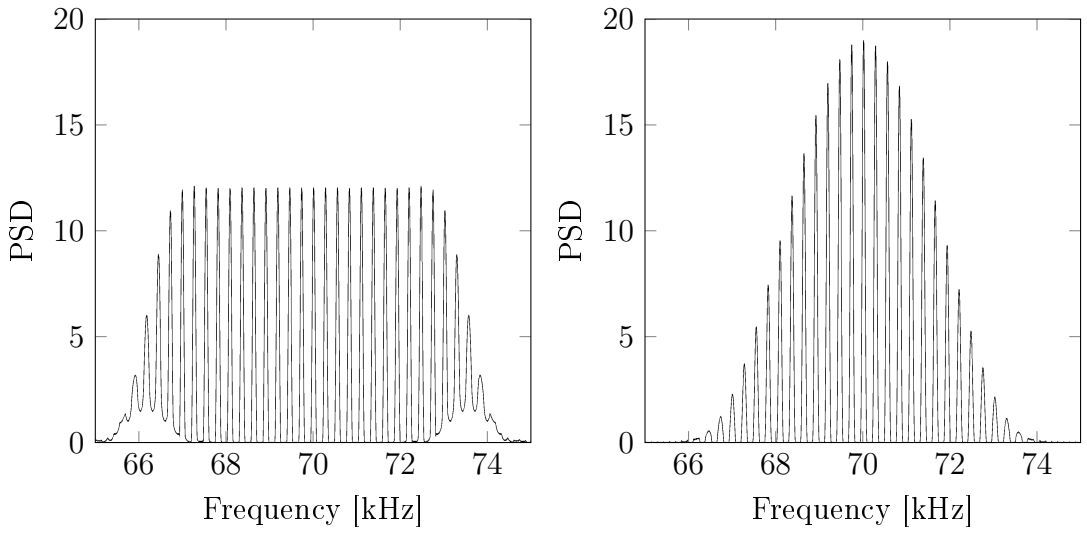

(a) Rectangular window

(b) Hann window

Figure 4.8: PSD of a cutFM signal with $T = 100$ ms, $BW = 7.5$ kHz, $D = 1/2$, and various windowing functions.

have a constant frequency spacing and the signal design has achieved its main goal of periodically removing frequency components from the underlying LFM signal. The spectra in Fig. 4.8 were for cutFM signals, where the cutter repetition period, T_r, was calculated via (4.9), hence $f_r = f_{diff}$. Fig. 4.9 shows what happens if T_r is increased by 1%, $T_r' = 1.01T_r$. The two frequencies are no longer matched, as according to (4.6) f_{diff} is increased by a factor of 1.01 and according to (4.7) f_r is decreased by a factor of 1.01. For better visualization, only for this plot, the $w_1(t)$ window function has been changed from Hann to rectangular. For the case, when the two frequencies are matched (blue curve with circle marks), one can see a clear separation of the existing and missing frequency components and the spectrum quite closely approximates the ideal rectangular frequency function depicted in Fig. 4.2, that illustrated the basic

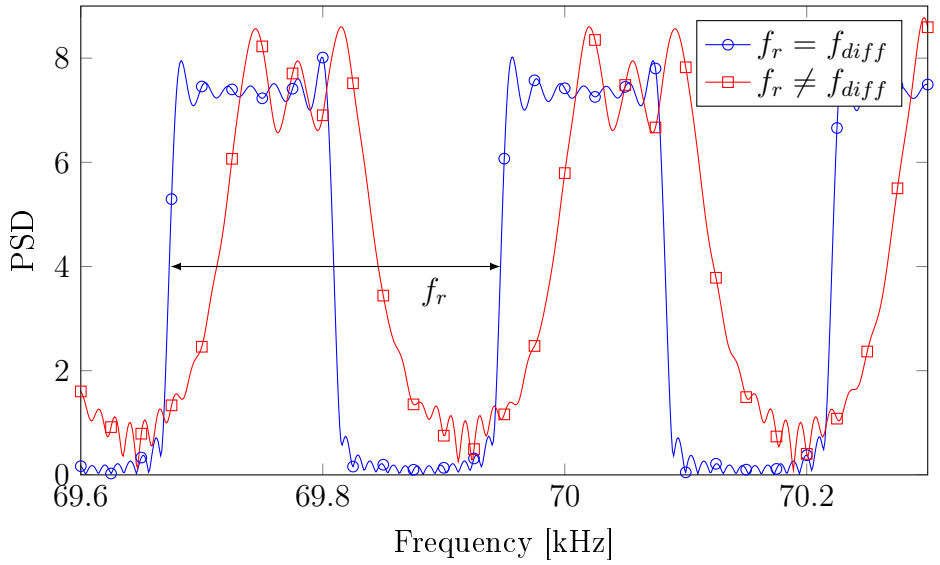

Figure 4.9: Central section of two cutFM signal spectra, with a rectangular $w_1(t)$ function and various cutter repetition period T_r.

cutFM signal design concept. Yet, as soon as the two frequencies are no longer perfectly matched, the near rectangular structure is lost. Based on the fact that the frequency components from the original LFM signal and the new frequency components from the cutter no longer perfectly overlap. The peak becomes smeared and the design no longer manages to (effectively) remove frequency components. Herewith, it is clearly evident why a proper T_r selection is crucial for the cutFM signal design, as already for just a 1% mismatch, the peak-to-valley separation is significantly reduced. Returning to the Hann windowed $w_1(t)$ and increasing the mismatch to 15%, the comparison of the two signal spectra are shown in Fig. 4.10. Both cutFM signals are rectangular windowed and hence, the black curve is identical to that seen in Fig. 4.8a, just that now the PSD is given in dB. Already from the left side figure, one can see that cutFM with a T_r selection that has a 15% longer duration than given by (4.9) does not produce a comb spectrum, instead one that is nearly constant over the signals bandwidth. The difference is better visible in the plot on the right side that shows the central region, namely the $\pm$1000 Hz around the center frequency. Comparing the two, for the case with matched frequencies, the peak-to-valley difference is about 70 dB and on the other hand for the red curve with 15% mismatch, the maximal difference is below 10 dB. Additionally, for the matched case the peak-to-valley difference would increase to about 100 dB, if the cutFM signal is Hann instead of rectangular windowed. Recalling Chapter 3 and the comb spectrum signals like SFM and Cox-comb, the peak-to-valley differences of around $70 - 80$ dB seen for the CW based signals are comparable to that of the cutFM signal.

4.4 Ambiguity Analysis

It has been confirmed that the cutFM signal has a comb spectrum. The next step is to analyze its ambiguity function. Figure 4.11 shows the ambiguity function for the cutFM with $T = 100$ ms, $BW = 7.5$ kHz, duty cycle 1/2, and the T_r is calculated to overlap the frequency components. First of all, the figure presents periodic ambiguities in range and Doppler. A very important property of such an ambiguity function is that for certain velocities the original signal and the reflected signal have a low cross-correlation over the whole pulse duration. This means that the signal is Doppler selective and will

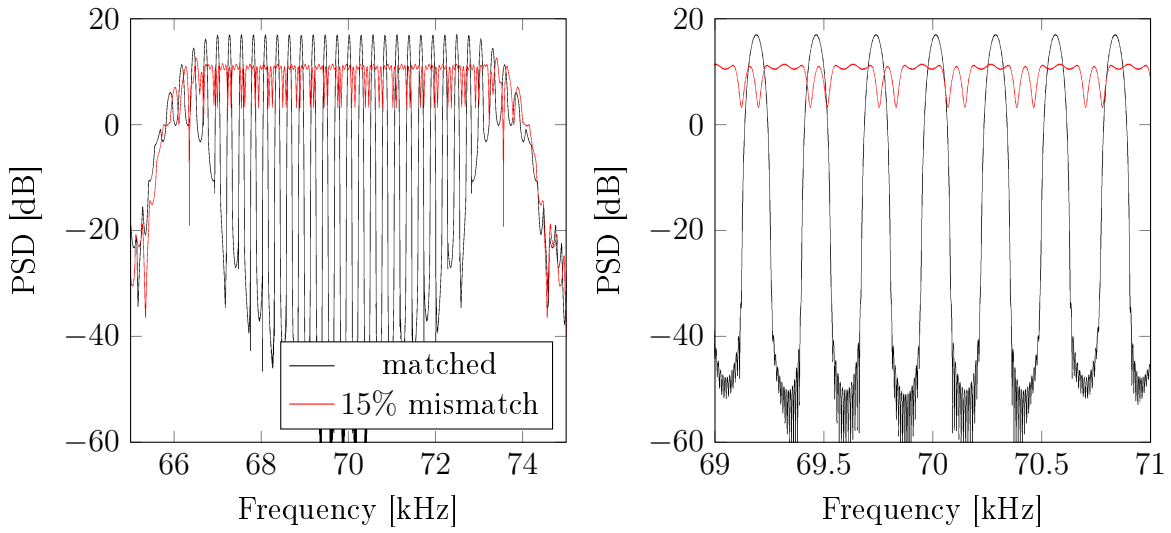

(a) Full range

(b) Central region

Figure 4.10: PSD of cutFM signals with $T = 100$ ms, $BW = 7.5$ kHz, $D = 1/2$, matched frequencies (black curve), and with a 15% longer cutting period T_r (red curve).

present a desirable Q-function, with significantly lower integration values for certain velocities.

Before advancing to the Q-function analysis, the effect of a frequency mismatch on the ambiguity function is presented. Fig. 4.12 shows a cutFM signal with a 1% increased cutting period and in Fig. 4.13 a signal with 15% increased T_r. If before in, Fig. 4.11, the periodic ambiguities were horizontally aligned, for $f_r \neq f_{diff}$, the periodic ambiguities in the time domain are slightly shifted in frequency. The low ambiguity tunnel is still there, but seen from the velocity axis, there is nearly no velocity that would have

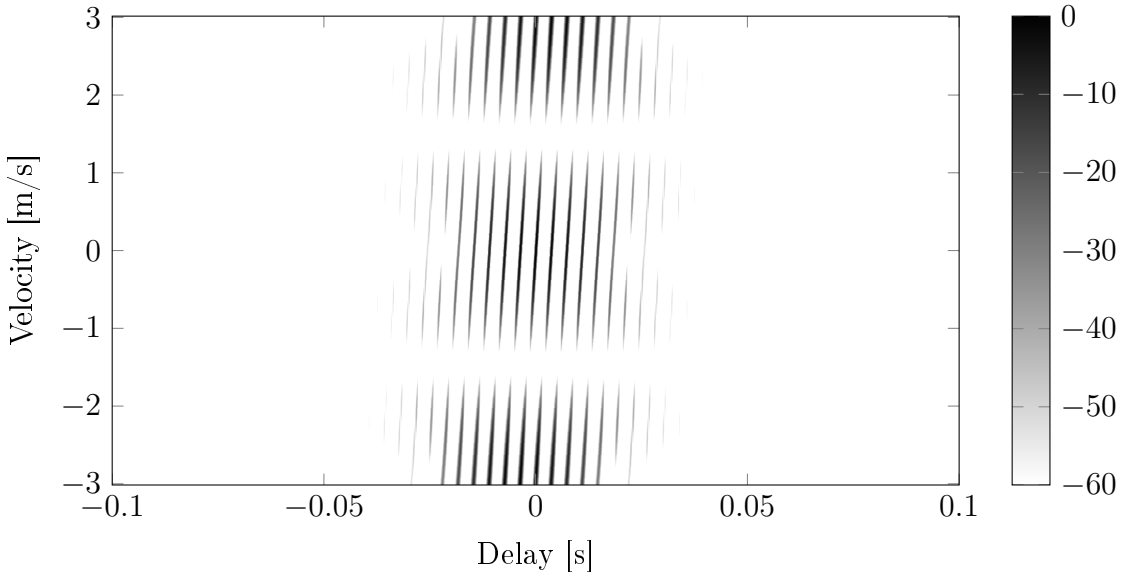

Figure 4.11: Ambiguity diagram of a Hann windowed cutFM signal with $T = 100$ ms, $BW = 7.5$ kHz, $D = 1/2$, and aligned frequency components.

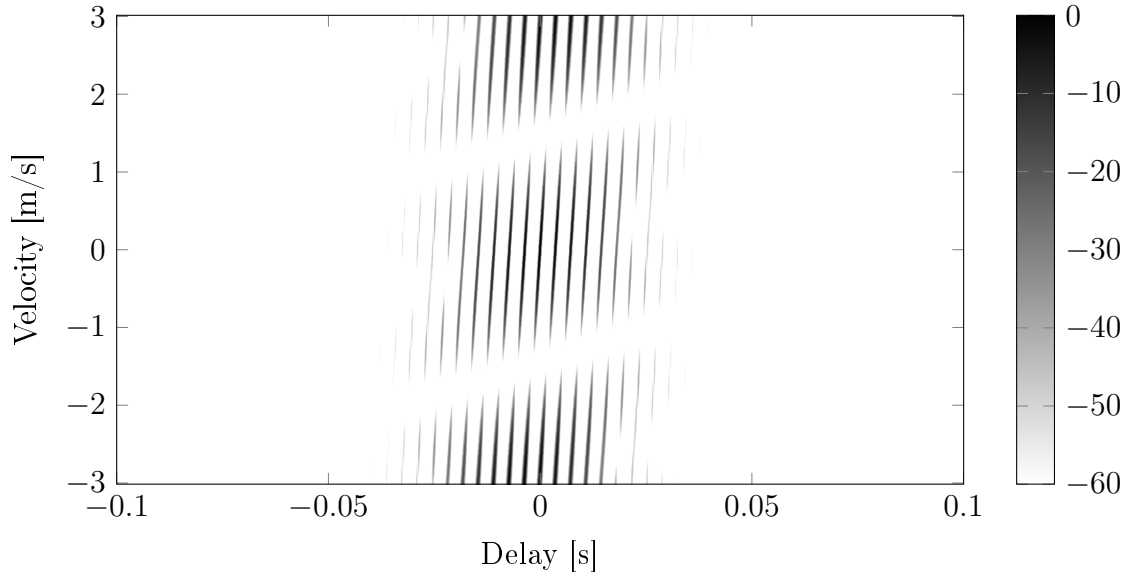

Figure 4.12: Ambiguity diagram of a Hann windowed cutFM signal with $T = 100$ ms, $BW = 7.5$ kHz, $D = 1/2$, and 1% increased T_r.

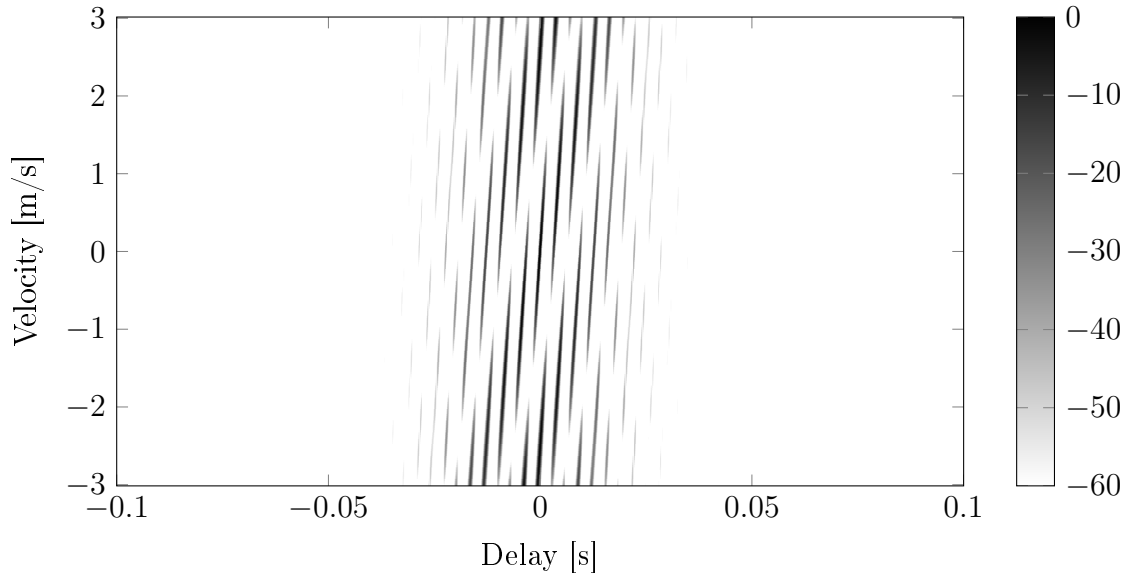

Figure 4.13: Ambiguity diagram of a Hann windowed cutFM signal with $T = 100$ ms, $BW = 7.5$ kHz, $D = 1/2$, and 15% increased T_r.

a low cross-correlation over all delays with the original (stationary) signal. This is caused by the fact that $f_r \neq f_{diff}$ and hence, the correlation peak will appear when the difference is compensated by the Doppler frequency shift. In Fig. 4.13, with the sever frequency mismatch, the shift is significantly bigger and one can hardly recognize the series of peaks that in Fig. 4.11 formed a horizontally aligned train of peaks. Herewith, again showing the importance of properly choosing the cutting repetition period T_r.

Analyzing all three ambiguity functions, the following properties emerge:

1. In the time domain, the ambiguities appear at multiples of T_r, which correspond to the time instances when the signal is shifted by delays that overlap the uncut signal sections with the next ones.

2. For a T_r selection that matches $f_r = f_{diff}$, the ambiguity peaks in time domain appear at zero velocity. In general, the ambiguities appear at a velocity shift that corresponds to a Doppler frequency shift that compensates the difference

$$f_D = f_{diff} - f_r \ , \tag{4.12}$$

   or equivalently according to (2.8)

$$v' = \frac{(f_{diff} - f_r) \cdot c}{2f_c} \ , \tag{4.13}$$

   where c is the speed of sound and f_c the center frequency of the signal.

3. In the frequency domain, the ambiguities occur at

$$f_D = f_{diff} = T_r k \ , \tag{4.14}$$

   or equivalently at

$$v'' = \frac{f_{diff} \cdot c}{2f_c} \ , \tag{4.15}$$

   corresponding to the frequency shift needed to match the frequency difference of neighboring uncut signal sections.

4. The width of the ambiguity peaks in time domain is approximately $1/BW$ or the pulse duration T divided by the BT product (a property kept from the LFM signal). In the frequency domain the width of the ambiguities is proportional to $T_w k$, but the true width is determined by the $w_1(t)$ windowing function.

Knowing these four properties, the ambiguity diagram can be roughly reconstructed or predicted. Earlier in (4.11), it was shown that T_r can also be calculated with a non-zero positive integer i in the denominator. For example, selecting $i = 2$, the relation between the two frequencies is $f_r = 2f_{diff}$ (cf. (4.10)). In this case, an interesting effect appears. According to property one, the ambiguity peaks in time will be at multiples of T_r. However, property two states that the ambiguity peaks will not appear at zero velocity (as $f_r \neq f_{diff}$), but at a Doppler frequency shift equal to $f_D = f_{diff} - f_r$. With $f_r = 2f_{diff}$, the peak will be at $f_D = -f_{diff}$. At the same time, according to property three, in frequency domain the periodic ambiguities will appear at multiples of a Doppler frequency shift of $f_D = f_{diff}$. Implying that the frequency shifts of property two and three are equal in magnitude and due to the symmetries, the corresponding ambiguities will overlap. As a result, an interesting property emerges, where in time domain the ambiguities will be at multiples of $2T_r$. This property holds in general, for any i value, therewith effectively increasing the ambiguity spacing in time domain from T_r to iT_r. This somewhat overwrites property one, but it is just a visual effect, the ambiguities are still there at multiples of T_r,

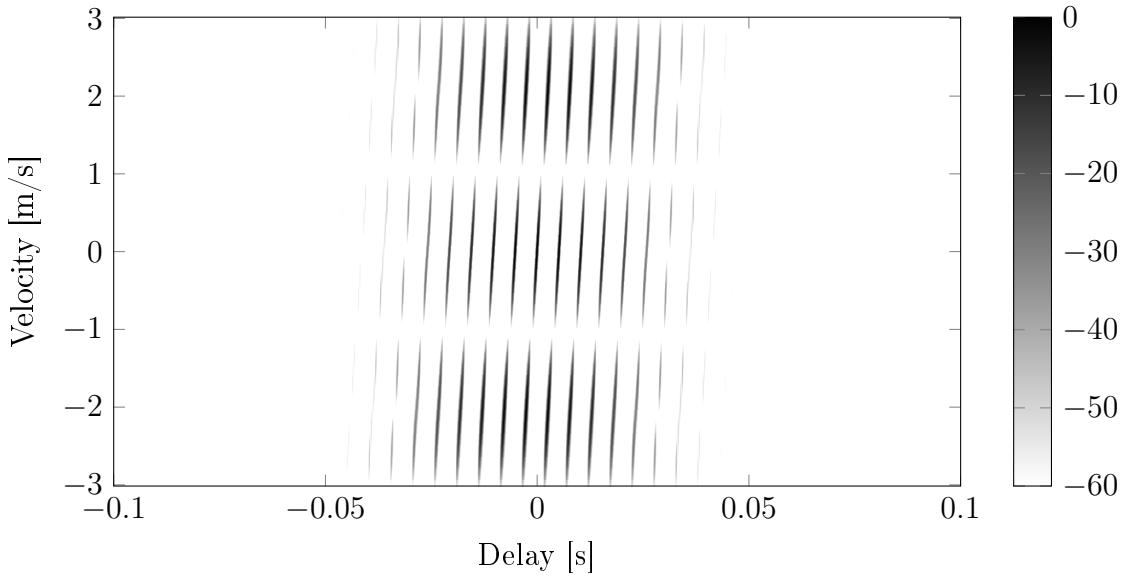

Figure 4.14: Ambiguity diagram of a Hann windowed cutFM signal with $T = 100$ ms, $BW = 7.5$ kHz, $D = 1/2$, and $i = 2$.

just shifted in frequency. Otherwise, the ambiguity function looks as usual and the diagram for a cutFM signal with $i = 2$ is shown in Fig. 4.14. The usefulness of the i coefficient is somewhat limited, while it does enable to reduce T_r without altering the pulse duration T or the signal bandwidth BW, it can not be used to widen the tunnel between the ambiguity peaks in frequency. In order to achieve that, one has to lower the T_w to T_r ratio, the duty cycle, or change the windowing function $w_1(t)$.

Based on properties three and four together with the T_r selection constraint, it can be concluded that the duty cycle is an important design parameter. Assuming the cutting period T_r, together with the pulse duration and signal bandwidth are fixed, the main parameter to increase the width of the tunnel between the ambiguities in the frequency domain is to lower the duty cycle. Reducing the duty cycle, decreases the $w_1(t)$ signal duration and that leads to a narrower ambiguity peak in the frequency domain and therewith to a wider tunnel, as according to property three the next ambiguity peaks in frequency will still appear at $f_D = f_{diff} = T_r k$. The ambiguity function for a cutFM signal with $D = 1/4$ and otherwise with the same parameters as earlier is shown in Fig. 4.15. Three aspects can be observed. The periodic ambiguities in time and frequency appear at the same positions as before with a 1/2 duty cycle (see Fig. 4.11). The differences are in the widths. The ambiguity width in the frequency domain has been halved and the tunnel has been significantly widened. Yet, the ambiguity can not be removed and has to appear somewhere else. In this case, the width of the ambiguity envelope in time domain has been increased. The benefit of the lower duty cycle is shown in the Q-function, cf. Fig. 4.16. The Q-function for $D = 1/4$ is somewhat increased for the zero velocity, but more importantly the Q-function falls off much faster and enables to suppress a wider range of velocities. Both curves have secondary peaks at the same position, which is determined by the ambiguity spacing in the frequency domain, given by property number three. In order to put these Q-function results in perspective, in Fig. 4.17 the cutFM signal with $D = 1/4$ is compared to the SFM and LFM signals with similar parameters. The peak of the SFM signal is slightly narrower than that for cutFM signal, but they both have a similar steep fall-off after a certain velocity. The goal of the cutFM design, to modify the LFM signal in a way to create a Doppler selective signal, has been achieved.

The last aspect to address is the autocorrelation function, as it determines how the cutFM signal

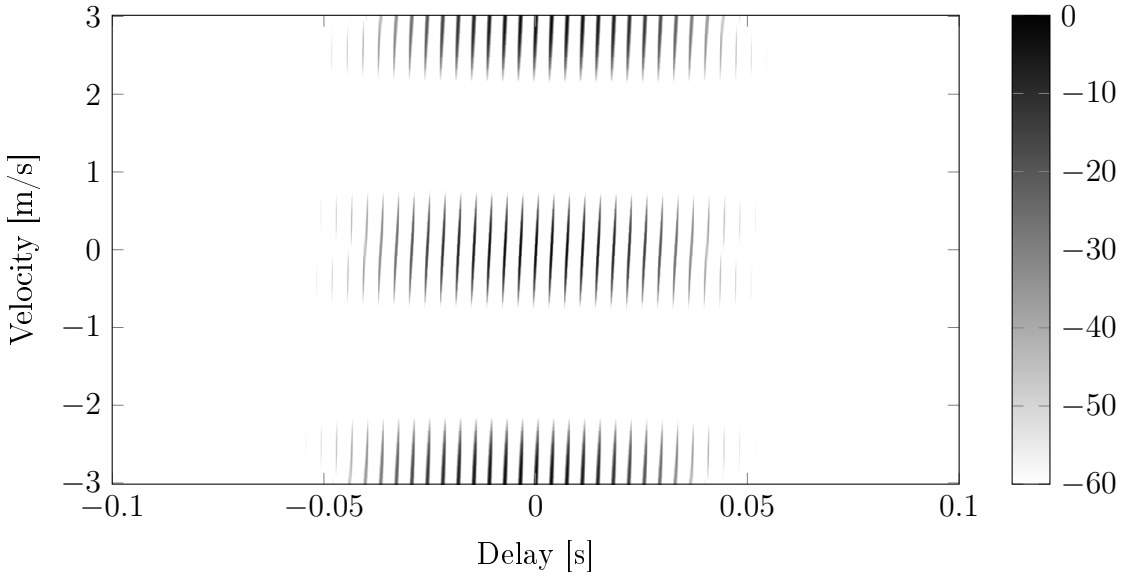

Figure 4.15: Ambiguity diagram of a Hann windowed cutFM signal with $T = 100$ ms, $BW = 7.5$ kHz, $D = 1/4$, and $w_1(t)$ is a Hann window.

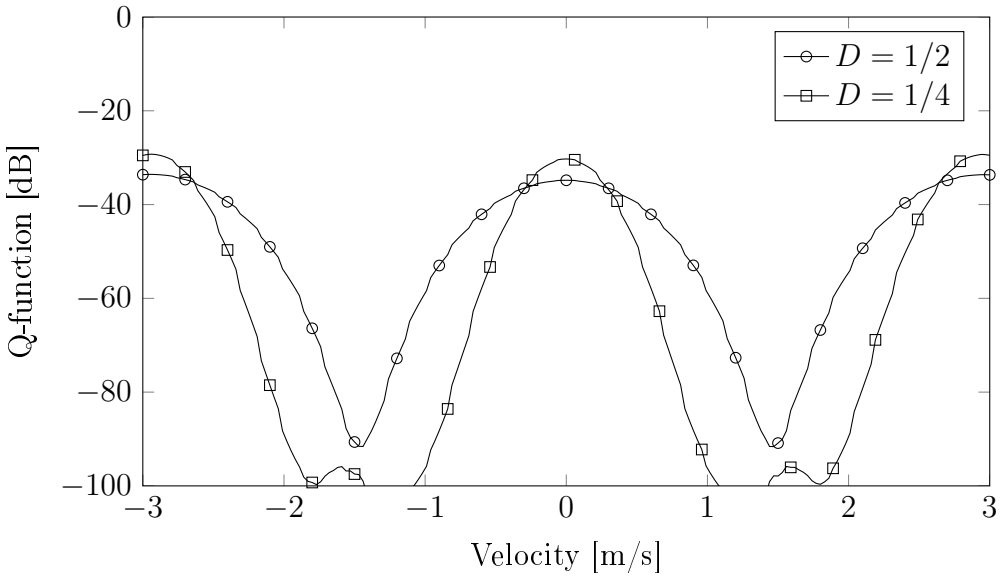

Figure 4.16: Q-function of Hann windowed cutFM signals with $T = 100$ ms, $BW = 7.5$ kHz, and varying duty cycle D.

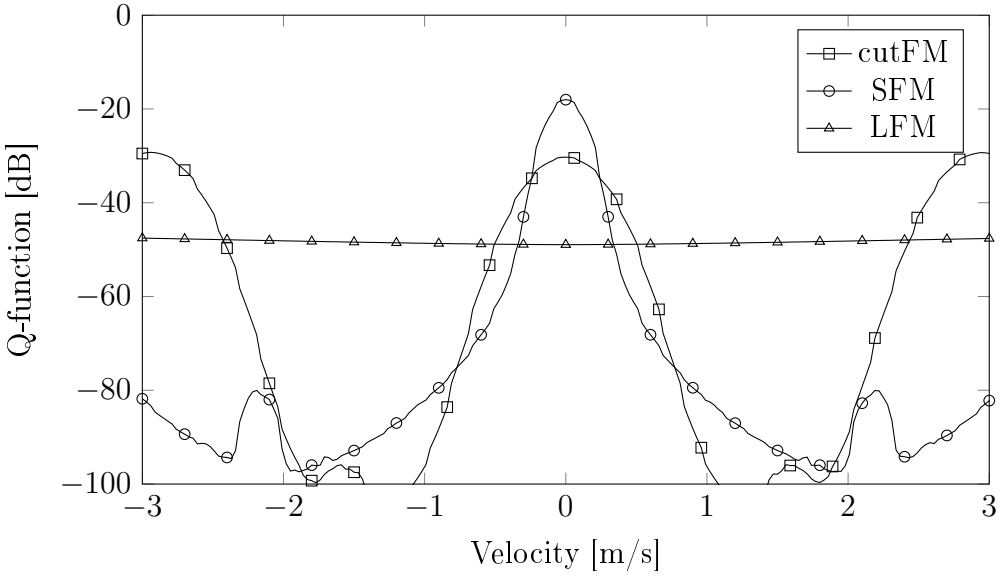

Figure 4.17: Q-function of various Hann windowed signals with $T = 100$ ms and $BW = 7.5$ kHz.

compares with the alternative Doppler selective signals, like SFM and Cox-comb signals. First, before comparing the cutFM with other signals, Fig. 4.18 shows the effect of the duty cycle on the autocorrelation function (ACF). The central peak is (nearly) identical for both cases and at the same time it corresponds to the ACF curve of the LFM signal. Therefore, the -3 dB width of the individual peaks is approximately $0.88/BW$. The expansion of the envelope width is clearly visible. Due to the periodic peaks, it is difficult to define the ACF -3 dB width for a cutFM signal. If an envelope over the peaks was considered, then for $D = 1/2$ the -3 dB width would be 12.5 ms and for the $D = 1/4$ the -3 dB width would be 22.8 ms. These values for the ACF -3 dB width can be seen as the worst case scenario, as in most cases the clear gaps between the periodic peaks can be used to improve the resolution. Additionally, due to the fact that the distance between the peaks is deterministic and known, the corresponding repetitions can be removed in later processing steps (e.g. by equalization or tracking).

A direct comparison of the CW, SFM and cutFM signals autocorrelation functions is given in Fig. 4.19. The left side figure illustrates the reduction of the ACF envelope of cutFM signal compared to that of the CW or SFM signals. The right side figure shows finer details and the difference between SFM and cutFM. Even though both have periodic peaks, the difference is in the ACF level between the peaks. For SFM the ACF level between the peaks reduces approximately by -15 dB, while for cutFM it disappears, as the overlapping signal components are zero (cut out).

In the end, ambiguities can not be avoided. In order to have a Doppler selective signal with a higher bandwidth, the spectrum should be comb like and based on the Fourier transform properties, a periodic spectrum will result in a periodic ACF function. A Doppler selective signal will have range ambiguities and hence a suitable trade-off has to be found.

4.5 Overview of Design Parameters

The aim of the cutFM signal design is to create a Doppler selective pulse based on an LFM signal, that together with Doppler processing can improve the detection of moving targets against stationary reverberation. The design efficiency can be evaluated from the Q-function. Hence, for cutFM it comes

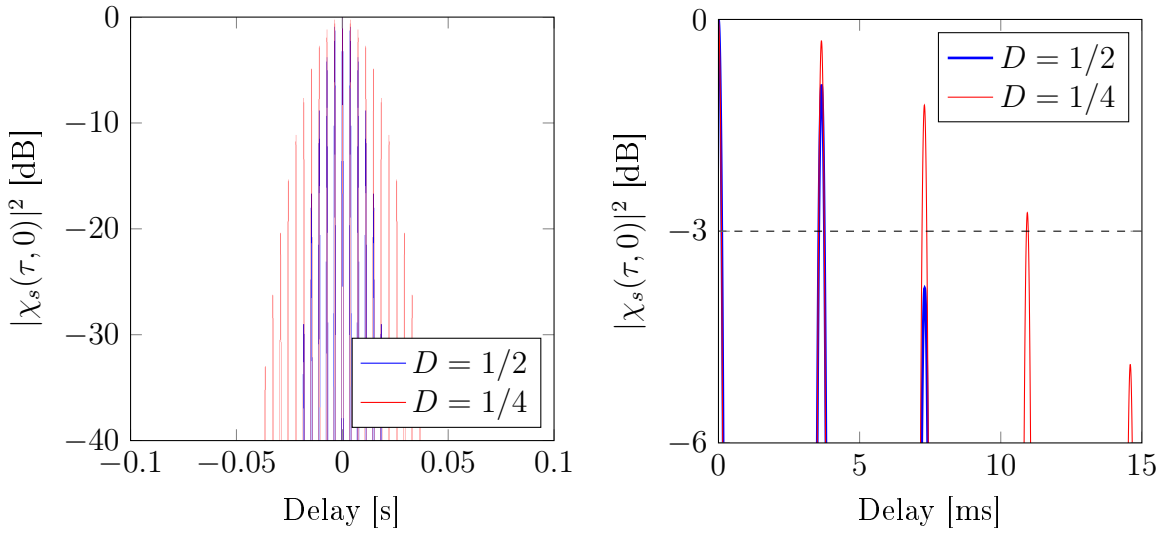

(a) Full ±100 ms

(b) Central 15 ms

Figure 4.18: Autocorrelation plots for Hann windowed cutFM signals with $T = 100$ ms, $BW = 7.5$ kHz, and varying duty cycle D.

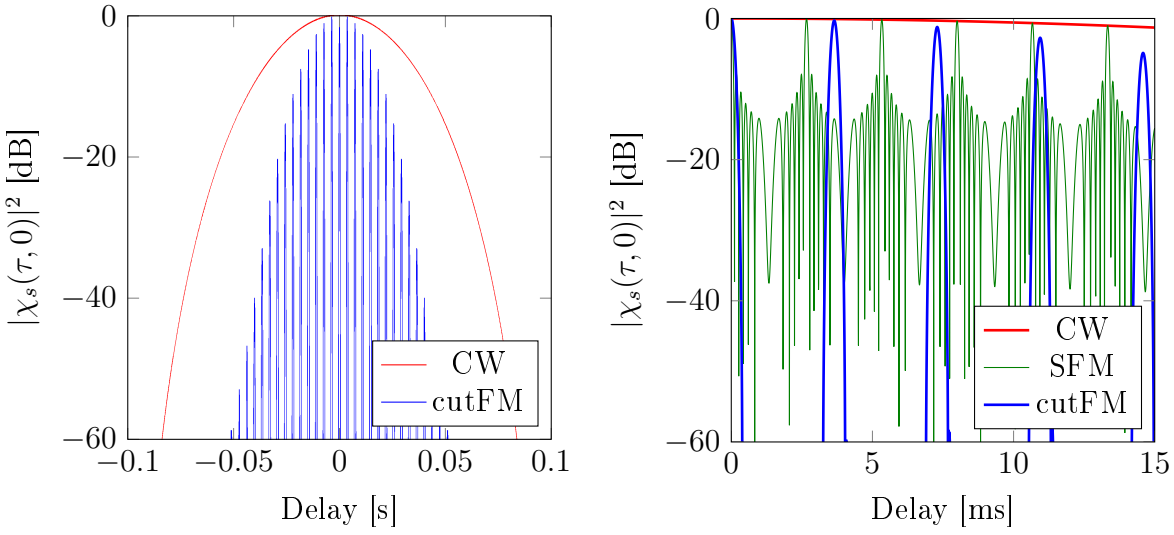

(a) Full ±100 ms

(b) Central 15 ms

Figure 4.19: Autocorrelation plots for Hann windowed CW, SFM and cutFM signals with $T = 100$ ms, $f_m = 375$ Hz, $\beta = 9$, $BW = 7500$ Hz, and cutFM with $D = 1/4$.

down to two main Q-function properties:

- The width of the ambiguity main lobe,

$$w \propto T_w k = T_r D \cdot k = T_r D \frac{BW}{T} \ , \tag{4.16}$$

  is proportional to $T_w k$, recall cutFM ambiguity function property four.

- The position of the secondary peak(s),

$$v'' = \frac{f_{diff} \cdot c}{2 f_c} \propto f_{diff} \ , \tag{4.17}$$

  is proportional to f_{diff} and can be calculated using (4.15). Additionally, f_{diff} can be written out in more detail, using (4.6) and (4.11)

$$f_{diff} = T_r k = T_r \frac{BW}{T} = \sqrt{\frac{T}{iBW}} \frac{BW}{T} = \frac{1}{\sqrt{i}} \sqrt{\frac{BW}{T}} \ , \tag{4.18}$$

  to show the influence of the main signal parameters.

Fig. 4.20 shows an illustrative Q-function and the two main properties. The cutFM has a number of design parameters that influence the ambiguity function and the Q-function, starting with the conventional signal parameters like:

- Signal bandwidth BW. In both equations, (4.16) and (4.18), BW is in the numerator, therewith the bandwidth increases the distance between the secondary peak and the main lobe, but it also increases the width of the main lobe.

- The signal duration T has the reversed effect as the bandwidth on f_{diff} and $T_w k$.

- Windowing function $w(t)$. As for any signal, the windowing function can be used to modify the spectrum and for cutFM, a window function like Hann, significantly improves the separation of ambiguities in time and frequency.

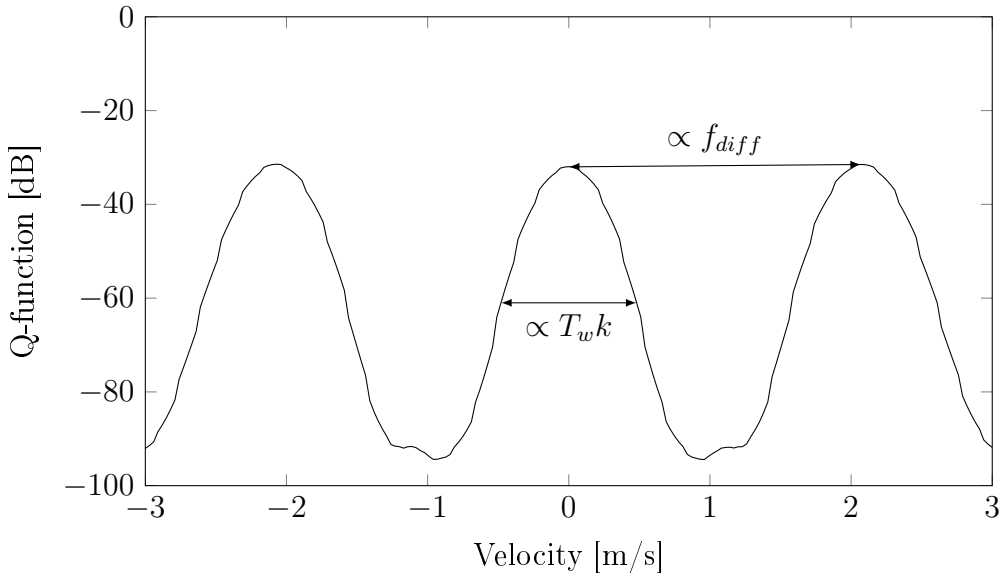

Figure 4.20: Illustrative Q-function of a cutFM signal.

Additionally, a number of cutFM specific parameters should be mentioned:

- The cutting repetition period T_r is the key parameter of the cutFM signal design that aligns the various frequency components and creates a comb spectrum. T_r can not be chosen arbitrarily, but should be calculated via (4.9) or (4.11). Therefore, it is not a freely adjustable signal parameter. Nevertheless, in both equations, (4.16) and (4.18), T_r is in the numerator and hence, both Q-function properties are proportional to it.
- The non-zero positive integer i gives certain freedom to the T_r calculation. It provides a possibility to reduce the value of T_r, without changing the conventional signal parameters. Effectively, the parameter i, scales down both $T_w k$ and f_{diff}, by a factor of $1/\sqrt{i}$. This provides an interesting possibility to compress the main lobe width without altering the base signal properties. Of course, it identically reduces f_{diff} and with that emphasizes secondary ambiguities.
- The duty cycle $D = T_w/T_r$ is one of the few design parameters that only affects the main lobe width and does not chance f_{diff}. Consequently, it can be used to further separate the ambiguities in the frequency domain and with that widening the low cross-correlation tunnel between the peaks. A decreased duty cycle reduces the width of ambiguity peaks in frequency domain, but increases the envelope of the ambiguity peaks in the time domain.
- Sub-pulse windowing function $w_1(t)$ is the second parameter that only affects the main lobe width. Together with the duty cycle and T_r, $w_1(t)$ determines the spectrum of the cutter signal, cf. Sec. 4.3, and with that also the shape of the cutFM signal's spectrum and the ACF.
- Last but not least, the center frequency f_c also has an impact on the Q-function. It does not directly affect T_w or f_{diff}, but it scales the velocity axis, cf. (4.15). Hence, as the center frequency increases both Q-function properties decrease.

These are the eight (seven, if discounting T_r) parameters available, when designing a cutFM signal that should fulfill certain criteria. Table 4.1 provides a minimalistic overview of the design parameters effect on Q-function properties, where ↑ denotes an increase and ↓ a decrease of a variable.

Table 4.1: Design parameters effect on Q-function properties

Parameter	Main lobe width	f_{diff}
$BW \uparrow$	↑	↑
$T \uparrow$	↓	↓
$T_r \uparrow$	↑	↑
$i \uparrow$	↓	↓
$D \downarrow$	↓	–
$f_c \uparrow$	↓	↓

4.6 Signal Design for Diver Detection

In reverberation limited environments, where the signal-to-reverberation ratio (SRR) is too low to use a traditional FM signal (like HFM or LFM), but the target can be differentiated from the reverberation by its relative velocity towards the receiver, Doppler processing can be used to emphasize the target against the reverberation. Most commonly, Doppler processing is done by altering the reference signal in the matched filter (MF). Instead of "looking" for the transmit signal in the received sequence, the reference

signal is Doppler shifted in order to match the reflections from targets with certain velocity. In case the transmit pulse is Doppler selective, due to the Doppler mismatch the reverberation level after the MF will be suppressed compared to the target response. The difference between the two levels is referred to as the Doppler processing gain (G_{DP}).

Instead of measuring the G_{DP} from simulations, the processing gain can be estimated from the Q-function, by comparing the Q-function levels at different velocities. The Q-function is based on certain assumptions about the reverberation sources (cf. Sec. 3.1.3), but unless more is known about the reverberation the Q-function levels can be used as baseline Doppler processing gain estimates, $\hat{G}_{DP}$.

For the initial analysis of cutFM signal design, the reverberation is assumed to be stationary and two design criteria are selected:

1. 20 dB suppression of the zero velocity compared to the lower target speed of 0.3 m/s,
2. Velocity range of interest is from $0.3 - 2.0$ m/s.

The following analysis is based on a cutFM signal with $f_c = 70$ kHz, $T = 100$ ms, and $BW = 7500$ Hz. The Q-function of a cutFM signal, with $D = 1/2$, $i = 1$ and Hann windows for $w(t)$ and $w_1(t)$, is plotted in Fig. 4.21 by the dashed line. The dashed curve is the baseline, it was already shown in Fig. 4.16, where

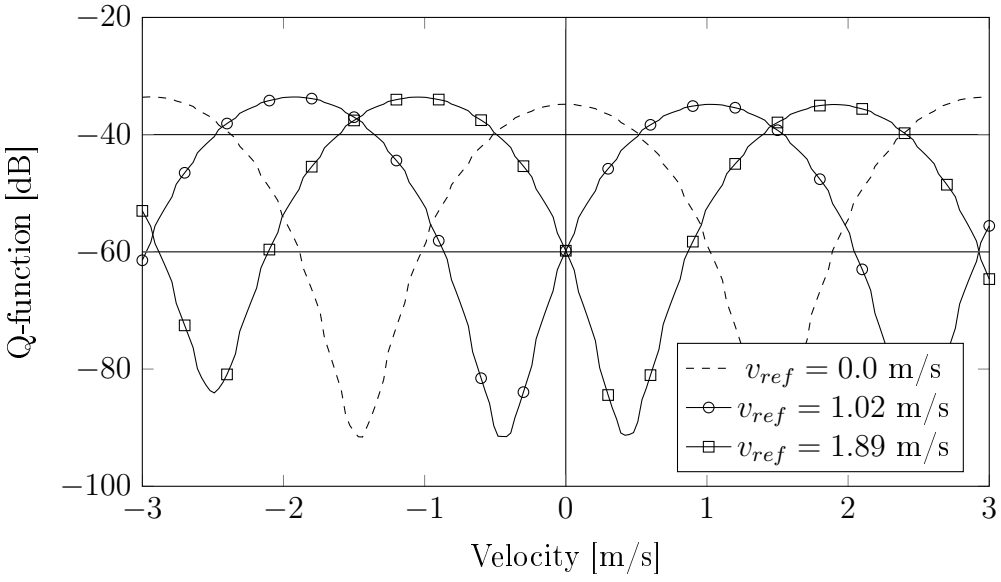

Figure 4.21: Q-function of Hann windowed cutFM signals, with $T = 100$ ms, $BW = 7500$ Hz, $D = 1/2$ and various reference signal velocities.

the effect of D was presented. The figure also exhibits two horizontal lines at -40 dB and at -60 dB, these two levels are freely chosen and correspond to the design goal number one that aims to suppress the stationary reverberation by 20 dB compared to the response from moving targets, i.e. minimum $\hat{G}_{DP} > 20$ dB. In other words, in the Q-function plot the response at 0.0 m/s should be below -60 dB and for the velocities of interest the Q-function should be higher than -40 dB.

The original Q-function is centered around the zero velocity, however, if a Doppler shifted reference signal is used for the Q-function calculation, then basically the Q-function is shifted by v_{ref}, cf. Fig. 4.21. Doppler shifting the reference signal also means that the matched filter is no longer matched to the transmit signal, but to a Doppler shifted signal, reflected from a object moving with a certain velocity, v_{ref}. This is the core technique in Doppler processing that allows the receiver to distinguish objects with

different velocities. Therewith, by selecting the proper v_{ref} the Q-function of the cutFM signal can be shifted to higher positive velocities, so that for zero velocity the curve is exactly at -60 dB, plotted by the solid curve with circle marks and $v_{ref} = 1.02$ m/s. In general, the required shift can be directly read out from the non-shifted Q-function. It is important to note that the reference signal can not be shifted arbitrarily. Due to the periodic ambiguities, eventually the secondary peak at negative velocities is shifted into the zero velocity. For the given cutFM signal, the maximum shift of the reference signal is $v_{ref} = 1.89$ m/s, plotted by the solid curve with square marks in Fig. 4.21. In such case, for zero velocity the response is exactly -60 dB and any further shift would violate the design criteria. This exhibits a limitation of the cutFM signal or in general of any signals with periodic ambiguities in the frequency domain. However, later it will be shown how this limitation can be circumvented, by using multiple transmit signals.

The given cutFM signal design with $D = 1/2$ can successfully suppress the stationary reverberation, but the velocity range where the response is above -40 dB is from 0.51 to 1.5 m/s. Recalling the desired velocity range, the given signal falls short on both ends. Therefore, especially in order to improve the velocity range on the lower end, the width of the main lobe has to be decreased. Utilizing Table 4.1 and the previous analysis of signal design properties, the value D is reduced from 1/2 to 1/4.

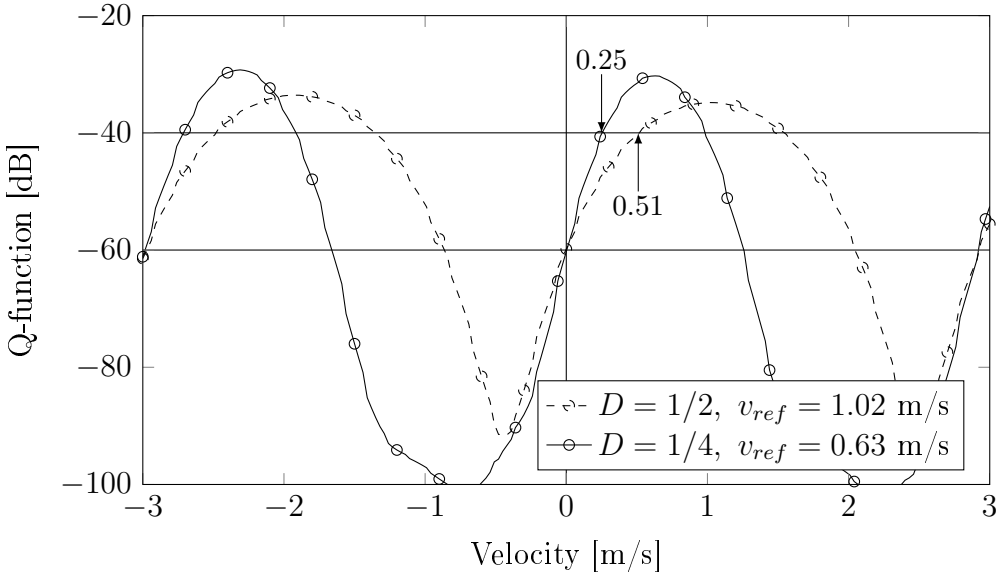

Figure 4.22: Comparison of cutFM signals, with $T = 100$ ms, $BW = 7500$ Hz, various D, and v_{ref}.

The Q-function of a cutFM signal with $D = 1/4$, otherwise same values as before, is shown in Fig. 4.23. The dashed line is from the previous figure, with $D = 1/2$. The width of the Q-functions main lobe for the signal with $D = 1/4$, plotted by a solid line, is significantly reduced. The improvement is clearly visible, when both reference signals are shifted with an appropriate v_{ref}, so that for zero velocity the levels are at -60 dB. Instead of reaching the -40 dB value at 0.51 m/s, with $D = 1/4$ the same level is reached already at 0.25 m/s. An additional benefit is that the distance between the ambiguity peaks stays unchanged as the parameter D does not alter f_{diff}.

Figure 4.23 shows the result of extending the Q-function plot for cutFM signal with $D = 1/4$ with additional reference signals. In this case, because the width of the initial Q-function higher than -40 dB is 0.7 m/s, the second and third reference signals are successively shifted by 0.7 m/s. The setup presented in Fig. 4.23 with $D = 1/4$, is one possible design that fulfills the previously selected design criteria. In order to cover the required velocity range, the receiver needs to use three reference signals in the correlation

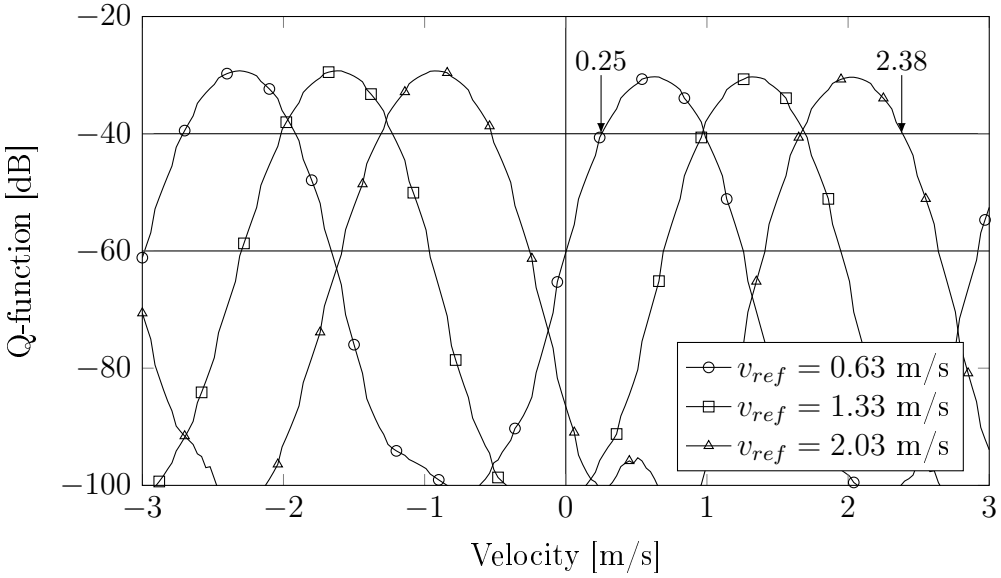

Figure 4.23: Signal design with three reference signals, $T = 100$ ms, $BW = 7500$ Hz, and $D = 1/4$.

process. Such a setup also enables to give a rough estimate for the velocity of the reflections. Another thing to note is that the 20 dB gain is the minimal difference between the reflections from stationary objects or objects moving with a velocity in a given range. For example, in Fig. 4.23, the peak at 0.63 m/s has a Q-function value of −30 dB, resulting in a 30 dB difference compared to the stationary case. This leads to the question of what are the optimal v_{ref} values for given velocity difference between the target and the reverberation. The following analysis is done for a cutFM signal with $f_c = 70$ kHz, $T = 100$ ms, $BW = 7500$ Hz, and $D = 1/4$.

The optimal reference signal velocity shift (v_{ref}) that maximizes the processing gain for a certain target versus reverberation velocity difference (v_{diff}) is not obvious. In order to find the optimum v_{ref}, the Q-function can be utilized to estimate the processing gain according to

$$\hat{G}_{DP}(v_{diff}, v_s) = Q_s(v_s + v_{diff}) - Q_s(v_s) \ , \tag{4.19}$$

where v_s is an arbitrary velocity shift. The analysis is based on the original Q-function, without any reference signal shift. Essentially, the estimated processing gain is the difference between Q-function levels at certain velocities. For example, assuming the Q-function level at 0.0 m/s is −30 dB and at −0.3 m/s it is −50 dB, the $\hat{G}_{DP}(0.3, -0.3)$ would be 20 dB. Both negative and positive v_s values could be used for the calculation, as the underlying ambiguity function is symmetric to the origin (cf. ambiguity function properties in Sec. 3.1.2), but as the v_{ref} shifts the Q-function to positive velocities, then it is more natural to use negative values.

The Q-function difference results for both SFM and cutFM signals are shown in Fig. 4.24. The plots show how the processing gain varies for different v_{diff}, over a range of velocity shifts, v_s. It is also evident that with increasing velocity difference, the maximum gain increases and the corresponding velocity shift moves to higher values.

As mentioned earlier, a Doppler shifted reference signal shifts the whole Q-function by v_{ref}, hence for $v_{ref} = -v_s$, the $\hat{G}_{DP}(v_{diff}, v_s)$ represents the processing gain between stationary reverberation and a target moving with v_{diff}. Herewith, given a v_{diff} between the reverberation and target velocity, in

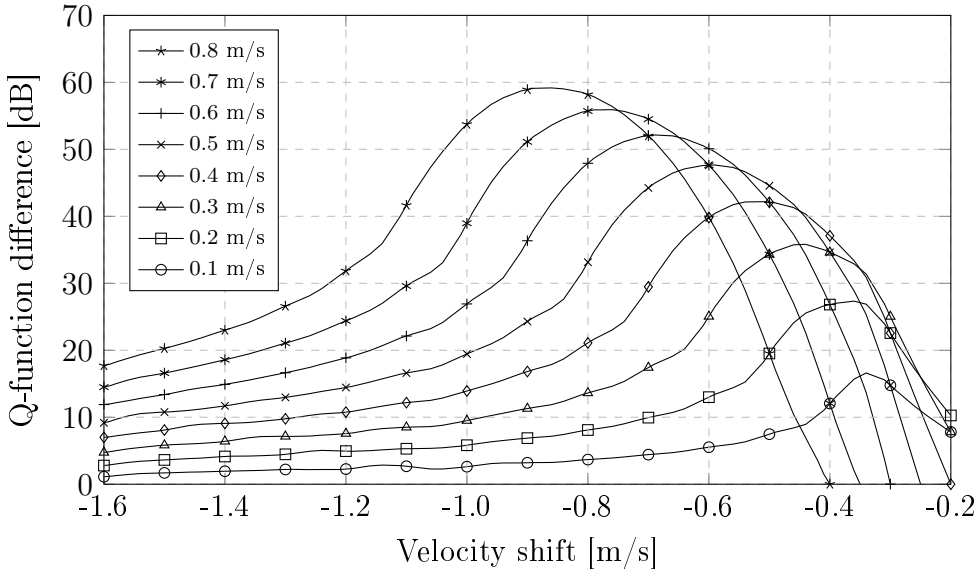

(a) SFM, $f_m = 375$ Hz, $\beta = 9$

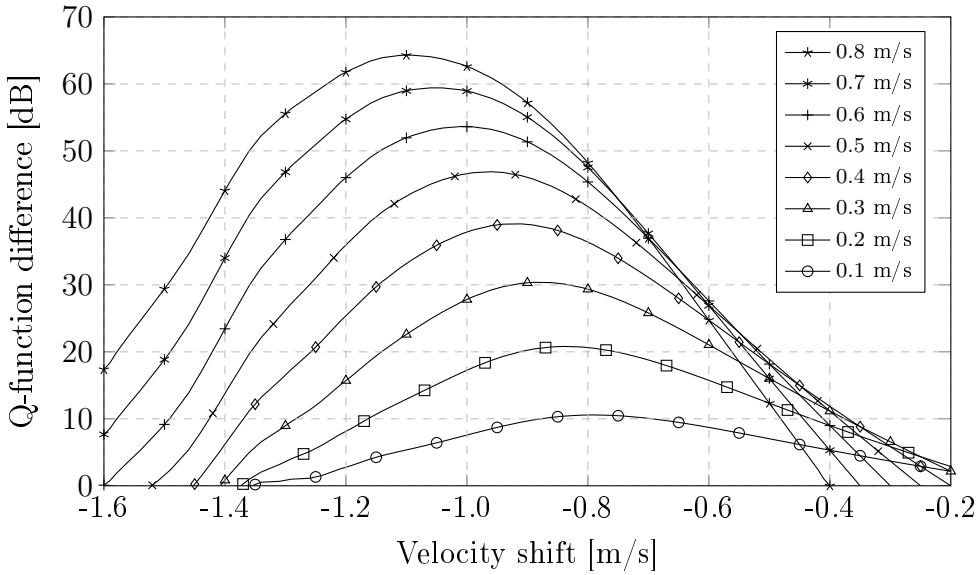

(b) cutFM, $D = 1/4$, $i = 1$

Figure 4.24: Processing gains for SFM and cutFM signals with $f_c = 70$ kHz, $T = 100$ ms, and $BW = 7500$ Hz, given various velocity differences v_{diff}.

order to maximize the reverberation suppression, the reference signal in the MF should be shifted by

$$v_{ref} = -\arg\max_{v_s} \hat{G}_{DP}(v_{diff}, v_s) \ . \tag{4.20}$$

The optimal v_{ref} values for a selection of v_{diff} and the corresponding processing gain estimates in dB are given in Table 4.2. The table with the maximum values, together with the Q-function difference plots, can be used to determine the optimal reference signal velocity shift in the MF detector or to predict the processing gain for a selected sub-optimal v_{ref}. Three properties can be observed from the above results:

- The optimal $v_{ref} > v_{diff}$ and for cutFM the difference is noticeably larger,
- For SFM the processing gain curves have narrower peaks, providing better velocity resolution, but on the other hand it means that multiple reference signals are needed to cover a wider velocity range,
- For cutFM the peaks are wider and the range for optimal v_{ref} values for various v_{diff} is much smaller. That provides a possibility to use a single reference signal to near optimally cover a wide velocity range.

For SFM the width of the Q-function main lobe is determined by the signal duration T, a property of the underlying CW signal. On the other hand, for cutFM multiple parameters can be used to further reduce the main lobe width, cf. Table 4.1. However, as most of the signal parameters come with a trade-off, then depending on the system requirements and channel conditions, the design should be adapted to the conditions, to maximize the benefits.

Table 4.2: Optimal v_{ref} values for cutFM and SFM

	cutFM		SFM	
v_{diff}	Gain [dB]	v_{ref}	Gain [dB]	v_{ref}
0.1	10.58	0.79	16.61	0.34
0.2	20.81	0.84	27.34	0.36
0.3	30.38	0.89	35.82	0.44
0.4	39.10	0.91	42.19	0.51
0.5	46.89	0.96	47.65	0.59
0.6	53.64	1.01	52.15	0.69
0.7	59.41	1.06	55.92	0.76
0.8	64.29	1.09	59.17	0.86
0.9	68.24	1.14	62.25	0.96

The reverberation suppression gains are high, way beyond the 20 dB that was used as a design criteria earlier. Let us consider a new scenario and utilize the knowledge about the optimal reference velocities. The velocity difference between the reverberation and target is assumed to be $v_{diff} \geq 0.3$ m/s. The first priority is to maximize the suppression gain for $v_{diff} = 0.3$ m/s that according to Table 4.2 is achieved with $v_{ref} = 0.89$ m/s. The first reference signal covers the lower velocities and provides the best separation between the stationary reverberation and the minimum target speed, shown in Fig. 4.25. The Q-function level at 0.0 m/s is at -89 dB, while for 0.3 m/s the Q-function level is already at -59 dB, a 30 dB difference. The second curve in Fig. 4.25 represents the case, where the reference signal is maximally shifted before the Q-function level at 0.0 m/s increases beyond -89 dB. With these two reference signals at $v_{ref} = 0.89$ m/s and $v_{ref} = 2.0$ m/s, the setup provides a minimum processing gain $\hat{G}_{DP}$ of 30 dB over the $0.3 - 2.61$ m/s velocity range. At the same time the $\hat{G}_{DP}$ varies in the range of $30 - 60$ dB,

depending on the target velocity. If needed, the $\hat{G}_{DP}$ around the 1.4 m/s velocity could be increased, by covering the gap with a third reference signal at $v_{ref} = 1.4$ m/s.

Nevertheless, the maximum shift or coverage limitation might be a problem for some systems. This can be circumvented by using a design with multiple transmit signals. Instead of transmitting the same signal every time, the system can alternate between various signal designs. For example, transmitting a signal with $D = 1/4$ in even time slots and a signal with $D = 1/2$ in odd time slots. Recalling the properties of the signal parameters, a signal with $D = 1/4$ has a narrow Q-function main lobe width and hence, is well suited for covering the lower velocities, while a signal with $D = 1/2$ is better suited to cover a wider velocity range. One possible two signal design is shown in Fig. 4.26.

Due to the very low zero velocity Q-function level, the bandwidth of the second signal is increased from 7.5 Hz to 10 kHz, in order to cover an even wider velocity range. In conjunction with the wider main lobe width provided by $D = 1/2$, the design covers the velocities till 3 m/s. It is interesting to note that by increasing the bandwidth even further to $BW = 12.5$ kHz, the peaks and valleys of the two signals would align such that the design provides $\hat{G}_{DP} > 30$ dB till 8 m/s.

The second signal is unsuited for lower velocities, but otherwise offers a wider velocity coverage and an improved range resolution (cf. Fig. 4.18, reduced ACF width). Signal properties that in one situation are unwanted are in other cases beneficial. Therefore, if the signal can be freely generated or selected, a multiple signal design provides the possibility to utilize the strengths of each cutFM signal parameter. In addition, an arbitrary velocity range can be covered, by selecting complimentary signals that cover the gaps and at the same time assure a minimum suppression level for the (stationary) reverberation. Surely, it adds a bit of complexity to the transmit/receive system, as it needs to alternate between transmit signals, but it clearly increases the systems capability to meet various design criteria.

At this point it is important to note that the v_{ref} values given in Table 4.2 are optimal regarding reverberation suppression. For signal detection in the presence of white Gaussian noise, the optimal v_{ref} is equal to the target velocity. In case the velocities match, the cross-correlation output for the signal is maximized, while at the same time the cross-correlation output level for white noise is "minimal", as it is constant for any v_{ref} selection. Herewith, as v_{ref} diverges from the relative target velocity towards

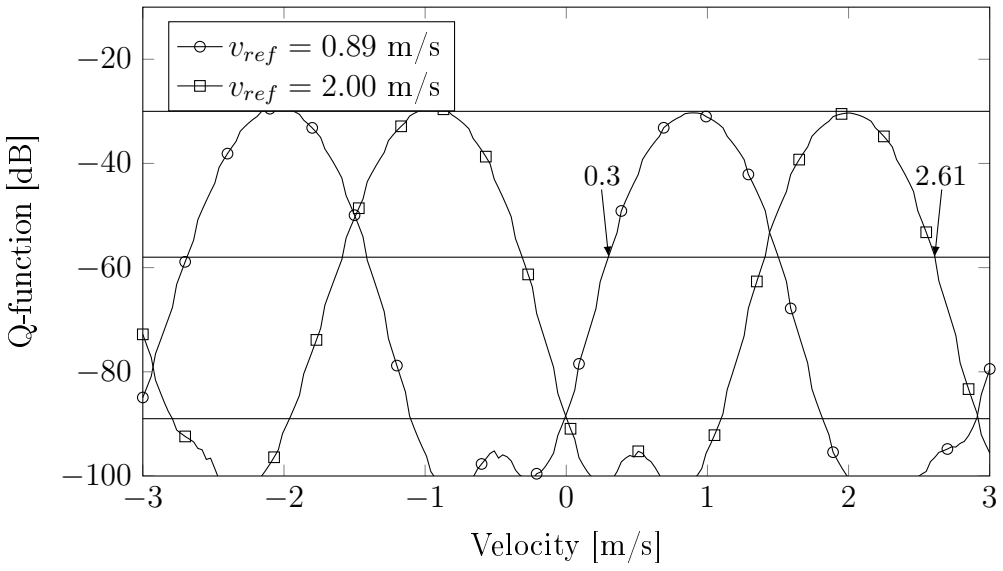

Figure 4.25: Signal design with two reference signals, selected to maximize the reverberation suppression for $v_{diff} \geq 0.3$ m/s.

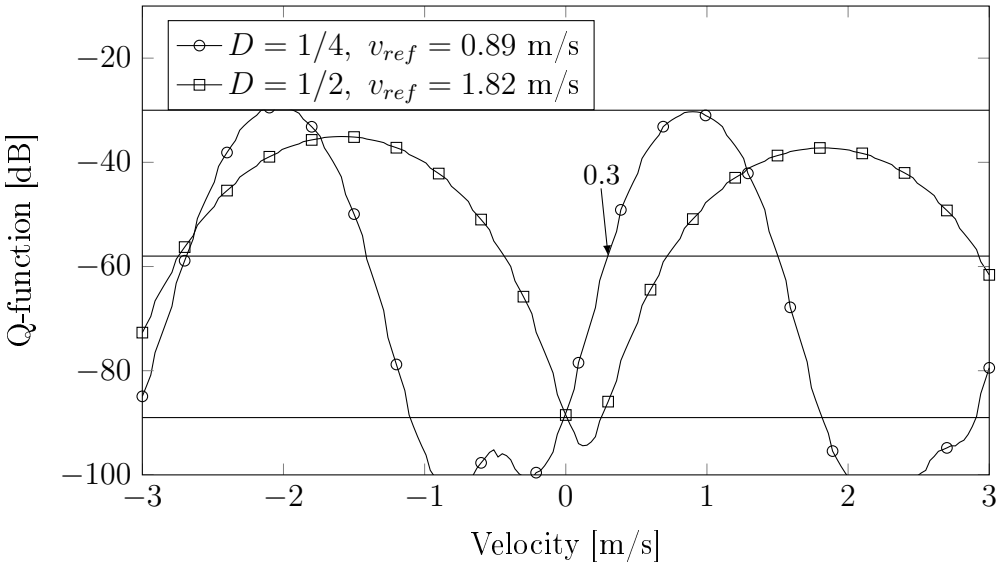

Figure 4.26: Two signal design, first signal with $D = 1/4$, $BW = 7.5$ kHz and second signal with $D = 1/2$, $BW = 10$ kHz.

the receiver, the MF output for the target is reduced compared to the maximum possible, lowering the SNR after the MF. The peak cross-correlation values for cutFM and SFM signals are given in Fig. 4.27.

Assuming the signal performance against noise should not degrade more than 10 dB, then v_{ref} minus the target velocity should not be greater than 0.36 m/s for cutFM and 0.17 m/s for SFM. This leads to a trade-off between target detection against reverberation or noise.

Therefore, in practice the v_{ref} value should be optimized jointly for reverberation and noise, depending on the specific environments (channels) reverberation and noise levels. For example, in Table 4.2 for cutFM with $v_{diff} = 0.3$ m/s, the optimal v_{ref} value is 0.59 m/s higher than the v_{diff} and the reverberation gain is 30.38 dB, but according to Fig. 4.27, the performance against noise is reduced by around −27.5 dB. Now, if the v_{ref} value would be lowered from 0.89 m/s to 0.69 m/s, the reverberation gain would degrade by 5 dB, from 30 dB to 25 dB, but considering noise there would be a 15 dB improvement, from −27 dB to −12 dB. Especially for cutFM (that has quite flat reverberation processing gains), the v_{ref} value can be lowered from the optimal value without significantly degrading the performance against reverberation, providing a possibility to find a good trade-off between the signal's efficiency against reverberation or noise.

The processing gain results given above are for a cutFM signal with $f_c = 70$ kHz, $T = 100$ ms, $BW = 7500$ Hz, and $D = 1/4$, $i = 1$. That is one specific parameter set, where all of the parameters influence the ambiguity diagram and correspondingly its Q-function. Therefore, depending on the specific system requirements and channel conditions, the transmit signal should be designed to provide a suitable Q-function and at the receiver side the reference signal(s) in the MF detector should be selected to maximize the detection probability against both reverberation and noise. In addition, due to the basic range versus Doppler ambiguity trade-off, multiple transmit pulses often provide the best performance. One pulse with good Doppler resolution (narrow Q-function main lobe) for detecting slow objects and a second pulse with emphasis on the range resolution/ambiguities to cover higher velocities.

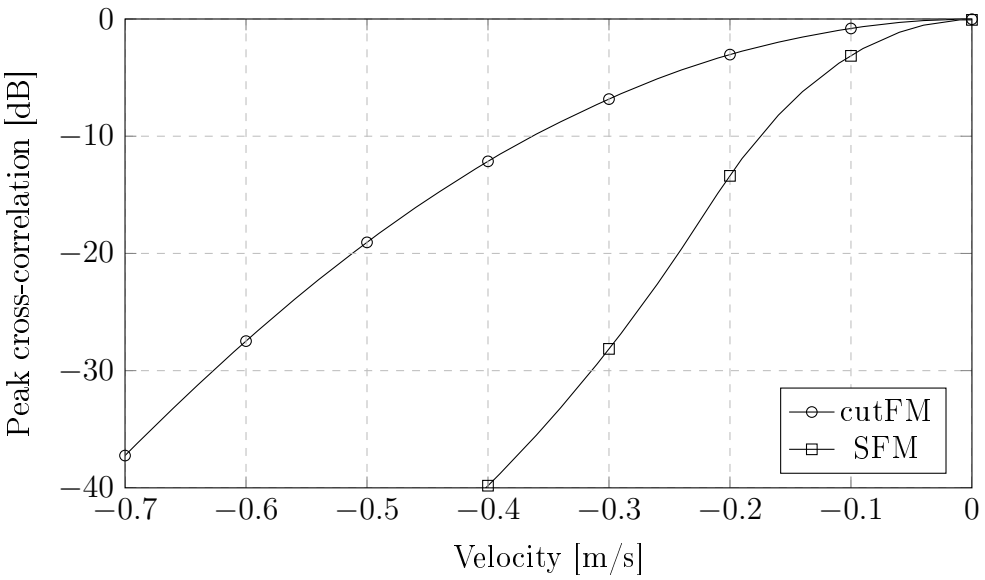

Figure 4.27: Peak cross-correlation values for cutFM and SFM signals.

Chapter 5

Receiver Structures

The task of a sonar receiver is to detect the objects of interest. In general, the receiver structures are independent of the transmit signal. The transmit signals introduced previously aid the receiver to improve the detection probability. In the early sonar systems, the target detection was done manually by trained operators. They either listened to hydrophone recordings (passive sonar) or observed the active sonar received signal power/energy levels from special screens. Today, digital signal processing algorithms are capable of detecting the targets automatically and the operator just needs to confirm the possible threat(s) and makes the decision on the appropriate countermeasures. An active sonar system can be illustrated by the block diagram shown in Fig. 5.1.

Figure 5.1: Illustration of an active sonar system.

The transmitter emits a signal, the signal propagates through the channel and in a monostatic system (transmitter and receiver in the same location), the reflections from the environment are recorded by the receiver. The channel can represent various underwater environments. However, underwater channel modeling is a vast topic and beyond the scope of this dissertation. In this work, a basic reverberation limited channel model for shallow-water diver detection will be introduced in the next section.

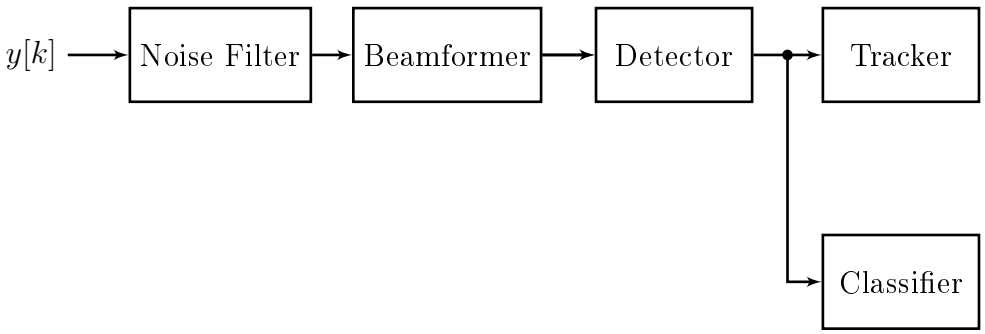

Figure 5.2: Illustration of a receiver structure.

The receiver withholds various components. The first digital signal processing components are usually the noise filter followed by the beamformer. Beamforming is used to improve the detection by separating

the area under surveillance into narrow sectors with reduced beamwidth. For example, this means that instead of a received signal withholding reflections from a 120° viewing angle, the 120° viewing angle can be split into forty sectors with 3° beamwidth. The reduced beamwidth directly reduces the reverberation area (cf. Sec. 2.8.5) and therewith the signal-to-reverberation ratio (SRR). The beamformer is followed by a detector. The detector is the core component that extracts possible targets (contacts) from the background interference. The detection can be based on various properties, like detected signal energy, correlation between the received signal and the transmit signal, or other signal statistics. A number of detector designs will be introduced in Sec. 5.2. The detector outputs can be visualized to the operator directly or they can be processed further by components like tracking and classification. The tracker utilizes movement models to "track" probable target and filter out random or stationary contacts. The classifier utilizes various a priori information about the reflected signals patterns, in order to distinguish between objects. These further processing components are optional, but both add additional intelligence to the system that aid to filter out desired targets from “false alarms”. In this work, only detection algorithms are briefly investigated and all other receiver components are out of scope.

5.1 Channel Model

In order to analyze the performance of the transmit signal in various environmental conditions, a channel model was implemented. Compared to measured data, where various environmental effects are simultaneously present and often inseparable, a channel model allows direct control over all channel parameters and makes it possible to test the signal in distinct channel conditions.

The channel model is based on three main components:

1. discrete objects/targets,
2. reverberation, and
3. noise.

The first two are directly related to sonar activity and are based on the transmit signal. The noise is independent of the transmit signal and is often modeled as additive white Gaussian noise (AWGN). The underwater diver detection channel models can be categorized based on the dominant interferer – either noise or reverberation limited.

5.1.1 Noise Limited Channel Model

The channel output in general can be written as

$$y(t) = h(t) * s(t) + n(t) \ , \tag{5.1}$$

where $h(t)$ is the channel impulse response, $s(t)$ is the transmit signal, and $n(t)$ is the noise. In the simplest case, the channel impulse response is a single Dirac at delay τ, attenuated by a coefficient $a(\tau)$ that depends on the propagation delay i.e. distance

$$h(t) = a(\tau)\delta(t-\tau) \ . \tag{5.2}$$

In contrast to the attenuation coefficient α in Sec. 2.2, in this context the attenuation coefficient $a(\tau)$ corresponds to the total two-way transmission loss that according to (2.1) increases with range. Inserting (5.2) into (5.1), the channel output for this special case becomes

$$y(t) = [a(\tau)\delta(t-\tau)] * s(t) + n(t) = a(\tau)s(t-\tau) + n(t) \ . \tag{5.3}$$

This is a noise limited channel, consisting of a single reflection observed at delay τ in AWGN. The receiver needs to detect the reflection in noise and the detection performance is determined by the signal-to-noise ratio (SNR). Therefore, for this channel the optimal detector maximizes the SNR – a matched filter detector (cf. Sec. 5.2). Considering that the received signal strength of the reflected signal is not only affected by the transmission loss, but also by the acoustic cross-section of the target (TS cf. Sec. 2.6), the received signal $y(t)$ in (5.3) can be further extended to

$$y(t) = a(\tau)TS_a \cdot s(t-\tau) + n(t) \ , \tag{5.4}$$

where TS_a is the target strength in dB converted to an amplitude coefficient. In order to complete the (single return) channel model for diver detection in a noise limited environment, the model should consider the Doppler effect (cf. Sec. 2.5) caused by target movement, by replacing the delayed transmit signal with a Doppler shifted signal

$$y(t) = a(\tau)TS_a \cdot s^D(t-\tau) + n(t) \ . \tag{5.5}$$

The discrete form of the channel output in (5.5) can be written as:

$$y[k] = a[l]TS_a \cdot s^D[k-l] + n[k] \ , \tag{5.6}$$

where the continuous signal $y(t)$ is sampled at time instances kT_s (T_s is the inverse of the sampling frequency) and l is the equivalent time delay τ in samples. The discrete representation is relevant from a digital signal processing aspect and will also be used for the reverberation limited case.

5.1.2 Reverberation Limited Channel Model

Shallow-water environments are typically reverberation dominated. For the reverberation there are two prevailing scattering models in the literature: cell-scattering and point-scattering [Ett96].

- Cell-scattering models assume that the scatterers are uniformly distributed over the area of interest. Additionally, it is assumed that the density of the scatterers is high enough to ensure that a large number of scatterers are present in every elemental volume or area. This means that reverberation is present at any given time and each cell contributes to the total reverberation. According to Etter [Ett96], cell-scattering is the most common choice for reverberation modeling.
- On the other hand, point-scattering models assume that the scatterers are randomly distributed over the area of interest and scattering strengths can vary for different locations. The point-scattering model is more suited for non-homogeneous environments, where the stochastic nature of the model provides greater flexibility to match the nature.

Regardless of the scattering model, the scattering amplitude is often assumed to be Rayleigh distributed. According to Lyons [LA99], if a high number of scatterers are present in each cell, then the scattering amplitude is expected to be Rayleigh distributed, as in such case the central-limit theorem holds and the summation results in a Gaussian reverberation. However, in the same paper the authors show that, if the seabed is patchy and the cells are not big enough to encompass a sufficient number of patches of different scatter densities, then this assumption does not hold. The patchiness leads to a non-Rayleigh probability density function with heavier tails (same effect observed in [WP83]). This effect is more pronounced for high grazing angles [AdMH92, LA99] with smaller reverberation areas. In such case, a Rayleigh mixture or K-distribution provide a better match for the measured reverberation. Similar analysis was done by Gaullaudet [GdM03] for all reverberation sources (seafloor, surface and volume) and it is brought out that especially for surface and volume backscattering, non-Rayleigh distributions

have a better fit. The paper also gives a very nice overview of the various distribution functions and tries to link the distributions to physical effects.

In this work, cell-scattering is selected for reverberation modeling. However, if the goal is to statistically better match a non-homogeneous environment, then a point-scattering model with a suitable scattering distribution, like clustered or large scatterer dominated Poisson distributions [AdMH92], should be used.

Based on the cell-scattering model, the received reverberation can be written out as a summation of M reverberation signal components,

$$y_R[k] = \sum_{m=0}^{M-1} a[k-m]\beta[k-m]s[k-m] \ , \tag{5.7}$$

where M is the transmit signal length in samples. The reverberation is modeled by one scatterer (cluster) per sample where the scattering amplitude, β, is Rayleigh distributed and the mean level is determined by the reverberation target strength (TS_R), cf. Sec. 2.8.5. Therewith, adding the reverberation signal to (5.6), the channel output becomes:

$$y[k] = \sum_{m=0}^{M-1} a[k-m]\beta[k-m]s[k-m] + a[l]TS_a \cdot s^D[k-l] + n[k] \ . \tag{5.8}$$

In addition to the cell-scattering assumption, this channel model makes a few simplifications. First, the reverberation is assumed to be stationary. This assumption is generally valid for bottom reverberation, but not for surface reverberation at higher wind speeds. Secondly, a single-path channel is assumed. The model could be extended to include multipath effects, by including multiple delays in (5.1) and (5.6). Thirdly, the speed of sound for Doppler shift calculation, cf. Sec. 2.5, is assumed to be constant at 1500 m/s. However, as already mentioned in Sec. 2.5, this simplification has a negligible effect on the simulation accuracy.

The channel implementation allows direct control over parameters like: transmission loss, target strength, target velocity, speed of sound, scattering distribution, reverberation backscattering strength, receiver horizontal beamwidth, noise strength, location of target(s), etc. This flexibility will be used to compare different detectors in various channel conditions.

5.2 Detector Algorithms

A detector can be split up into two main components. The first signal processing step converts the received signal into a more suitable form, e.g. power, energy or correlation. In the second step, based on the given signal characteristic, a decision is made on if a target is present or not. The constant false-alarm rate (CFAR) algorithm is one (very common) possibility to make this decision automatically, by comparing each cell to the estimated background level. In the following, three detector algorithms are introduced, but before moving to the specific detectors it is first fitting to introduce the cell-averaging constant false-alarm rate (CA-CFAR) algorithm.

5.2.1 Cell-Averaging CFAR

The squared channel output of a reverberation limited channel is shown in Fig. 5.3. The received power decreases with increasing distance (or two-way propagation time), due to the increasing transmission loss, cf. Sec. 2.2. In fact, the plot shows both reverberation and noise dominated sections. At first, the received signal is reverberation dominated and from around 1500 m the noise becomes the main interferer. The

target at 500 m is visually "detectable", but at the same time one can also detect multiple false alarms till 1500 m.

The standard detection procedure is to compare the signal level in the given cell under investigation with the background/noise level and if the signal level is higher than the background by a certain threshold, then the detector outputs a positive detection. The difficulty is to estimate the noise power, as it is not known a priori. In the range CA-CFAR (averaging done over range), the background interference level is estimated from leading and lagging reference windows [Roh83], illustrated in Fig. 5.4.

The estimated average noise power is calculated by averaging over the N cells/samples in the reference windows

$$Z_{CA} = \frac{1}{N} \sum_{n=1}^{N} X_n \ , \tag{5.9}$$

where X_n denotes the nth position in the sliding reference window. Ideally, the reference windows should only withhold noise and therefore, in order to avoid the signal from the target being included to the background, guard cells are placed between the cell under test (CUT) and the reference windows. The detection threshold, TH, is calculated by multiplying the average noise power with a scaling factor S [Roh83],

$$TH = Z_{CA} \cdot S \ , \tag{5.10}$$

where S is calculated from the desired probability of false alarm (P_{fa})

$$S = \ln \frac{1}{P_{fa}} \ . \tag{5.11}$$

The derivation for the scaling factor calculation formula can be found in [Roh83] or [Roh11], but essentially it is based on the assumption of exponentially distributed $\mathbb{X}$

$$p(x) = \begin{cases} \frac{1}{\mu} e^{-\frac{x}{\mu}}, & x \geq 0 \\ 0, & \text{otherwise.} \end{cases} \tag{5.12}$$

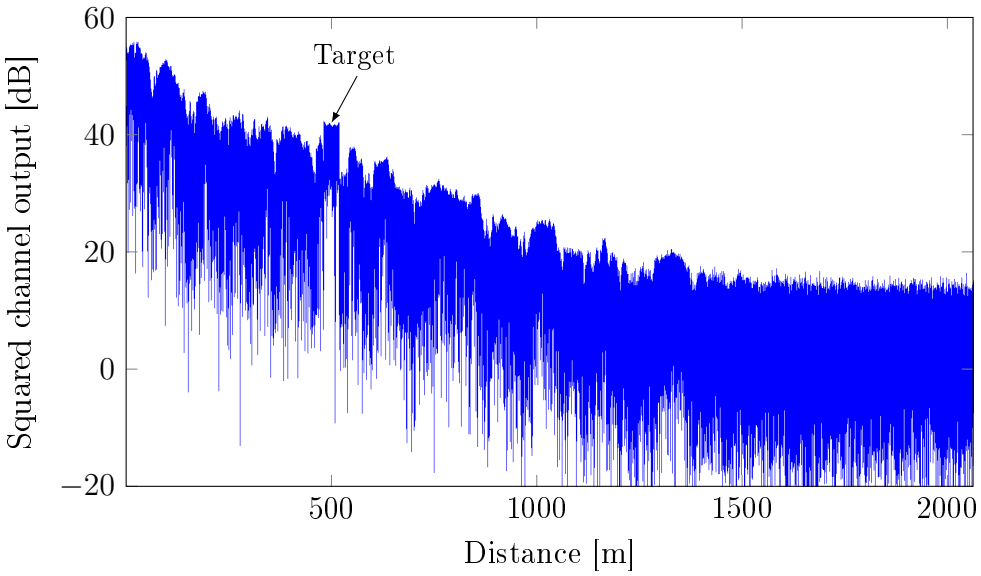

Figure 5.3: Squared reverberation channel output.

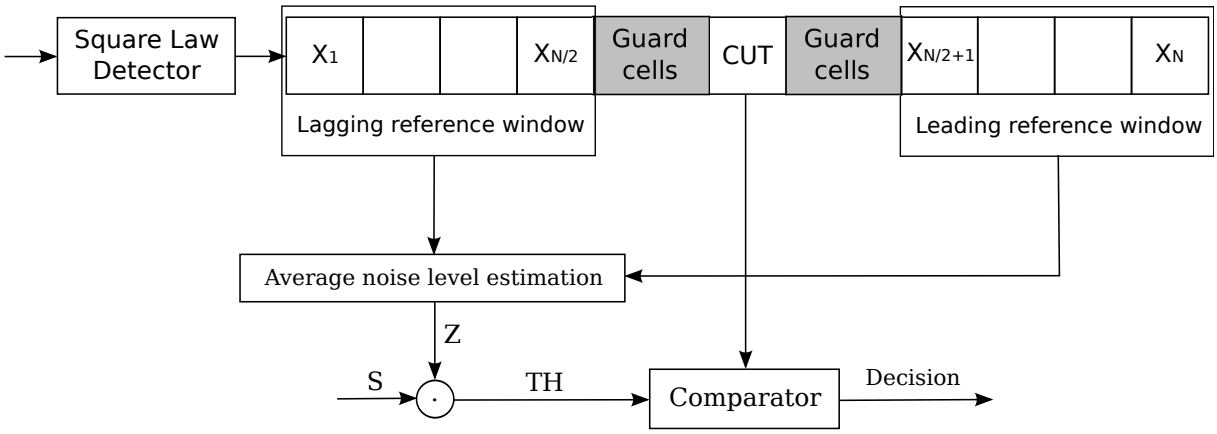

Figure 5.4: Illustration of the CFAR algorithm.

According to [Roh83], this is justified for the square-law detector with complex Gaussian distributed noise. For different noise distributions, the calculation for the threshold or scaling factor should be analyzed and adapted accordingly.

In the CFAR algorithm, the threshold is calculated for every cell, based on the estimate for the average noise power plus the scaling factor S and the cell under test is compared to the threshold. This is done to assure an acceptable false alarm rate.

The CA-CFAR can be implemented by sliding windows, where the sum is updated by subtracting the oldest element from the sum and adding the new element, providing an efficient realization. The CA-CFAR performs well with homogeneous noise, but has difficulties at clutter edges and in multiple target situations [Roh11]. Clutter represents an area with significantly higher backscattering strength (e.g. clouds and coastal lines for radar, reefs and harbor walls for sonar). At clutter edges, the CA-CFAR performance degrades due to averaging over the two reference windows that contain signal sections with various mean levels. This drawback is the motivation for a number of modifications.

- Cell-averaging "greatest of" CFAR (CAGO-CFAR) [HS80]. The aim of the CAGO-CFAR is to improve the detection performance at clutter edges. Instead of estimating the average noise level from both the leading and lagging windows, the "greatest of" algorithm selects the window with the highest level,

$$Z_{CAGO} = \frac{1}{N/2} \max \left(\sum_{n=1}^{N/2} X_n, \sum_{n=N/2+1}^{N} X_n \right) . \tag{5.13}$$

  Therewith, avoiding false alarms at clutter edges that occur for CA-CFAR due to the averaging over both windows.

- "Smallest of" CFAR (CASO-CFAR). This algorithm does the opposite of CAGO-CFAR. It selects the minimum of the two windows for the noise power estimation,

$$Z_{CASO} = \frac{1}{N/2} \min \left(\sum_{n=1}^{N/2} X_n, \sum_{n=N/2+1}^{N} X_n \right) . \tag{5.14}$$

  The aim is to improve target detection in presence of multiple targets, in which case for CA-CFAR and CAGO-CFAR the threshold would be high and the target stays undetected due to masking.

- Ordered statistics CFAR (OS-CFAR) [Roh83]. The ordered statistics CFAR aims to combine the strengths of the previous two, by taking a different approach. Instead of estimating the noise power

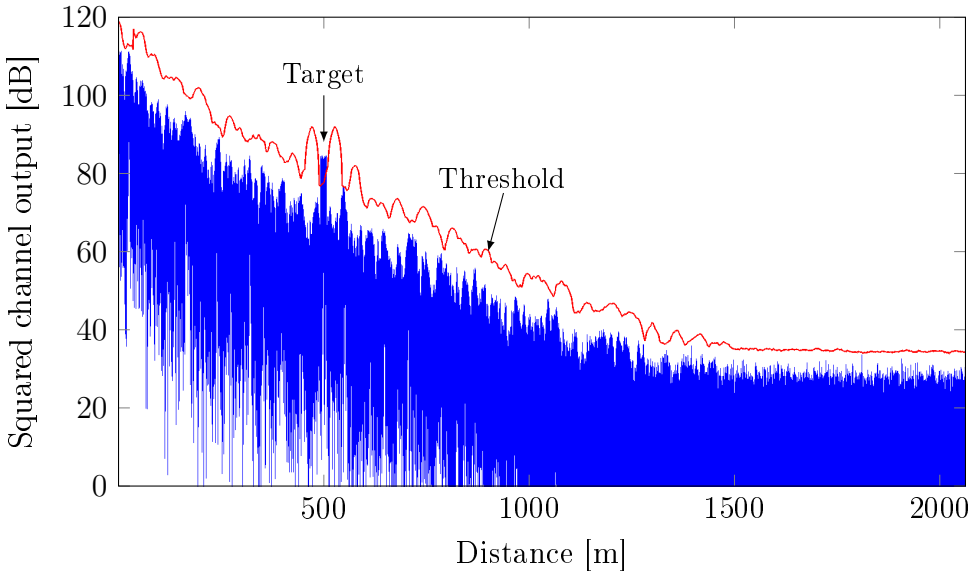

Figure 5.5: Squared reverberation channel output together with the CA-CFAR detection threshold.

by averaging, it selects a single value from $\mathbb{X}$ to represent the background level. The selection is done by ranking the X_n in ascending order

$$X_{(1)} \leq X_{(2)} \leq \cdots \leq X_{(N)} \ , \tag{5.15}$$

where the parentheses denote the rank-order number. $X_{(1)}$ denotes the minimum value and $X_{(N)}$ the maximum value. A single value $X_{(k)}$, $k \in \{1, 2, \cdots, N\}$ is used to estimate the average noise power

$$Z_{OS} = X_{(k)} \ . \tag{5.16}$$

Typical values for k are $k = 3N/4$ and $k = N/2$ [Roh83]. Essentially, the parameter k can be used to alter the influence of the clutter. With $k > N/2$ the clutter areas are expanded and for $k < N/2$ they are shrunk. The OS-CFAR improves the detection performance and increases the flexibility of the algorithm, but it has a significantly higher computational complexity.

Considering the cell-scattering reverberation model without additional emphasized clutter regions, the CA-CFAR is already suitable and the extensions are not needed. Exemplary, the CA-CFAR algorithm threshold is shown in Fig. 5.5. The estimated average interference plus the scaling factor create a threshold (plotted by the red curve) that is above the squared channel output. Only at the target location the squared signal level is above the threshold and would result in a positive detection.

The CFAR is just one algorithm to automatically detect possible targets. The true performance of a detector is determined by the first processing step that converts the received signal into a more suitable form, e.g. power, energy or correlation.

5.2.2 Square-Law Detector

The square-law detector is based on the received power, illustrated in Fig. 5.6. The received signal $y[k]$ is noise filtered, squared and the output $x[k]$ is used in the CFAR algorithm. The noise filter is optional. If the receiver already applies a noise filter before beamforming (cf. Fig. 5.2), then a second noise filter might be redundant. The power of the signal is the simplest characteristic and this type of detection is

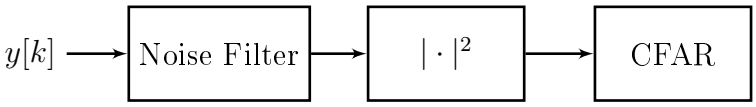

Figure 5.6: Illustration of a square-law detector.

used in situations where nothing is known about the transmit signal [Urk67] (i.e. passive sonar). The squarer is a simple function and can be easily realized in hardware or in software. The detector is also suitable for systems, where the transmit pulse is ultra-short, i.e. just a few samples long, as in such case the energy or correlation detectors bring nearly no advantage. In case of longer signals, instead of the power the detection should be based on the energy of the signal, in order to improve the SNR.

5.2.3 Energy Detector

The energy detector integrates the power of the signal over the signal duration T, illustrated in Fig. 5.7

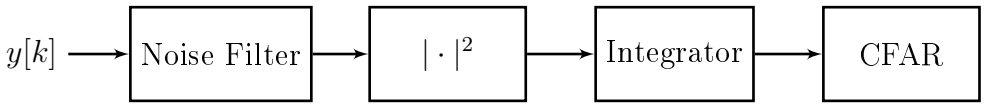

Figure 5.7: Illustration of an energy detector.

The discrete output signal is given by

$$x_E[k] = \sum_{m=0}^{M-1} |y[k+m]|^2 \,, \tag{5.17}$$

where M is the transmit signal length in samples. For an AWGN channel, the performance of the energy detector compared to the square-law detector is improved by utilizing the total signal energy instead of the instantaneous power. With increasing M, the background noise level variance decreases and eventually converges to the noise energy. A receive signal and the corresponding signal power and energy are exemplary shown in Fig. 5.8.

In this example, the received signal consists of a 1000 samples long CW signal with $f_c = 100$ Hz starting at sample 2000 in AWGN ($f_s = 1000$ Hz). The SNR is 1.4 dB. Already from the received signal, one can see a certain change in the signal structure, but the peak levels for the noise and noise plus CW pulse are very close. The separation of the peaks in the squarer output in Fig. 5.8b is a bit better, but the detection is still prone to errors. On the other hand, the energy of the received signal in Fig. 5.8c shows a clear peak at sample 2000. The base integrator output value around 1000 is the noise level (energy) and at sample 2000 the received energy withholds the noise plus the desired signal. Therewith, the difference between the base and the peak level corresponds to the SNR. For such a 1000 samples long signal, the detection is vastly improved and the probability of error is small. Figure 5.8c also shows another effect of the energy detector.

As the signal length increases the integrator output converges to the signal energy. This means that the threshold for the CA-CFAR should be adjusted, as the CFAR input $\mathbb{X}_E$ has a different distribution as for the square/law detector case. Essentially, $\mathbb{X}_E$ follows a Gamma distribution, with mean equal to the noise energy and decreasing variance as M increases. Unfortunately, a closed form $\mathbb{X}_E$ distribution as a function of noise power and M could not be found. At high M values, according to the central-limit theorem the $\mathbb{X}_E$ can also be approximated by a Gaussian distribution. Hence, there exist a possibility to select the distribution that is more convenient to handle.

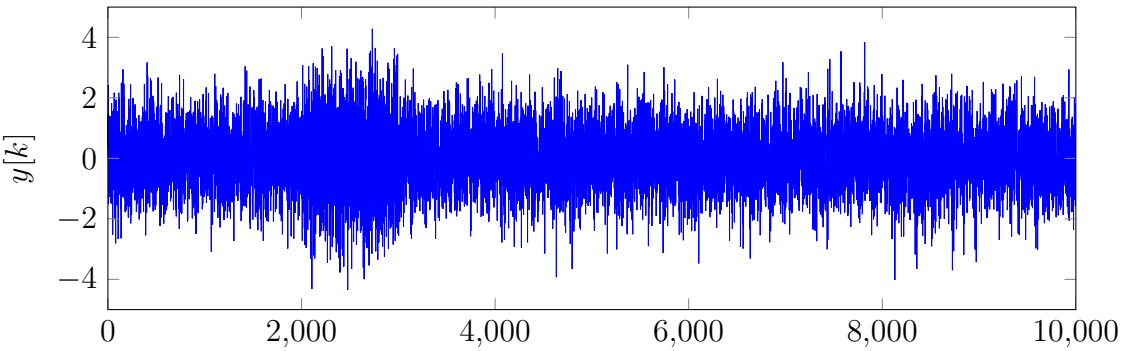

(a) Received signal

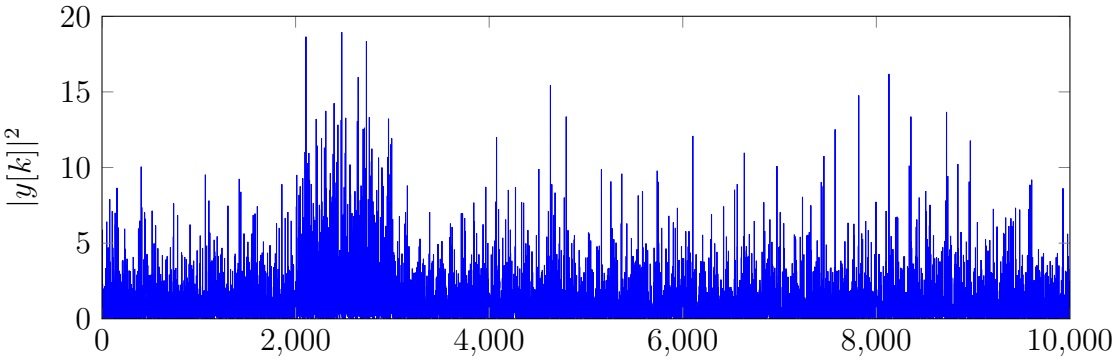

(b) Signal power

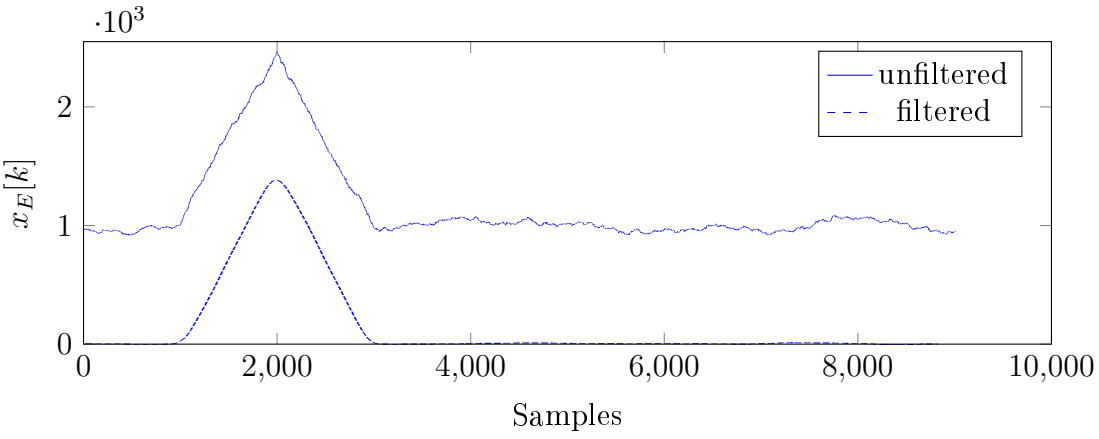

(c) Signal energy

Figure 5.8: An example received signal and its corresponding signal power and energy.

Therewith, the optimal selection of the threshold for CFAR in combination of energy signal is not straightforward. First, the $\mathbb{X}_E$ probability distribution function should be estimated from interference only signal sections and then a proper threshold can be obtained given a certain false alarm rate. In practice, often the CFAR threshold is kept as a tunable parameter that is adjusted to the channel conditions, to achieve a wanted false alarm rate and therewith, also appropriate threshold values are found with testing.

It was pointed out that the background to peak level in Fig. 5.8c corresponds to the SNR. For a CW signal, in order to maximize the SNR, the noise filter should be matched to the transmit signal's center frequency and bandwidth. The dashed curve in Fig. 5.8c is obtained by applying a narrow bandpass filter before the integrator. By filtering out everything but the frequency range of the narrowband transmit signal, the noise energy is minimized and with that the SNR maximized (a mathematical proof can be found in [Ric03]). However, for a frequency modulated signal the corresponding filter design that maximizes the SNR is not a simple bandpass filter, but a matched filter.

5.2.4 Matched Filter Detector

The matched filter, also known as correlator or replica correlator, correlates the received signal with the transmit signal. The MF detector structure is illustrated in Fig. 5.9.

Figure 5.9: Illustration of a matched filter detector.

In case the interference is AWGN, the MF or the correlator detector is the maximum likelihood detector that maximizes the SNR [Ric03, Höh13]. The matched filter was already introduced in Chapter 3 and the first representation of the MF output was given via the convolution (the input/output notations have been adjusted to comply with the receiver structure)

$$x_{MF}(t) = y(t) * h(t) = \int_{-\infty}^{\infty} y(\alpha)h(t-\alpha)d\alpha \ , \tag{5.18}$$

where the impulse response of the matched filter $h(t)$ is given as

$$h(t) = s(-t) \ . \tag{5.19}$$

Equivalently, the convolution can be written as a cross-correlation function, cf. (3.19)

$$x_{MF}(t) = y(t) * h(t) = y(t) * s(-t) = s(\tau) ** y(\tau) = R_{sy}(\tau) \ . \tag{5.20}$$

The cross-correlation maximizes the signal response and with that also maximizes the SNR in AWGN. The matched filter is optimal for any transmit signal $s(t)$, but as pointed out earlier, for a CW signal the MF can have multiple forms and realizations. The signal $s(t)$ in the MF can be replaced by a Doppler shifted reference signal $s_{ref}(t)$ (cf. Sec. 4.6). The resulting more general algorithm is optimal for any $s_{ref}(t)$ selection in AWGN and is sometimes also termed as the optimal mismatched filter [Ric03].

In the energy detector example, a CW transmit signal was used, in this example an FM transmit signal with 100 Hz bandwidth is used and the corresponding received signal, the signal energy and matched filter outputs are shown in Fig. 5.10. Figure. 5.10b shows two signal energy curves. The first, plotted by a solid line, is nearly identical to that seen for the CW signal in Fig. 5.8c. The second curve plotted by a dashed line, is again the result with noise filtering. Due to the increased signal bandwidth, the residual

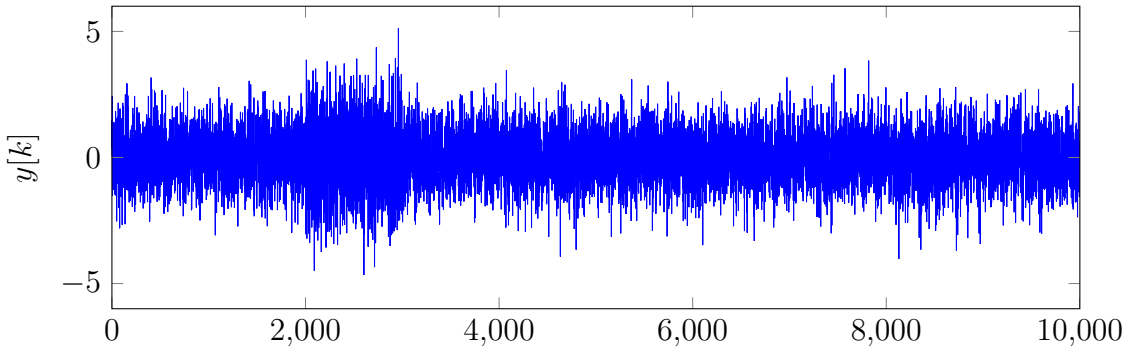

(a) Received signal

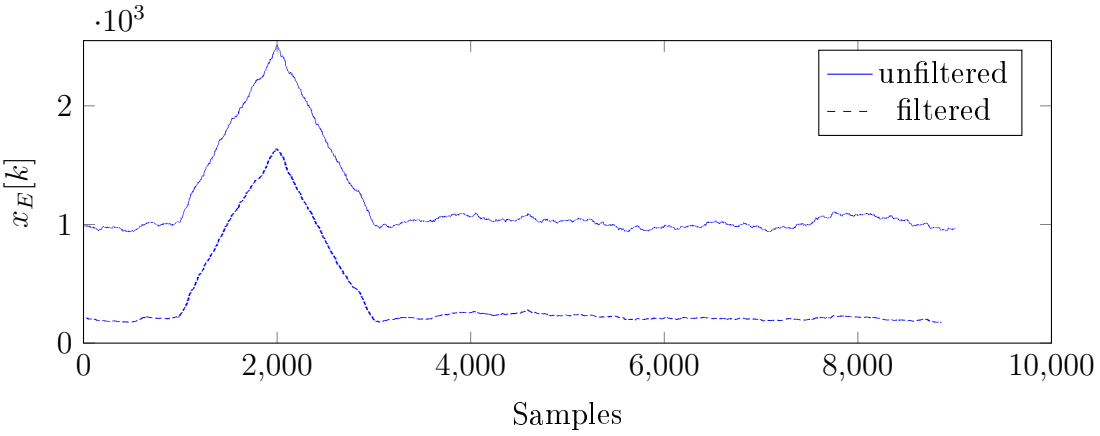

(b) Signal energy

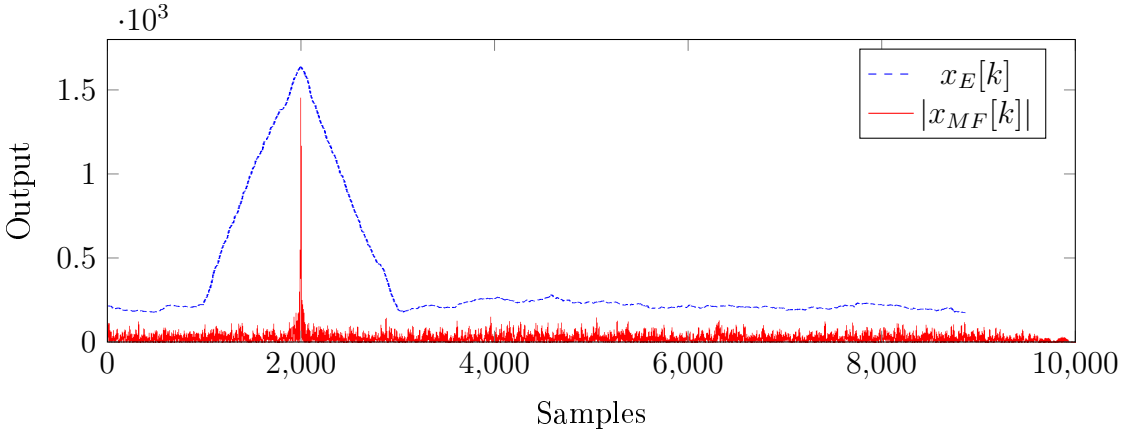

(c) Matched filter output

Figure 5.10: An example received signal and its corresponding signal energy and matched filter output.

noise energy after filtering is noticeably higher than in Fig. 5.8c. Nevertheless, the gain of applying a noise filter is significant. The SNR improves from 1.4 dB to 8.1 dB. However, the SNR for the FM signal can be further improved by using a MF, shown in Fig. 5.10c. The resulting SNR after the MF is around 11.5 dB. Yet, maybe an even more important benefit of the MF is that it utilizes the bandwidth of the signal to bring forth the compression gain. Instead of a triangle, the MF output for the FM signal is a narrow sinc function (cf. Sec. 3.4). The pulse compression greatly improves the range resolution and performance in reverberation channels or multiple target scenarios.

For CW signals, the energy detector is an efficient detection algorithm, where the main challenge is designing the best possible narrowband noise filter. On the other hand, the MF is optimal (for AWGN channels) for any transmit pulse form. This is also the reason why today's digital receiver systems widely use the MF detector.

As modern receiver systems have more computational power available, the MF detector has become the favored detection algorithm, due to its optimality in the AWGN scenario. Nevertheless, in reverberation limited environments MF detection is no longer optimal. Various algorithms exist that try to use some knowledge about the reverberation to improve the detection performance. One of such algorithms is the principle component inverse (PCI) detector [TKK82, GJ02].

5.2.5 PCI Detector

The PCI algorithm aims to estimate and suppress the reverberation before applying the matched filter. The method utilizes the fact that the received signal is a superposition of multiple reverberation components and the target echo. The PCI algorithm attempts to split the received signal into two subspaces – reverberation subspace and target echo plus noise subspace. Singular value decomposition (SVD) is used for separating the signal into low rank subspaces. Given the separation is successful the estimated reverberation signal components are subtracted from the received signal and the residual signal with improved SRR is processed by the MF. A block diagram of the PCI detector is shown in Fig. 5.11.

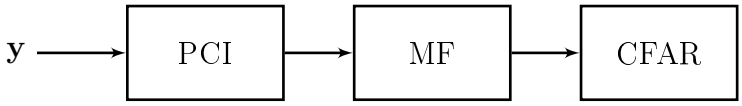

Figure 5.11: Illustration of a PCI detector.

The core of the PCI algorithm is the SVD. The SVD factorizes an $m \times n$ matrix $\mathbf{M}$ into

$$\mathbf{M} = \mathbf{U}\mathbf{\Sigma}\mathbf{V}^H \ , \tag{5.21}$$

where $\mathbf{U}$ is an $m \times m$ unitary matrix, $\mathbf{\Sigma}$ is an $m \times n$ non-negative real-valued diagonal matrix, and $\mathbf{V}^H$ denotes an $n \times n$ complex conjugate transposed (also known as Hermitian transposed) unitary matrix. The diagonal entries $\Sigma_{j,j}$ in $\mathbf{\Sigma}$ are the singular values (SVs) of $\mathbf{M}$ and the columns of $\mathbf{U}, \mathbf{V}$ are called the left-singular and right-singular vectors of $\mathbf{M}$.

In order to use the SVD for receive signal factorization, an input matrix has to be generated. In [TKK82] it is first proposed to compose the matrix from a block of the receive signal $\mathbf{y}$, denoted as $\mathbf{y}_i$. The resulting matrix, $\mathbf{Y}_i$ from block i, is termed the forward matrix

$$\mathbf{Y}_i = \begin{bmatrix} y_i[p] & y_i[p-1] & \cdots & y_i[1] \\ y_i[p+1] & y_i[p] & \cdots & y_i[2] \\ \vdots & \vdots & \vdots & \vdots \\ y_i[L] & y_i[L-1] & \cdots & y_i[L-p+1] \end{bmatrix} \tag{5.22}$$

where L is the block length and p is $L/2$, rounded up if L is odd. The $m \times n$ $\mathbf{Y}_i$ matrix is generated from L received values of block i. The aim of the PCI is to split $\mathbf{Y}_i$ into two matrices, $\mathbf{Y}_i^r$ and $\mathbf{Y}_i^o$

$$\mathbf{Y}_i = \mathbf{Y}_i^r + \mathbf{Y}_i^o \ , \tag{5.23}$$

where $\mathbf{Y}_i^r$ spans the reverberation subspace and $\mathbf{Y}_i^o$ spans the target echo plus the noise subspace. Assuming that the reverberation is stronger than the target echo, the best rank r estimate of $\mathbf{Y}_i^r$ is represented by the r largest singular values of $\mathbf{Y}_i$. The reverberation subspace $\mathbf{Y}_i^r$ can be obtained via the SVD and the Eckart and Young theorem [EY36]:

$$\mathbf{Y}_i = \mathbf{U}\mathbf{\Sigma}\mathbf{V}^H = [\mathbf{U}^r|\mathbf{U}^o] \begin{bmatrix} \mathbf{\Sigma}^r & 0 \\ 0 & \mathbf{\Sigma}^o \end{bmatrix} [\mathbf{V}^r|\mathbf{V}^o]^H \ , \tag{5.24}$$

where $\mathbf{\Sigma} = \text{diag}(\sigma_1, \sigma_2, \cdots, \sigma_{R_Y})$ is a diagonal matrix that consists of the R_Y singular values of $\mathbf{Y}_i$, in descending order. In [GJ02], the estimated reverberation signal is reconstructed from $\mathbf{U}\mathbf{\Sigma}\mathbf{V}^H$ by retaining only the r bigger singular values in $\mathbf{\Sigma}$ and collecting the reverberation vector, $\mathbf{y}^r$ from $\mathbf{Y}_i^r$. The reverberation signal is subtracted from the receive signal and the resulting signal is processed by the MF.

The main difficulty of the algorithm is to estimate the rank r or more explicitly, how do determine which singular values represent the reverberation. Depending on the selection, the signal $\mathbf{y}^r$ may include only part of the reverberation signal or it may also include the target echo. In [GJ02], the rank r estimation is based on the signal power. As the sum of the singular values is linked to the received signal power, then r is estimated by summing the squared singular values of $\mathbf{Y}_i$ and comparing it to a threshold P that is selected using a priori knowledge about the singular values associated to target echo and noise. Therefore, if there exists an index K, smaller than the rank R_Y of $\mathbf{Y}_i$, for what the sum of the singular values exceeds P,

$$\sum_{k=0}^{K} \sigma_{R_Y-k}^2 > P \ , \tag{5.25}$$

then r is selected to be equal to $r = R_Y - K + 1$. If no such index K exists, the signal block is not altered by the PCI.

As stated in [GJ02], the PCI has two requirements for good performance:

- the reverberation signal has to be more powerful than the target echo and the noise,
- the rank r of $\mathbf{Y}^r$ must be small.

The first condition is needed to achieve the subspace separation in (5.24) and the second condition is necessary to have a good separation of the signal subspaces. However, the PCI has one more fundamental requirement: the superimposed signals have to be distinguishable in frequency.

5.2.5.1 Rank Estimation

The bandwidth of the (transmit) signal determines the rank of the subspace. The rank of a CW (monochromatic) signal is one. Hence, if k CW signals with differing frequencies are present in one block, then the rank is equal to k. In such scenario, each of the CW signals is represented by one of the singular values.

For wideband signals it is more complicated to determine the rank, as the instantaneous frequency is not constant and as pointed out in Sec. 3.4 it does not need to be linearly increasing. Considering a linear frequency modulated signal, according to [GJ02], the subspace rank can be estimated using the

intrinsic bandwidth of the signal. The intrinsic bandwidth, b, is calculated via the signal duration and bandwidth

$$b = \sqrt{\frac{BW}{T}} \ . \tag{5.26}$$

The intrinsic bandwidth is considered to be the minimum frequency difference needed to separate two LFM signals. The same separation bandwidth can be used to estimate the rank of a forward matrix of an LFM signal block, by calculating the number of intrinsic bandwidths in a signal block. Figure 5.12 illustrates the relation between the intrinsic bandwidth, block length and the rank.

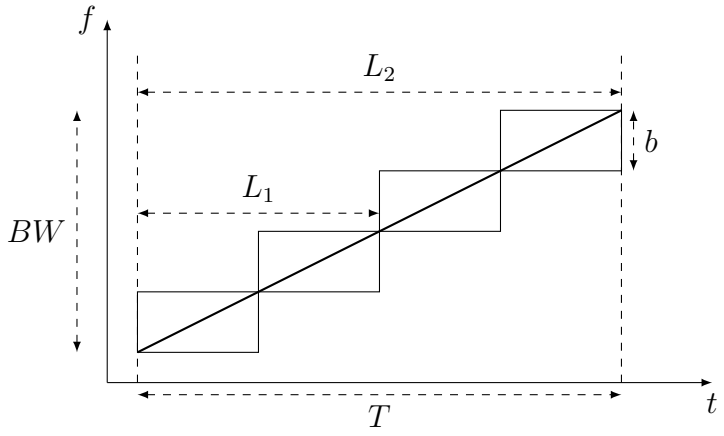

Figure 5.12: Rank estimation.

The exemplary LFM signal consists of four times the intrinsic bandwidth. If the block length is selected to be L_1, the block withholds two times the intrinsic bandwidth and hence, the rank of the forward matrix would be $R_{FM} = 2$. For a block length of L_2 the rank would be four. Recalling the PCI requirements, it is better to use a shorter block length that results in a lower forward matrix rank and additionally the SVD calculation is less complex for smaller matrix sizes.

Mathematically, the estimated rank can be calculated via

$$R_{FM} = \frac{BW}{b} \cdot \frac{L}{T} \ . \tag{5.27}$$

In the following PCI simulations, the block length is chosen to be $L = T/10$, additionally considering the standard signal properties, like $T = 100$ ms and $BW = 7500$ Hz, then $b = \sqrt{BW/T} = 273$ Hz and the estimate for the rank of the LFM signal would be

$$R_{FM} = \frac{7500}{273 \cdot 10} = 2.74 \approx 3 \ . \tag{5.28}$$

The resulting rank is low and hence, there is no need to further reduce the block length. Before moving to the PCI results, it is important to mention that in order to reduce the computational complexity the bandpass signal is shifted to baseband and the signal is downsampled to $f_s = 20$ kHz. This reduces the block length from 2000 to 200 and significantly lowers the processing time.

The results of the SVD factorization are shown in Fig. 5.13. The figure presents the amplitudes of the 20 largest singular values for CW, LFM, and two cutFM signals. The first cutFM signal is created with $D = 1/2$ and the second with $D = 1/4$.

First of all, the result for CW is as expected. A single larger singular value that concurs with $r = 1$ for monochromatic signals. For LFM the number of significant singular values is less obvious. Essentially, there are 3 to 4 bigger singular values. According to (5.28), we would expect that only the first 3 are

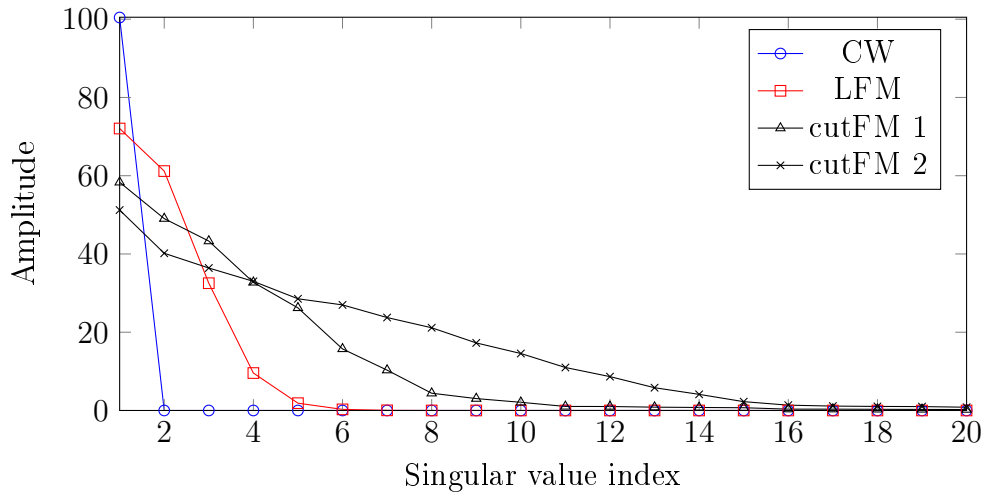

Figure 5.13: Twenty largest singular values for CW, LFM, cutFM with $D = 1/2$ (cutFM 1), and cutFM with $D = 1/4$ (cutFM 2).

required to reconstruct the original LFM signal with sufficient precision. For the cutFM signals, the number of larger singular values increases with the duty cycle D, around 8 for $D = 1/2$ and around 14 for $D = 1/4$. In order to determine the sufficient rank r, the mean squared error (MSE) between the original input signal $\mathbf{y}$ and the rank r estimate $\mathbf{y}^r$ is calculated.

Earlier, it was not explicitly explained how to get $\mathbf{y}^r$ from $\mathbf{Y}_i^r$. There are two methods:

1. Reverse the $\mathbf{Y}_i$ creation process and collect the $\mathbf{y}^r$ values from the first row and column,
2. Utilize the full information in the Toeplitz structure of $\mathbf{Y}_i^r$ by calculating the arithmetic mean of the diagonals.

Concerning the second method, as some of the diagonals are very short, then the PCI blocks should be selected with an overlap (e.g. 50%). The MSE comparison of the two methods is shown in Fig. 5.14.

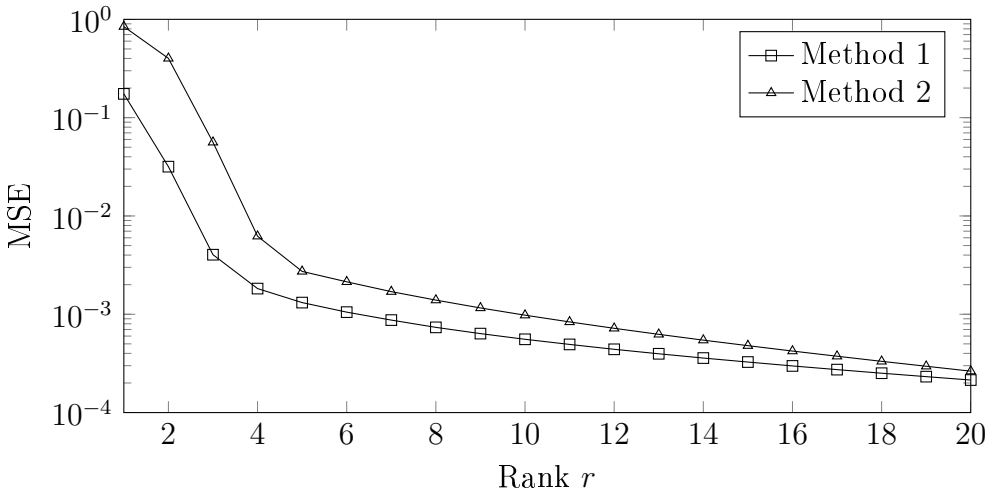

Figure 5.14: Comparison of the MSE between $\mathbf{y}$ and $\mathbf{y}^r$ obtained with either method 1 or with method 2.

Method 2 achieves the same MSE with $r = 3$, as method 1 with $r = 4$. A clear advantage of utilizing the complete information in $\mathbf{Y}_i^r$, by averaging over the diagonals. The squared differences between $\mathbf{y}$ and $\mathbf{y}^r$ of the three most interesting parameter combinations are shown in Fig. 5.15.

The black curve obtained with method 1 and $r = 3$, presents periodic high peaks at multiples of half of the block length ($L = 200$), implying that the matrix elements near the corners of $\mathbf{Y}_i^r$ have poor accuracy. Applying the 50% overlap and using the diagonal averages of $\mathbf{Y}_i^r$ significantly improves the estimate. However, a similar accuracy is achieved with method 1 by increasing the rank to 4, which is an interesting result that might be useful for low complexity realizations. Figure 5.15 also shows a second important effect. All three curves have a high mismatch with the input signal between $50 - 100$ samples. This is caused by edge effect. Till sample 58, the input signal is zero and then the selected CW, LFM or cutFM signal begins. This sharp transition can not be represented by a few singular values. The same effect is also evident for CW. The first block has more than one non-zero singular values and hence, with increasing r the MSE gradually decreases, cf. Fig. 5.16. This edge issue could be avoided by using a smoother windowing function, e.g. Hann or Hamming.

Figure 5.16 shows the MSE depending on the rank r for various signals. For CW the signal is represented by a single singular value, therefore the MSE is below 10^{-2} already with $r = 1$. LFM reaches an MSE of 10^{-2} with $r = 3$. Both CW and LFM show the same error-floor, caused by the edge effect. CutFM 1 with $D = 1/2$ reaches an MSE of 10^{-2} with $r = 6$, but $r = 7$ improves the MSE nearly by a magnitude and is a better choice. CutFM 2 with $D = 1/4$ reaches an MSE of 10^{-2} with $r = 12$, but $r = 13$ is a better choice. The cutFM signals to not encounter the strong edge issue at the beginning and at the end of the signal, due to sub-pulse Hann windowing, but instead the PCI algorithm has difficulties with the cut-out signal sections. The SFM signal with its modulated phase appears to be difficult to estimate with a low rank r. SFM requires a rank $r > 20$. For more visualization about $\mathbf{y}^r$ signal evolution with increasing r, cf. Appendix A.

Concerning the PCI requirement of a low subspace rank r, only the CW and LFM signals fulfill it. The additional modulation introduced to the cutFM and SFM signals in order to improve their Doppler selectivity, increases the amount of frequency components present at each PCI signal block (cf. Sec. 4.3) and therewith, increasing the rank r of the forward matrix. This does not imply that the PCI

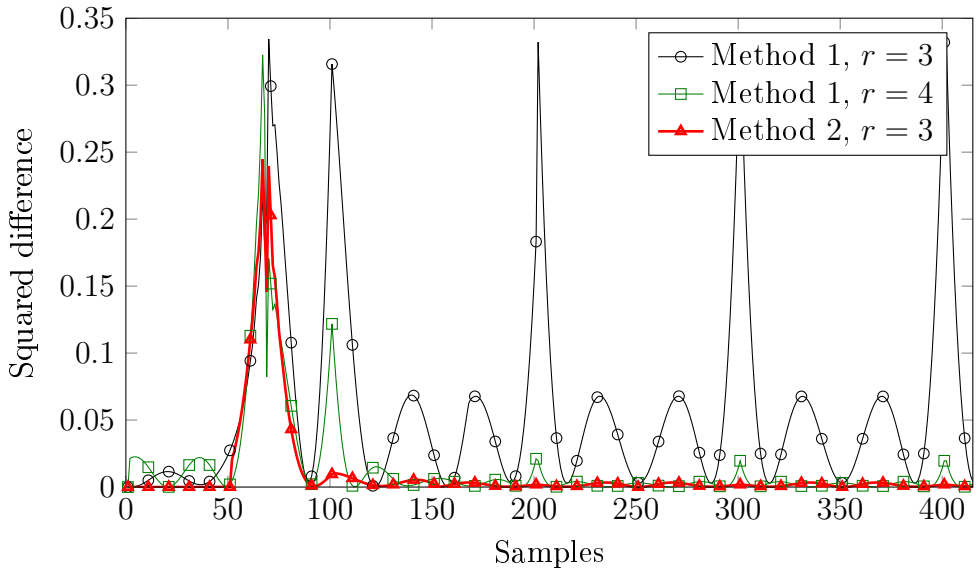

Figure 5.15: Squared differences between $\mathbf{y}$ and $\mathbf{y}^r$.

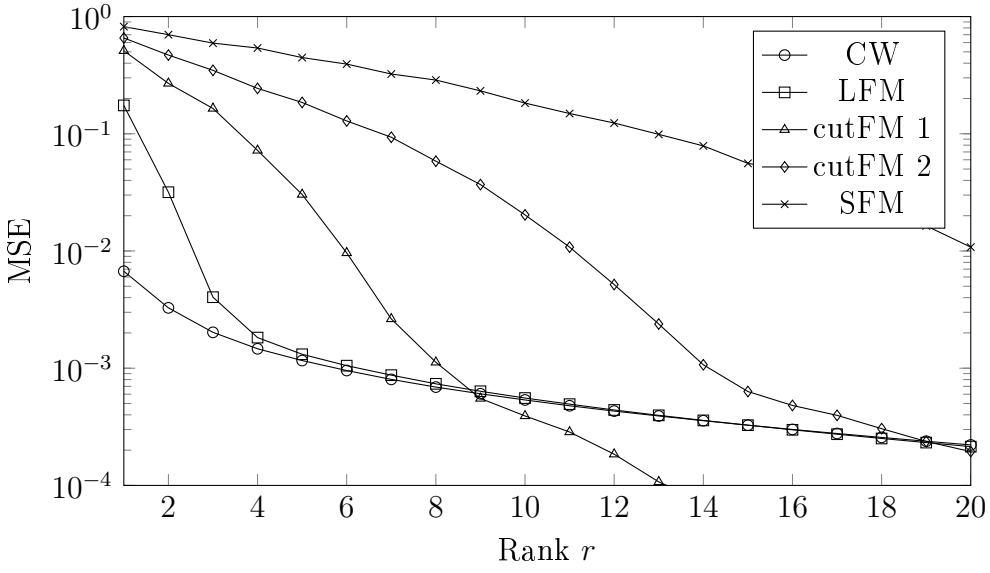

Figure 5.16: MSE of various signals depending on rank r.

is unusable with cutFM and SFM signals, but that good reverberation separation is harder to achieve. Good separation according to (5.24) is possible if the unwanted signals singular values are the r largest ones.

5.2.5.2 Power Difference

In order to visualize the effect of the power difference, a two echo scenario is created. The first echo arrives at $t = 10$ ms and the second at $t = 40$ ms, shown in Fig. 5.17a. The second echo is 10 times stronger (20 dB higher signal power). Both echos are LFM signals with $T = 100$ ms and $BW = 7500$ Hz. The MF output for the two echo signal is shown in Fig. 5.17b. The MF is implemented using the cross-correlation function and echo 1 is used as the reference. Therefore, the first peak in Fig. 5.17b at $\tau = 60$ ms has a 0 dB amplitude and the second peak has a 10 dB value at $\tau = 90$ ms (MF outputs are normalized by the signal power of the echo 1). Figures 5.17c-5.17f show the PCI processed signals and the corresponding MF outputs. Figures 5.17c-5.17d are obtained using $r = 3$ and Fig. 5.17e-5.17f with $r = 4$. With the given power difference, PCI can separate the two echos and can nearly completely remove the second echo from $\mathbf{y}$. The residual edge effects are still visible in both Fig. 5.17c and Fig. 5.17e, but otherwise echo 1 is clearly visible. Additionally, the MF peak for the first echo is unchanged, meaning that the first $3 - 4$ large singular values do not contain information about echo 1.

The first 10 singular values of a PCI block withholding both echos are shown in Fig. 5.18. The figure shows two scenarios. The first one with circle marks corresponds to the echo power difference used earlier in Fig. 5.17. The second curve in red is obtained by lowering the power difference to 14 dB.

In the first scenario the power difference splits the singular values into two groups. The first four belonging to echo 2 and the second four to echo 1. Earlier, in Fig. 5.13, the largest singular value for the LFM signal was equal to 72. In fact, the first four LFM singular values from Fig. 5.13 are nearly identical to singular values $5 - 8$ of $P_2 = 20$ dB. The first eight singular values are extra brought out in Table 5.1.

The SVs of echo 2 are 10 times bigger than those of echo 1. In case of $P_2 = 20$ dB, the SVs of echo 2 and echo 1 are nicely separated. This also explains the PCI requirement number one, that said that the reverberation signal should be more powerful than the signal and noise. As long as the singular values of

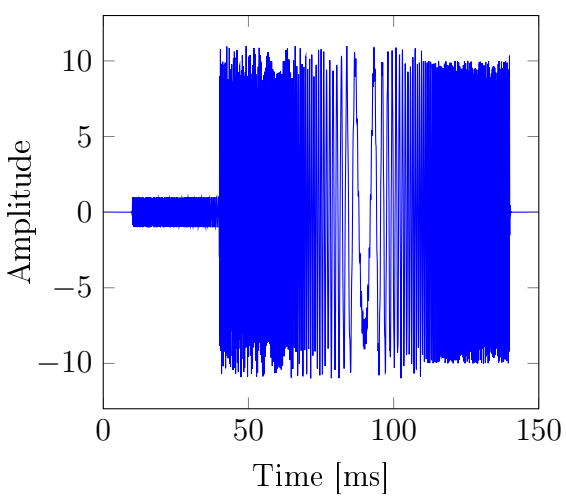

(a) Re{**y**}

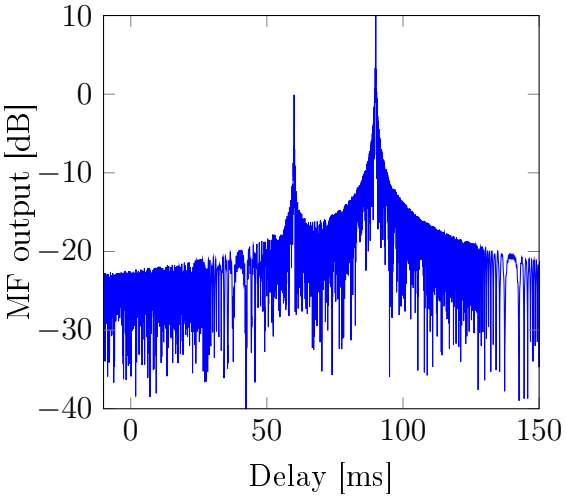

(b) Original MF output

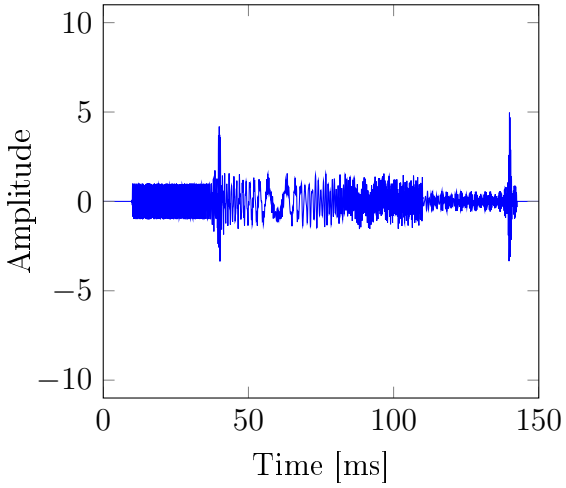

(c) Re{$\mathbf{y} - \mathbf{y}^r$}, $r = 3$

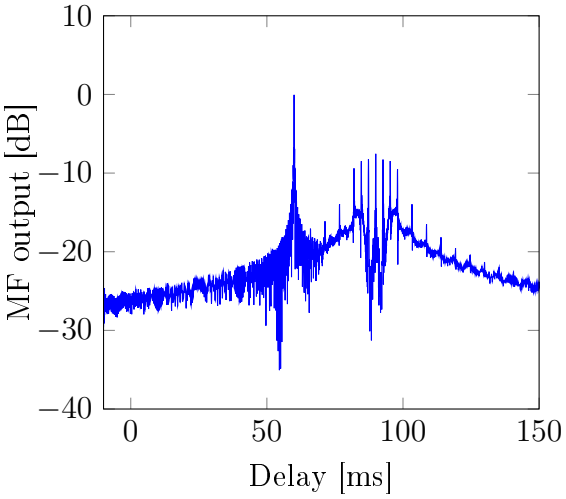

(d) MF output after PCI with $r = 3$

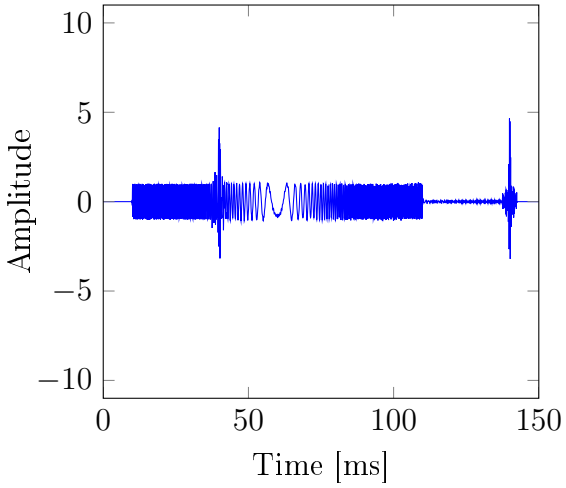

(e) Re{$\mathbf{y} - \mathbf{y}^r$}, $r = 4$

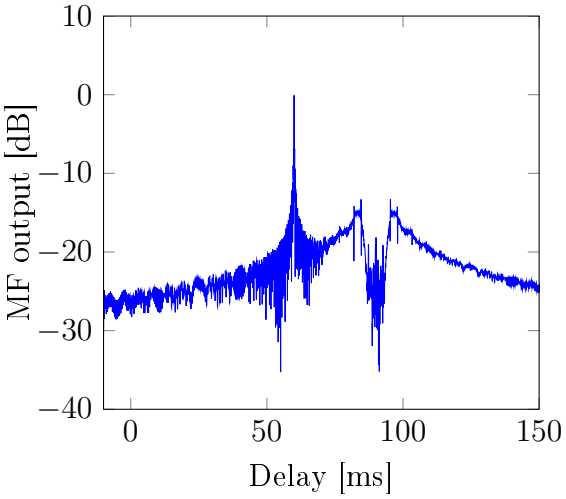

(f) MF output after PCI with $r = 4$

Figure 5.17: Time signals and the corresponding MF outputs.

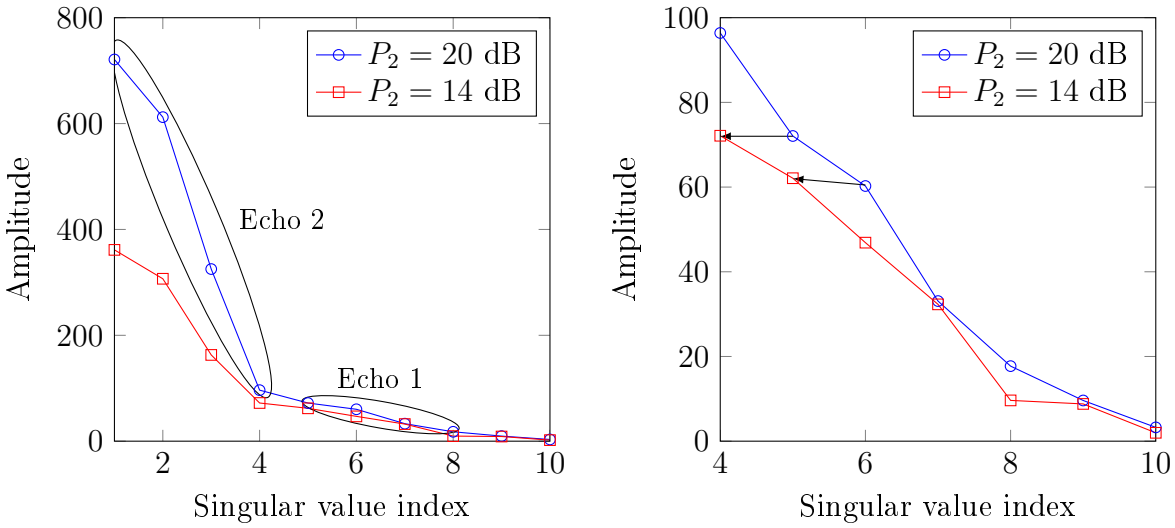

(a) Singular values $1 - 10$

(b) Singular values $4 - 10$

Figure 5.18: Influence of power difference to SV ordering.

Table 5.1: Eight largest singular values from Fig. 5.18

	Singular value index r							
P_2 [dB]	1	2	3	4	5	6	7	8
20	721	612	325	96	72	60	33	18
14	361	306	163	72	62	47	32	10

the interfering signal are the r largest ones, then the PCI algorithm can "easily" remove them. However, as the power difference decreases, the order of the SVs changes. In the $P_2 = 14$ dB case, the SVs of echo 2 are halved and with that the fourth SV is no longer the 4th largest, but the 6th largest SV. As the power of echo 1 stayed unchanged, then it's corresponding SVs did not reduce and earlier 5th and 6th SVs became the 4th and 5th, illustrated in Fig. 5.18b. This means that if for the $P_2 = 14$ dB case, the PCI would remove $r = 4$ largest SVs, then it would already also remove a large part of echo 1. The power difference does not alter the number of relevant SVs, it only changes their order and the order determines how simple it is to separate the interference from the rest. Hence, theoretically even with equal echo powers, the two signals could be separated. A more crucial constraint is the frequency difference between the interfering signal and the rest.

5.2.5.3 Frequency Difference

We are again assuming a two echo scenario. The two signals can be separated as long as the arrival delay τ between the two signals is greater than the PCI block length L. The scenario with $\tau = L$ is illustrated in Fig. 5.19.

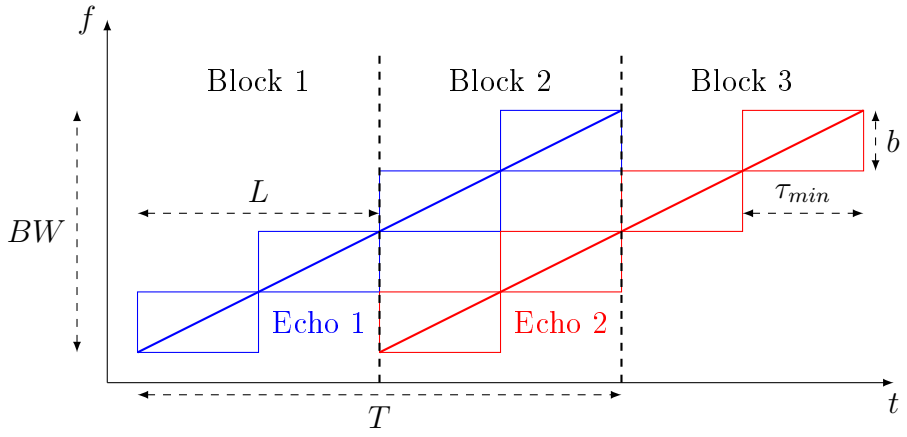

Figure 5.19: Illustration of PCI blocks with two echos apart by $\tau = L$.

As long as the delay between the arriving signals is larger than L, then the frequency ranges of the two signals in a given block (e.g. block 2) do not overlap and the individual signal components are represented by unique singular values. As the delay reduces beyond L, the SVD merges the frequency components that are present twice. Therefore, in order to improve the range resolution, L has to be decreased. However, the range resolution can not be made arbitrarily small. The intrinsic bandwidth represents the minimum bandwidth needed to separate two LFM signals, hence the minimum arrival delay τ_{min} corresponds to the signal duration when the instantaneous frequency increases by b,

$$\tau_{min} = b \cdot \frac{T}{BW} \ . \tag{5.29}$$

For a signal with $T = 100$ ms, $BW = 7500$ Hz, and $f_s = 20$ kHz, $\tau_{min} = 3.65$ ms $= 73$ samples. Basically, the block length could be reduced below τ_{min}, but doing so does not improve the signal separation.

The effect of decreasing τ (given in samples) to the singular values are shown in Fig. 5.20. The scenario uses two LFM signals with equal power (identical to P_2). The main reference is the blue curve with circle marks that corresponds to $\tau \geq L$, $L = 200$ samples. There are 8 larger singular values, two groups of four SVs. Theoretically, the two signals can still be perfectly separated. Lowering the delay below L, reduces the number of relevant SVs. For $\tau = 150$ samples, the last larger SV is 7th, for $\tau = 120$ it is 6th

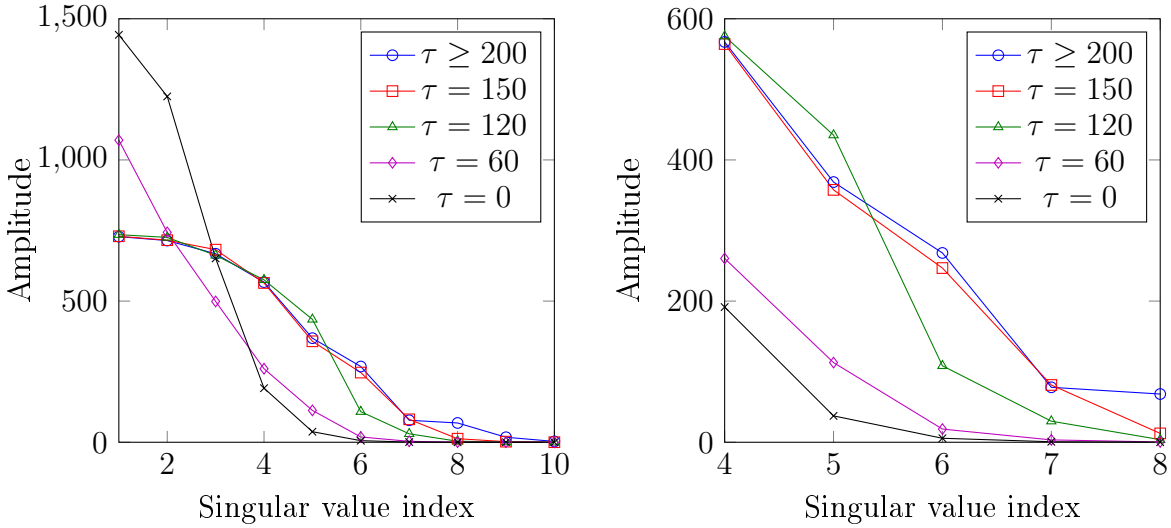

(a) Singular values $1 - 10$

(b) Singular values $4 - 8$

Figure 5.20: Influence of the arrival delay (given in samples) to the singular values.

and for $\tau = 60$ it is 5th. Finally for $\tau = 0$, the two signals are coherently added and the amplitude is doubled, leaving four bigger singular values with doubled amplitudes. Effectively, as τ decreases below L, the SVD merges the twofold present signal components, reducing the number of unique SVs.

Therefore, in order to separate the reverberation from the received signal, first of all the signals in a PCI block should not have common frequency components and the frequency distance should be minimally b. Secondly, the interference signal should be more powerful than the rest to assure easier separation. Based on this it can be concluded that the PCI is better suited for shorter signals – lower number of reflections in a PCI block, and for channels that are dominated by spatially separated strong reflectors. In such scenario, each PCI block has a small number of relevant SVs and a large portion of the reverberation is represented by the r biggest SVs. With this knowledge it becomes clear that the PCI is not well suited for the reverberation channel model described in Sec. 5.1.2. Given such a channel, each PCI block will have around T/L sets of significant singular values that would mean for the LFM signal with $r = 4$ around 40 SVs. Four out of the 40 SVs will correspond to the target echo plus the reverberation from the same distance, but their ordering will be random, due to the Rayleigh distributed scattering amplitudes. Even if we could determine the right SVs, the range resolution τ_{min} of the PCI algorithm is much larger than the range resolution of the MF, determined by the coherence time T_c. Therewith, for such a channel model, the PCI algorithm can not effectively separate the reverberation from the target echo.

The PCI could be used to separate CW signals with different center frequency. Exemplary, extracting the dominant stationary reverberation from the received signal and therewith improving the visibility of the moving targets. However, as it has been shown earlier, the same can be achieved with bandpass filtering or with a proper MF. The fact that the PCI algorithm can separate LFM signals is indeed very attractive, but has severe constraints. Only a few LFM signals should be overlapped, to assure a low number of singular values for a PCI block and the signals have to be separated in frequency. One possible usage would be to remove strong stationary objects from the received signal – check the constraint P and remove signal components that are too powerful for target echo plus noise, as used in [TKK82, GJ02]. Yet, a similar effect can be achieved with tracking that neglects strong stationary contacts (objects). The

PCI has specific usages, but serves not as an all around solution for reverberation suppression.

5.3 Simulation Results

The introduced MF and energy detection algorithms are compared via simulations. First, the simulation results for a noise limited channel are presented, showing the advantage of the MF detector. In the second subsection the focus is on signal selection for a reverberation limited channel. Finally, a small summary for signal selection is given.

Two modifications are done to the channel and the detector algorithms – the channel model is made range independent and the CFAR algorithm has been replaced. It was mentioned before that the received signal experiences an increasing transmission loss. One possibility to mitigate the effect, is to precompensate the transmission loss at the receiver side by increasing the receiver gain over time. The other possibility is to use the CFAR algorithm as it inherently compensates for the transmission loss (cf. Fig. 5.5), by averaging over both the leading and the lagging reference window. (The two-reference-window compensation or averaging method is sometimes also called normalization [Mor87].)

However, as the transmission loss is not a linear function, but an exponential function, the average noise power estimate is not unbiased. Hence, for the simulation results the channel is altered to become range independent, i.e. a system with perfect normalization. The goal of the simulations is to compare different detectors in a reverberation limited environment and to give a general performance comparison simply based on the SRR. By removing the range dependent components from the channel, the performance results are no longer affected by the selected target range, transmission loss calculation, nor the target/reverberation strengths. This means the results depend on a single variable, the SRR, and not on any specific parameter selection.

Additionally, due to the non-straightforward CA-CFAR threshold calculation, caused by the various distributions of the signal energy and MF output, the CFAR will be replaced by a maximum level comparison algorithm, to decide between positive target detection or false alarm. Decision is done comparing target vs. maximum interference level. A positive detection is declared if the target response is 1 dB higher than the maximum interference response over 100000 samples. Utilizing the exact knowledge about the target position, together with the range independent channel, this direct comparison algorithm provides for all detectors and signals a identical detection criterion and the threshold levels need not to be manually adapted.

5.3.1 Noise Limited Channel

The detection probabilities in noise limited channel are shown in Fig. 5.21.

The simulations are done for CW, LFM, and cutFM signals, with energy and MF detectors. The results are obtained with the following system parameters: $f_c = 70$ kHz, $T = 100$ ms, and frequency modulated signals have a $BW = 7.5$ kHz. The cutFM signal used in the simulations is with $D = 1/4$, $i = 1$. The signal energies are normalized to $E_s = 1$ for all $T = 100$ ms pulses. The given SNR is before the detector and the receiver pre-filter has a 7500 Hz bandwidth around the center frequency.

The simulation results confirm the expectations. For FM and cutFM the energy detector achieves an error free detection around SNR $= -3$ dB. This is a reasonable result, as at SNR $= 0$ dB the noise and desired signal have equal energies and hence, at the target position the superimposed energy level can be clearly distinguished against the background noise level. Eventually, the noise becomes dominant and reliable detection is no longer possible. For the CW signal, reliable detection is possible until an SNR of -13 dB. A result of reducing the bandpass filter -3 dB bandwidth from 7500 Hz to 50 Hz (-60 dB stopbands at $f_c \pm 200$ Hz).

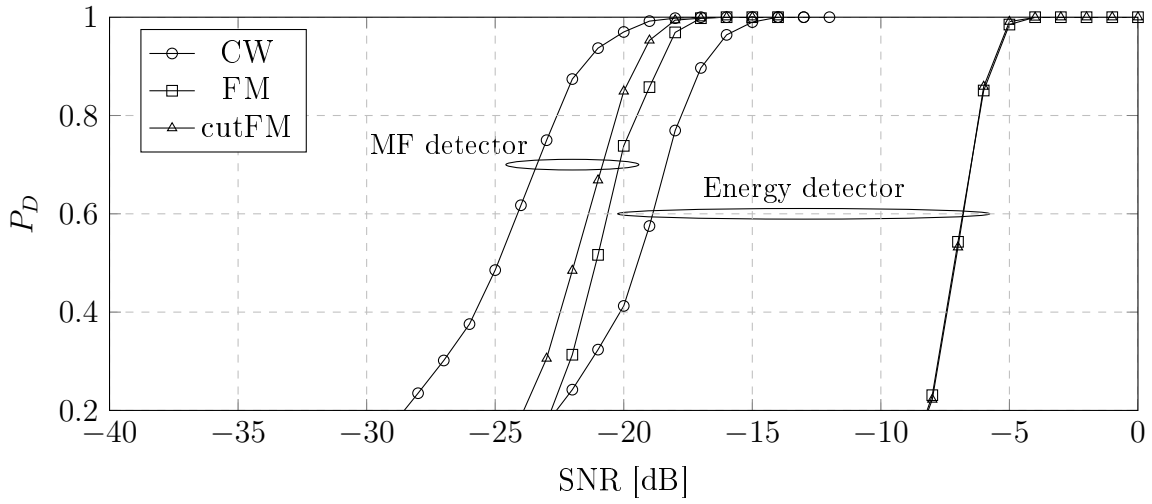

Figure 5.21: Energy and MF detector detection probabilities for CW, LFM, and cutFM signals vs. SNR.

The MF results for all three signals are close together. As expected, the MF brings a significant gain for the frequency modulated signals, improving the detection performance by around 13 dB. For the CW pulse the improvement is only around 4 dB and can be explained by the fact that the noise filter bandwidth of the energy detector is not ideal, but has a wider bandwidth than the minimum ($1/T$) required, caused by the 70 kHz center frequency. A problem of bandpass processing that could be alleviated by performing the processing in baseband (shifting the center frequency from 70 kHz to 0 Hz). Most importantly, the MF shows good performance for all pulse selections.

According to Fig. 5.21, the CW appears to have the best performance in noise, but the signals with larger bandwidth benefit from pulse compression. Exemplary, two-target noise limited MF outputs for all signals are shown in Fig. 5.22.

The sub-figures on the left side show MF outputs for two targets at 100 m distance. CW presents two wide correlation peaks close next to each other, but still separable. At the same time for LFM and cutFM the two responses are well apart. For LFM each target has a single thin peak, while cutFM additionally presents periodic range ambiguities (cf. Sec. 4.4). Clearly, for LFM and cutFM the distance between the targets could be significantly reduced. The minimum distance, d_{min}, for frequency modulated signals can be calculated from the coherence time

$$d_{min} = \frac{1}{2} c T_c = \frac{1500}{2BW} \ . \tag{5.30}$$

The factor 1/2 stems from the two-way propagation and therewith for $BW = 7500$ Hz, $d_{min} = 0.1$ m. MF results for $d = 0.1$ m are shown on the right. LFM and cutFM present two distinguishable peaks next to each other. The cutFM signal has preserved the fundamental range resolution of the LFM base signal. Concerning the CW signal, in order to reach such range resolution, the signal duration has to be reduced by a factor of 1000, to $T = 0.1$ ms. The CW result in Fig. 5.22b looks very similar to the LFM plot in Fig. 5.22d, but the signal energy for the CW has reduced by −30 dB. In order to compensate for the reduced signal energy, the SNR has been increased by 30 dB from −12 dB to +18 dB, to have a comparable detection capability as for the frequency modulated signals.

Figure 5.22f illustrates the fact that even when cutFM has periodic range ambiguities, the targets can be distinguished also at very close distances. The receiver can utilize the a priori knowledge about the positions of the periodic ambiguities and therewith differentiate between neighboring target peaks and periodic ambiguities.

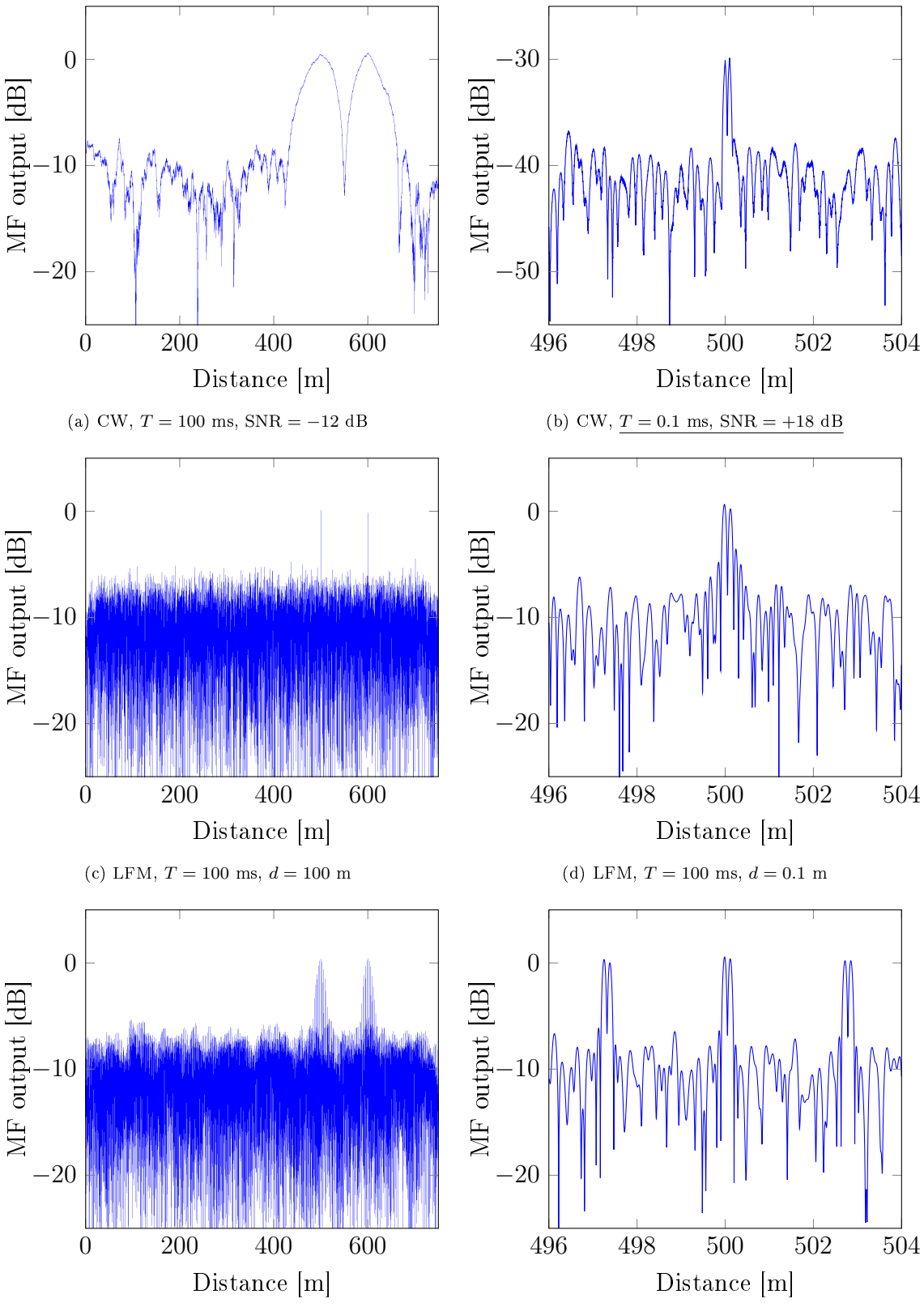

(a) CW, $T = 100$ ms, SNR $= -12$ dB

(b) CW, $T = 0.1$ ms, SNR $= +18$ dB

(c) LFM, $T = 100$ ms, $d = 100$ m

(d) LFM, $T = 100$ ms, $d = 0.1$ m

(e) cutFM, $T = 100$ ms, $d = 100$ m

(f) cutFM, $T = 100$ ms, $d = 0.1$ m

Figure 5.22: Two-target MF outputs, $d = 100$ m on the left and $d = 0.1$ m on the right.

In case the transmitter has a fixed maximal output power, the cutFM signal suffers a −3 to −10 dB SNR penalty, due to the reduced signal energy caused by the cut out signal sections and the selected $w_1(t)$ windowing function. However, if the maximum output power is limited by cavitation, then the transmission pauses should enable the system to use a higher output power before reaching cavitation.

For the noise limited channel an LFM or HFM signal with a MF detector provides very good performance in all situations: single target, multiple targets, moving targets, multipath channels. However, in reverberation limited channels the same signal and detector combination reaches it's limit.

5.3.2 Reverberation Limited Channel

When dealing with a noise limited channel, if the SNR is too low for successful detection, the solution is to increase the signal energy. For a reverberation limited channel the main means to improve the detection, is to utilize the Doppler effect to suppress the reverberation. The effect of Doppler processing is visualized in Fig. 5.23. In these examples, the target is moving with 0.3 m/s towards the receiver, the reverberation is assumed to be stationary and the scatterers are uniformly distributed over the range.

An HFM (or LFM) signal with $T = 100$ ms and $BW = 7500$ Hz is detectable until an SRR of −12 dB. The HFM signals are Doppler invariant and hence, the receiver can not use Doppler processing to better separate the moving target from reverberation. However, when a Doppler selective transmit signal like cutFM or SFM is used, then at the receiver side the reference signal in the MF can be Doppler shifted to provide a Doppler processing gain. Figures 5.23b-5.23e show how the MF output alters as the v_{ref} increases from 0.3 m/s to 0.89 m/s. Two effects can be observed. Most importantly, with increasing v_{ref}, the reverberation level after MF is reduced. However, at the same time also the peak target level reduces, but at a lower rate. As a result, the target response becomes more and more prevailing as v_{ref} increases. The reduction of the peak target level corresponds to the SNR loss or the performance degradation in noise limited channels discussed in Sec. 4.6. Namely, for $v_{ref} = 0.5$ m/s the peak level is at −1.6 dB, for $v_{ref} = 0.7$ m/s at −6 dB and for $v_{ref} = 0.89$ m/s at −13.5 dB. Therefore, even though for $v_{diff} = 0.3$ m/s the maximum reverberation suppression is achieved at $v_{ref} = 0.89$ m/s (cf. Table 4.2), unless the full gain is needed, a lower v_{ref} selection would improve the systems performance against noise. Hence, for real channels, it is best to measure the noise and reverberation levels and adapt the receiver accordingly.

The Doppler processing gain allows the receiver to reliably detect the target at much challenging channel conditions. Figure 5.23f shows the MF output with $v_{ref} = 0.89$ m/s and SRR = −36 dB. Even at 24 dB lower SRR the target is clearly visible.

A comparison of detection probabilities of various transmit signals at a certain SRR is shown in Fig. 5.24. In the simulations, the signal energy is normalized to unity and the SRR is controlled by changing the reverberation backscatter strength. First of all, three general conclusions can be drawn from the results:

1. Up to a certain SRR, in this case around an SRR of −12 dB, the system with HFM can detect all moving targets in a reasonable velocity range (with LFM, the exact SRR value would depend on the target velocity and the corresponding loss in the maximum cross-correlation value (cf. Fig. 3.28)). This operating point is important, as until the SRR is sufficient for HFM to reliably detect the target, it provides the best possible range resolution with minimal ambiguities. Moreover, only a single reference signal is needed to cover the velocity range of interest.

2. In case the SRR is lower than that required by the HFM signal, the performance can be improved by utilizing Doppler selective signals like cutFM and SFM in conjunction with reverberation processing.

3. Depending on the relative velocity difference (v_{diff}) between the reverberation and the target, significant performance gains (reliable detection at as low as −55 dB SRR) can be achieved, by

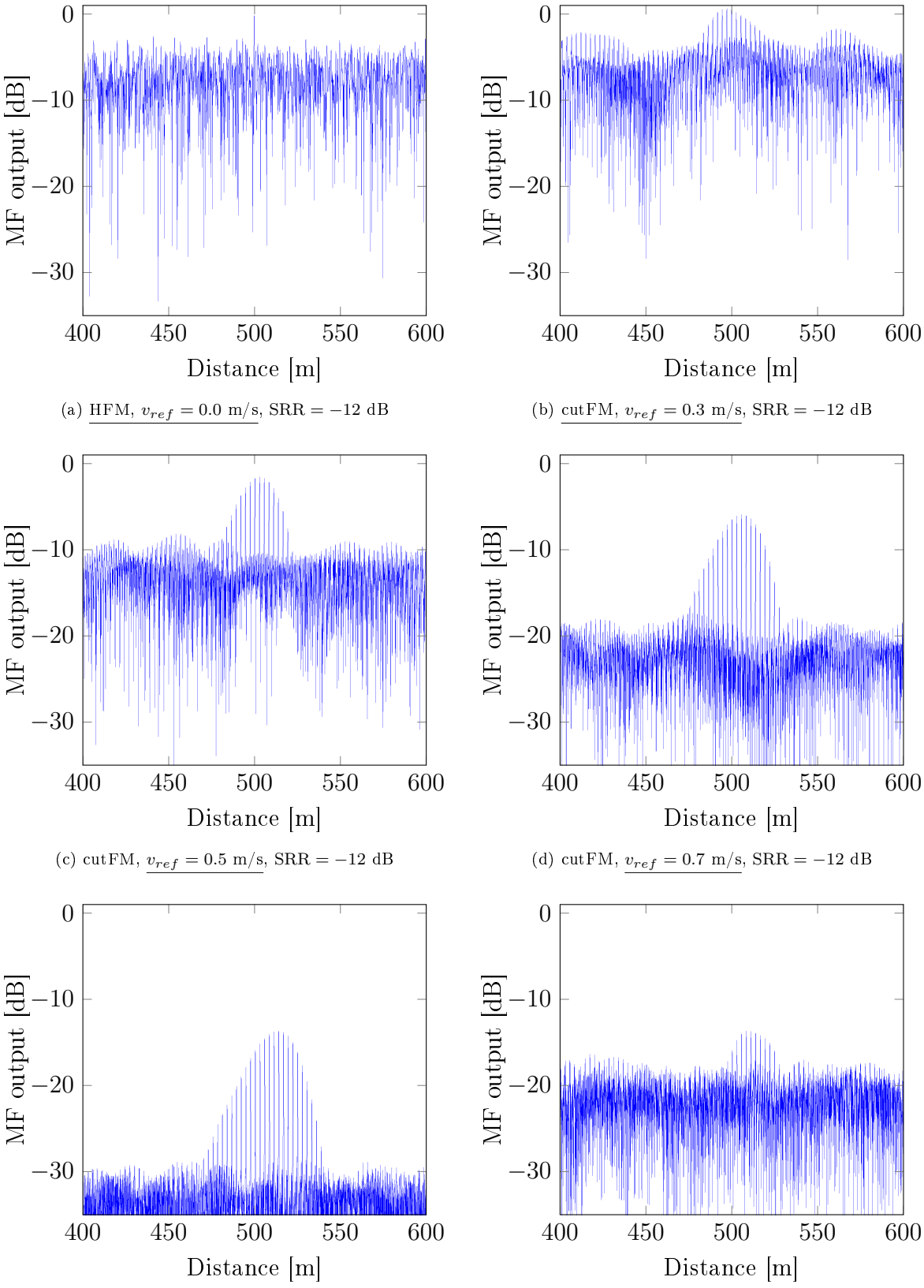

(a) HFM, $v_{ref} = 0.0$ m/s, SRR $= -12$ dB

(b) cutFM, $v_{ref} = 0.3$ m/s, SRR $= -12$ dB

(c) cutFM, $v_{ref} = 0.5$ m/s, SRR $= -12$ dB

(d) cutFM, $v_{ref} = 0.7$ m/s, SRR $= -12$ dB

(e) cutFM, $v_{ref} = 0.89$ m/s, SRR $= -12$ dB

(f) cutFM, $v_{ref} = 0.89$ m/s, SRR $= -36$ dB

Figure 5.23: Visualization of Doppler processing.

optimizing the MF reference signal's velocity shift. The optimization is done to maximize the difference of the MF response levels between the target and the reverberation.

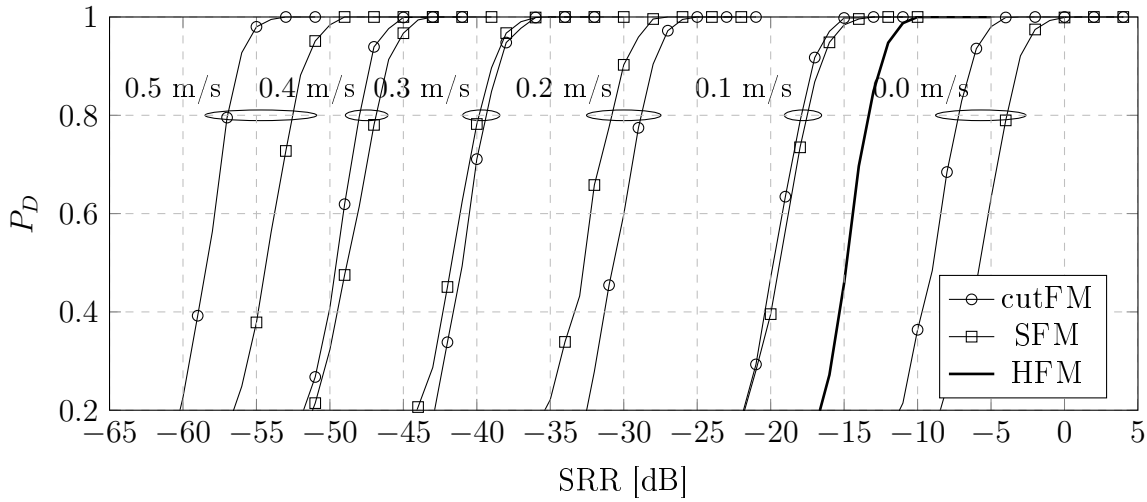

Figure 5.24: Detection probabilities for cutFM, SFM, and HFM signals vs. SRR, for various target and reverberation velocity difference, v_{diff}.

Secondly, a comparison between the Doppler selective cutFM and SFM signals can be made. The cutFM and SFM show similar performance for the selected v_{diff} values, with cutFM having a slight edge. Tab. 5.2 gives the SRR values when the detection probability reaches 95%. Both signals significantly

Table 5.2: SRR values for cutFM and SFM, at $P_D = 0.95$

v_{diff}	0.0	0.1	0.2	0.3	0.4	0.5
cutFM	-5.6	-16.4	-27.3	-37.9	-46.7	-55.5
SFM	-2.4	-15.9	-29.1	-38.2	-45.3	-51.0

improve the detection probability of a moving target against reverberation. Comparing tables Tab. 4.2 and Tab. 5.2, the estimated processing gains from the Q-function quite well comply with the simulation results. However, according to the Q-function analysis results in Table 4.2, SFM should be superior till $v_{diff} \leq 0.5$ m/s, but in the simulation results SFM signal has better performance only for 0.2 m/s and 0.3 m/s, otherwise cutFM is superior.

The disparity can be explained by the narrower ACF width of the cutFM signal (cf. Fig. 5.25). Due to the superposition of numerous reflections, the wider width of the SFM signal's ACF leads to an increased probability for a higher reverberation peak that degrades the detection performance. For the same reason, HFM with its minimum ACF width has the best performance for $v_{diff} = 0.0$ m/s. All of the above results are for a single target scenario. In case of multiple objects/targets, the cutFM signal would further benefit from its superior ACF width and peak separation.

In summary, for noise limited channels HFM or LFM signals provide the best range resolution and only a single reference signal is needed to cover the velocity range of interest. For reverberation limited channels, the signal selection is a bit more complicated. As long as the SRR is not to low, the HFM or LFM signals are still a good choice. In situations, where the SRR is beyond this threshold, a Doppler selective signal can be used to improve the target vs. reverberation separation. Signals like cutFM and SFM, provide significant Doppler processing gains and are capable of reliable target detection at SRR

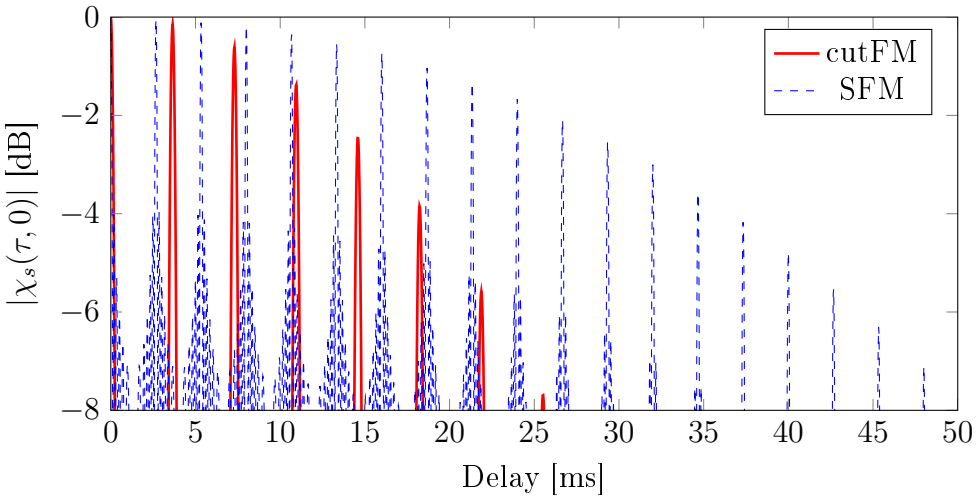

Figure 5.25: ACF width comparison between cutFM and SFM.

as low as −55 dB or even lower. The Doppler processing gains of cutFM and SFM signals are nearly the same with slight edges to either sides, but at the same time the cutFM signal provides a 50% lower auto-correlation width (cf. Fig. 5.25). Confirming the hypothesis that the range resolution of a Doppler selective signal can be improved by using a frequency modulated pulse as the base signal.

Chapter 6

Summary

The main goal of this thesis is to investigate transmit signal designs from the perspective of diver detection and to develop a new signal with improved properties.

The focus was set on the challenging scenario of diver detection in reverberation limited environments, like harbors and coastal areas. The ideal transmit signal for diver detection would be able to suppress stationary reverberation and would at the same time provide very good range resolution to discriminate between any moving object in the vicinity.

In Chapter 3 existing signal designs are thoroughly analyzed. It comes out that all existing designs have their flaws. The CW signal can provide the necessary Doppler selectivity, but it comes at the cost of range resolution. On the other hand FM signals are nearly perfect: very good range resolution, low receiver complexity due to the requirement of only a single reference signal to cover the velocities of interest and it is relatively robust from implementation aspect. It only lacks the Doppler selectivity. This leads to the idea to alter an FM signal in a way to make it Doppler selective and to preserve as much of its advantages as possible.

FM signals are (nearly) Doppler invariant. This property can be attributed to its continuous frequency function. For any Doppler frequency shift the frequency components of the original signal and the Doppler shifted signal are still largely the same. It is shown that a wide-band Doppler selective signal needs to have a comb spectrum, with gaps between the peaks. In order to achieve this with an FM based signal, the idea is to periodically cut out parts of the pulse. The design is called the cutFM signal. In Chapter 4 the properties of the cutFM signal are thoroughly analyzed and it is shown that if the signal properties are carefully selected, the spectrum will become comb like and the signal Doppler selective. The key is in selecting the appropriate cutting period that overlaps the uncut and new frequency components. Based on the analysis, an overview of the influence of the signal parameters to the Doppler selectivity (based on the Q-function) is given. These guidelines are then used to create a diver detection system that (with two reference signals) covers the velocities from 0.3 m/s to around 2.0 m/s, while suppressing the stationary reverberation by at least 20 dB. From this design process it became clear that it is not obvious what are the optimal reference signal velocity shifts given a velocity difference between the target and the reverberation. The optimal values are found using the Q-function and the corresponding maximum theoretical Doppler processing gain estimates are brought out.

In order to confirm the Doppler processing gains, a reverberation limited channel model is introduced and using appropriate detector schemes the signals are compared via simulations. In the comparison of square-law, energy and matched filter detectors, the matched filter detector is shown to be the most efficient choice and in noise limited channels the matched filter is the optimal detector that maximizes the SNR for any transmit signal. Concerning reverberation limited channels, the matched filter is no

longer optimal and therefore the principle component inverse (PCI) detector is investigated as a possible improvement. The analysis shows that even as the PCI detector has attractive capabilities and specific use cases, it is not generally applicable to separate reverberation from the received signal.

Finally, cutFM is directly compared with SFM. The SFM signal is another viable Doppler selective signal that also causes a wideband pulse, but based on the CW waveform. The two show similar Doppler processing gains, enabling reliable detection at an SRR as low as -55 dB or even lower. However, while having the same Doppler selectivity, cutFM has only half of the ACF width of the SFM signal, that translates into a 50% improved range resolution, especially for multipath environments. Unfortunately, in the course of this work, the performance of the cutFM signal could not be tested in practice and the results are limited to simulations only. It would be very interesting to see the waveform in usage.

In conclusion, there is no perfect signal. A trade-off has to be made between range resolution and Doppler selectivity. The signal selection should be based on the channel conditions and the waveforms capabilities. A good diver detection system is adaptive and utilizes multiple transmit signals to capitalize on their strengths.

Appendix A

Supplementary Results

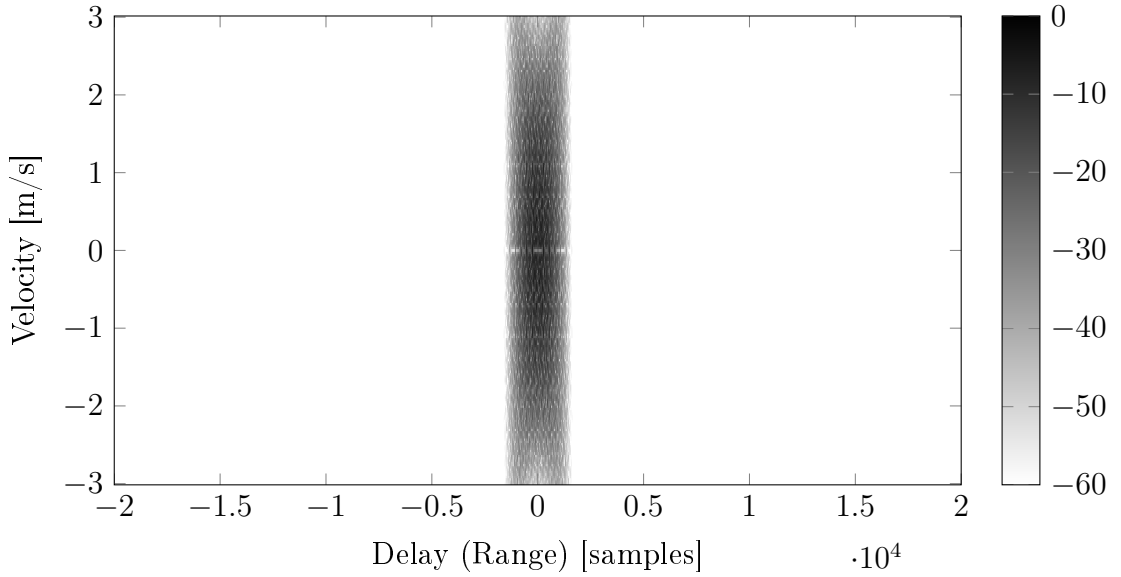

Figure A.1: Ambiguity diagram of a Hann windowed sub-pulse Costas code signal with $T = 100$ ms, $BW = 7500$ Hz, and code length $N = 10$.

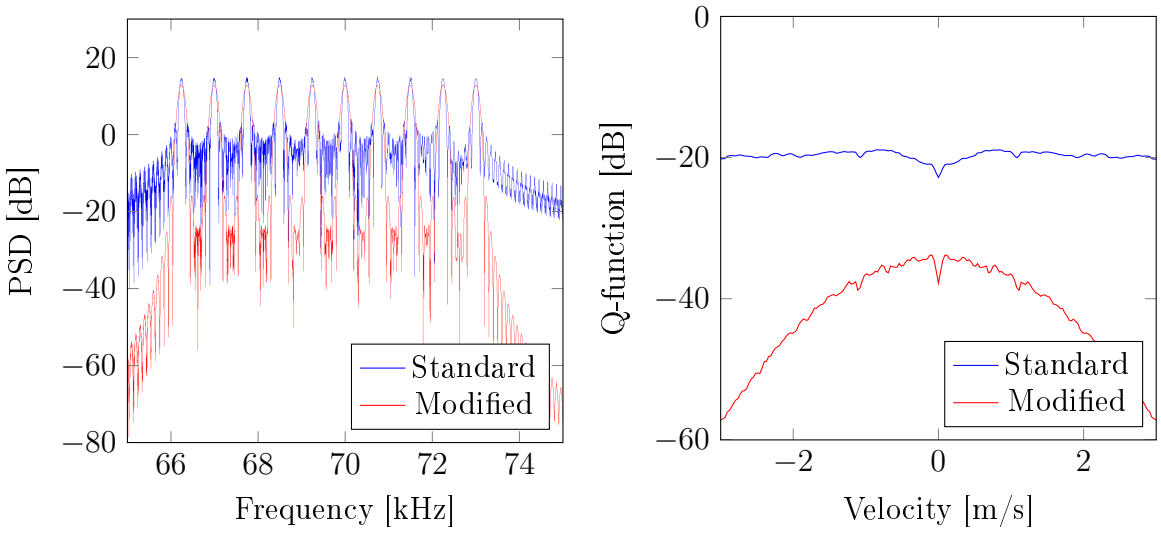

(a) PSD (b) Q-function

Figure A.2: Characteristic plots for a Hann windowed sub-pulse Costas code signal with $T = 100$ ms, $BW = 7500$ Hz, and code length $N = 10$.

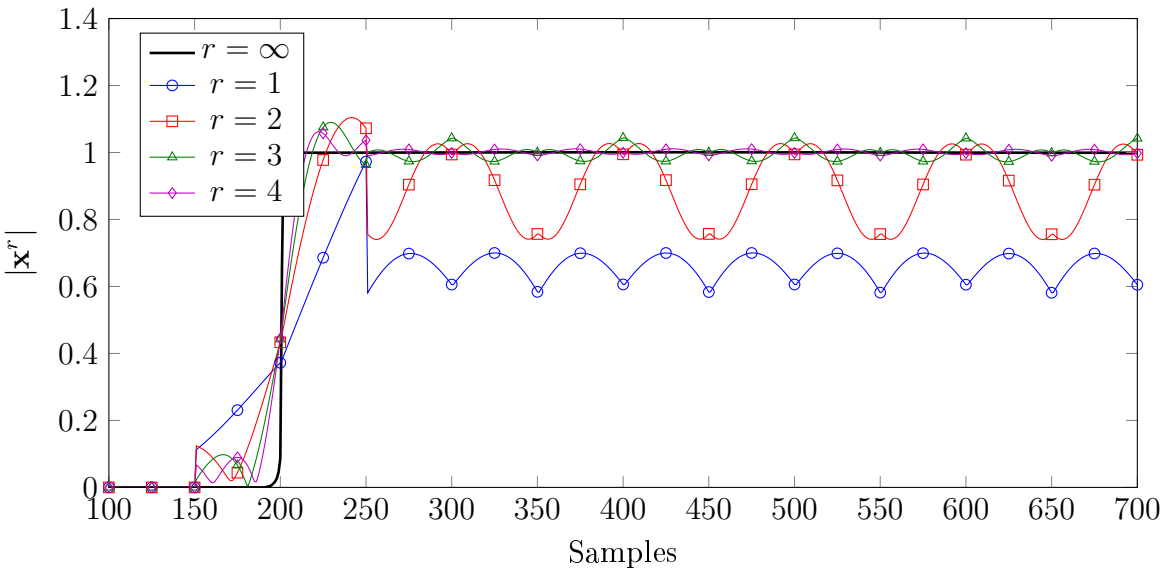

Figure A.3: PCI signal evolution for a complex-valued LFM waveform with increasing rank r.

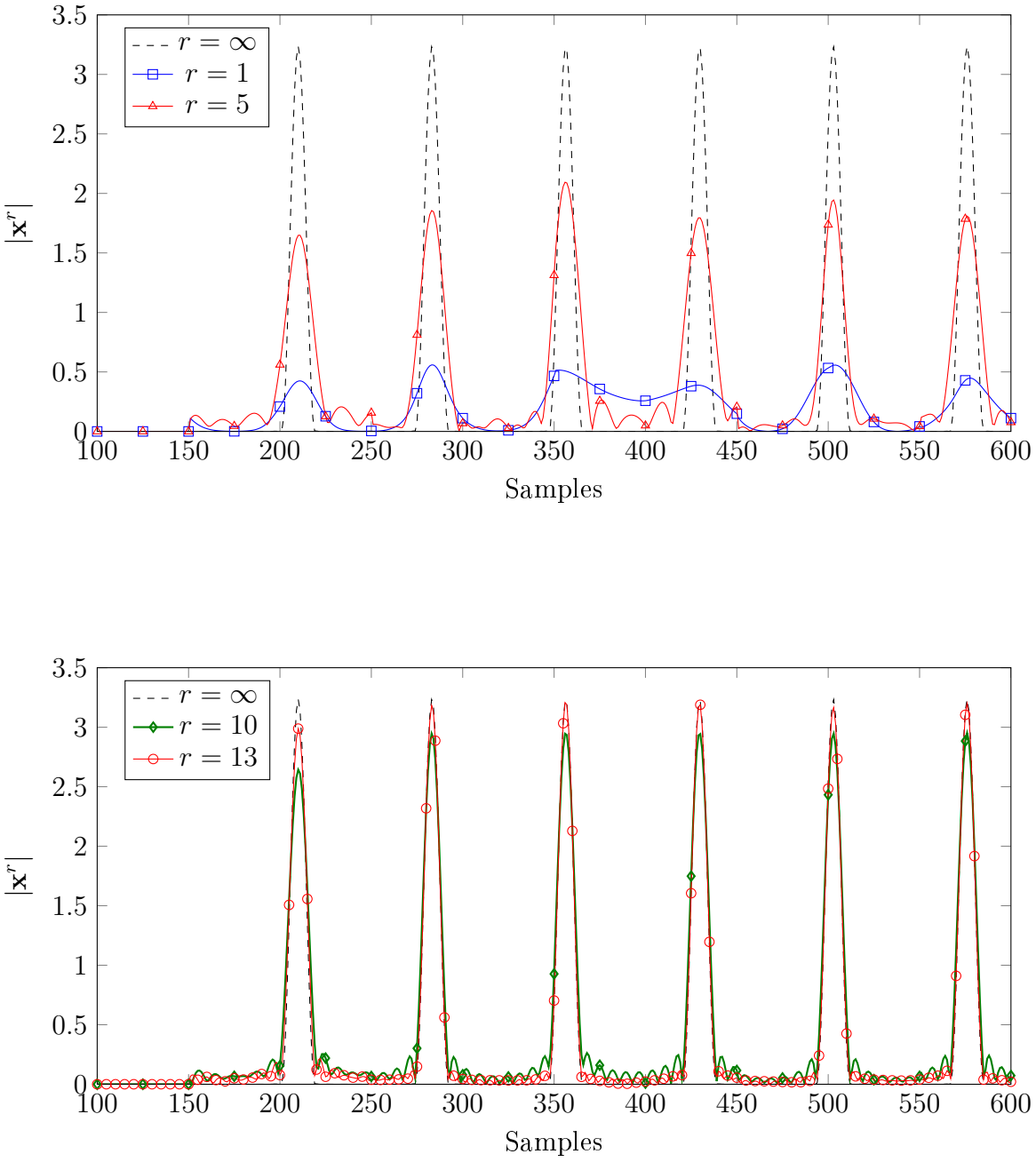

Figure A.4: PCI signal evolution for a complex-valued cutFM waveform with increasing rank r.

Appendix B

Notation

Functions and Operators

$\mathrm{x}(\cdot)$	Function with continuous argument $\cdot$
$\mathrm{x}[\cdot]$	Function with discrete argument $\cdot$
$\mathbb{X}$	Set
$\circ$	Code concatenation
$*$	Convolution
$**$	Cross-correlation
$\propto$	Proportional to
$(\cdot)^*$	Complex conjugate of a variable
$(\cdot)^D$	Doppler shifted variable
$\arg\max(\cdot)$	Argument of the maximum
$\cos(\cdot)$	Cosine function
$\delta(\cdot)$	Dirac impulse
$\exp(\cdot)$	Exponential function
$\mathcal{F}\{\cdot\}$	Fourier transform
$\ln(\cdot)$	Natural logarithm
$\log_{10}(\cdot)$	Logarithm to the base 10
$\max(\cdot)$	Maximum
$\min(\cdot)$	Minimum
$(\cdot) \bmod (\cdot)$	Modulo operator
$\sin(\cdot)$	Sine function

Abbreviations

ACF	Autocorrelation function
AWGN	Additive white Gaussian noise
BPSK	Binary phase-shift keying
CA-CFAR	Cell-averaging constant false-alarm rate
CFAR	Constant false-alarm rate
CUT	Cell under test
cutFM	Cut frequency modulation
CW	Continuous wave
DDS	Diver detection sonar
EFM	Exponential frequency modulation
FM	Frequency modulation
HFM	Hyperbolic frequency modulation
LFM	Linear frequency modulation
LPM	Linear period modulation
MF	Matched filter
MLS	Maximum length sequences
MSE	Mean squared error
OS-CFAR	Ordered statistics constant false-alarm rate
PAPR	Peak-to-average power ratio
PCI	Principle component inverse
PCR	Pulse compression ratio
PRN	Pseudo-random noise
PSD	Power spectral density
PSL	Peak sidelobe level
SFM	Sinusoidal frequency modulation
SNR	Signal-to-noise ratio
SRR	Signal-to-reverberation ratio
SSP	Sound speed profile
SV	Singular value
SVD	Singular value decomposition

List of Variables

A	Spreading coefficient
α	Attenuation coefficient
β	Modulation index of SFM signal
b	Intrinsic bandwidh
BS	Backscattering strength
BT	Time-bandwidth product
BW	Bandwidth
c	Speed of sound
$\chi_s(\tau, f_D)$	Ambiguity funciton of a narrowband signal
$\chi_s(\tau, \eta)$	Ambiguity funciton of a wideband signal
d	Distance
D	Duty cycle
E_s	Signal energy
η	Doppler scaling factor
f^D	Doppler shifted frequency
f_{diff}	Frequency difference between neighboring sub-pulses
f_0	Starting frequency
f_c	Center frequency
f_D	Doppler frequency shift
f_m	Modulation frequency of SFM signal
f_r	Modulation frequency caused by cutting
$\hat{G}_{DP}$	Estimate of Doppler processing gain
ϕ	Angle of incidence
$Q_s(\eta)$	Q-function
r	Propagation range in meters
$R_x(\tau)$	Autocorrelation function
$R_{xh}(\tau)$	Cross-correlation function
T	Signal duration
T_c	Coherence time
T_r	Repetition period
T_w	Sub-pulse signal duration
τ	Delay
θ	Grazing angle
TL	Transmission loss
TL_s	Spreading loss
TS	Target strength
v	Radial signal velocity towards the receiver
v_{diff}	Velocity difference between the reverberation and target
v_{ref}	Velocity of the reference signal
$w_1(t)$	Sub-pulse window function
$w(t)$	Window function

Appendix C

Own Publications

M. Noemm, T. Wo, and P. A. Hoeher, "Multilayer APP detection for IDM," *Electronics Letters*, vol. 46, no. 1, pp. 96–97, Jan. 2010.

T. Wo, M. Noemm, D. Hao and P. A. Hoeher, "Iterative processing for superposition mapping", *J. Electrical and Computer Engineering*, vol. 2010, no. 6, pp. 1–13, Jan. 2010.

M. Noemm, P. A. Hoeher, and Y. Wang, "Phase allocation aspects of interleave-division multiplexing from PAPR prospective", in *Proc. IEEE Vehicular Technology Conference*, Budapest, Hungary, May 2011.

C. Knievel, M. Noemm, and P. A. Hoeher, "Low-complexity receiver for large-MIMO space-time coded systems", in *Proc. IEEE Vehicular Technology Conference*, San Francisco, USA, Sep. 2011.

M. Noemm, N. ul Hassan, P. A. Hoeher, and Y. Wang, "Channel coding for IDM: High-rate convolutional code concatenated with irregular repetition code", in *Proc. IEEE Globecom*, Houston, USA, Dec. 2011.

M. Noemm, A. Mourad, and P. A. Hoeher, "Superposition modulation with irregular convolutional coding", in *Proc. IEEE Globecom*, Anaheim, USA, Dec. 2012, pp. 2346–2350.

M. Noemm and P. A. Hoeher, “CutFM: A novel sonar signal design,” in *Proc. Future Security Conf.*, Sep. 2013.

M. Noemm and P. A. Hoeher, “CutFM sonar signal design,” *Applied Acoustics*, vol. 90, pp. 95 – 110, Apr. 2015.

Bibliography

[AdMH92] D. Alexandrou, C. de Moustier, and G. Haralabus, "Evaluation and verification of bottom acoustic reverberation statistics predicted by the point scattering model," *J. Acoustical Society of America*, vol. 91, no. 3, pp. 1403–1413, Mar. 1992.

[AG71] A. L. Anderson and G. J. Gruber, "Ambient-noise measurements at 30, 90, and 150 kHz in five ports," *J. Acoustical Society of America*, vol. 49, no. 3B, pp. 928–930, 1971.

[Ain10] M. A. Ainslie, *Principles of Sonar Performance Modelling.* Springer, 2010.

[Bar53] R. H. Barker, "Group synchronizing of binary digital systems," *in Communication Theory*, pp. 273–287, 1953.

[BF05] P. Borwein and R. Ferguson, "Polyphase sequences with low autocorrelation," *IEEE Trans. Information Theory*, vol. 51, no. 4, pp. 1564–1567, Apr. 2005.

[BT88] J. R. Bellegarda and E. L. Titlebaum, "Time-frequency hop codes based upon extended quadratic congruences," *IEEE Trans. Aerospace and Electronic Systems*, vol. 24, no. 6, pp. 726–742, Nov. 1988.

[BZHE93] M. H. Brill, X. Zabal, M. E. Harman, and A. Eller, "Doppler-based detection in reverberation-limited channels: effects of surface motion and signal spectrum," in *Proc. Conf. Oceans '93*, Oct. 1993, pp. I220–I224.

[CA98] T. Collins and P. Atkins, "Doppler-sensitive active sonar pulse designs for reverberation processing," *IEE Proc. Radar, Sonar and Navigation*, vol. 145, no. 6, pp. 347–353, Dec. 1998.

[CCHM09] A. Crawford, D. V. Crowe, D. Hopkin, and D. Maxwell, "Summary of the Maritime Force Protection Technology Demonstration Project Underwater Threats Component Build 1 Trial," Defence R&D Canada, Tech. Rep., Jun. 2009.

[CCR02] A. B. Carlson, P. B. Crilly, and J. C. Rutledge, *Communication Systems: An Introduction to Signals and Noise in Electrical Communication*, 4th ed. McGraw-Hill, 2002.

[CL77] M. Cohn and A. Lempel, "On fast M-sequence transforms," *IEEE Trans. Information Theory*, vol. 23, no. 1, pp. 135–137, Jan. 1977.

[CL94] H. Cox and H. Lai, "Geometric comb waveforms for reverberation suppression," in *Proc. 28th Asilomar Conf. Signals Systems Computers*, vol. 2, 1994, pp. 1185–1189.

[CM77] C.-T. Chen and F. J. Millero, "Speed of sound in seawater at high pressures," *J. Acoustical Society of America*, vol. 62, no. 5, pp. 1129–1135, Nov. 1977.

[Col96] T. Collins, "Active sonar pulse design," Ph.D. dissertation, The University of Birmingham, Nov. 1996.

[Cos84] J. P. Costas, "A study of a class of detection waveforms having nearly ideal range-Doppler ambiguity properties," *Proc. IEEE*, vol. 72, no. 8, pp. 996–1009, Aug. 1984.

[Dav70] W. D. T. Davies, *System Identification for Self-Adaptive Control.* Wiley-Interscience, 1970.

[Del74] V. A. Del Grosso, "New equation for the speed of sound in natural waters (with comparisons to other equations)," *J. Acoustical Society of America*, vol. 56, no. 4, pp. 1084–1091, Oct. 1974.

[DMCA07] P. H. Dahl, J. H. Miller, D. H. Cato, and R. K. Andrew, "Underwater ambient noise," *Acoustics Today*, vol. 3, no. 1, pp. 23–33, Jan. 2007.

[Ett96] P. C. Etter, *Underwater Acoustic Modeling: Principles, techniques and applications*, 2nd ed. E & FN Spon, 1996.

[EY36] C. Eckart and G. Young, "The approximation of one matrix by another of lower rank," *Psychometrika*, vol. 1, no. 3, pp. 211–218, Sep. 1936.

[FG82] R. E. Francois and G. R. Garrison, "Sound absorption based on ocean measurements. Part II: Boric acid contribution and equation for total absorption," *J. Acoustical Society of America*, vol. 72, no. 6, pp. 1879–1890, Dec. 1982.

[Fra80] R. Frank, "Polyphase complementary codes," *IEEE Trans. Information Theory*, vol. 26, no. 6, pp. 641–647, Nov. 1980.

[GBS70] T. H. Glisson, C. Black, and A. P. Sage, "On sonar signal analysis," *IEEE Trans. Aerospace and Electronic Systems*, vol. AES-6, no. 1, pp. 37–50, Jan. 1970.

[GdM03] T. C. Gallaudet and C. P. de Moustier, "High-frequency volume and boundary acoustic backscatter fluctuations in shallow water," *J. Acoustical Society of America*, vol. 114, no. 2, pp. 707–725, Aug. 2003.

[GHM04] C. F. Greenlaw, D. V. Holliday, and D. E. McGehee, "High-frequency scattering from saturated sand sediments," *J. Acoustical Society of America*, vol. 115, no. 6, pp. 2818–2823, Jun. 2004.

[GJ02] G. Ginolhac and G. Jourdain, ""Principal component inverse" algorithm for detection in the presence of reverberation," *IEEE J. Oceanic Engineering*, vol. 27, no. 2, pp. 310–321, Apr. 2002.

[GS65] S. Golomb and R. Scholtz, "Generalized Barker sequences," *IEEE Trans. Information Theory*, vol. 11, no. 4, pp. 533–537, Oct. 1965.

[GT84] S. W. Golomb and H. Taylor, "Constructions and properties of Costas arrays," *Proc. IEEE*, vol. 72, no. 9, pp. 1143–1163, Sep. 1984.

[HCT97] P. C. Hines, A. J. Collier, and J. A. Theriault, "Two-way time spreading and path loss in shallow water at 20-40 kHz," *IEEE J. Oceanic Engineering*, vol. 22, no. 2, pp. 299–308, Apr. 1997.

[HE97] P. C. Hines and D. D. Ellis, "High-frequency reverberation in shallow water," *IEEE J. Oceanic Engineering*, vol. 22, no. 2, pp. 292–298, Apr 1997.

[HKP06] R. D. Hollett, R. T. Kessel, and M. Pinto, "At-sea measurements of diver target strengths at 100 kHz: Measurement technique and first results," DTIC Document, Tech. Rep., 2006.

[Hod11] R. P. Hodges, *Underwater Acoustics: Analysis, Design and Performance of Sonar*. Wiley, 2011.

[Höh13] P. Höher, *Grundlagen der digitalen Informationsübertragung: Von der Theorie zu Mobilfunkanwendungen*, 2nd ed. Springer Fachmedien Wiesbaden, 2013.

[HS80] V. G. Hansen and J. H. Sawyers, "Detectability loss due to "greatest of" selection in a cell-averaging CFAR," *IEEE Trans. Aerospace and Electronic Systems*, vol. AES-16, no. 1, pp. 115–118, Jan. 1980.

[JH91] G. Jourdain and J. P. Henrioux, "Use of large bandwidth-duration binary phase shift keying signals in target delay Doppler measurements," *J. Acoustical Society of America*, vol. 90, no. 1, pp. 299–309, Jul. 1991.

[KH06] R. T. Kessel and R. D. Hollett, "Underwater intruder detection sonar for harbour protection: state of the art review and implications," DTIC Document, Tech. Rep., 2006.

[Kro69] J. J. Kroszczynski, "Pulse compression by means of linear-period modulation," *Proc. IEEE*, vol. 57, no. 7, pp. 1260–1266, Jul. 1969.

[KW65] E. J. Kelly and R. P. Wishner, "Matched-filter theory for high-velocity, accelerating targets," *IEEE Trans. Military Electronics*, vol. 9, no. 1, pp. 56–69, Jan. 1965.

[LA99] A. P. Lyons and D. A. Abraham, "Statistical characterization of high-frequency shallow-water seafloor backscatter," *J. Acoustical Society of America*, vol. 106, no. 3, pp. 1307–1315, Sep. 1999.

[Ler69] C. C. Leroy, "Development of simple equations for accurate and more realistic calculation of the speed of sound in seawater," *J. Acoustical Society of America*, vol. 46, no. 1B, pp. 216–226, Jul. 1969.

[Lin88] Z. Lin, "Wideband ambiguity function of broadband signals," *J. Acoustical Society of America*, vol. 83, no. 6, pp. 2108–2116, Jun. 1988.

[LZ13] J. Li and H. Zhou, "Tracking of time-evolving sound speed profiles in shallow water using an ensemble Kalman-particle filter," *J. Acoustical Society of America*, vol. 133, no. 3, pp. 1377–1386, Mar. 2013.

[MA64] C. M. McKinney and C. D. Anderson, "Measurements of backscattering of sound from the ocean bottom," *J. Acoustical Society of America*, vol. 36, no. 1, pp. 158–163, Jan. 1964.

[May83] G. A. May, "Correlation sonar using pseudo-random noise codes," Ocean Sciences, Sidney, Tech. Rep., 1983.

[McD93] S. T. McDaniel, "Sea surface reverberation: A review," *J. Acoustical Society of America*, vol. 94, no. 4, pp. 1905–1922, Oct. 1993.

[Min02] J. Minkoff, *Signal Processing Fundamentals and Applications for Communications and Sensing Systems*. Artech House, 2002.

[Mor87] D. R. Morgan, "Two-dimensional normalization techniques," *IEEE J. Oceanic Engineering*, vol. 12, no. 1, pp. 130–142, Jan 1987.

[Nas04] G. Nash, "Preliminary report on pulse compression waveforms and their application to waveform agility," DTIC Document, Tech. Rep., 2004.

[NH13] M. Noemm and P. A. Hoeher, "CutFM: A novel sonar signal design," in *Proc. Future Security Conf.*, Sep. 2013.

[NH15] ——, "CutFM sonar signal design," *Applied Acoustics*, vol. 90, pp. 95 – 110, Apr. 2015.

[Nut81] A. H. Nuttall, "Some windows with very good sidelobe behavior," *IEEE Trans. Acoustics, Speech and Signal Processing*, vol. 29, no. 1, pp. 84–91, Feb. 1981.

[OL02] J.-R. Ohm and H. D. Lüke, *Signalübertragung: Grundlagen der digitalen und analogen Nachrichtenübertragungssysteme*, 8th ed. Springer, 2002.

[Pac09] P. E. Pace, *Detecting and Classifying Low Probability of Intercept Radar*. Artech House, 2009.

[PW72] W. W. Peterson and E. J. J. Weldon, *Error-Correcting Codes*. The MIT Press, 1972.

[Ric03] D. W. Ricker, *Echo Signal Processing*. Kluwer Academic Publishers, 2003.

[Roh83] H. Rohling, "Radar CFAR thresholding in clutter and multiple target situations," *IEEE Trans. Aerospace and Electronic Systems*, vol. AES-19, no. 4, pp. 608–621, July 1983.

[Roh11] ——, "Ordered statistic CFAR technique - an overview," in *Proc. Int. Radar Symposium (IRS)*, Sep. 2011, pp. 631–638.

[RZ96] K. Rosenbach and J. Ziegenbein, "Method and device for determining target speed and distance with frequency modulated pulses," Jan. 1996, U.S. Patent 5 481 504.

[Sko90] M. I. Skolnik, *Radar Handbook*, 2nd ed. McGraw-Hill, 1990.

[SS64] M. Schulkin and R. Shaffer, "Backscattering of sound from the sea surface," *J. Acoustical Society of America*, vol. 36, no. 9, pp. 1699–1703, Sep. 1964.

[ST81] L. H. Sibul and E. L. Titlebaum, "Volume properties for the wideband ambiguity function," *IEEE Trans. Aerospace and Electronic Systems*, vol. AES-17, no. 1, pp. 83–87, Jan. 1981.

[SW59] J. L. Stewart and E. Westerfield, "A theory of active sonar detection," *Proc. IRE*, vol. 47, no. 5, pp. 872–881, May 1959.

[Tho62] R. C. Thor, "A large time-bandwidth product pulse-compression technique," *IRE Trans. Military Electronics*, vol. MIL-6, no. 2, pp. 169–173, Apr. 1962.

[Tho67] W. H. Thorp, "Analytic description of the low-frequency attenuation coefficient," *J. Acoustical Society of America*, vol. 42, no. 1, pp. 270–270, Jan. 1967.

[TKK82] D. W. Tufts, R. Kumaresan, and I. Kirsteins, "Data adaptive signal estimation by singular value decomposition of a data matrix," *Proc. IEEE*, vol. 70, no. 6, pp. 684–685, June 1982.

[Urk67] H. Urkowitz, "Energy detection of unknown deterministic signals," *Proc. IEEE*, vol. 55, no. 4, pp. 523–531, Apr. 1967.

[Wai02] A. D. Waite, *Sonar for Practising Engineers*, 3rd ed. Wiley, 2002.

[War01] S. Ward, "The use of sinusoidal frequency modulated pulses for low-Doppler detection," in *Proc. MTS/IEEE Conf. OCEANS*, vol. 4, Nov. 2001, pp. 2147–2151.

[WP83] G. R. Wilson and D. R. Powell, "Probability density estimates of surface and bottom reverberation," *J. Acoustical Society of America*, vol. 73, no. 1, pp. 195–200, Jan. 1983.

[Yar10] R. K. R. Yarlagadda, *Analog and Digital Signals and Systems*. Springer US, 2010.

[Zha07] Z. Y. Zhang, "Diver detection sonars and target strength: review and discussions," in *Proc. 14th Inter. Conf. Sound and Vibration (ICSV14)*, Jul. 2007.